



HAL
open science

Etude du phénomène de fretting-usure d'un contact plan/plan 34NiCrMo16 : application et modélisation du concept d'oxygénation de l'interface

Soha Baydoun

► **To cite this version:**

Soha Baydoun. Etude du phénomène de fretting-usure d'un contact plan/plan 34NiCrMo16 : application et modélisation du concept d'oxygénation de l'interface. Other. Université de Lyon, 2020. English. NNT : 2020LYSEC030 . tel-03167098

HAL Id: tel-03167098

<https://theses.hal.science/tel-03167098>

Submitted on 11 Mar 2021

HAL is a multi-disciplinary open access archive for the deposit and dissemination of scientific research documents, whether they are published or not. The documents may come from teaching and research institutions in France or abroad, or from public or private research centers.

L'archive ouverte pluridisciplinaire **HAL**, est destinée au dépôt et à la diffusion de documents scientifiques de niveau recherche, publiés ou non, émanant des établissements d'enseignement et de recherche français ou étrangers, des laboratoires publics ou privés.



ÉCOLE
CENTRALE LYON

N° d'ordre NNT: 2020LYSEC30

THÈSE de DOCTORAT DE L'UNIVERSITÉ DE LYON

Présentée devant l'École Centrale de Lyon

École Doctorale N° 34

École Doctorale des Matériaux de Lyon

Spécialité de doctorat: Matériaux

Soutenue publiquement le 12/11/2020, par:

Soha BAYDOUN

**Etude du phénomène de fretting-usure d'un contact plan/plan
34NiCrMo16: Application et modélisation du concept
d'oxygénation de l'interface**

**Investigation of fretting wear of a flat-on-flat 34NiCrMo16
interface: Application and modelling of the contact oxygenation
concept**

Devant le jury composé de:

Philip SHIPWAY	Professeur, University of Nottingham	Rapporteur
Cécile LANGLADE	Professeur, Université de Technologie de Belfort-Montbéliard	Rapporteuse
Pierre MONTMITONNET	Directeur de Recherches CNRS, MINES ParisTech	Président du jury
Christian GEINDREAU	Professeur, Université Grenoble Alpes	Examineur
Vladislav YASTREBOV	Chargé de Recherche CNRS, MINES ParisTech	Examineur
Siegfried FOUVRY	Directeur de Recherche CNRS, École Centrale de Lyon	Directeur de thèse
Sylvie DESCARTES	Ingénieur de Recherche HDR, INSA de Lyon	Co-directrice de thèse

Abstract

This PhD thesis aims at understanding and modelling dry fretting wear of a flat-on-flat steel contact submitted to various loading conditions including number of fretting cycles, sliding amplitude, contact pressure, sliding frequency, contact size and contact orientation with respect to the sliding direction. Fretting-wear kinetics was studied by varying these loading conditions which affect wear mechanisms including debris formation and ejection in addition to tribo-oxidation, abrasion and adhesion. This investigation shows that, in most cases, a composite wear scar is detected combining oxidative-abrasive and adhesive wear. A wear-kinetics model was proposed by empirically extending the existing classical wear laws taking into account the aforementioned loading parameters. Nevertheless, this model assumed an averaged global wear-rate description neglecting the composite abrasive-adhesive nature of wear and consequently the inherited wear-rate local variations along the fretting scar.

Achieving a dynamic wear-kinetics description incorporating the partition of abrasive and adhesive wear necessitates understanding the evolution of these mechanisms. To attain this goal, Contact Oxygenation Concept (COC) is assumed. This approach suggests that adhesion appears in the contact center if the di-oxygen partial pressure is below a threshold value. In the lateral sides, where di-oxygen molecules are sufficient, oxidation and abrasion prevail. COC was quantified using the “oxygen-distance” parameter defined as the averaged width of the external abrasion-corona. Oxygen-distance evolution was formalized versus loading conditions using a power-law formulation which allowed predicting wear transitions for plain and macro-textured surfaces. However, this formulation remained parametric; hence, more physical interpretation of COC is pursued.

To achieve the latter objective, an advection-dispersion-reaction approach (ADR) is introduced to model oxygen transport within fretting interface assuming debris bed as a compact porous medium. This ADR approach not only predicted the partition of abrasion and adhesion but also captured the transition from pure abrasive to mixed abrasive-adhesive wear at different loading conditions.

Keywords: Fretting wear; Flat-on-flat contact; Contact oxygenation concept (COC); Oxidational-abrasive adhesive wear; Advection-Dispersion-Reaction model (ADR).

Résumé

Cette thèse vise à comprendre et modéliser l'usure par fretting à sec d'un contact plan/plan en acier soumis à diverses conditions de chargement, notamment le nombre de cycles de fretting, l'amplitude de glissement, la pression de contact, la fréquence de glissement, la taille du contact et l'orientation du contact par rapport à la direction de glissement. La cinétique d'usure a été étudiée en variant ces conditions qui affectent les mécanismes d'usure, y compris la formation et l'éjection de débris en plus de la tribo-oxydation, de l'abrasion et de l'adhésion. Cette investigation montre que, dans la plupart des cas, une trace d'usure composite est détectée combinant une usure oxydo-abrasive et adhésive. Une formulation de cinétique d'usure a été proposée en étendant empiriquement les lois d'usure classiques existantes en tenant compte des paramètres de chargement susmentionnés. Néanmoins, cette formulation supposait une description du taux d'usure global moyen négligeant la nature composite abrasive-adhésive de l'usure et, par conséquent, les variations locales du taux d'usure le long de la trace d'usure.

La réalisation d'une description dynamique de la cinétique d'usure intégrant la répartition de l'usure abrasive et adhésive nécessite de comprendre l'évolution de ces mécanismes. Pour atteindre cet objectif, le Concept d'Oxygénation de Contact (COC) est supposé. Cette approche suggère que l'adhésion apparaît dans le centre de contact si la pression partielle de dioxygène est inférieure à une valeur seuil. Dans les côtés latéraux, où les molécules de dioxygène sont présentes en quantité suffisante, l'oxydation et l'abrasion prévalent. Le COC a été quantifié à l'aide du paramètre «distance d'oxygène» défini comme la largeur moyenne de la couronne d'abrasion externe. L'évolution de la distance d'oxygène a été formalisée par rapport aux conditions de chargement en utilisant une formulation de loi puissance qui a permis de prédire les transitions d'usure pour les surfaces lisses et macro-texturées. Cependant, cette formulation est restée paramétrique; par conséquent, une interprétation plus physique du COC est recherchée.

Pour atteindre ce dernier objectif, une approche d'Advection-Dispersion-Réaction (ADR) est introduite pour modéliser le transport d'oxygène dans l'interface de fretting en supposant que le lit de débris est un milieu poreux compact. Cette approche ADR a non seulement prédit la répartition de l'abrasion et de l'adhésion, mais a également capturé la transition de l'usure abrasive pure à l'usure adhésive-abrasive mixte pour différentes conditions de chargement.

Mots-clés: Usure-Fretting; Contact plan/plan; Concept d'Oxygénation de Contact (COC); Usure adhésive oxydo-abrasive; Modèle d'Advection-Dispersion-Réaction (ADR).

To my parents

“And lower to them the wing of humility out of mercy and say: My Lord, bestow on them your mercy as they brought me up when I was young” Al-Isra (The Night Journey) 17:24

Acknowledgement

This PhD thesis is the fruit of collaboration between LTDS Laboratory (ECL) and LAMCOS Laboratory (INSA) funded by the French ANR agency. The goal of this work would not have been fulfilled without the constant support of many kind people to whom I express my deepest gratitude.

I would like to thank firstly Dr. Siegfried Fouvry, the PhD director at LTDS, for accepting me in this PhD and for integrating me in the Fretting-Fatigue team which I was honored to be part of. Thank you for your time, smart scientific advice, valuable discussions and for introducing me to the world of tribology and materials which broadened my experience in the field of vibration, friction and interfaces. I am equally indebted to Dr. Sylvie Descartes, the PhD co-director at LAMCOS, for her time and for integrating me in the family of LAMCOS Laboratory where I had the chance to know the field of the third body rheology. Thank you both for believing in my potentials since our very first meeting and for giving me the freedom to manage my targets during this PhD.

I wish to express my sincere appreciation to the jury members starting from Pr. Pierre Montmitonnet for accepting to be the president of the jury and Pr. Cécile Langlade and Pr. Philip Shipway for being the thesis referees and for the time you spent on qualifying my work. My warm thanks go to Dr. Vladislav Yastrebov and Pr. Christian Geindreau for accepting to examine this PhD thesis. It was a big honor to have you as jury members and to discuss with you this work.

I wouldn't want to forget Pierre Arnaud for the prolific participation in this PhD especially in the numerical simulations (Wear box) and in the ADR model which was a wonderful output of this collaboration. Many thanks to Julie Laporte, Jean-Michel Vernet, Olivier Graton, Sebastien Henry, Gaylord Guillonnet, Bernard Beaugiraud and Odin Sassy for their scientific and technical support. I would like to thank also Dominique Vincentelli, Sylvie Navarro and Hélène Schoch for their administrative help.

Not to forget my kind-hearted friends and officemates at the "Bureau des filles" and the "Open space-4008": Alixe for the valuable advice, nice discussions and for her strong passion and confident personality which inspired me a lot; Jean for his infinitely kind spirit, boundless assistance, generosity, and for sure the interesting conversations, and for introducing me to

the world of polishing, cracks and microstructures; Julien Saïd for integrating me in the lab since my day one, teaching me new French terms, organizing exciting activities at D4, and of course for introducing us to the “Petit Gandalf”; finally Benjamin Dieu for his constructive advice, kindness and for spreading good vibes in 4008. I would like to equally thank all the other PhD students from the Fretting-Fatigue team starting by the “old”: Florent with whom the conferences were interesting, Pierre, Nora, Julien Ferniot, Estelle, and Ariane, then by the “new”: Sebastien, Théo, Pauline, Mélody, and Hugo, ending by good wishes for the future PhD students. Besides, I would like to thank all the interns at LTDS for the nice moments especially Sibel, Solène, Clotilde and Paco. I won’t forget of course all the kind persons I got to know during the PhD including Simon, Bruno, Michelle, Sylvain, “les deux Stephane”, Elise, Mingfa, Synthia, Clémence, Mathilde, Vincent, Quentin, Li, Yinyin, Johann, Andi, Kévin, Salomé, Mariana, Nasrya, Mayssa, Amal, Vilayvone, Thibaut, . . .

I am deeply grateful to my friends in Lyon starting from Hadi and Sara for being respectively my brother and sister in Lyon, for the exciting debates, scientific discussions, and the delicious meals; Batoul and Riva for the delightful vacations and support. Besides, I would like to thank the best couple Zahraa and Haidar for all the support and the enchanted moments. I would like also to thank Noha, Nour, and Shaymaa for the nice time we spent. I am also grateful to Dr. Jeanne Doreau-Malioche, my Master two internship supervisor in Grenoble, for constantly encouraging me along the thesis.

Finally, I wish to acknowledge my parents whose unconditional love, unwavering support, and tender heart backed me all the way. Thank you for believing in my potentials and sacrificing a lot to help me achieve my goals. Big thanks to my lovely sisters Israa and Maysaa and my cute brother Firas, and specifically my sister Orsola, the big heart who has been always understanding and supporting me in the hard moments, and whose advice is always the key to wise decisions.

Contents

Abstract	iii
Résumé	v
Acknowledgement	ix
List of Figures	xxvii
List of Tables	xxix
General Introduction	2
1 Literature review	5
1.1 Introduction	6
1.2 Fretting wear	7
1.3 Sliding modes	8
1.4 Contact configurations	9
1.5 Fretting cycle	10
1.6 Sliding conditions	12
1.7 Characterization of sliding regimes	13
1.8 Sliding regimes and fretting maps	14
1.9 Sliding transition criteria	15
1.10 Qualitative description of wear	16
1.10.1 Abrasive wear	17
1.10.2 Adhesive wear	17
1.10.3 Fatigue wear	18
1.10.4 Corrosive wear	18
1.10.5 Composite wear	19
1.11 Tribologically transformed structures	19
1.11.1 Description of the main features of TTS	19
1.11.2 TTS formation mechanisms	20
1.12 Quantitative description of wear	22
1.12.1 Approaches for wear kinetics quantification	23
1.12.2 Approaches for wear mechanisms description	30
1.13 Conclusion	38

2	Materials and experimental procedure	40
2.1	Material	41
2.1.1	Chemical composition	41
2.1.2	Microstructure	41
2.1.3	Mechanical properties	41
2.2	Contact configuration	42
2.2.1	Surface roughness	42
2.2.2	Plain flat-on-flat samples	43
2.2.3	Textured samples: access to smaller contact sizes	44
2.3	Numerical investigation of the pressure distribution in the studied flat contact . .	45
2.4	Fretting wear experimental set-up	47
2.5	Data acquisition	48
2.6	Experimental strategy	48
2.6.1	Plain samples	48
2.6.2	Textured samples test strategy	49
2.7	Damage characterization	50
2.7.1	Optical observation	50
2.7.2	Wear analysis	50
2.7.3	Scanning by electron microscopy (SEM)	52
2.7.4	Raman spectroscopy	53
2.7.5	Nano-indentation	54
2.8	Conclusion	56
3	Fretting wear kinetics of flat-on-flat contact	58
3.1	Introduction	59
3.2	Plain crossed flat-on-flat contact configuration	59
3.2.1	Friction analysis	59
3.2.2	Wear evolution	62
3.2.3	Wear volume prediction model	77
3.3	Results validation using textured samples: access to smaller contact sizes	83
3.3.1	Grooves' fill-up mechanism	84
3.3.2	Rheology of the third body particles	86
3.3.3	Qualitative validation of the contact size effect	89
3.3.4	Quantitative validation of experimental results	92
3.4	Stability of the composite-wear model using tests outside calibration domain . .	93
3.5	Wear depth prediction	94
3.6	Conclusion	97
4	Experimental investigation of adhesive wear extension in fretting interface	99
4.1	Introduction	100
4.2	Experimental procedure	101
4.2.1	Surface observation of abrasion and adhesion zones	102
4.2.2	Experimental estimation of oxygen distance " d_O " parameter from fretting scar expertise	104
4.3	Experimental results	106
4.3.1	Plain crossed flat-on-flat contact configuration	106

4.3.2	Textured crossed flat-on-flat contact	115
4.4	Discussion	120
4.4.1	Frequency effect	120
4.4.2	Contact pressure effect	120
4.4.3	Test duration effect	122
4.4.4	Sliding amplitude effect	122
4.4.5	Contact size and sliding orientation	123
4.4.6	Summary	124
4.5	Conclusion	124
5	ADR Modelling of adhesive fretting wear extension	127
5.1	Introduction	128
5.2	ADR model	129
5.2.1	Gas transport in debris bed	130
5.2.2	Reaction term	133
5.2.3	ADR continuity equation	134
5.3	Numerical solution of the ADR continuity equation	134
5.3.1	Finite difference scheme	134
5.3.2	Solution method	136
5.3.3	Steady-state solution	136
5.4	Parameters identification and model calibration	137
5.4.1	Illustration of the studied interface	137
5.4.2	Properties of the debris layer porous medium	139
5.4.3	Threshold partial pressure ($P_{O_2,th}$)	141
5.4.4	Identification of the reaction rate coefficient (r_{O_2})	142
5.4.5	Qualitative comparison with fretting experiments	143
5.5	Model validation	145
5.5.1	Test strategy	145
5.5.2	Effect of sliding frequency (f)	145
5.5.3	Effect of contact pressure (p)	148
5.5.4	Archard power density factor formulation	149
5.5.5	Effect of contact area (A)	150
5.5.6	Quantitative validation of ADR approach	152
5.6	Discussion	154
5.7	Conclusion	158
	General conclusion and perspectives	161
	References	164

List of Figures

1.1	Early tribological achievements: (a) Paleolithic method of igniting fire by rotating a wooden stick on a dry rock or wood as an early testimonial on tribological application; (b) a Mesopotamian wheel around 3500 B.C; (c) using lubricants by Egyptians to transport a statue to the grave of Tehuti-Hetep, El-Bersheh around 1880 B.C; (d) tribological experiments proposed by Leonardo da Vinci (1452–1519).	6
1.2	Fretting damage in industrial applications.	8
1.3	Fretting damage in civil engineering structures [17–20].	8
1.4	Sliding modes of a sphere-on-flat contact configuration (after Blanpain et al. (1995) [21]).	9
1.5	Contact configurations used in fretting wear tests.	10
1.6	Schematic representation of the fretting cycle (after [27]).	11
1.7	Definition of the sliding ratio “e” and identification of the transition state between alternating sliding and fretting regimes [30, 31].	13
1.8	(a) Partial slip condition characterized by an elliptic fretting loop and a mixed stick and slip surface; (b) gross slip condition characterized by a quadratic fretting loop and a slip worn surface (After Vingsbo et al. (1988) [12]).	14
1.9	Transition between partial slip and gross slip on one side and fretting and reciprocating sliding on the other side.	15
1.10	Fretting maps: (a) running condition fretting map (RCFM); (b) material response fretting map (MRFM) [35].	15
1.11	Quantification of the sliding transition through transition criteria [14].	16
1.12	Schematic presentation of two-body and three-body abrasive wear.	17
1.13	Schematic illustration of adhesive wear.	18
1.14	Schematic presentation of fatigue wear.	18

1.15	Schematic presentation of corrosive wear [27].	19
1.16	SEM images and EDX maps showing a composite abrasive-adhesive wear of titanium alloy after fretting test [31].	19
1.17	(a) BSE observations of the TTS in a sectional view of etched cylindrical specimen of high strength steel (BS S132) [51]; (b) schematic illustration of a metallographic cross section of a fretting scar revealing the location of the TTS [49].	20
1.18	TTS formation by recrystallization due to high plastic deformation [49, 64].	21
1.19	Illustration of the limitation of Archard's approach regarding the coefficient of friction [35]: (a) evolution of the friction coefficient for the high porosity side of the material (side 1); (b) evolution of the friction coefficient for the low porosity side of the material (side 2); (c) distribution of the wear volume versus Archard work.	24
1.20	Wear map taking into account the shakedown behavior for high wear regime (side 1) $16,000 < K(\mu\text{m}^3/\text{N.m}) < 38,000$ and low wear regime (side 1) $K(\mu\text{m}^3/\text{N.m}) < 3000$ [35].	25
1.21	Stability of the friction energy wear approach with the coefficient of friction [35]: (a) evolution of the friction coefficient for the high porosity side of the material (side 1); (b) evolution of the friction coefficient for the low porosity side of the material (side 2); (c) distribution of the wear volume versus the cumulated dissipated friction energy.	26
1.22	Schematization of the wear process through the energy approach: initial activation energy is required for the genesis of TTS before generating the debris particles [35].	27
1.23	Evolution of the (a) friction coefficient and the (b) energy wear coefficient versus the contact radius and the contact area respectively for Hertzian sphere-on-flat and cylinder-on-flat contacts in a dry chromium steel interface [82]; (c) evolution of the wear rates versus the applied load for two contact geometry orientations with respect to sliding direction (after [86]).	28
1.24	Evolution of the energy wear rate as a function of the friction energy density for a TA6V / TA6V contact [56].	29
1.25	Schematic illustration of the wear model proposed by Dreano et al. [91] describing the low and high temperature fretting wear response of a cobalt-based alloy using a combined friction energy and tribo-oxidation formulation.	30
1.26	Velocity accommodation mechanisms. After Berthier et al. (1988) [13].	31
1.27	Tribological circuit for an elementary 2D interface [50].	32

1.28	Relative influence of the detachment of particles, the thickness of third body at the interface, and the ejection of these particles [93].	33
1.29	Competition of the source flow and wear flow as a function of the thickness of the third body [93].	33
1.30	Explanation of the methodology used to quantify the fretting scar morphology from fretting wear experiment through the: (a) identification of the worn profiles; (b) identification of the third body profile; and (c) extrapolation of the third body and wear profiles. (d) Comparison of the evolution of the maximum wear thickness and maximum third body thickness versus the number of fretting cycles [96].	34
1.31	Comparison between the experimental and simulated wear profiles on the flat counterpart of a dry homogeneous TA6V cylinder-on-flat configuration (a) without third body consideration ($\gamma=0$); (b) with third body consideration ($\gamma(x) = \gamma_0 + K_\gamma \cdot x$) [96].	35
1.32	Relative cohesion of the solid third body, SEM images: (a) very low; (b) low; (c) high. Relative ductility of the solid third body, SEM images: (d) low; (e) not very high; (f) high [50].	36
1.33	Schematic illustration of the contact oxygenation concept for a fretting contact submitted to different loading conditions [56].	37
2.1	(a) Martensite structure of 34NiCrMo16 after chemical etching with nital; (b) phase transition from a cubic body-centered (BCC) alpha iron (α -Fe or ferrite) to a cubic face-centered (FCC) gamma iron (γ -Fe or austenite).	42
2.2	(a) Optical image of 34NiCrMo16 flat surface; (b) one-dimensional roughness profile along the sampling distance “ l ”.	43
2.3	(a) Schematic presentation of the studied crossed flat-on-flat contact configuration; (b) flat-on-flat configuration in turbine engine dovetail blade/disk contact.	43
2.4	(a) Crossed flat-on-flat configuration with textured bottom samples; (b) geometrical description of the textures orientation with respect to the sliding direction.	45
2.5	Illustration of the: (a) 2D contact configuration injected in the “wear box” model; (b) finite element flat-on-flat contact model and the loading criteria (after [95, 116]).	46
2.6	(a) Contact pressure distribution along the interface of the bottom sample; (b) evolution of the maximum, mean and central contact pressure versus the number of cycles for the bottom sample under the reference test conditions: N=20000 cycles, p=100 MPa, and $\delta_g = \pm 100 \mu m$	47

2.7	(a) Fretting wear experimental set-up at LTDS Laboratory; (b) schematic illustration of the experimental set-up.	47
2.8	(a) Illustration of the parameters obtained from fretting cycle under gross slip condition; (b) fretting log with δ_g maintained constant by adjusting δ^*	48
2.9	Multi-scale experimental strategy involving different loading conditions: (a) contact pressure versus sliding amplitude; (b) fretting cycles versus frequency; and (c) contact length ($L_{\perp\delta}$) versus contact length ($L_{\parallel\delta}$).	49
2.10	Experimental campaigns for textured samples at variable: (a) contact pressure (b) sliding amplitude, and (c) frequency.	50
2.11	Optical observations of the fretting scar: (a) before and (b) after cleaning.	50
2.12	Illustration of the computation of the wear volume using 3D profilometry.	51
2.13	3D profiles of the top and bottom samples and schematic illustration of the computation of the average 2D wear profiles ($2D_{ave}$).	52
2.14	Different types of signals generated from electron-matter interaction and the resulting images for each signal (SE, BSE, EDX).	53
2.15	(a) Raman spectroscopy components; (b) scattering of light by the sample molecules; (c) illustration of the Raman spectrum [117].	54
2.16	Illustration of the nano-indentation loading and unloading curves and the models applied for computing the projected contact area.	55
3.1	Variation of the friction coefficients (μ & μ_e) with test duration for the reference test (N=20000 cycles, p=100 MPa, $\delta_g = \pm 100 \mu m$, f=1 Hz and A=25 mm^2).	59
3.2	(a) Experimental fretting cycle at N=20000; (b) comparison between FEM and the corrected experimental fretting cycle using Equation 3.1 (test system compliance correction) under reference test conditions (N=20000 cycles, p=100 MPa, $\delta_g = \pm 100 \mu m$, f=1 Hz and A=25 mm^2).	60
3.3	Variation of the average energy friction coefficient μ_e as a function of the (a) number of cycles; (b) contact pressure; (c) sliding amplitude; (d) frequency (e) contact length $L_{\parallel\delta}$; and (f) contact length $L_{\perp\delta}$	61
3.4	(a) Variation of the wear volumes of the top and bottom samples with the number of cycles; (b) evolution of the total wear volume with the number of cycles; and (b) variation of the total wear volume with the cumulated dissipated friction energy (N=5000-40000 cycles such that: p=100 MPa, $\delta_g = \pm 100 \mu m$, f=1 Hz and A=25 mm^2).	62

3.5	Raman spectra of the fretting scar (external abrasion corona) for N=5000, 20000 and 40000 cycles (p=100 MPa, $\delta_g = \pm 100 \mu m$, f=1 Hz and A=25 mm ² , for Laser wavelength $\lambda = 785$ nm, Laser power=0.35 mV, and acquisition time=150 s). . .	64
3.6	Variation of total wear volume with the (a) contact pressure and (b) cumulated friction energy; (c) variation of the individual energy wear rate α with the contact pressure (p=10-175 MPa such that N=20000 cycles, $\delta_g = \pm 100 \mu m$, f=1 Hz, and A=25 mm ²).	64
3.7	(a) Evolution of the ratio of the depth wear rate to the normal stress of a steel conical rider plotted against the normal stress [131]. Sketch of stress distribution in and around local asperities which are in contact: (b) at very low stress; (c) at stress equal to one third of the hardness [131].	65
3.8	(a) Experimental results from Welsh [133] displaying load-dependent wear kinetics; (b) load-displacement map showing change of transition loads (p_1 and p_2) with the sliding speeds (after Welsh [133]).	66
3.9	Raman spectra of the fretting scar (external abrasion corona) for p=10, 100, and 175 MPa (N=20000, $\delta_g = \pm 100 \mu m$, f=1 Hz and A=25 mm ² , for Laser wavelength $\lambda = 785$ nm, Laser power=0.35 mV, and acquisition time=150 s).	68
3.10	Variation of total wear volume with the: (a) the sliding amplitude and (b) cumulated friction energy; (c) variation of the individual energy wear rate with the sliding amplitude ($\delta_g = \pm 25$ - $\pm 200 \mu m$ such that N=20000 cycles, p=100 MPa, f=1 Hz and A=25 mm ²).	69
3.11	Raman spectra of the fretting scar (external abrasion corona) for $\delta_g = \pm 25$, ± 100 and $\pm 200 \mu m$ (N=20000 cycles, p=100 MPa, f=1 Hz and A=25 mm ² , for Laser wavelength $\lambda = 785$ nm, Laser power=0.35 mV, and acquisition time=150 s). . .	70
3.12	Variation of the (a) total wear volume and the (b) energy wear rate with frequency (f=0.5-10 Hz such that N=20000 cycles, p=100 MPa, $\delta_g = \pm 100 \mu m$ and A=25 mm ²).	70
3.13	Raman spectra of the fretting scar (external abrasion corona) for three frequencies f=0.5, 1 and 10 Hz (N=20000 cycles, p=100 MPa, $\delta_g = \pm 100 \mu m$ and A=25 mm ² , for Laser wavelength $\lambda = 785$ nm, Laser power=0.35 mV, and acquisition time=150 s).	72
3.14	Evolution of the (a) mean wear depth and the (b) energy wear rate as a function of the contact length $L_{\parallel\delta}$ (N=20000 cycles, p=100 MPa, $\delta_g = \pm 100 \mu m$, f=1 Hz and $L_{\perp\delta} = 5$ mm).	73

3.15	Evolution of the debris ejection (TBA) (optical images) and the contact oxygenation (COC) (EDX maps) as a function of the contact length $L_{\parallel\delta}$ (N=20000 cycles, p=100 MPa, $\delta_g=\pm 100 \mu m$, f=1 Hz and $L_{\perp\delta}=5$ mm).	73
3.16	Evolution of the energy wear rate “ α ” versus $\delta_g/L_{\parallel\delta}$ (N=20000 cycles, p=100 MPa, f=1 Hz, and $L_{\perp\delta}=5$ mm).	74
3.17	Comparison of the (a) mean wear depth; (b) energy wear rate and the (c) relative wear contributions of COC and TBA as a function of the contact lengths $L_{\parallel\delta}$ and $L_{\perp\delta}$ such that $L_{\parallel\delta}=5$ mm if $L_{\perp\delta}$ varies and $L_{\perp\delta}=5$ mm if $L_{\parallel\delta}$ varies (N=20000 cycles, p=100MPa, $\delta_g=\pm 100 \mu m$ and f=1 Hz).	75
3.18	Reduction in the stabilized thickness of the third body caused by the faster ejection of debris particles (after [93]).	76
3.19	Raman spectra of the fretting scar (external abrasion corona) for three contact configurations $L_{\parallel\delta}=L_{\perp\delta}=5$ mm (O), $L_{\parallel\delta}=2$ mm & $L_{\perp\delta}=5$ mm (I) and $L_{\perp\delta}=2$ mm & $L_{\parallel\delta}=5$ mm (J) (N=20000 cycles, p=100 MPa, $\delta_g=\pm 100 \mu m$, and f=1 Hz, for Laser wavelength $\lambda = 785$ nm, Laser power=0.35 mV, and acquisition time=150 s).	77
3.20	Variation of the total predicted wear volume ($V_{pred} = \alpha_{ref} \cdot \sum Ed$, Equation 3.5) as a function of the experimental wear volume (V_{exp}) considering all the tested loading conditions.	78
3.21	Compiling all the loading conditions to study the (a) variation of the energy wear rate as a function of the friction power density and (b) the evolution of the total predicted wear volume ($V_{pred} = \alpha_{\varphi*} \sum Ed$) as a function of the experimental wear volume (V_{exp}).	79
3.22	Variation of the standard deviation (E%) for all the loading conditions versus the exponent corresponding to the studied parameters: (a) number of cycles, (b) contact pressure, (c) frequency, (d) sliding amplitude, (e) $L_{\perp\delta}$, and (f) $\delta_g/L_{\parallel\delta}$ parameter.	81
3.23	Variation of total wear volume versus the: (a) weighted cumulated friction energy (Equation 3.11) and (b) weighted Archard work for all the loading conditions (Equation 3.12).	82
3.24	Grooves’ fill-up mechanism obtained from textured samples with $L_{\perp\delta}=2$ mm, and $L_{\parallel\delta}=5$ mm, for N=20000 cycles, p=100 MPa, $\delta_g=\pm 100 \mu m$ and f=1 Hz.	84

3.25	Schematic illustration of the grooves' fill-up mechanism: (1) initial stage; (2) ejection of debris particles; (3) agglomeration of debris particles on the top; (4) formation of a bridge of agglomerated debris on the top; (5) collapse and fall of some debris particles to the bottom; (6) accumulation of debris particles at the bottom; (7) clustering of debris particles on the top and bottom; (8) fill up of the hole with uncompact debris; (9) continuous compaction of the debris filling the hole.	85
3.26	SEM observations of grooves in: (a) textured sample with $L_{\perp\delta}=1.25$ mm and $L_{\parallel\delta}=5$ mm (before cleaning with ethanol); and (b) textured sample with $L_{\perp\delta}=5$ mm and $L_{\parallel\delta}=1.25$ mm (before cleaning with ethanol) (N=20000 cycles, p=100 MPa, $\delta_g=\pm 100$ μm and f=1 Hz).	86
3.27	SEM and BSE observations of a thin wear sheet (platelet) embedded in the ejected third body outside the grooves in a textured sample with $L_{\perp\delta}=1.25$ mm, and $L_{\parallel\delta}=5$ mm, N=20000 cycles, p=100 MPa, $\delta_g=\pm 100$ μm and f=1 Hz (before cleaning with ethanol).	87
3.28	SEM observations of the agglomerated powdery debris at the borders of the contact in: (a) textured sample with $L_{\perp\delta}=1.25$ mm and $L_{\parallel\delta}=5$ mm (before cleaning with ethanol); and (b) textured sample with $L_{\perp\delta}=5$ mm and $L_{\parallel\delta}=1.25$ mm (before cleaning with ethanol) (N=20000 cycles, p=100 MPa, $\delta_g=\pm 100$ μm and f=1 Hz).	87
3.29	Comparison of the compaction of the third body ejected within the grooves and outside the contact for: (a) textured sample $L_{\perp\delta}=1.25$ mm and $L_{\perp\delta}=5$ mm (before cleaning with ethanol); and (b) textured sample with $L_{\perp\delta}=5$ mm and $L_{\perp\delta}=1.25$ mm (before cleaning with ethanol) (N=20000 cycles, p=100 MPa, $\delta_g=\pm 100$ μm and f=1 Hz).	88
3.30	BSE observations of the (a) primary and secondary flows in a textured sample having $L_{\perp\delta}=1.25$ mm and $L_{\parallel\delta}=5$ mm (before cleaning with ethanol); and (b) primary and secondary flows in a textured sample having $L_{\perp\delta}=5$ mm and $L_{\parallel\delta}=1.25$ mm (before cleaning with ethanol) (N=20000 cycles, p=100 MPa, $\delta_g=\pm 100$ μm and f=1 Hz).	89
3.31	Comparison of the (a) optical observations, (b) EDX maps and (c) Oxygen to Iron ratio "[O]/[Fe]" of the bottom textured samples for both orientations with variable $L_{\perp\delta}$ and $L_{\parallel\delta}$ (after cleaning with ethanol) as a function of contact size per textures (N=20000 cycles, p=100 MPa, $\delta_g=\pm 100$ μm and f=1 Hz).	90

3.32	(a) Illustration of the binarization method used to estimate the ratio of oxidized area over unoxidized one for uncleaned top and bottom samples; (b) comparison of the ratio of oxidized area over unoxidized one for ($L_{\perp\delta}=1.25$ mm and $L_{\parallel\delta}=5$ mm) and ($L_{\perp\delta}=5$ mm and $L_{\parallel\delta}=1.25$ mm) orientations for both top and bottom samples (before cleaning with ethanol); (c) comparison of oxygen to iron ratio “[O]/[Fe]” of the top and bottom textured samples for ($L_{\perp\delta}=1.25$ mm and $L_{\parallel\delta}=5$ mm) and ($L_{\perp\delta}=5$ mm and $L_{\parallel\delta}=1.25$ mm) orientations (before cleaning with ethanol) (N=20000 cycles, p=100 MPa, $\delta_g=\pm 100$ μm and f=1 Hz).	90
3.33	Evolution of the (a) debris color with the textures orientations by varying $L_{\perp\delta}$ and $L_{\parallel\delta}$ (before cleaning with ethanol); (b) XRD patterns of the ejected debris with the textures orientations for ($L_{\perp\delta}=0.81$ mm and $L_{\parallel\delta}=5$ mm) and ($L_{\perp\delta}=5$ mm and $L_{\parallel\delta}=0.81$ mm) orientations (N=20000 cycles, p=100 MPa, $\delta_g=\pm 100$ μm and f=1 Hz).	91
3.34	Evolution of the (a) energy wear rate and the (b) relative energy wear rate contributions of COC and TBA versus contact size for plain and textured samples. .	92
3.35	Illustration of the quantitative cross-validation strategy of the wear kinetics model with X and Y \in [N, p, δ_g , f, $L_{\perp\delta}$ and $L_{\parallel\delta}$] [80, 145].	93
3.36	Correlation between the experimental and predicted fretting wear volumes by compiling all the tests inside and outside the calibration domain using: (a) extended friction energy wear approach (Equation 3.11) and (b) extended Archard approach (Equation 3.12).	94
3.37	Comparison between the experimental and numerical $2D_{ave}$ wear profiles at f=1 Hz for the loading conditions: (a) N=5 000 cycles (G), (b) N=20 000 (O), (c) N=40 000 (H), (d) p=10 MPa (A), (e) p=100 MPa (O), (f) p=175 MPa (B), (g) $\delta_g=\pm 25$ μm (C), (h) $\delta_g=\pm 100$ μm (O), and (i) $\delta_g=\pm 200$ μm (D).	95
3.38	(a) Evolution of h_{max} versus $h_{max,FEM}$ by taking into account all the loading conditions; (b) evolution of $\Delta h_{max}\%$ versus $h_{max,FEM}$ by compiling all the test conditions.	96
4.1	Schematic presentation of the transition of wear regimes from pure abrasive wear at high oxygen partial pressure ($P_{O_2} > P_{O_2,th}$) to a mixed abrasive-adhesive wear regime at low oxygen partial pressure ($P_{O_2} < P_{O_2,th}$), After [56].	101
4.2	BSE and EDX observations of the top and cross section views of mixed abrasive-adhesive wear scar detected at the bottom sample (N=20000 cycles, p=100 MPa, $\delta_g = \pm 100$ μm , f=5 Hz and A=25 mm^2).	102

4.3	BSE and optical observations of the TTS structure (N=20000 cycles, p=100 MPa, $\delta_g = \pm 100 \mu m$, f=5 Hz and A=25 mm ²).	103
4.4	(a) Comparison of the nano-indentation force-displacement curve of the TTS and the bulk; (b) Evolution of the nano-scale Vickers hardness profile by passing from the superficial tribologically transformed surface towards the bulk; (c) Evolution of the modulus of elasticity profile by passing from the superficial tribologically transformed surface towards the bulk (N=20000 cycles, p=100 MPa, $\delta_g = \pm 100 \mu m$, f=5 Hz and A=25 mm ² . Force-controlled constant strain rate loading nano-indentation with acquisition rate=10 Hz, maximum normal load=25 mN, loading rate/load=0.10 s ⁻¹ , and pause=10 s).	103
4.5	Computation of the oxygen distance “ d_O ” and the adhesion and abrasion areas by using crossed EDX oxygen line scans method.	105
4.6	Variation of $d_{O,Y}$ versus $d_{O,X}$ by compiling all the loading conditions.	106
4.7	Optical images and EDX observations showing the recession of abrasive wear with the increase in frequency from 0.5 to 10 Hz (N=20000 cycles, p=100 MPa, $\delta_g = \pm 100 \mu m$, and A=5×5=25 mm ²).	107
4.8	Evolution of the (a) percentage of abrasive wear area “% A_{ab} ” and (b) the oxygen distance “ d_O ” as a function of the frequency (N=20000 cycles, p=100 MPa, $\delta_g = \pm 100 \mu m$, and A=5×5=25 mm ² with $f_{ref} = 1$ Hz and $d_{O,ref} = 1.51$ mm).	108
4.9	Optical images and EDX observations showing the extension of the inner adhesive zone with the increase in contact pressure from 25 to 175 MPa (N=20000 cycles, $\delta_g = \pm 100 \mu m$, f=1 Hz, and A=5×5=25 mm ²).	109
4.10	Evolution of the (a) percentage of abrasive wear area “% A_{ab} ” and (b) the oxygen distance “ d_O ” as a function of the mean contact pressure (N=20000 cycles, $\delta_g = \pm 100 \mu m$, f=1 Hz, and A=5×5=25 mm ² with $p_{ref} = 100$ MPa and $d_{O,ref} = 1.51$ mm).	109
4.11	Optical images and EDX observations showing the evolution of abrasive wear with the increase in number of cycles from 5000 to 30000 cycles (p=100 MPa, $\delta_g = \pm 100 \mu m$, f=1 Hz, and A=5×5=25 mm ²).	110
4.12	Evolution of the (a) percentage of abrasive wear area “% A_{ab} ” and (b) the oxygen distance “ d_O ” as a function of fretting cycles (p=100 MPa, $\delta_g = \pm 100 \mu m$, f=1 Hz, and A=5×5=25 mm ² with $N_{ref} = 20000$ cycles and $d_{O,ref} = 1.51$ mm).	111
4.13	Optical images and EDX observations showing the evolution of abrasive wear with the increase in sliding amplitude from ± 75 to $\pm 200 \mu m$ (N=20000 cycles, p=100 MPa, f=1 Hz, and A=5×5=25 mm ²).	112

4.14	Evolution of the (a) percentage of abrasive wear area “% A_{ab} ” and (b) the oxygen distance “ d_O ” as a function of the sliding amplitude (N=20000 cycles, p=100 MPa, f=1 Hz, and A=5×5=25 mm ² with $\delta_{g,ref} = \pm 100 \mu m$ and $d_{O,ref} = 1.51$ mm).	112
4.15	Optical images and EDX observations showing the recession of adhesive wear with the decrease of the contact area from 25 to 12.5 mm ² (N=20000 cycles, p=100 MPa, $\delta_g = \pm 100 \mu m$, and f=1 Hz): (a) variable $L_{\perp\delta}$ and (b) variable $L_{\parallel\delta}$.	113
4.16	Evolution of the (a) percentage of abrasive wear area “% A_{ab} ” and (b) the oxygen distance “ d_O ” as a function of the contact size by varying either the longitudinal length ($L_{\parallel\delta}$) or the transverse width ($L_{\perp\delta}$) (N=20000 cycles, p=100 MPa, $\delta_g = \pm 100 \mu m$, and f=1 Hz with $A_{ref} = 5 \times 5 = 25$ mm ² and $d_{O,ref} = 1.51$ mm).	114
4.17	Comparison between the predicted and experimental oxygen distance using Equation 4.20 applied on plain and textured samples at different loading conditions and contact geometries.	115
4.18	Crossed flat-on-flat configuration with textured bottom sample.	116
4.19	Prediction of the transition of wear regime by using the predicted threshold oxygen distance (Equation 4.20) for: (a) variable contact area under reference loading conditions; (b) variable contact area at low sliding amplitude, $\delta_g = \pm 50 \mu m$; and (c) variable contact area at high sliding amplitude, $\delta_g = \pm 150 \mu m$.	117
4.20	Prediction of the transition of wear regime by using the predicted threshold oxygen distance (Equation 4.20) for: (a) variable contact area at low contact pressure, p=50 MPa; (b) variable contact area at high contact pressure, p=150 MPa; (c) variable contact area at low frequency, f=0.5 Hz; and (d) variable contact area at high frequency, f=5 Hz.	118
4.21	Illustration of the effect of internal grooves on the oxygen distance sample (N=20000 cycles, p=100 MPa, $\delta_g = \pm 100 \mu m$, f=5 Hz, $L_{\perp\delta} = 2.25$ mm and $L_{\parallel\delta} = 5$ mm).	118
4.22	Illustration of the simplified partition of the abrasive and adhesive wear areas.	119
4.23	Correlation between the experimental and the predicted results (Equations 4.12, 4.20 & 4.21) for (a) the adhesion area “ A_{ad} ”; (b) the abrasion area “ A_{ab} ” and (c) the relative proportion of abrasion area “% A_{ab} ” by compiling all the tests for plain and textured samples.	120
4.24	Illustration of the contact oxygenation concept to interpret the effect of contact pressure and sliding frequency regarding the evolution of d_O and the related partition between adhesive and abrasive areas.	121

5.1	Illustration of the ADR model to predict the extension of adhesive / abrasive wear distribution within a fretting interface.	129
5.2	Schematic presentation of the powdery porous debris bed allowing gas transport.	130
5.3	Flow chart summarizing the input data, models and the numerical solution of the ADR model.	138
5.4	SEM-BSE images showing the size of the particles constituting the debris bed after a fretting test (N=20000 cycles, p=100 MPa, $\delta_g = \pm 100 \mu m$, f=5 Hz and A=25 mm ²).	139
5.5	Porosity estimation by assuming cubic packing of identical spheres in the debris bed.	140
5.6	Raman spectra of the oxide debris layer (external abrasive corona) related to the calibration tests (Table 5.1): f=0.5, 1 and 10 Hz (N=20000 cycles, p=100 MPa, $\delta_g = \pm 100 \mu m$ and A=25 mm ² , for Laser wavelength $\lambda = 785 \text{ nm}$, Laser power=0.35 mV, and acquisition time=150 s).	142
5.7	Comparison between the 2D simulation of the dioxygen partial pressure at steady state ($r_{O_2} = \beta (\omega/\omega_{ref})^\gamma$ with $\beta=394.63$ and $\gamma=0.47$, $\omega_{ref}=0.04 \text{ W/mm}^2$, $P_{O_2,th}=0.1 \text{ Pa}$, $a=0.48$, $d_p=1 \mu m$, $k=2.27 \times 10^{-15} \text{ m}^2$, and $\alpha_{L,x}=\alpha_{L,y}=0.0005 \text{ m}$) and EDX mapping of the studied fretting scar (34NiCrMo16 / 34NiCrMo16 , N=20000 cycles, p=100 MPa, $\delta_g = \pm 100 \mu m$, f=10 Hz and A=25 mm ²) with: (a) ADR map showing the evolution of the total pressure; (b) ADR map showing the evolution of dioxygen partial pressure (log scale); (c) ADR map representing the partition between abrasion and adhesion; (d) EDX map showing the fretting scar top view.	144
5.8	Cross-experimental strategy to validate the ADR approach for plain crossed flat-on-flat samples: (a) contact pressure versus frequency; and (b) apparent contact area versus frequency.	145
5.9	Evolution of the oxygen partial pressure with the increase in frequency from 0.5 to 10 Hz (N=20000 cycles, p=100 MPa, $\delta_g = \pm 100 \mu m$, and A=5x5=25 mm ²). . .	146
5.10	Correlation between EDX and numerical ADR maps and the corresponding line scans revealing the growth of adhesion zone with the increase in the sliding frequency from 0.5 to 10 Hz (N=20000 cycles, p=100 MPa, $\delta_g = \pm 100 \mu m$, and A=5x5=25 mm ²).	147
5.11	Correlation between the experimental ($d_{O,exp}$) and the predicted oxygen distance from ADR approach ($d_{O,ADR}$) as a function of the sliding frequency (N=20000 cycles, p=100 MPa, $\delta_g = \pm 100 \mu m$, and A=5x5=25 mm ²).	148

5.12	Evolution of the oxygen partial pressure with the increase in contact pressure from 25 to 175 MPa (N=20000 cycles, f=1 Hz, $\delta_g=\pm 100 \mu m$, and A=5x5=25 mm^2).	149
5.13	Correlation between EDX and numerical ADR maps and the corresponding line scans showing the growth of adhesion zone with the increase in the contact pressure from 25 to 175 MPa (N=20000 cycles, f=1 Hz, $\delta_g=\pm 100 \mu m$, and A=5x5=25 mm^2).	150
5.14	Correlation between the experimental ($d_{O,exp}$) and the predicted oxygen distance from ADR approach ($d_{O,ADR}$) as a function of the contact pressure from 25 to 175 MPa (N=20000 cycles, f=1 Hz, $\delta_g=\pm 100 \mu m$, and A=5x5=25 mm^2).	151
5.15	Correlation between the experimental ($d_{O,exp}$) and the predicted oxygen distance from ADR approach ($d_{O,ADR}$) as a function of Archard power density factor ω (N=20000 cycles, $\delta_g=\pm 100 \mu m$, and A=5x5=25 mm^2).	151
5.16	Evolution of the oxygen partial pressure with the increase in the apparent contact area from 10 to 25 mm^2 (N=20000 cycles, p=100 MPa, $\delta_g=\pm 100 \mu m$, and f=1 Hz).	152
5.17	Correlation between EDX and numerical ADR maps and the corresponding line scans showing the growth of adhesion area with the increase of the apparent contact area from 10 to 25 mm^2 (N=20000 cycles, p=100 MPa, $\delta_g=\pm 100 \mu m$, and f=1 Hz).	153
5.18	Correlation between the experimental ($d_{O,exp}$) and the predicted oxygen distance from ADR approach ($d_{O,ADR}$) as a function of the apparent contact area for $A_{ad} > 0$ (N=20000 cycles, p=100 MPa, $\delta_g=\pm 100 \mu m$, and f=1 Hz).	154
5.19	Comparing the experimental and the predicted results (ADR approach) for (a) the oxygen distance “ d_O ”; and (b) the abrasion area “ A_{ab} ”.	154
5.20	Evolution of the oxygen distance d_O as a function of (a) the particle size “ d_p ”, (b) the intrinsic permeability of the debris bed “ k ” and (c) the porosity “ a ” computed for the reference loading conditions (i.e. N=20000 cycles, p=100 MPa, $\delta_g=\pm 100 \mu m$, f=1 Hz and A=25 mm^2).	156
5.21	(a) 2D and 3D graphs showing the evolution of the partial pressures of oxygen and nitrogen gases along with the total pressure within the debris bed at the reference test; (b) XPS spectra of the inner adhesion zone and the surrounding oxidized abrasion corona giving evidence of Ti17 nitriding inside the TTS (after [55]).	157
5.22	Summary of the research work conducted in this manuscript (2017-2020).	163

List of Tables

2.1	Chemical composition of 34NiCrMo16 [112].	41
2.2	Mechanical properties of 34NiCrMo16 (obtained from the documentation of material supplier [115]).	42
3.1	Evolution of the optical images, 3D fretting scars and $2D_{ave}$ wear profiles with the number of cycles for the top and bottom samples (N=5000, 20000 and 40000 cycles such that: p=100 MPa, $\delta_g = \pm 100 \mu m$, f=1 Hz and A=25 mm ²).	63
3.2	Evolution of the optical images, EDX analysis, 3D fretting scars and $2D_{ave}$ wear profiles with the contact pressure for the bottom samples (p=10, 100, and 175 MPa such that N=20000 cycles, $\delta_g = \pm 100 \mu m$, f=1 Hz and A=25 mm ²).	67
3.3	Evolution of the optical images, EDX analysis, 3D fretting scars and $2D_{ave}$ wear profiles with the sliding amplitude for the bottom samples ($\delta_g = \pm 25, \pm 100$ and $\pm 200 \mu m$ such that N=20 000 cycles, p=100 MPa, f=1 Hz and A=25 mm ²).	69
3.4	Evolution of the optical images, EDX analysis, 3D fretting scars and $2D_{ave}$ wear profiles with the frequency for the bottom samples (f=0.5, 1 and 10 Hz such that N=20000 cycles, p=100 MPa, $\delta_g = \pm 100 \mu m$ and A=25 mm ²).	71
3.5	Comparison of phase fractions in the ejected debris analyzed by XRD for ($L_{\perp\delta}=0.81$ mm and $L_{\parallel\delta}=5$ mm) and ($L_{\perp\delta}=5$ mm and $L_{\parallel\delta}=0.81$ mm) orientations (N=20000 cycles, p=100 MPa, $\delta_g = \pm 100 \mu m$ and f=1 Hz).	92
5.1	Input parameters of the ADR model.	137
5.2	Calibration of the reaction rate coefficient (r_{O_2}) (Equation 5.45) ($\beta=394.63$ and $\gamma=0.47$) for 34NiCrMo16 interface with N=20000 cycles, p=100 MPa, $\delta_g = \pm 100 \mu m$ and A=25 mm ²	143

List of Abbreviations

ADR	Advection-Dispersion-Reaction
BCC	Body-Centered Cubic
BCT	Body-Centered Tetragonal
BSE	Back-Scattered Electrons
COC	Contact Oxygenation Concept
CSSM	Critical State Soil Mechanics
DEM	Discrete Element Modelling
EDM	Electrical Discharge Machining
EDX	Energy Dispersive X-ray spectrometry
FCC	Face-Centered Cubic
FEM	Finite Element Modelling
GSR	Gross Slip Regime
HPT	High Pressure Torsion
LTDS	Laboratory of Tribology and Systems Dynamics
MRFM	Material Response Fretting Map
PDE	Partial Differential Equation
PM	Powder Metallurgy
PSR	Partial Slip Regime
RCFM	Running Condition Fretting Map
RH	Relative Humidity
SEM	Scanning Electron Microscope
SE	Secondary Electrons
TBA	Third Body Approach
TB	Third Body
TTS	Tribologically Transformed Structures
XRD	X-Ray Diffraction

List of Symbols

Sample dimensions

A	Contact area	mm^2
a_H	Hertzian contact half width	mm
$L_{\parallel\delta}, L_x$	Longitudinal contact length parallel to the sliding direction (δ)	mm
$L_{\perp\delta}, L_y$	Transverse contact length perpendicular to the sliding direction (δ)	mm

Material properties

ν	Poisson's ratio	
σ_u	Ultimate stress	MPa
$\sigma_{y,0.2\%}$	Yield stress	MPa
A_c	Residual projected indentation contact area	m^2
E	Young's modulus of elasticity	GPa
E^*	Plane modulus of elasticity	GPa
H	Hardness	Hv
h	Indenter penetration depth	μm
h_0	Defect of the indenter tip	μm
h_c	Contact depth	μm
S	Contact stiffness	N/m

Elements

CO_2	Carbon dioxide gas
Fe	Iron
Fe_2O_3	Hematite
Fe_3O_4	Magnetite
N_2	Dinitrogen gas
O	Oxygen
O_2	Dioxygen gas

Fretting and loading parameters

δ	Displacement	μm
----------	--------------	---------

δ^*	Displacement amplitude	μm
δ_0	Cycle aperture	μm
δ_g	Sliding amplitude	μm
δ_t	Transition amplitude from partial to gross slip	μm
μ	Conventional friction coefficient	
μ_e	Energy friction coefficient	
e	Sliding ratio	
f	Sliding frequency	Hz
F_n	Normal force	N
F_r	Radial force	N
F_t	Tangential force	N
F_t^*	Tangential force amplitude	N
K_s	Machine tangential stiffness	N/m
L	Sliding distance	m
N	Number of fretting cycles	cycles
T	Temperature	$^{\circ}\text{C}$ or $^{\circ}\text{K}$
p	Contact pressure	MPa
q	Tangential shear stress	MPa
v	Sliding speed	m/s

Wear volume and profilometry

$2D_{ave}$	Averaged 2D wear profile	
h_{max}	Averaged experimental maximum wear depth	μm
h_{mean}	Average experimental mean wear depth	μm
H_w	Worn material thickness	μm
l	Sampling length of roughness measurements	μm
Ra	One-dimensional arithmetic mean height roughness	μm
Rz	Maximum height of the surface profile	μm
V	Total experimental wear volume	mm^3
V^+	Positive wear volume	mm^3
V^-	Negative wear volume	mm^3
V_t	Wear volume	mm^3

Archard approach

$\sum W$	Cumulated Archard work	J
K	Archard wear coefficient	mm^3/J
K^*	Weighted Archard wear coefficient	mm^3/J
W	Archard work	J
p.v= ω	pv factor or Archard power density factor	W/mm^2

Friction energy approach

α	Energy wear rate	mm^3/J
α^*	Weighted energy wear rate	mm^3/J
α_{φ^*}	Energy wear rate obtained as a function of φ^*	mm^3/J
$\sum Ed$	Cumulated dissipated friction energy	J
φ^*	Friction power density	W/mm^2
Ed	Dissipated friction energy	J
Ed_{th}	Threshold activation friction energy	J
Et	Total friction energy	J

Third Body Approach (TBA)

H_{ss}	Steady state debris layer thickness	μm
H_{TB}	Thickness of the TB	μm
Q_e	Ejection external flow of TB	g/s
Q_i	Internal flow of TB	g/s
Q_r	Recirculation flow of TB	g/s
Q_s	Source flow of TB	g/s
Q_s^e	External source flow of TB	g/s
Q_s^i	Internal source flow of TB	g/s
Q_w	Wear flow of TB	g/s

Contact Oxygenation Concept (COC)

$\%A_{ab}$	Relative proportion of abrasion area	
$\%A_{ad}$	Relative proportion of adhesion area	
A_{ab}	Abrasion area	mm^2
A_{ad}	Adhesion area	mm^2
d	Minimum distance from the contact center to its borders	mm
d_O	Oxygen distance	mm
d_{ab}	Width of the abrasion-corona	mm
$d_{ad,X}$	Length of adhesion along the longitudinal sliding axis (X)	mm
$d_{ad,Y}$	Length of adhesion along the transversal axis (Y)	mm
$d_{O,X}$	Oxygen distance along the longitudinal sliding axis (X)	mm
$d_{O,Y}$	Oxygen distance along the transversal axis (Y)	mm

Advection-Dispersion-Reaction (ADR) model

α_L	Longitudinal dispersivity of the gas mixture	m
α_T	Transverse dispersivity of the gas mixture	m
β	Power-law parameter of the reaction rate coefficient	
Δt	Time step	s
Δx	Distance between nodes in x direction	m

Δy	Distance between nodes in y direction	m
γ	Power-law parameter of the reaction rate coefficient	
λ	Loading slope of the yield surface in CAM-Clay model	Pa^{-1}
μ	Gas mixture viscosity	$kg.m^{-1}.s^{-1}$
Φ	Porosity of the debris bed	
τ	Tortuosity	
ε	Steady state condition of ADR-PDE	Pa
a	Air-filled porosity	
C_i	Molar concentration of a component i	$mol.m^{-3}$
D_i	Dispersion coefficient of a gas component i	$m^2.s^{-1}$
d_p	Average particle size	m
$D_{diffusion}$	Molecular diffusion coefficient	$m^2.s^{-1}$
D_{im}	Diffusion coefficient of a gas component in a homogeneous gas mixture	$m^2.s^{-1}$
D_{mixing}	Mechanical mixing dispersion coefficient	$m^2.s^{-1}$
J_i	General molar flux of gas component i	$mol.m^{-2}.s^{-1}$
$J_{a,i}$	Advective flux of gas component i	$mol.m^{-2}.s^{-1}$
$J_{d,i}$	Dispersive flux of gas component i	$mol.m^{-2}.s^{-1}$
k	Intrinsic permeability of the debris bed	m^2
M_i	Molar mass of gas component i	$kg.mol^{-1}$
n_i	Number of moles of gas component i	mol
n_x	Number of nodes in x direction	
n_y	Number of nodes in y direction	
P	Total pressure of the gas mixture	Pa
P_{N_2}	Dinitrogen partial pressure	Pa
P_{O_2}	Dioxygen partial pressure	Pa
$P_{O_2,th}$	Threshold dioxygen partial pressure	Pa
R	Universal gas constant	$J.mol^{-1}.K^{-1}$
R_i	Reaction rate of a gas component i	$mol.m^{-3}.s^{-1}$
r_i	Reaction rate coefficient of a gas component i	s^{-1}
$T_{C,i}$	Critical temperature	K
v	Advection velocity of the gas mixture	$m.s^{-1}$
$V_{C,i}$	Critical volume of gas component i	$m^3.kmol^{-1}$
y_i	Mole fraction of gas component i	

Statistical tools and variables

E	Standard deviation	$\%$
R^2	Coefficient of determination	
X	Arbitrary loading parameter (N, p, δ_g , f, $L_{\parallel\delta}$, $L_{\perp\delta}$), 1D spatial position	
Z	Depth or height	μm

Subscripts and superscripts

<i>ADR</i>	Corresponds to the ADR model results
<i>exp</i>	Corresponds to the experimental results
<i>FEM</i>	Corresponds to FEM results
n_X	Power corresponding to a loading parameter X
<i>pred</i>	Corresponds to the predicted results
<i>ref</i>	Corresponds to the reference conditions
<i>th</i>	Corresponds to threshold value

General Introduction

Fretting wear resulting from micro-displacement oscillatory motion is considered a serious impediment for many industrial applications from bridge cables and turbojet engines to railway axles. It leads to substantial expenses for the maintenance and replacement of engineering equipment causing inevitable financial and environmental losses for the modern industry. Improving machine performance necessitates a balance between its initial and maintenance costs which essentially rely on materials' resistance to wear degradations. Hence, the comprehension and prediction of wear behavior are the cornerstones of the majority of studies addressing fretting in tribology. This helps uncover the hidden safeties which are indispensable for economically improving the design standards and the performance of mechanical contacts.

Fretting wear involves several damage mechanisms at the interface including abrasion, adhesion, oxidation, debris formation and debris ejection. This highly affects wear kinetics, thus more efforts are needed to better understand fretting wear. The main thrust of this PhD is to extensively investigate fretting wear behavior of large low-alloyed steel interfaces. The tested configuration is flat-on-flat which is barely explored although it is close to wide range of industrial assemblies which are more likely conformal. Following this, the transition of wear mechanisms from abrasion to adhesion is studied at different loading conditions and modelled using an advection-dispersion-reaction (ADR) approach. So, this manuscript will embrace five chapters summarized as follows:

- **Chapter 1** is devoted to a bibliographic research introducing the elementary principles which will be used later in this manuscript. It reviews the advances and the most significant findings in fretting wear. It is initiated by defining the tribology then it is narrowed down by introducing and describing fretting wear, sliding modes, and wear mechanisms (abrasion, adhesion, corrosion, fatigue, etc.). Finally, this chapter is terminated by reviewing the recent approaches aiming at qualitatively and quantitatively describing wear.

- **Chapter 2** presents the studied material along with the contact configurations. It also describes the tribological system, the experimental strategy applied in the whole manuscript, along with the damage characterization techniques.

- **Chapter 3** details friction and wear response of the studied interface at several loading conditions including number of cycles, contact pressure, sliding amplitude, frequency, and contact size

as well as contact orientation with respect to the sliding direction. Then, it introduces a wear volume prediction model taking into account the aforesaid parameters. Besides, this chapter reveals a composite abrasive-adhesive wear interface underlining the necessity to further inspect this mixed aspect of wear.

- **Chapter 4** investigates the evolution and transition of wear mechanisms from abrasive to adhesive wear assuming the contact oxygenation concept which suggests that adhesion appears in the inner part of the interface if the di-oxygen partial pressure is below a threshold value. Contact oxygenation is quantified using the “oxygen-distance, d_O ” parameter defined as the averaged width of the external abrasion-corona. d_O evolution is formalized using a power law formulation which allowed predicting wear transitions for a wide range of loading conditions.

- **Chapter 5** aims at explaining and modeling the contact oxygenation observed in fretting contacts and the associated partition between abrasive and adhesive wear domains in fretting wear scars. This is achieved by modelling oxygen transport using an advection-dispersion-reaction (ADR) approach by considering debris bed as a compact powdery porous medium traversed by atmospheric gases. This chapter details the model calibration and validation showing that ADR approach can capture the transition of wear mechanisms from pure abrasive to mixed abrasive-adhesive wear at different loading conditions.

Chapter 1

Literature review

Contents

1.1	Introduction	6
1.2	Fretting wear	7
1.3	Sliding modes	8
1.4	Contact configurations	9
1.5	Fretting cycle	10
1.6	Sliding conditions	12
1.7	Characterization of sliding regimes	13
1.8	Sliding regimes and fretting maps	14
1.9	Sliding transition criteria	15
1.10	Qualitative description of wear	16
1.10.1	Abrasive wear	17
1.10.2	Adhesive wear	17
1.10.3	Fatigue wear	18
1.10.4	Corrosive wear	18
1.10.5	Composite wear	19
1.11	Tribologically transformed structures	19
1.11.1	Description of the main features of TTS	19
1.11.2	TTS formation mechanisms	20
1.12	Quantitative description of wear	22
1.12.1	Approaches for wear kinetics quantification	23
1.12.2	Approaches for wear mechanisms description	30
1.13	Conclusion	38

1.1 Introduction

Understanding the sciences of surfaces and friction is gaining an increased attention in research fields and engineering applications. Inspired from human necessities, “Tribology” or “the science of rubbing” arose as the study of interacting surfaces in relative motion. It is the art of applying operational analysis to substantial economic problems such as maintenance, reliability, and wear of technical equipment, ranging from spacecraft to household appliances [1].

Tribology is multidisciplinary in nature involving many fields including physics, chemistry, mathematics, mechanics, material sciences, metallurgy, fluid mechanics, thermodynamics, rheology, and lubrication. This originates from the fact that understanding surface interactions is inherently complex and requires interdisciplinary expertise.

The word “Tribology” stems from the Greek word “tribo” which means rubbing. Although this term was coined only recently by Peter Jost in 1966 [2] while underlining the cost of friction, wear and corrosion to the UK economy, humans have utilized this concept since thousands of years. Historical records show that around 3500 B.C, fire and wheel were used reflecting the very first useful applications of friction (Figure 1.1a & 1.1b)[1]. The use of lubricants traces back to Sumerians and Egyptians who used bitumen, animals, oils and water to reduce friction. Figure 1.1c shows 172 men dragging an Egyptian statue to the grave of Tehuti-Hetep in 1880 B.C., along with one man pouring a liquid (oil or water) as a lubricant to reduce friction between the sledge and the ground. This reflects the know-how of friction and lubrication notions in transportation of heavy building blocks and monuments [1].

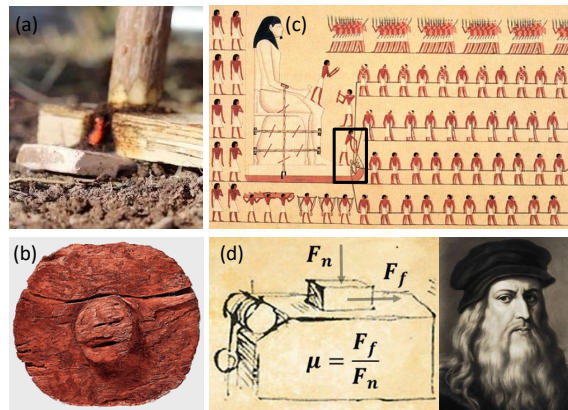


Figure 1.1: Early tribological achievements: (a) Paleolithic method of igniting fire by rotating a wooden stick on a dry rock or wood as an early testimonial on tribological application; (b) a Mesopotamian wheel around 3500 B.C; (c) using lubricants by Egyptians to transport a statue to the grave of Tehuti-Hetep, El-Bersheh around 1880 B.C; (d) tribological experiments proposed by Leonardo da Vinci (1452–1519).

Following Romans and Greeks, the renaissance period had its big contributions to tribology thanks to Leonardo Da Vinci who introduced the concept of the friction coefficient in 1493 as the ratio of the friction force to the normal load (Figure 1.1d). Then, Amontons published the

fundamental friction laws in 1699 stating that the friction force is independent of the contact between two surfaces. These laws were further developed by Coulomb in 1785 who distinguished between static and kinetic friction [1].

After the industrial revolution and since the beginning of the twentieth century, the machinery production increased the need for friction and wear reduction to eliminate financial losses. Recent estimates [3] revealed that nearly 23% of the world's energy consumption originates from tribological contacts. Besides, they showed that friction and wear reduction reduce energy losses by 40% leading to potential savings of natural resources. These advantages launched tribology on the right track of worldwide recognition and expansion in different engineering and research areas.

Modern tribology encompasses three principles which are friction, wear and lubrication. Wear is generally defined as the progressive loss of substance from the operating surface of a body occurring as a result of relative motion at the surface [4]. Wear can be broadly classified into severe and mild. However, some authors distinguish different classes of wear including impact, erosion, delamination, scoring, metal transfer and finally fretting wear which will be investigated in details in this thesis.

1.2 Fretting wear

Fretting phenomenon was first investigated by Eden et al. (1911) [5] who noticed iron oxide debris between the steel grids and the specimen in their fatigue machine. Then, Tomlinson (1927) [6] reported that damage can be caused by very small amplitudes of relative movement referred to as slip. Following this, series of studies were carried over fretting by many researchers including Godfrey and Bailey (1951 & 1953) [7, 8], Halliday and Hirst (1956) [9], Wayson (1964) [10], Hurricks (1970) [11], Vingsbo and Soderberg (1988) [12], Berthier et al. (1988) [13], Fouvry et al. (1996) [14], Shipway and co-workers (2007) [15] and so many others.

Fretting can be used to describe a phenomenon where two contacting surfaces submitted to normal load undergo micro-displacement oscillatory motion [12, 16]. Such displacements are very small in comparison to the contact size. Fretting leads to surface degradation that can be considered a reason behind the failure of several mechanical assemblies. As a result, fretting is currently a critical issue for several industrial applications where structures are submitted to oscillatory motion such as mechanical and civil engineering structures, transportation, aeronautics, nuclear power plant industries, and biomedical applications (Figure 1.2).

In civil engineering for instance, fretting can be encountered in a wide range of applications (Figure 1.3). Examples about this are the seismic friction dampers which are used to damp the oscillations of buildings and bridges during an earthquake [17]. The friction damper helps the structure move elastically by dissipating part of the kinetic seismic energy in the form of friction. Building protection is hence carried on the expense of the damper which will undergo micro displacements that can be accompanied by fretting wear. The second application is the bridge

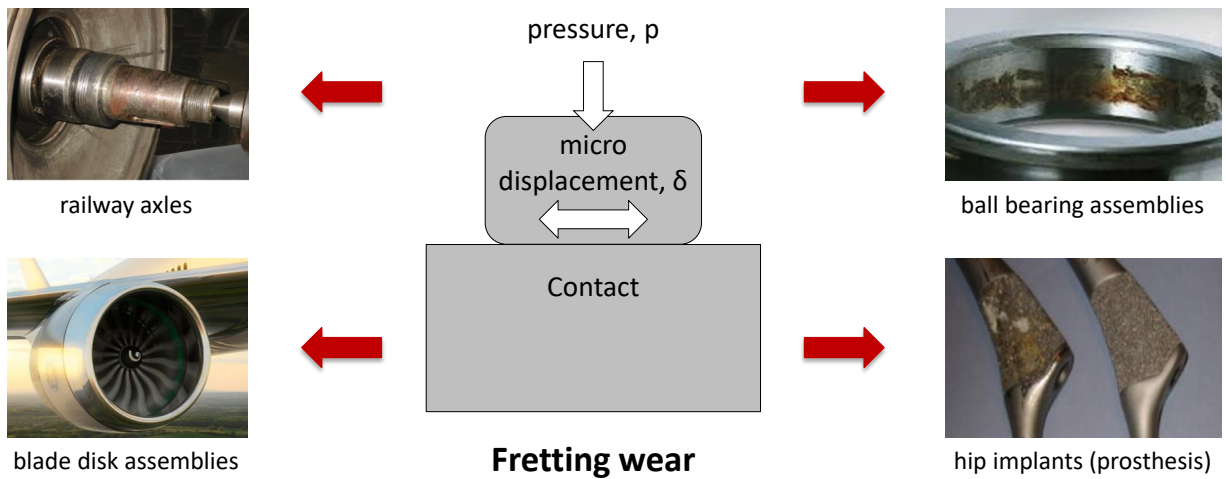


Figure 1.2: Fretting damage in industrial applications.

cables which are submitted to transverse vibrations caused by wind and mechanical loadings [18]. This triggers substantial relative displacements between the strands and the anchorage regions causing essential fretting failure. Besides, such inter-wire motion considerably decreases the life expectancy of the cable and the service life of the supported structure. Additionally, bolted joints [19] which are widely used in metallic structures undergo significant dynamic loadings. These loadings induce micro-slip between the contacting surfaces leading to fretting damage (wear and cracking).

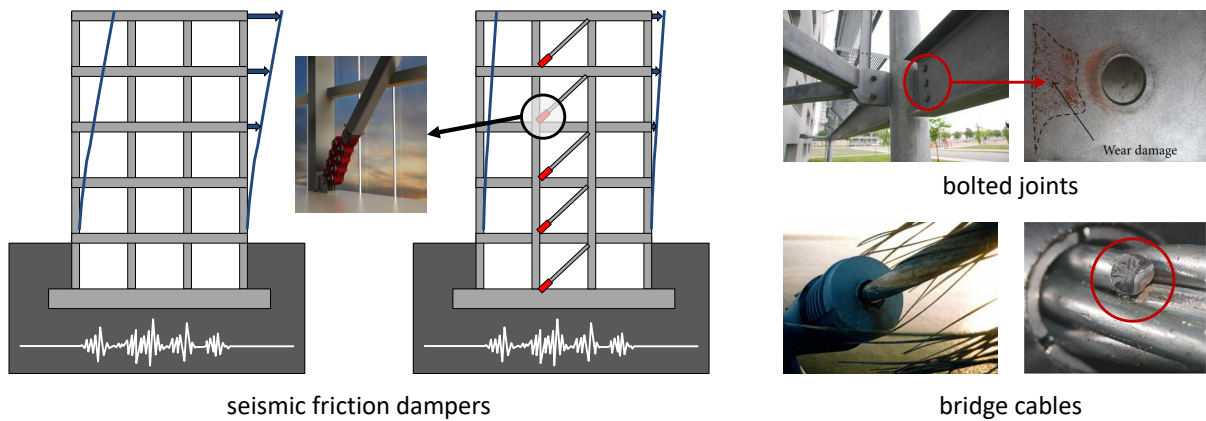


Figure 1.3: Fretting damage in civil engineering structures [17–20].

1.3 Sliding modes

To better understand fretting contact, it is necessary to distinguish three sliding modes defined over a contact configuration consisting of a sphere placed over a flat surface (Figure 1.4). The contact parameters are the normal force F_n , the radial force F_r and the cyclic tangential displacement δ . Based on Blanpain et al. (1995) [21] and Mohrbacher et al (1995) [22], three

sliding modes can be distinguished:

- Mode I: The contact undergoes linear sliding where F_n is constant, F_r is null and δ is variable.
- Mode II: The contact undergoes radial displacement where F_n is variable, and F_r and δ are null.
- Mode III: The contact undergoes circumferential displacement where F_n is constant, F_r is variable and δ is null.

Mode I can be alternatively referred to as fretting where the key contact parameters are the normal force F_n and the cyclic tangential displacement δ which generates the tangential force F_t .

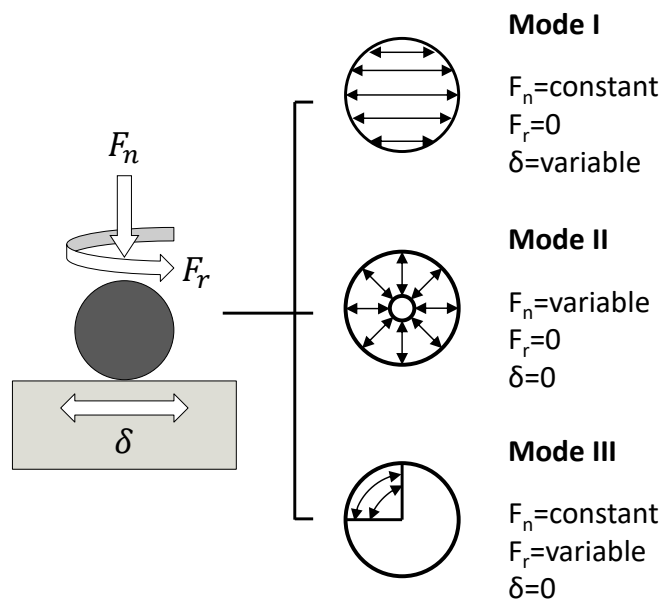


Figure 1.4: Sliding modes of a sphere-on-flat contact configuration (after Blanpain et al. (1995) [21]).

1.4 Contact configurations

The real contact configurations in industrial applications are very complicated and practically difficult to reproduce at laboratory scale. To simplify the latter, simple contact geometries are studied by researchers including (Figure 1.5):

- Flat-on-flat configuration: this configuration was extensively used by many researchers including Lindley (1997) [23] and Hintikka et al. (2016) [24] as it allows good description of the real interfaces in mechanical systems. Besides, it maintains the area of friction surfaces constant disregarding the wear taking place at the interface. This leads to a constant mean contact pressure whatever the surface wear extension which facilitates wear modelling. However, flat-on-flat configuration exhibits some drawbacks including its high sensitivity to alignment issues and manufacturing errors. Besides, one main problem of this configuration is the discontinu-

ity of the contact pressure distributions due to edge effects. Yet, the latter problem can be encountered by adjusting the edges' curvature.

- Convex configuration: these configurations were formalized by Hertz analysis (1881) [25]. Contact pressure in the latter configuration falls continuously to zero at the edges of the contact without singularities resulting in complete analytical solution for subsurface stress and strain fields in case the loads are within elastic domain (Johnson 1985 [26]). Convex pads can be spherical or cylindrical. However, with the surface wear, the contact area extends and the mean contact pressure changes so it is very difficult to establish wear modelling in Hertzian contacts.
 - a. Sphere-on-flat configuration: this configuration is easy to implement experimentally as no alignment is needed because of the point contact. Yet, one of the disadvantages of this configuration is the complicated three-dimensional cracking analysis which is costly in time computation.
 - b. Cylinder-on-flat configuration: cylindrical configurations are simpler to manufacture compared to spherical pads but they are more difficult to align. Besides, they allow a straightforward two-dimensional elastic analysis of contact problems.

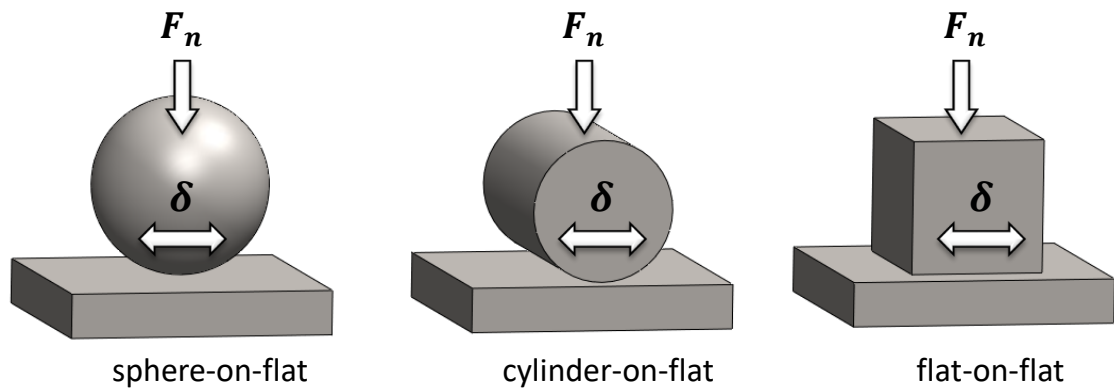


Figure 1.5: Contact configurations used in fretting wear tests.

1.5 Fretting cycle

Figure 1.6 shows a gross-slip fretting cycle representing the tangential force F_t plotted against the micro-displacement δ . From the fretting loop, the following parameters can be extracted:

- Displacement amplitude “ δ^* ”: it is the maximum displacement reached in a cycle. In fact, δ^* does not reflect the real displacement at the interface due to the tangential accommodation of the test rig.
- Cycle aperture “ δ_0 ”: it is equal to the residual displacement when $F_t=0$. It corresponds to the real displacement taking place at the interface as it is independent of the tangential

accommodation of the test rig. So, fretting tests are usually controlled by δ_0 instead of δ^* as this allows comparing fretting test whatever the test system compliance.

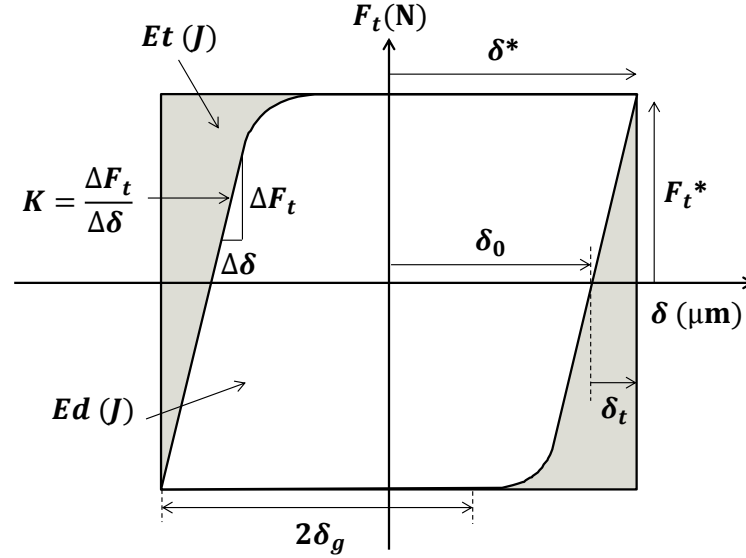


Figure 1.6: Schematic representation of the fretting cycle (after [27]).

- Transition amplitude “ δ_t ”: it defines the transition from partial to gross-slip sliding conditions (See section 1.7). Under gross slip condition, the contact first undergoes partial slip before reaching a full sliding plateau. Hence, δ_t can be expressed as the difference value between the displacement amplitude δ^* and the cycle aperture δ_0 (Equation 1.1). Note that δ_t includes the contact but also the test system accommodation; hence, it depends on the stiffness of the test rig.

$$\delta^* = \delta_0 + \delta_t \quad (1.1)$$

- Sliding amplitude “ δ_g ”: it is the operating sliding distance of the bodies in contact. It is considered to be equal to the cycle aperture ($\delta_g \approx \delta_0$).
- The tangential stiffness “ K_s ”: it is determined by the slope of the fretting cycle after changing the sliding direction. This value is representative to the mechanical compliance of the test rig. For a contact displacement amplitude “ δ_c ” at instant (t), K_s is estimated as follows:

$$K_s = \frac{\Delta F_t}{\Delta \delta} = \frac{\Delta F_t(t)}{\delta(t) - \delta_c(t)} \quad (1.2)$$

- Tangential force amplitude “ F_t^* ”: corresponds to the maximum tangential force transmitted in the interface. This allows computing the conventional friction coefficient “ μ ” which is equal to the ratio of F_t^* to the normal load “ F_n ”.

$$\mu = \frac{F_t^*}{F_n} \quad (1.3)$$

- The dissipated friction energy “Ed”: it corresponds to the area of the cycle (Equation 1.4). Ed constitutes of the different dissipative phenomena such as elastic and plastic deformations of the bodies in contact, cracks, physico-chemical transformations, corrosion, creation and ejection of debris, contact thermodynamics, etc.

$$Ed = \int_{-\delta^*}^{\delta^*} F_t(\delta) d\delta \approx 4.\delta_g.F_t^* \quad (1.4)$$

- Energy friction coefficient “ μ_e ”: introducing Ed allows the calculation of an averaged energy friction coefficient μ_e (Equation 1.5). μ_e is considered more accurate than the conventional friction coefficient “ μ ” especially in case of ploughing. This latter is caused by the plastic draughts generated at the contact borders resulting in a peak value of tangential force.

$$\mu_e = \frac{Ed}{4.F_n.\delta_g} \quad (1.5)$$

- Total energy “Et”: it corresponds to the area of the rectangular region enclosing the fretting cycle.

$$Et \approx 4.\delta^*.F_t^* \quad (1.6)$$

1.6 Sliding conditions

According to many authors, the sliding slip ranges between few microns to several hundred micrometers as noted by Halliday et al. (1956) [9], Ohmae et al. (1974) [28], and Gordelier et al. (1979) [29]. The transition between alternating and fretting sliding was clearly illustrated by Fouvry et al (1995) [30] (Figure 1.7) who introduced the sliding ratio “e” between the sliding amplitude δ_g and the Hertzian contact half width in the sliding direction “ a_H ” such that:

$$e = \frac{\delta_g}{a_H} \quad (1.7)$$

For elastic contact configuration the sliding ratio “e” can be computed using Hertz theory (1881) [25]. Alternating (reciprocating) sliding condition corresponds to the case where the whole interface is exposed to the outer environment and the sliding ratio is larger than 1 ($e > 1$). Fretting loading is characterized by a value smaller than 1 ($e < 1$). In this case, the central zone of the interface is not exposed to the external environment.

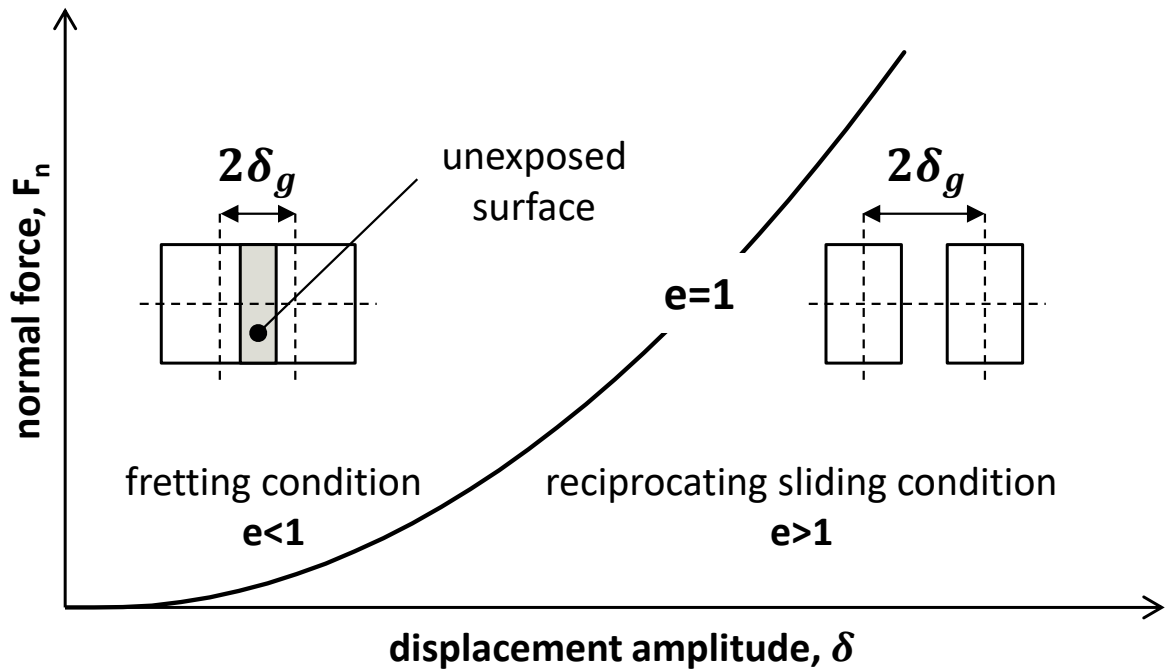


Figure 1.7: Definition of the sliding ratio “ e ” and identification of the transition state between alternating sliding and fretting regimes [30, 31].

1.7 Characterization of sliding regimes

Mindlin and Cattaneo [32] distinguished two sliding conditions:

- Partial slip: takes place for displacement lower than gross slip full sliding condition. The contact exhibits a composite structure of sticking central zone surrounded by two sliding zones according to Mindlin and Cattaneo [32]. Fretting loop (F_t - δ) has a closed elliptical shape in case of an elastic contact. In the condition that the relative displacements decrease, the stick zone will enlarge and the fretting loops will have the form of closed cycles as a result of the linear mechanical response (Figure 1.8a). In the sliding regions, Coulomb’s law is applicable such that the coefficient of friction can be calculated from the ratio of the contact pressure (p) and tangential shear stress (q) ($q=\mu p$). However, in sticking zone the coefficient of friction can no longer be computed out of the ratio of the contact pressure and tangential shear stress. Therefore, the global full sliding condition is not satisfied which implies $F_t < \mu F_n$.
- Gross slip: by increasing the sliding amplitude, we reach a limit where the entire contact surface is a sliding area with no longer existence of a stick zone. The Fretting loop (F_t - δ) will have a quadratic form (Figure 1.8b). In this case, the coefficient of friction can be calculated from the ratio of the tangential to the normal force such that ($F_t=\mu F_n$). Additionally, the maximum tangential force F_t^* is independent of the displacement amplitude (Figure 1.8b).

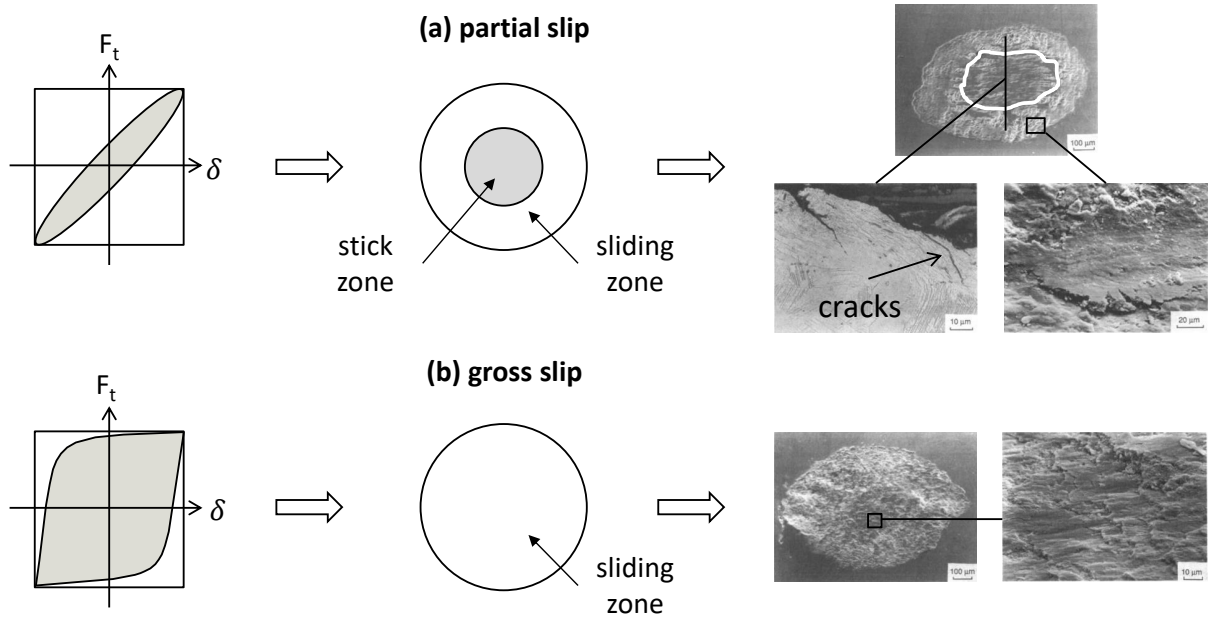


Figure 1.8: (a) Partial slip condition characterized by an elliptic fretting loop and a mixed stick and slip surface; (b) gross slip condition characterized by a quadratic fretting loop and a slip worn surface (After Vingsbo et al. (1988) [12]).

1.8 Sliding regimes and fretting maps

Following Vingsbo et al. (1988) [12], the concept of running condition fretting map (RCFM) was developed by Vincent et al. (1992) [33]. In this map, the normal force is plotted against the displacement amplitude allowing identification of three fretting regimes (Figures 1.9 & 1.10a):

- Partial slip regime (PSR): it takes place when the displacement amplitudes are systematically smaller than a threshold value referred to as transition displacement δ_t . In this case, the partial slip condition prevails over the whole test duration.
- Gross slip regime (GSR): it is activated when the displacement amplitudes are systematically higher than the threshold displacement δ_t . In this case, gross slip condition controls the interface over the whole test duration, and the tangential force F_t^* is independent of the displacement amplitude δ^* .
- Mixed fretting regime (MFR): it takes place for intermediate displacement amplitudes resulting in occurrence of gross slip and partial slip conditions within a single test.

Additional fretting map was introduced by Blanchard et al. (1991) [34], who investigated material response and its degradation due to fretting introducing in turn material response fretting maps (MRFM) (Figure 1.10b). In case the displacements under partial slip condition are so small, the contact stresses will not be able to initiate cracks which leads to ‘no damage state’. Starting from a certain threshold value, the stresses become sufficiently large to initiate a crack. For gross slip regime, displacement amplitudes become high enough to induce surface wear.

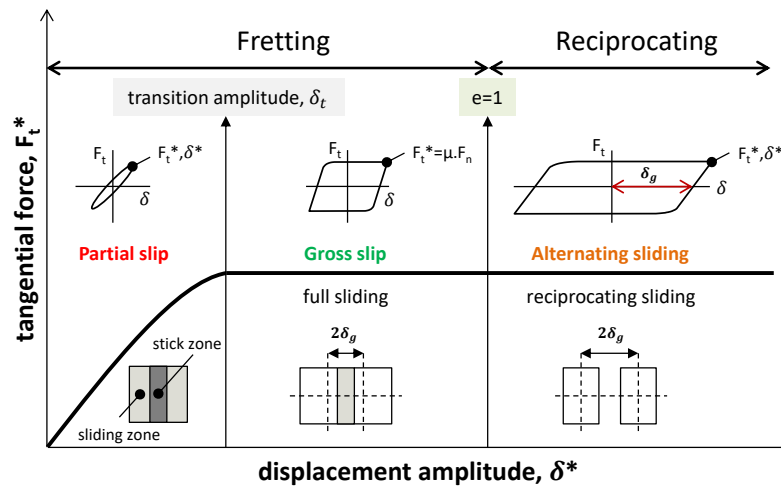


Figure 1.9: Transition between partial slip and gross slip on one side and fretting and reciprocating sliding on the other side.

On the other hand, intermediate displacement amplitudes of mixed fretting regime induce a competition between crack initiation and surface wear.

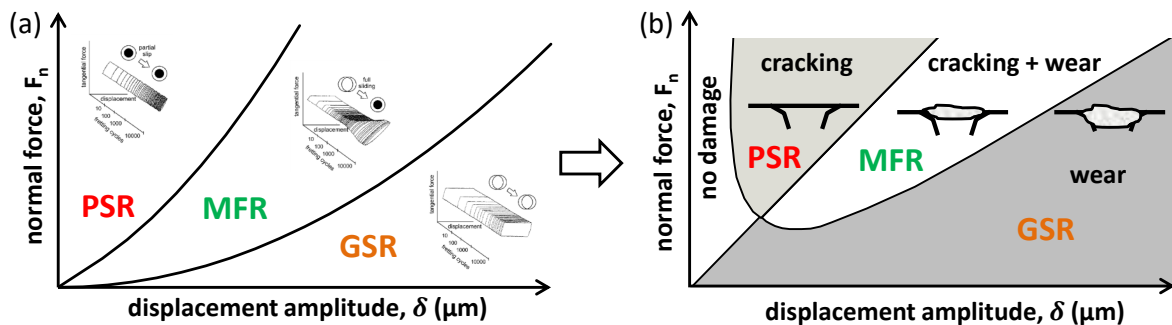


Figure 1.10: Fretting maps: (a) running condition fretting map (RCFM); (b) material response fretting map (MRFM) [35].

1.9 Sliding transition criteria

The sliding conditions were identified in a qualitative way based on the form of the fretting loop. For better quantitative qualification of the latter, Fouvry et al (1997) [36] proposed three transition criteria (Figure 1.11) for elastic sphere-on-flat contact configuration assuming Mindlin's hypothesis:

- The energy criterion A : defined as the ratio between the dissipated energy in a given cycle E_d and the total energy $E_t = 4 \cdot \delta^* \cdot F_t^*$ which corresponds to the energy dissipated for a system of infinite tangential stiffness ($A = E_d / E_t$). By defining a sliding transition value of $A_t = 0.2$, partial sliding appears for $A < A_t$ and gross slip condition for $A > A_t$.

- Cycle opening criterion B : defined as the ratio of the sliding amplitude δ_g corresponding to zero tangential force and the displacement amplitude δ^* ($B = \delta_g / \delta^*$). By defining a sliding transition value of $B_t = 0.26$, partial sliding prevails for $B < B_t$ and gross slip condition for $B > B_t$.
- The independent energy criterion C : defined as the ratio E_d / E_{dg} with $E_{dg} = 4 \cdot \delta_g \cdot F_t^*$. By defining a sliding transition value of $C_t = 0.77$, partial sliding prevails for $C < C_t$ and gross slip condition for $C > C_t$.

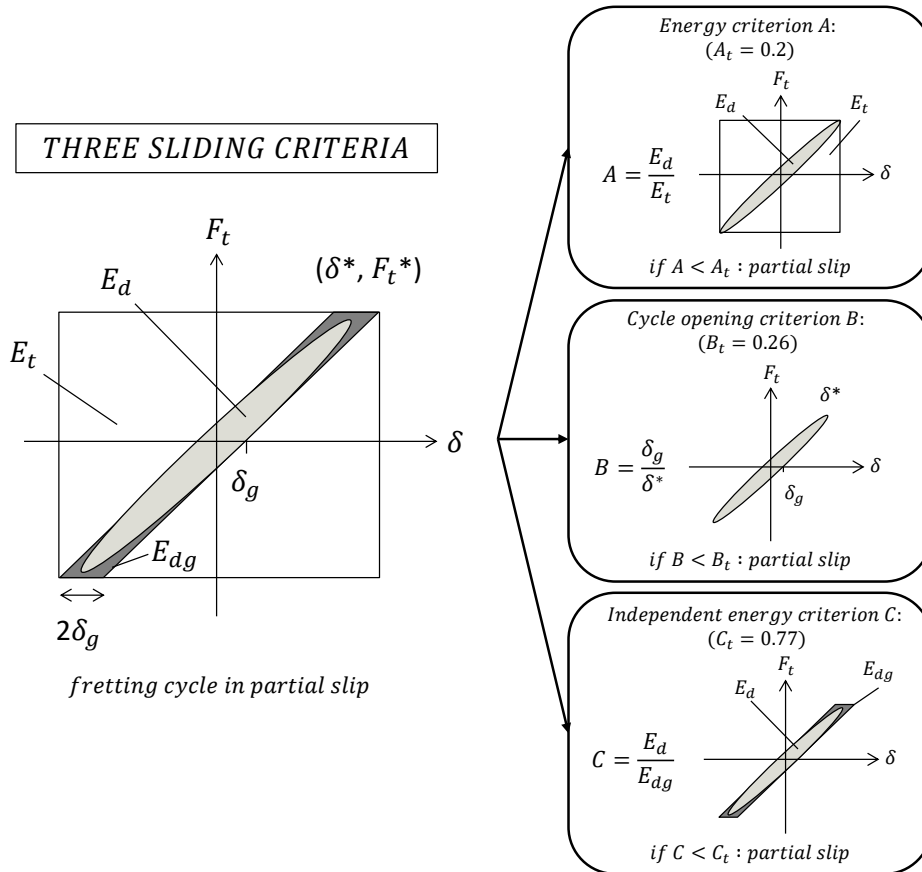


Figure 1.11: Quantification of the sliding transition through transition criteria [14].

1.10 Qualitative description of wear

Wear description and classification was the subject of many studies in literature. A broad classification of wear processes was suggested by Quinn (1983) [37] who differentiated severe and mild wear phenomena. The term severe wear describes the phenomena of adhesion, local partial welding, material transfer, and plastic deformation in addition to processes leading to drastic surface degradation. On the other hand, the term mild wear brings together all the mechanisms producing smooth surfaces and fine debris and generally resulting from interactions with the environment. After this simple classification, other wear classification mechanisms were brought to light later defining five types of wear processes:

1.10.1 Abrasive wear

Abrasive wear occurs when a hard rough surface slides across a softer one (Figure 1.12). This results in material removal by plowing or gouging instead of sticking or being pulled of as the case of adhesion. This wear can be classified into two situations according to the contact type and the outer environment [38]. The contact type determines the mode of abrasive wear which is classified into two-body and three-body abrasion according to [38, 39]. Two-body abrasive wear also known as cutting [40] occurs when two materials with different hardness interact abrasively where a hard asperity cuts one of the sliding surfaces or when a rough surface abrades a smoother one by asperity interaction. In this case, abrasion is observed on the softer surface. Three-body abrasive wear occurs when hard third body particles are interposed between the two surfaces abrading one of them or both of them.

The contact environment determines whether the wear is classified as open or closed. An open contact environment occurs when the surfaces are sufficiently displaced to be independent of one another. During fretting, abrasive wear usually interacts with surface corrosion which results in creation of oxide films.

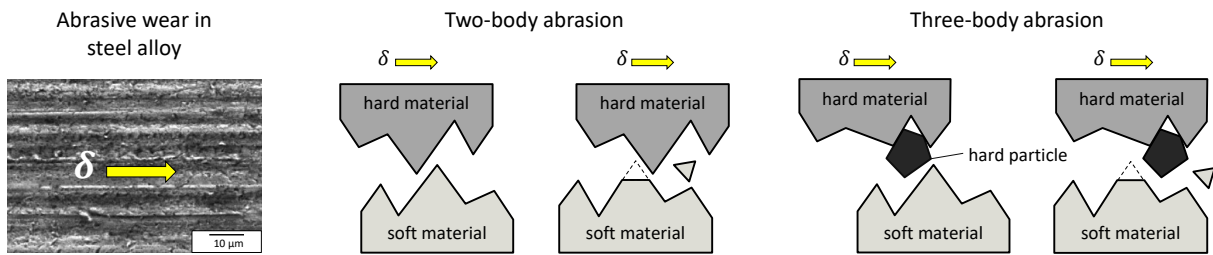


Figure 1.12: Schematic presentation of two-body and three-body abrasive wear.

1.10.2 Adhesive wear

It corresponds to the severe wear definition of Quinn, and it takes place whenever two virgin surfaces mechanically contact and bond each other [41]. It is linked to the formation of metallic junctions caused by the high pressure exerted on the sliding asperities causing localized welding and adhesion [38, 42]. It is also attributed to the strong attraction forces between surfaces leading to tearing of the material and to important transfer phenomena (Figure 1.13). Adhesive wear between metallic surfaces was shown to be strongly linked with the processes of friction, fatigue, cold welding, powder compaction and grain boundary strength [43]. Ambient conditions and surface nature are also vital parameters in adhesive transfers. As for surface nature effect, it was noticed that similar materials exhibit higher adhesion compared to the case of dissimilar ones [38, 40]. Besides, Bowden [44] revealed experimentally that surface cleanliness highly facilitates adhesion due to the absence of oxide films which limit sticking of the counter bodies. Based on the same concept, the composition of the atmosphere is inherently a crucial factor in adhesive wear. Indeed, a significant increase in friction coefficient along with severe adhesion

were recorded in vacuum environments [45–47]. This was attributed to the absence of oxidation and consequently lack of surface oxide particles at the interface providing in turn more intimate asperities which can be readily welded.

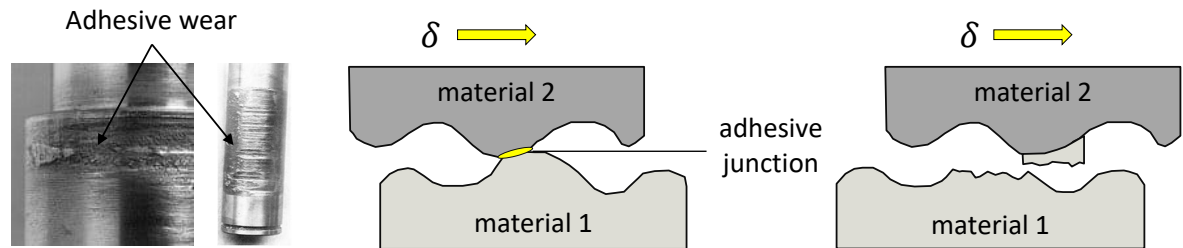


Figure 1.13: Schematic illustration of adhesive wear.

1.10.3 Fatigue wear

Fatigue wear of a material is caused by a cycling loading during friction (Figure 1.14). Fatigue occurs if the applied load is higher than the fatigue strength of the material. Fatigue cracks start at the material surface and spread to the subsurface regions. The cracks may connect to each other resulting in separation and delamination of the material pieces.

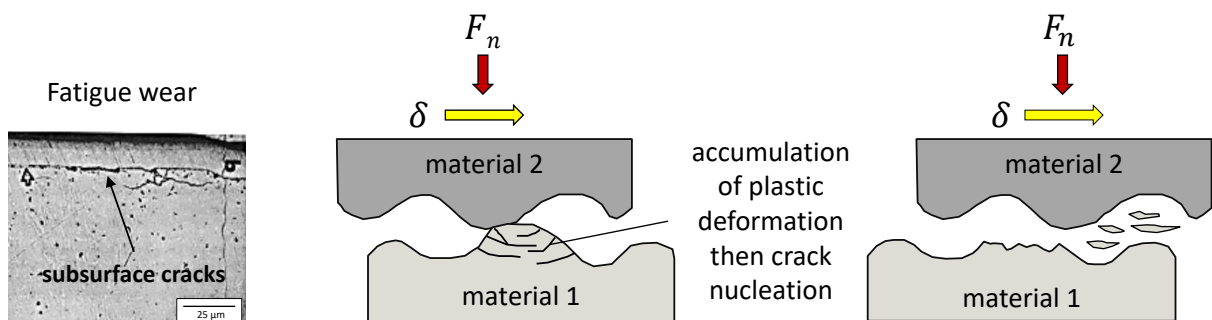


Figure 1.14: Schematic presentation of fatigue wear.

1.10.4 Corrosive wear

Corrosive wear is defined as the damage caused by synergistic attack of wear and corrosion when the latter occurs in a corrosive environment (Figure 1.15). In the literature, the term tribo-corrosion also refers to corrosive wear. Wear may be accelerated by corrosion (oxidation) of the rubbing surfaces. Increased temperature in addition to the removal of the protective oxide films from the surface during sliding promotes the oxidation process. Friction hence leads to a continuous removal followed by a continuous formation of oxide films.

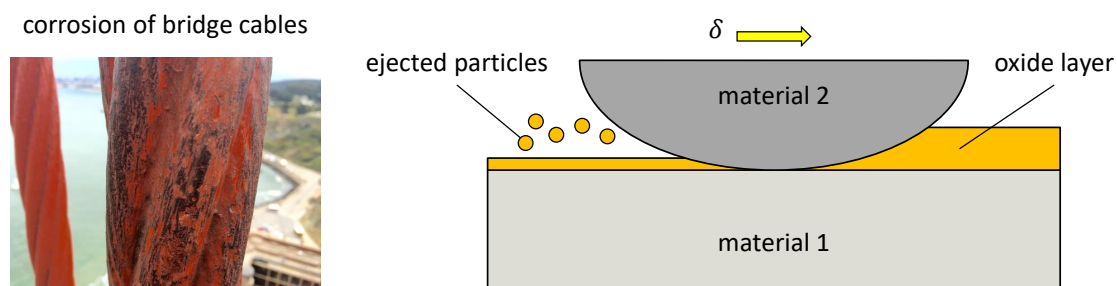


Figure 1.15: Schematic presentation of corrosive wear [27].

1.10.5 Composite wear

Composite wear is defined as a mixture of adhesive and abrasive wear mechanisms which is the case of most sliding interfaces [40] (Figure 1.16). It is characterized by presence of metal surfaces covered by thin oxide films where abrasive-oxidational wear is predominant. On the other hand, adhesive wear prevails when metal-metal contact takes place giving birth to a hard “white layer” [48] commonly referred to as “tribologically transformed surface (TTS)” [49, 50] which will be illustrated in more details in the following section. Note that adhesion zone is characterized by very low oxygen content as reflected in the inner part of oxygen EDX maps (Figure 1.16) in contrary to the abrasion zone at the borders where the oxygen concentration is relatively high.

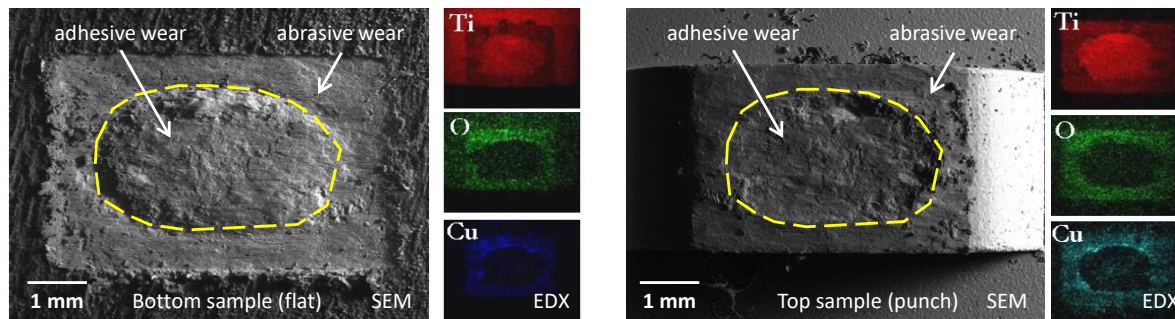


Figure 1.16: SEM images and EDX maps showing a composite abrasive-adhesive wear of titanium alloy after fretting test [31].

1.11 Tribologically transformed structures

1.11.1 Description of the main features of TTS

Tribologically transformed structures or TTS are detected in fretting whenever adhesive wear prevails. TTS were observed in different materials (steel alloys [34, 49, 51–53], titanium alloys [34, 49, 54–56], aluminum alloys [34] etc.) and under wide range of loading conditions. Eyre and Baxter [48] reported that one of the earliest observations of “TTS” dates back to 1911 where Stead found hard white layers on the surfaces of used steel wire. Stead proposed that this layer is due to martensite transformation as a result of frictional heating in service followed

by quenching by the colder sublayers. Following this, tribologically transformed structures were called “white layer” or “white etching layers” due to their white appearance under microscopic observations after chemical etching metallographic preparation for steels [57]. Zhou, Sauger and their collaborators [49, 57] summarized the main features of the TTS as follows:

- Location: cross-section observations of a contact after a certain number of fretting cycles reveal three layers as shown in Figure 1.17. A thin superficial oxide layer is often formed of compacted debris on the top of the wear scar. Below it, a poorly oxidized TTS layer appears with a similar chemical composition as that of the bulk material. Sometimes, a plastically deformed area is detected below TTS.

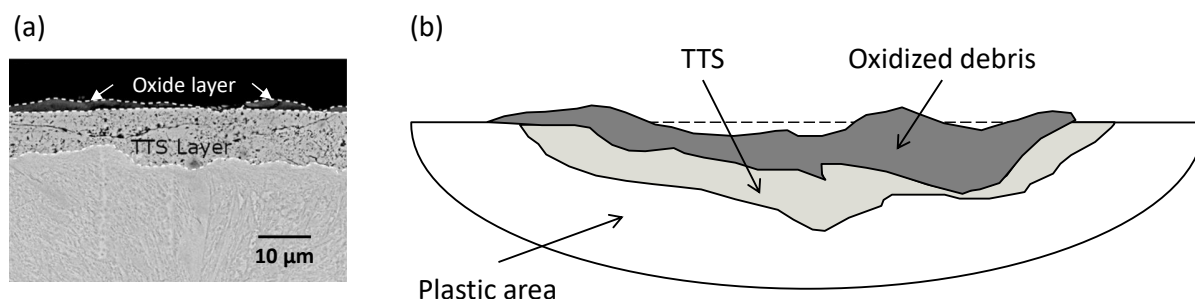


Figure 1.17: (a) BSE observations of the TTS in a sectional view of etched cylindrical specimen of high strength steel (BS S132) [51]; (b) schematic illustration of a metallographic cross section of a fretting scar revealing the location of the TTS [49].

- Hardness: TTS is extremely hard. Its hardness can be two or three times that of the bulk.
- Grain size: TTS is composed of ultra-fine grains (few tens of nanometers).
- Chemical composition and structure: TTS has the same chemical composition as that of the bulk. Its crystallographic structure converges to a thermodynamically stable structure. For instance, martensite structure systematically evolves towards a ferrite structure.

1.11.2 TTS formation mechanisms

Several mechanisms were suggested to illustrate TTS formation in sliding contacts including:

- Temperature: Following Stead’s assumption that frictional heat is the precursor of TTS [48], Vitzintin and co-workers [58] supported this claim linking TTS formation to a martensite transformation induced by high flash temperatures at asperity scale based on Archard’s calculations [59]. However, experimental measurements and theoretical calculations [60–62] showed that temperature increases only few degrees at low sliding velocities which are not sufficient to solely explain TTS formation in that case.
- Strain-induced mechanisms:
 - Mechanical mixing: Rigney [63] explained the formation of TTS by high plastic deformation

and material transfer. Local shear stresses induce high plastic deformations in the vicinity of the surface, producing significant transformations within the material. On the other hand, adhesion at the level of metal-metal junctions favors material transfer. The transferred particles are deformed and mixed with the material of the counter body while reacting with the atmosphere in order to form a hard nano-crystalline layer of this mixture of metallic grains and oxides. Rigney [63] called this layer “mechanically mixed layer” or even “transfer layer”. According to this author, the mechanism of formation of this surface layer is akin to a phenomenon of “mechanical alloying”. This layer then gives rise to debris of relatively uniform thickness or “flake-like debris” similar to those produced by delamination phenomena.

- Dynamic recrystallization: Blanchard [64] proposed a model for TTS formation based on a dynamic recrystallization phenomenon due to strong plastic deformations induced by fretting solicitations.

The beginning of the transformation always takes place at the interface between the matrix and the inclusion. The latter locally accentuates the constraints (discontinuity in plastic deformations) and sources of dislocations can be activated. If the dislocation density becomes sufficiently high within a critical volume, phase transformation takes place (germination or nucleation phase) resulting in the formation of new nuclei (Figure 1.18a). After that, growth phase starts where the nuclei grow forming nano-grains. The grains thus formed act in their turn as stress concentration zones. Hence, new germination (nucleation) sites appear at the interface between the matrix and the transformed grains (Figure 1.18b). The zones thus develop progressively until the stress field becomes so low that it can’t generate new nuclei (Figure 1.18c).

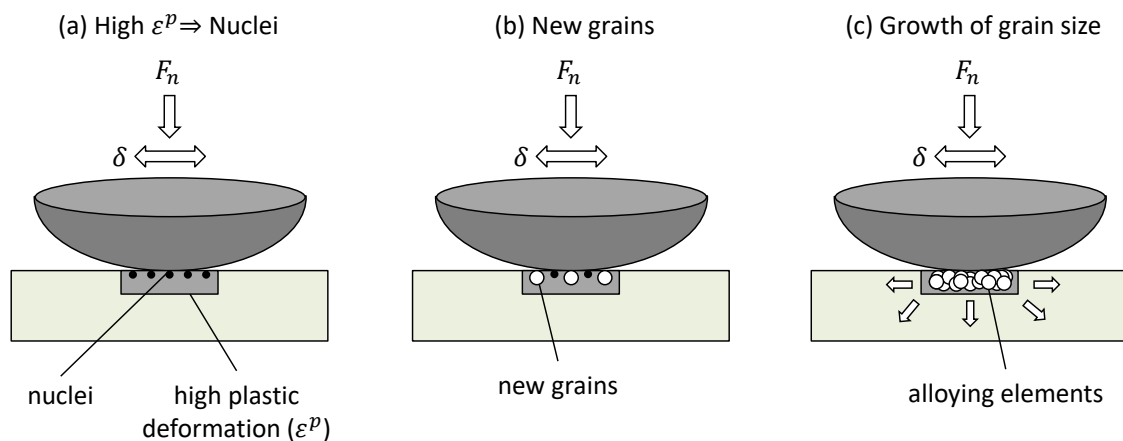


Figure 1.18: TTS formation by recrystallization due to high plastic deformation [49, 64].

This three-phase explanation could thus clarify the lamellar aspect of TTS, which would therefore be due to the succession of transformation fronts. This approach may also explain the fact that TTS has the same chemical composition as the base material. Other observations have also shown the presence of a clear transition between the TTS and the original material,

corresponding to the depth below which the plastic deformations are no longer sufficient to cause recrystallization. Finally, observations show that the size of the nano-grains forming the TTS is very homogeneous and that the latter is a function of the hardness measured: the finest grains will be found at the limit of the TTS zone and the untransformed zone [65]. As it is impossible to make local observations of the stress-strain conditions causing dynamic recrystallization for the material inside a tribological contact, unconstrained high pressure torsion (HPT) was considered to study the mechanisms occurring at the early stage of tribological process (i.e. deformation of the near surface layer just before particle detachment). Using HPT, Descartes and co-workers [66–68] showed that severe plastic deformation and strain gradients of high purity iron generated TTS of submicronic grain structure. This was accompanied by considerable grain refinement and increase in the uniformity as the deformation increases suggesting that continuous dynamic recrystallization may be one of the formation mechanisms of TTS. This latter observation was also detected in fretting contacts by Zhang et al. [69] where severe strain gradients induce significant grain refinement through dynamic recrystallization.

- Energy approach: Sauger and co-workers [49] suggested that TTS formation is due to plastic deformation which causes recrystallization of the microstructure based on Blanchard model [64]. They also showed that the TTS transformation can be related to a critical dissipated energy. Below this energy, the microstructure is unchanged and above it, the microstructure is transformed to TTS. Under steady-state wear, the TTS layer remains constant which implies that the rate of TTS transformation next to the inner plastic domain must be equal to the rate of TTS destruction on the fretted surface.

- Diffusion: oxygen diffusion is thought to play an important role in the formation of TTS according to many authors. Mary and co-workers suggested that the absence of oxygen in the inner part of the contact favors adhesive wear, seizure and plastic deformation. These accumulated plastic strains engender TTS through dynamic recrystallization [56, 70]. Additionally, these authors also detected nitriding phenomenon which results from the oxygen depletion towards the center of the scar resulting in poorly oxidized TTS.

The different approaches proposed in literature reflect the fact that TTS formation can't be explained by a sole mechanism. It is perhaps due to several phenomena taking place together which suggests that more efforts should be done to better understand this key feature of fretting wear.

1.12 Quantitative description of wear

Wear involves several mechanisms which result from complex phenomena that are difficult to study in a quantitative way. This arises from the fact that several factors must be taken into account including material properties, structural aspects (elastic, plastic, fatigue properties, hardness, etc.), and kinematics factors (surface geometry and the nature of movement) which

generate thermo-mechanical fields responsible for wear. However, having these properties highly coupled adds more complexity to the problem. For instance, the properties of materials evolve with the loading. An example about this is the fact that hardening modifies ductility and yield strength. Besides, contact geometries and consequently boundary conditions evolve during wear process which constitutes an additional difficulty for predictive wear estimation. In the view of all these complexities, it is conceivable that quantitative approaches of wear processes are mostly global or macroscopic like the Archard's model and its derivatives which are to be discussed later. Meng and Ludema (1995) [71] reviewed 5466 articles published in the *Wear* journal and *Wear of Materials* conferences and they were able to list more than 300 different formulations between 1947 and 1992, often specific to a test or a range of given solicitations. These formulations were classified by authors into three categories: empirical laws, laws based on contact mechanics, and laws based on damage mechanisms. In this study, we are interested in studying four main approaches to quantify and describe wear phenomena including: Archard approach, friction energy wear approach, third body, and contact oxygenation concepts.

1.12.1 Approaches for wear kinetics quantification

1.12.1.1 Archard approach

One of the most used models of wear today is that of Archard (1953) [72] which expresses wear volume V as a function of Archard's work W which is equal to the product between the normal load F_n and the sliding distance L (Equation 1.8). This relationship considers the normal force and the sliding distance as major factors of wear. Besides, it permits defining the so-called wear coefficient K which reflects the probability that two opposing asperities of the two bodies in contact produce a wear particle.

$$V = K.F_n.L = K.W \quad (1.8)$$

In case of fretting test of N cycles where the contact is submitted to a normal load F_n and a sliding amplitude δ_g , Archard approach can be expressed according to Equation 1.9 as follows:

$$V = K. \sum_{i=1}^N 4.\delta_g(i).F_n(i) \quad (1.9)$$

Archard approach is widely used as it provides interesting wear predictions for tribo-systems displaying a stable friction evolution. Besides, it is simple enough to implement in FEM simulations, hence consistent with the current industrial design strategies which are based on modeling.

On the other hand, the absence of the coefficient of friction in Archard's formulation is considered a limiting factor. In Figures 1.19 a & b, the coefficient of friction is plotted versus the number of fretting cycles for two sides of the same specimen, one exhibiting relatively high porosity (side 1) and the the other has a lower porosity (side 2). It was shown by Fouvry et al. (2001) [35]

that the friction behavior of side 1 having higher porosity increases and strongly depends on the loading conditions. On the other hand, this is not the case for side 2 where the coefficient of friction appears to be independent of the loading condition. Two tendencies are observed in Figure 1.19c. When the coefficient of friction has a stable evolution which is the case of side 2, a linear evolution is observed which permits the calculation of a wear coefficient K . This is not the case of side 1 which presents a large dispersion of the coefficient of friction where no linear extrapolation can be defined which prevents the determination of the wear coefficient.

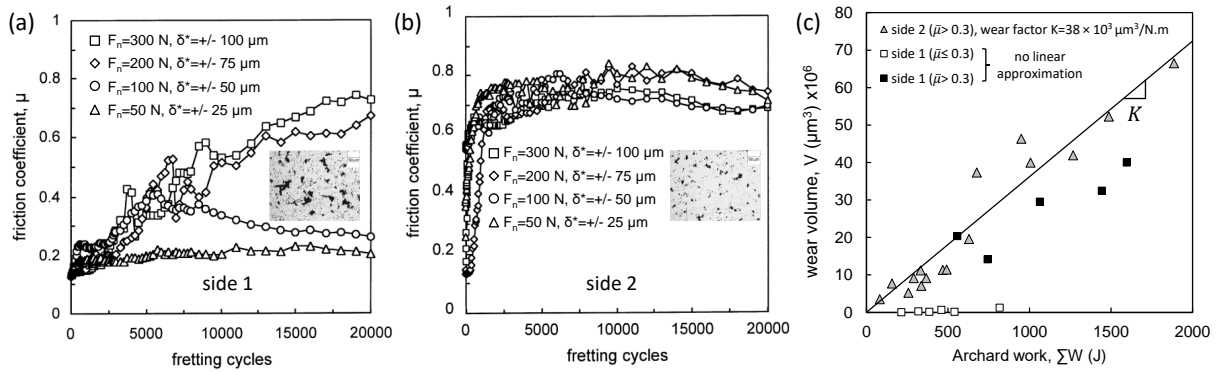


Figure 1.19: Illustration of the limitation of Archard's approach regarding the coefficient of friction [35]: (a) evolution of the friction coefficient for the high porosity side of the material (side 1); (b) evolution of the friction coefficient for the low porosity side of the material (side 2); (c) distribution of the wear volume versus Archard work.

Hence, it can be concluded that the Archard's approach is well adapted to quantify wear behaviors of tribosystems exhibiting a stable friction behavior. In contrary, for tribosystems having a varying friction behavior, Archard approach seems to be inappropriate for describing wear response.

Indeed, according to Johnson (1985) [26], it is demonstrated that the coefficient of friction plays a key role in the activation of the surface damage in fretting process (Figure 1.20). In fact, low wear mechanisms (such as those observed in case of side 1 at low loading conditions) are effectively independent of the coefficient of friction as shown by Johnson (1995) [73] through a local plastic work analysis. Yet, when the coefficient of friction becomes higher, macroscopic plasticity is introduced through the whole contact surface. The maximum equivalent stress spreads over the whole contact surface resulting in severe wear mechanisms.

Another limitation of Archard approach is that it is valid for abrasive wear phenomena. Additionally, it does not take into account the influence of fine particles existing at the interface referred to as third bodies. It is based on the fact that no particle stays in the contact. Hence, Archard approach appears to be a limit case in the third body approach which takes into account the influence of debris layer at the interface as shown by Fillot et al. (2005) [74].

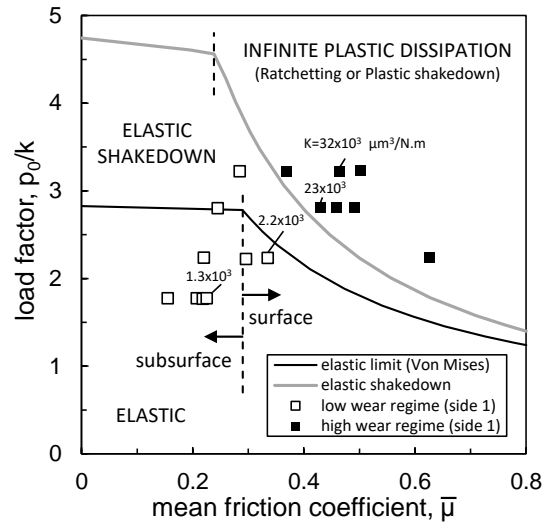


Figure 1.20: Wear map taking into account the shakedown behavior for high wear regime (side 1) $16,000 < K(\mu\text{m}^3/\text{N.m}) < 38,000$ and low wear regime (side 1) $K(\mu\text{m}^3/\text{N.m}) < 3000$ [35].

1.12.1.2 Friction energy approach

Few years following Archard approach, an energy approach was proposed based on the friction energy dissipated in the interface. Mohrbacher et al. (1995) [75] and Fouvry et al. (1995) [30] introduced the concept of cumulative dissipated energy as the sum of friction energy dissipated within a fretting test of N cycles (Equation 1.10). The dissipated energy (Ed) is calculated from the relative displacement of the two contacting surfaces (δ_g) and the value of the tangential force (F_t) and it corresponds to the area of the fretting cycle.

$$\sum Ed = \sum_{i=1}^N Ed(i) = \sum_{i=1}^N 4\delta_g(i)F_t(i) \quad (1.10)$$

Following this, Fouvry et al. [14, 36] revealed that wear volume V varies linearly with the cumulated dissipated friction energy Ed calculated from Equation 1.10 by defining the so-called energy wear rate α (Equation 1.11). This coefficient allows the comparison of wear resistance of different materials and surface treatments, such that high values of α reflect low wear resistance.

$$V = \alpha \cdot \sum Ed = \alpha \cdot \sum_{i=1}^N 4\delta_g(i) \cdot F_t(i) \quad (1.11)$$

Compared to Archard approach, energy wear formulation is more stable as it integrates the influence of friction coefficient in its formulation. By comparing Figure 1.21 to Figure 1.19, it can be seen that energy wear coefficient α can be extrapolated for stable and unstable coefficients of friction (Figure 1.21c). Hence, such shear work approach is much more relevant to identify the intrinsic wear resistance of the microstructure.

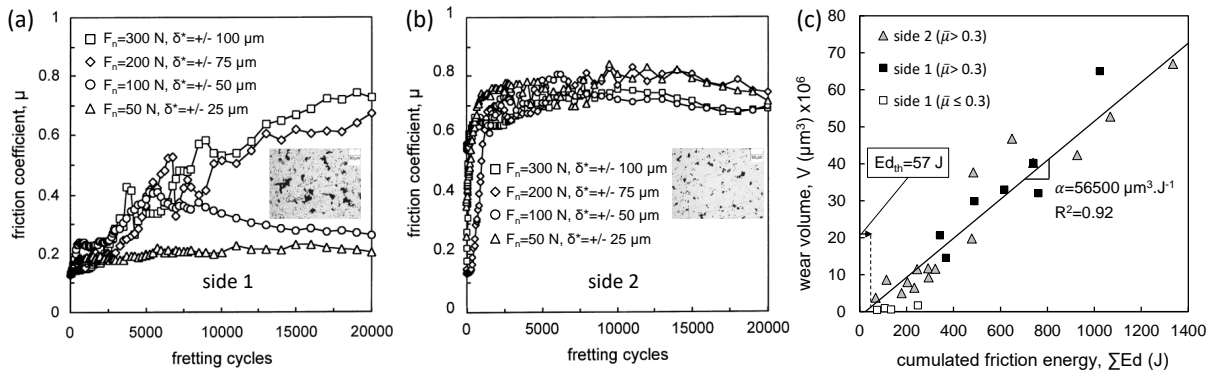


Figure 1.21: Stability of the friction energy wear approach with the coefficient of friction [35]: (a) evolution of the friction coefficient for the high porosity side of the material (side 1); (b) evolution of the friction coefficient for the low porosity side of the material (side 2); (c) distribution of the wear volume versus the cumulated dissipated friction energy.

It is important to note that the energy wear approach is equivalent to Archard approach for constant coefficient of friction (Equation 1.12).

$$K = \mu \cdot \alpha \quad (1.12)$$

Friction energy approach was further extended by Sauger and co-authors [49] (Equation 1.13) to consider the formation of the TTS by defining a threshold activation energy Ed_{th} (Figure 1.22). This threshold is related to the amount of energy necessary for the plastic transformation of materials and the generation of TTS such that below it, there is no wear and above it, wear starts and is characterized by the creation and ejection of debris particles.

$$V = \begin{cases} 0 & \sum Ed \leq \sum Ed_{th} \\ \alpha \cdot \sum (Ed - Ed_{th}) & \text{else} \end{cases} \quad (1.13)$$

Following this, energy wear approach was validated for a wide range of materials (steel, titanium, aluminum, cobalt, etc...) by many authors [35, 36, 76, 77]. Besides, it was largely extended to include the effect of several loading conditions (contact pressure “ p ”, sliding amplitude “ δ_g ”, sliding frequency “ f ”, temperature “ T ”, contact size “ A ”, etc.) by introducing a weighted energy wear coefficient “ α^* ”.

The influence of sliding amplitude “ δ_g ” was first integrated in the energy wear formulation by Paulin and co-authors [78, 79] to account for the role of debris ejection on the energy dissipation and wear kinetics where the effect of sliding amplitude is primordial. By introducing a normalized sliding amplitude to the energy wear rate (Equation 1.14), wear kinetics was notably accurately predicted for variable stresses in titanium alloys. This formulation was validated on other tribo-systems [65, 80].

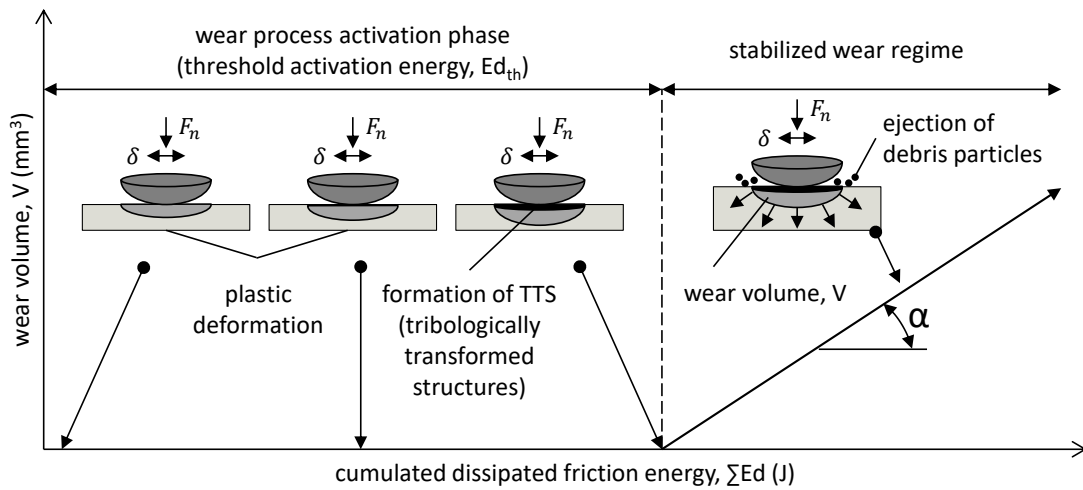


Figure 1.22: Schematization of the wear process through the energy approach: initial activation energy is required for the genesis of TTS before generating the debris particles [35].

$$V = \alpha^* \cdot \sum Ed = \alpha_{ref} \cdot \frac{\delta_g}{\delta_{g,ref}} \sum Ed \quad (1.14)$$

Moreover, the effect of contact size “ A ” on the fretting wear was presented in the energy approach for titanium alloy by Paulin and co-authors [79] and for steel alloy by Merhej and co-authors [81, 82] who underlined an asymptotic decrease of the energy friction coefficient (Figure 1.23a) and the energy wear rate (Figure 1.23b) with the contact size with a power equals $n_A = -0.8$ (Equation 1.15) for the energy wear rate of steel alloy in both sphere-on-flat and cylinder-on-flat configurations. This tendency was explained by the entrapment of debris particles with the increase in the contact size in addition to the limited access of the oxygen to the inner part of the surface which favors adhesive transfers and consequently lower rate as also shown by Warmuth et al. [83, 84]. On the other hand, the effect of contact geometry orientation with respect to the sliding direction was not integrated in the energy wear formulation though the latter was shown to play significant role in wear kinetics (Figure 1.23c). Play and Godet [85, 86] and other authors as Heshmat [87, 88] showed that wear rate, at a given load, increases significantly if the shorter side of the specimen is oriented parallel to the sliding direction (Figure 1.23c). This can be explained by the faster ejection of the third body particles which if trapped for longer time in the contact tend to protect the surface against wear degradations as will be detailed in Section 1.12.2.1.

$$V = \alpha^* \sum Ed$$

$$\alpha^* = \alpha_\infty + \alpha_{ref} \left(\frac{A}{A_{ref}} \right)^{n_A} \quad (1.15)$$

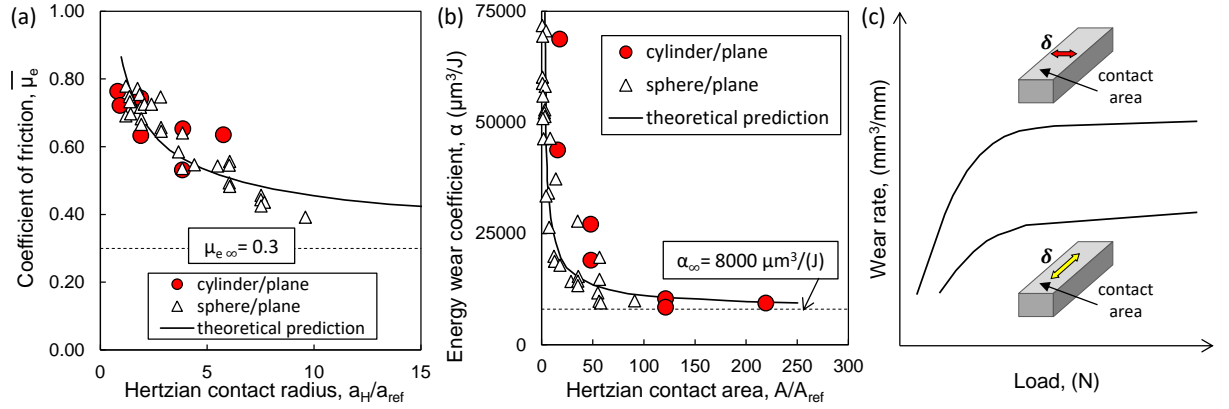


Figure 1.23: Evolution of the (a) friction coefficient and the (b) energy wear coefficient versus the contact radius and the contact area respectively for Hertzian sphere-on-flat and cylinder-on-flat contacts in a dry chromium steel interface [82]; (c) evolution of the wear rates versus the applied load for two contact geometry orientations with respect to sliding direction (after [86]).

Sliding frequency “ f ” and contact pressure “ p ” were recently introduced to the energy approach by Fouvry and co-authors (2017) [56] through the definition of friction power density φ^* (Equation 1.16). This extension is inspired from the “ $p.v$ ” factor (with p being the contact pressure and v being the sliding speed) which is a common approach used in seizure and adhesion processes [89]. Indeed, seizure is detected when the “ $p.v$ ” factor exceeds a certain threshold value below which abrasion is detected [89]. Since, the friction coefficient plays a significant role in wear kinetics [14, 26], friction power density φ^* (i.e. $q.v$ factor) is used instead of the “ $p.v$ ” factor.

$$\varphi^* = \frac{\sum Ed}{N.A} f \quad (1.16)$$

This extended formulation (Equation 1.17) allowed wear prediction in case of abrasive and adhesive wear. It suggested also that the transition from abrasive wear (U-shaped fretting scar) to adhesive wear (W-shaped wear scar) is linked to a threshold friction power density condition ($\varphi^* = \varphi_{th}^*$) (Figure 1.24).

$$V = \alpha^* \cdot \sum Ed = \alpha_{ref} \cdot (\varphi^*)^n \cdot \sum Ed \quad (1.17)$$

Following the extensive work of Quinn [37, 90] over the oxidative wear, the tribo-oxidation process was integrated newly in the energy wear approach by Dreano and co-authors [91] who introduced a pertinent model that takes into account the influence of frequency, sliding amplitude and temperature on wear kinetics (Equation 1.18). This model allows a reliable prediction of the transition from severe abrasive-oxidative wear at low temperature to mild wear at high temperature.

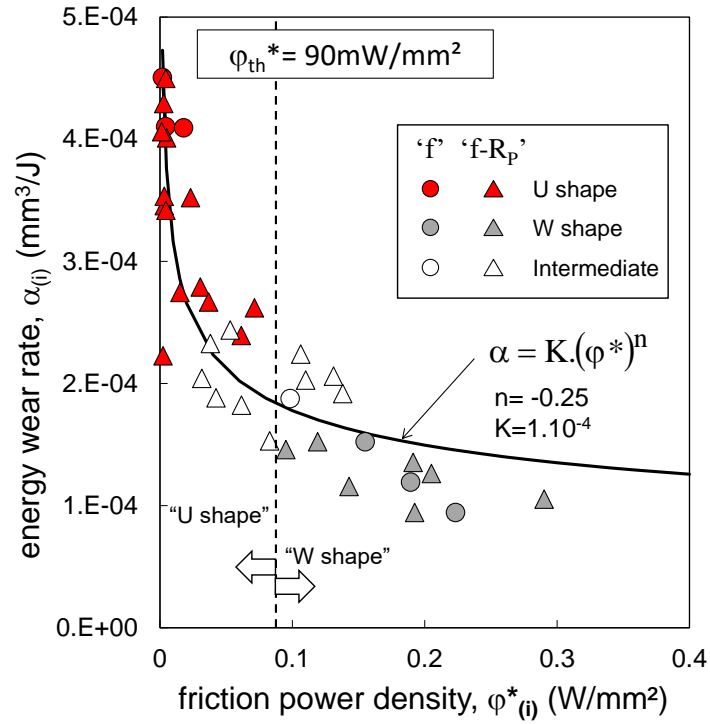


Figure 1.24: Evolution of the energy wear rate as a function of the friction energy density for a TA6V / TA6V contact [56].

$$V = \alpha^* \cdot \sum_{i=1}^{N_{eff}} Ed + V_{\Phi} \quad \text{and} \quad N_{eff} = \begin{cases} N & N \leq N_{GL}, \\ N_{GL} & \text{else} \end{cases} \quad (1.18)$$

$$\alpha^* = \alpha_{ox} \cdot \Psi \quad \text{and} \quad \Psi = \frac{1}{\sqrt{f}} \exp\left(\frac{-E_a}{RT}\right) \delta_0$$

$$N_{GL} = \frac{S_{GL}}{\delta_0^2 \exp\left(\frac{-E_a}{RT}\right)} f$$

Where V_{Φ} is an offset of wear, α_{ox} being the oxidative energetic coefficient of friction, Ψ a tribo-oxidation parameter, α^* the apparent energetic wear coefficient, f is the frequency, E_a is the activation energy for the oxidation process, R is the universal constant, T is the temperature, δ_0 is the sliding amplitude and finally N is the number of fretting cycles.

The transition from severe wear to mild wear is predicted by defining a number of cycles sufficient to create a protective tribo-film referred to as glaze layer (N_{GL}) (Figure 1.25). Before the glaze layer activation ($N < N_{GL}$), the wear volume is proportional to the friction energy dissipated at the interface weighted by the effect of the corrosive environment (linear phase I). When the glaze layer is formed ($N > N_{GL}$), no additional wear is generated (linear phase II) and the friction energy is dissipated in the accommodating third body [91].

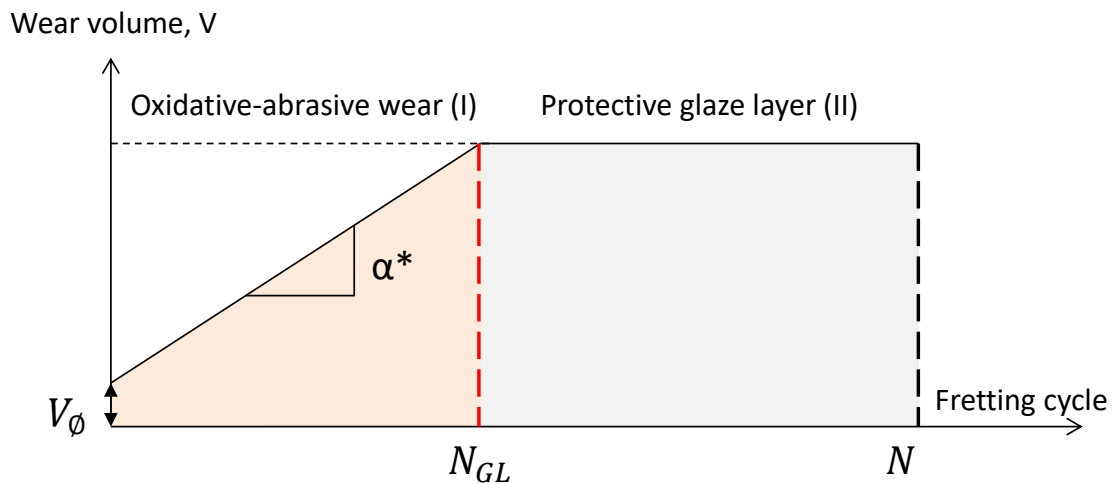


Figure 1.25: Schematic illustration of the wear model proposed by Dreano et al. [91] describing the low and high temperature fretting wear response of a cobalt-based alloy using a combined friction energy and tribo-oxidation formulation.

1.12.2 Approaches for wear mechanisms description

1.12.2.1 Third Body Approach (TBA)

The concept of the third body (TB) was introduced by Godet (1984) [85] who defined the third body as a “debris bed” or an “intermediate film” or a zone having a different composition from that of the first bodies. It constitutes of the interfacial elements separating the two solids in contact. Consequently, based on this concept the “two-body” contact, in its literal sense, does not exist. Many roles of the third body were underlined by [13, 50, 85, 92] including contact separation, load support and accommodation of the difference in the velocity between the first bodies.

From industrial point of view, wear is nothing but loss of functionality of contacting surfaces [93]. This can be translated by the loss of detached particles that protect the surface and prevent further degradation of the latter. Therefore, according to Godet, the so-called wear mechanisms (adhesion, abrasion, corrosion, fatigue, etc.) do not represent wear but rather particle detachment mechanisms [94]. In fact, Godet has more general vision of wear which to him extends the process of particles detachment, to the way the latter behave inside the contact as a third body until being ultimately ejected out of the contact.

To better understand friction phenomenon based on the third body concept, three conceptual tools were developed by Berthier and others since the end of 80’s [13]. These structuring tools include:

- Tribological triplet: it allows the description of the tribo-system taking into account the interaction between the third body and the applied loads at the contact. Hence, a tribo-system is studied at three levels according to Descartes and Berthier [50]:

- a. Mechanism: includes the entire system containing the contact.
 - b. First bodies: include the materials that border the contact which interact to tribological stresses in two behaviors:
 - Changes of phase and structure such as tribologically transformed structures (TTS). TTS constitute an integral part of the first body although their mechanical properties differ from those of the bulk; hence, they should be distinguished from the third body.
 - Cracking and fracture of this superficial structure represent one of the sources of the debris formation flow of the natural third body.
 - c. Third body: represents the layer of materials separating the first bodies. It could be artificial by injecting lubricants at the interface or could be natural third body obtained by detachment of particles from the rubbed surfaces in case of dry contact.
- Accommodation mechanisms: they describe the modes and the sites involved in accommodating velocity. Interface friction observations permitted Berthier et al. (1988) [13] to introduce the concept of velocity accommodation that describes the manner by which the difference in velocity between rubbing solids is accommodated across the interface (Figure 1.26).

Velocity can be accommodated at five different sites (S_i) which include the two first bodies $S1$ and $S5$, the two screen layers $S2$ and $S4$, and the third body $S3$. The mechanisms in which the velocity is accommodated constitute of four modes denoted by (M_j) which include elastic $M1$, rupture $M2$, shear $M3$, and the rolling $M4$. Hence, 20 velocity accommodation mechanisms can be encountered and identified by $SiMj$ code.

(S1) $\wedge \wedge \parallel = \circ \circ$	Sites	Modes
(S2) $\wedge \wedge \parallel = \circ \circ$	(S1) First Body	$\wedge \wedge$ M1, Elastic
(S3) $\wedge \wedge \parallel = \circ \circ$	(S2) Screen	\parallel M2, Normal breaking
(S4) $\wedge \wedge \parallel = \circ \circ$	(S3) Third body	$=$ M3, Shearing
(S5) $\wedge \wedge \parallel = \circ \circ$	(S4) First Body	$\circ \circ$ M4, Rolling
(S5) $\wedge \wedge \parallel = \circ \circ$	(S5) Screen	

Figure 1.26: Velocity accommodation mechanisms. After Berthier et al. (1988) [13].

- Tribological circuit: it describes the flow of particles within the contact region. The tribological circuit synthesized by Descartes and Berthier [50] depicts the flow of the third body within the interface. It constitutes of the following flows (Figure 1.27):
 - a. The source flow Q_s which feeds the contact with the third body and it includes:

- The internal source flow Q_s^i which is generated from the detachment of particles due to abrasion, adhesion, cracking, tribological transformations of the surface (TTS) etc. This flow results in the creation of the natural third body.
 - The external source flow Q_s^e which is due to the introduction of artificial third body at the interface such as lubricants.
- b. The internal flow Q_i that corresponds to the flow of the third body circulating between the first bodies.
- c. The external flow Q_e (or ejection flow) which stands for the particles leaving the interface and it is divided into:
- The recirculation flow Q_r that constitutes of the particles that are reintroduced in the contact carried by one of the first bodies and which will participate once again in the velocity accommodation of the contact.
 - Wear flow Q_w stems from the third body (wear debris) that is ultimately ejected from the interface and will no longer contribute to the velocity accommodation.

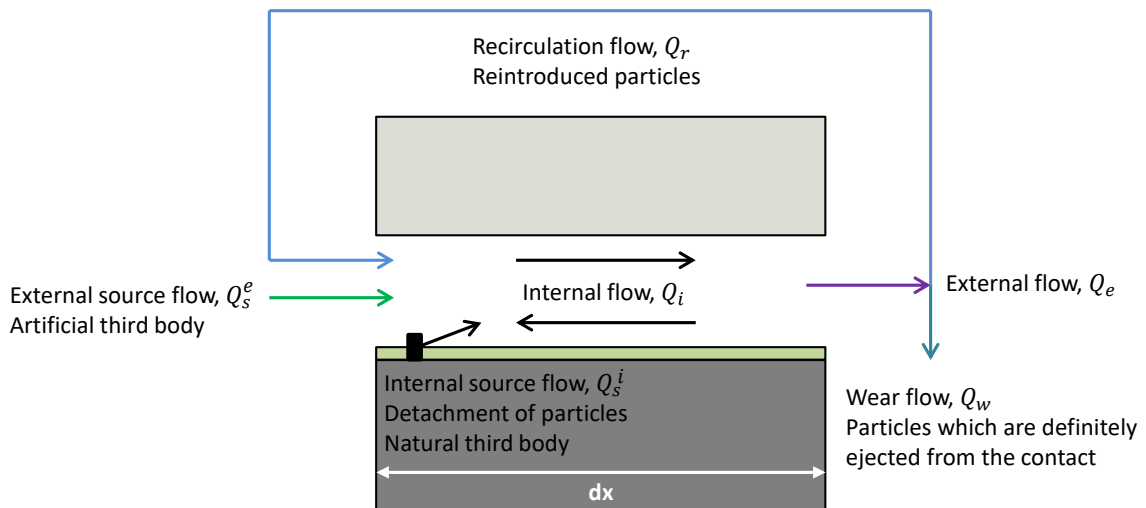


Figure 1.27: Tribological circuit for an elementary 2D interface [50].

Modelling third body flows

Indeed, wear process involves competition between the source flow and the wear flow as reported by Fillot et al. (2007) [93]. Actually, there is no direct relation between both flows. However, they tend to modify the thickness of the third body that in turn represents the way through which the source and the debris flows communicate.

Figure 1.28 displays the interaction between the source and the wear flow through their influence on the third body. In fact, the increase in the particle detachment increases the mass and consequently the thickness of the third body (H_{TB}) (I). On the other hand, lower source flow and

particle detachment are rationally expected when there is sufficient accumulation of interfacial layer which can support the applied load and accommodate velocity difference between first bodies (II). However, when the third body becomes sufficiently thick, particle ejection flow will be triggered (III) which in turn decreases the thickness of the third body (IV).

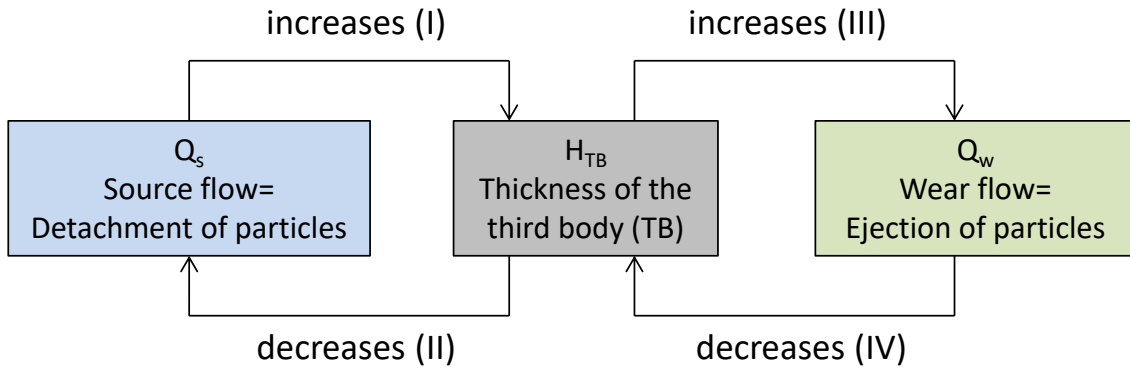


Figure 1.28: Relative influence of the detachment of particles, the thickness of third body at the interface, and the ejection of these particles [93].

After the genesis of the tribological circuit, Fillot and co-authors elegantly described debris flows by introducing an analytical model based on the sliding velocity accommodation role of the third body [93]. In this model, it was shown that the stabilized or the “steady state” thickness of third body (H_{ss}) at the interface is highly dependent on the equilibrium values of the source flow Q_s and the wear flow Q_w of the debris bed. Figure 1.29 clarifies the way the mass of the third body affects the source and ejection flows. As said in the previous paragraph, an increase in the mass of the debris layer trapped in the interface increases the debris ejection flow from the contact zone (Figure 1.29).

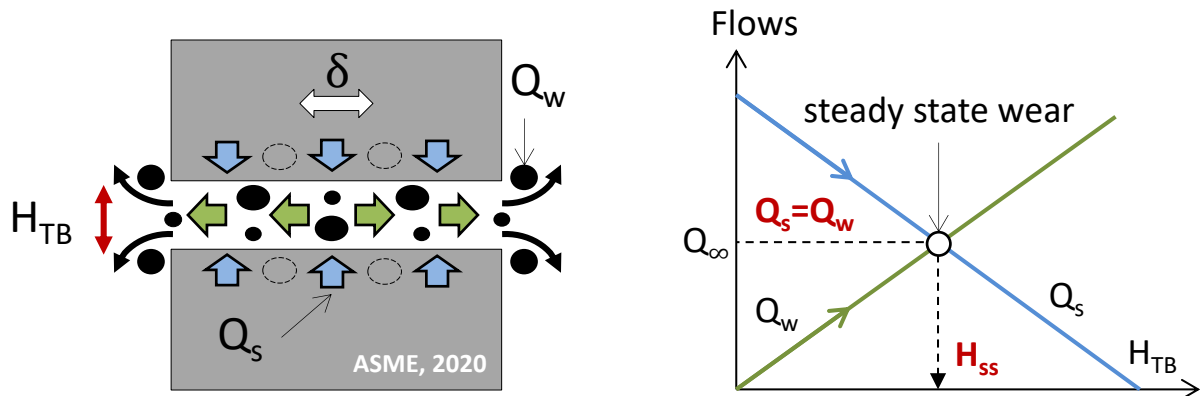


Figure 1.29: Competition of the source flow and wear flow as a function of the thickness of the third body [93].

On the other hand, an increase in the thickness (i.e. the mass) of the third body minimizes the debris formation flow. This is attributed to the fact that the third body protects the surface by consuming a significant part of the friction energy.

Finally, a steady state can be defined which corresponds to the balance between the debris ejection flow and the debris formation flow. At this state, a stabilized mass of the third body is obtained after which it will no longer change.

This analytical model was recently validated through fretting-wear experiments and finite element wear simulations taking into account the evolution of the third body thickness at the interface by Arnaud and co-workers [95, 96]. By superposing the 2D wear profiles of the cylinder and the flat counterparts of a Ti-6Al-4V contact (Figure 1.30a, b & c), the thickness of the third body trapped within the interface can be estimated from the gap obtained between the worn profiles.

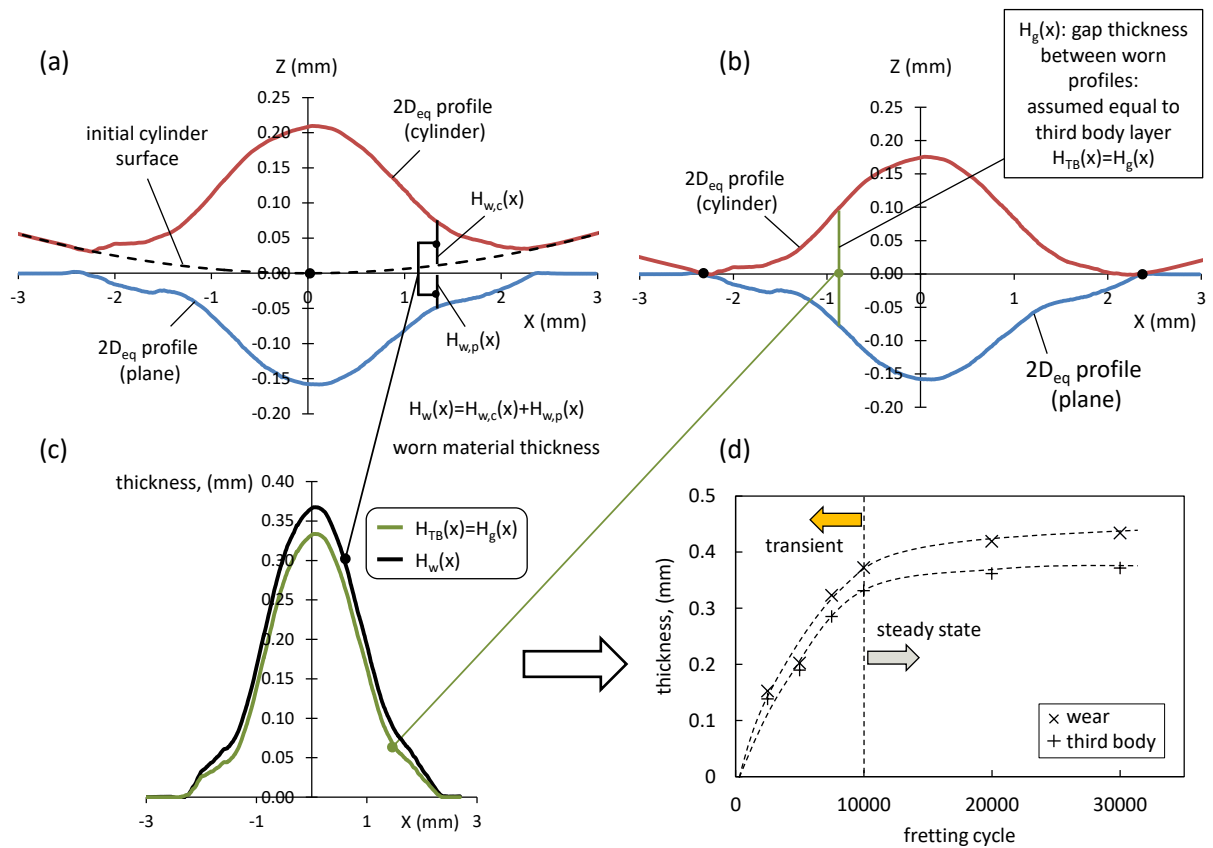


Figure 1.30: Explanation of the methodology used to quantify the fretting scar morphology from fretting wear experiment through the: (a) identification of the worn profiles; (b) identification of the third body profile; and (c) extrapolation of the third body and wear profiles. (d) Comparison of the evolution of the maximum wear thickness and maximum third body thickness versus the number of fretting cycles [96].

Figure 1.30d compares the evolution of the maximum wear depth $H_w(0)$ and third body thickness $H_{TB}(0)$ at the center of the scar. A fast increase of the latter is observed until steady state is reached. Following this, the maximum wear depth keeps increasing whereas the third body thickness stabilizes. This stabilization is in agreement with the third body approach and the TB model proposed by Fillot (Figure 1.29) [93]. When the third body thickness increases, a larger part of the friction energy is consumed by the third body layer, so the debris formation rate

decreases. Alternatively, an increase of the third body thickness increases the debris ejection flow. Bearing this hypothesis in mind, a steady state wear regime is reached when both formation and ejection flows are equal leading to a constant third body thickness.

The TB was then introduced by the same authors in a finite element wear-model by defining a conversion factor ($\gamma(x) = H_{TB}(x)/H_w(x)$) which expresses the proportion of worn thickness transformed into third body layer at a given position “x” in the fretted interface [95, 96]. This so-called conversion factor was shown to be dependent on the fretting cycles and the sliding amplitude. Thanks to this dynamic coupled TB-wear modelling it was possible to precisely predict the wear depth at a variable number of fretting cycles, sliding amplitudes and contact sizes (Figure 1.31b) which is not the case in wear models neglecting the effect of TB where wear profiles can be critically underestimated (Figure 1.31a). It should be equally remarked that this investigation was preceded by previous studies aiming at modelling third body effect at the interface including Ding et al. [97] then Ghosh et al. [98] and Basseville et al. [99] who were the first to examine the influence of debris particles in FEM fretting interfaces. Besides, FEM (finite element method) and DEM (discrete element method) were also suggested by Haddad et al. [100] and Leonard et al. [101] to estimate the impact of the TB on friction, contact pressure and stress fields.

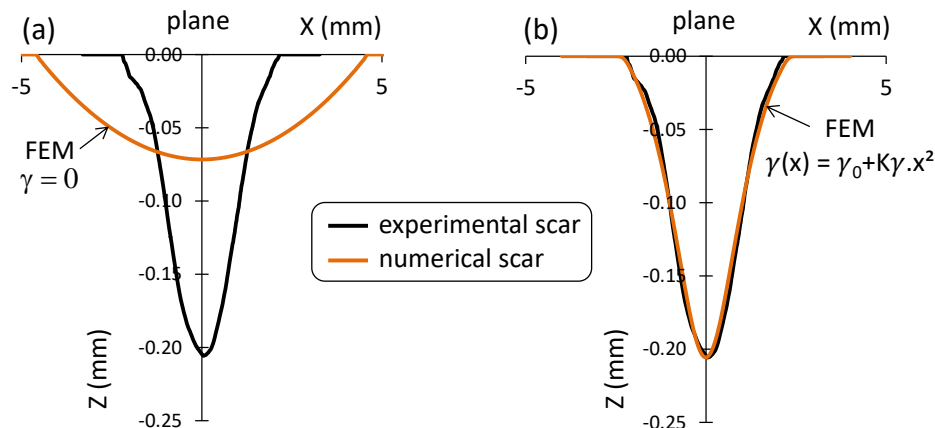


Figure 1.31: Comparison between the experimental and simulated wear profiles on the flat counterpart of a dry homogeneous TA6V cylinder-on-flat configuration (a) without third body consideration ($\gamma=0$); (b) with third body consideration ($\gamma(x) = \gamma_0 + K_\gamma \cdot x^2$) [96].

Rheology of the third body

Studying the rheology of the third body was the subject of several authors including Descartes et al. [50], and Iordanoff et al. (2002) [102]. Two main properties can be used to describe the latter which are the cohesion and the ductility of the third body (Figure 1.32).

- Cohesion: this term is selected in correlation with the cohesion of powdery materials [103]. In fact, the observations of the third bodies allow qualitative comparison between their cohesion as illustrated in Figure 1.32. Third body having very low cohesion is very powdery and constitutes of small particles (Figure 1.32a). On the other hand, highly cohesive third body

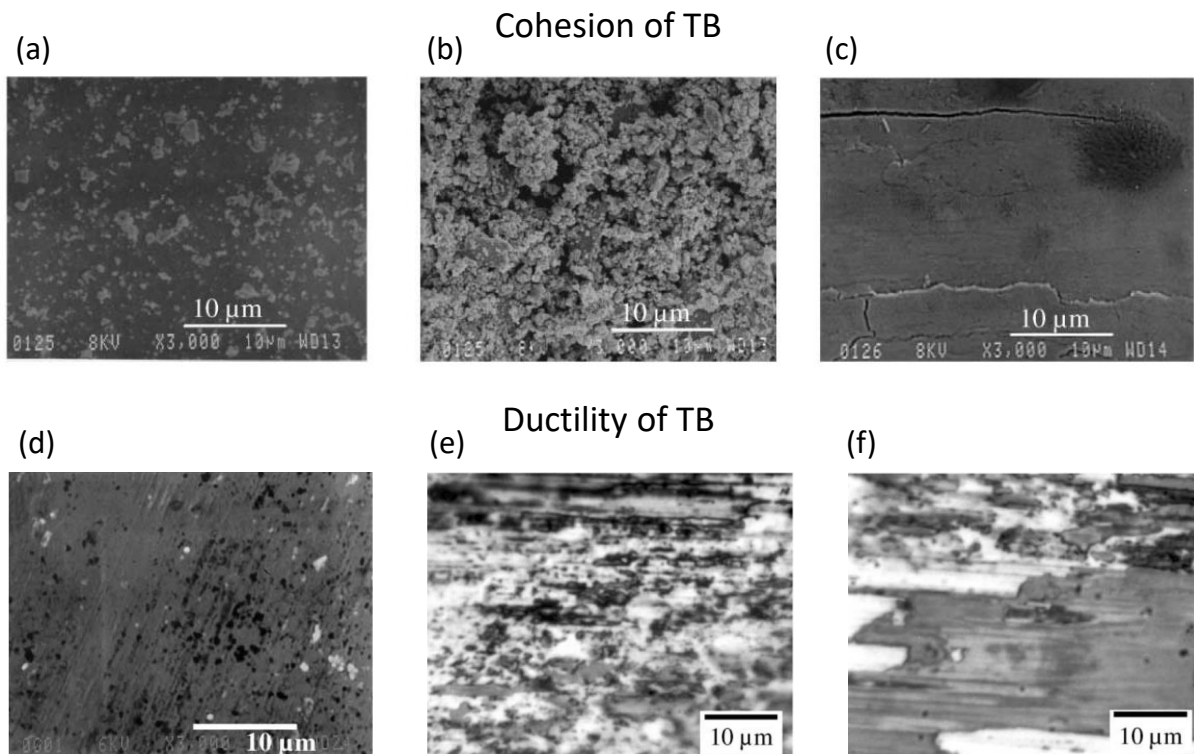


Figure 1.32: Relative cohesion of the solid third body, SEM images: (a) very low; (b) low; (c) high. Relative ductility of the solid third body, SEM images: (d) low; (e) not very high; (f) high [50].

is very compact and the particles seem to be highly compressed.

- **Ductility:** the term ductility is selected by resemblance with the plastic flow characteristics of metals and it corresponds to the ease with which the third body spreads and extrudes in the contact [50]. Low ductility is detected when the third body flows with difficulty and covers only a small area of the contact zone as can be seen in Figure 1.32d. Yet, high ductility is observed when the third body extends easily covering a large zone of the contact area (Figure 1.32f).

1.12.2.2 Contact Oxygenation Concept (COC)

Several authors in literature tried to predict transitions in wear mechanisms from pure abrasive to mixed abrasive-adhesive wear. Lim and co-authors [104, 105] proposed a wear-mode map for unlubricated sliding whereby the transitions between mild and severe wear are dictated by the effects of the normal load and the sliding velocity. On the other hand, the transition from adhesive to oxidative wear was shown to be highly dependent on the atmospheric environments [106–108] where adhesion is favored when the oxygen partial pressure is relatively low [42].

Recent approach linking wear transitions to the external environment was suggested by Mary and co-workers [55]. While investigating the influence of contact pressure on titanium alloy, the authors suggested that the significant adhesive wear observed at high pressure is associated to

the very poor oxygen supply to the center of the scar. This triggers adhesive wear and severe plastic shear strains giving birth to a hard TTS [49, 50, 57]. It also promotes nitriding processes. The authors underlined that abrasive wear is favored at the edges of the contact due to the easier access of dioxygen molecules from the external ambient air. On the other hand, an abrasion-oxidation process is activated over the whole interface at low pressure because of the easier oxygen penetration to the inner part of the contact. Based on these findings, Mary et al. [55] introduced the concept of “air distillation”. In the same sense, Warmuth and co-authors [83, 84] noticed that high radius contacts showed preferential adhesive damage towards their centers due to the oxygen limitation imposed by the contact size. They called this “oxygen exclusion”. Besides, the effect of frequency on adhesive wear extension was equally investigated by many researchers including Shipway and co-authors [51, 84, 109] who revealed that increasing the sliding frequency tends to increase adhesion due to the lower time given for asperity interactions and for oxide formation. Besides, it triggers higher friction power dissipation [110] which leads to more oxygen consumption resulting in an oxygen-starved environment towards the center of the contact [56].

Studying several loading conditions, Fouvry and co-workers [56] finally combined the preceding notions under a more generalized “Contact Oxygenation Concept” (COC). This latter could be formalized assuming the interfacial di-oxygen partial pressure “ P_{O_2} ” parameter. P_{O_2} is very high at the contact borders, equivalent to the ambient air, but tends to decrease inside the interface. The decreasing evolution of “ P_{O_2} ” toward the inner part of the contact illustrated by the hyperbolic function in Figure 1.33 is related to a balance between the diffusion of dioxygen molecules from the external part of the contact and the consumption rate induced by the oxidation of the fresh surface metal exposed by the friction processes.

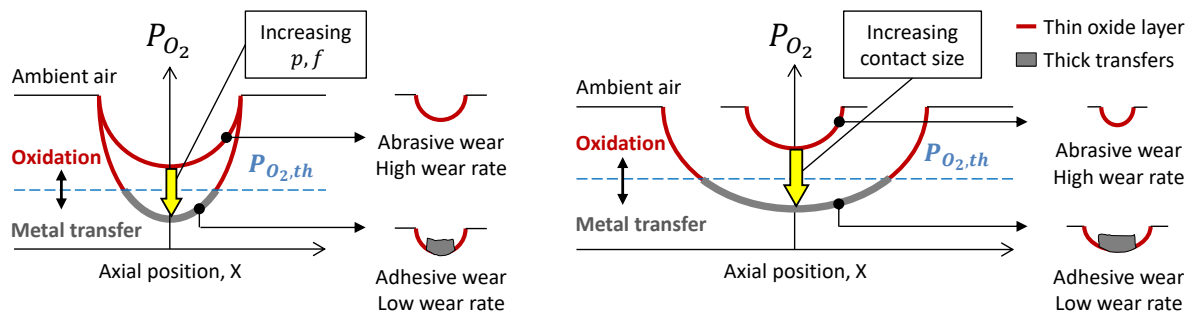


Figure 1.33: Schematic illustration of the contact oxygenation concept for a fretting contact submitted to different loading conditions [56].

The dioxygen diffusion process is controlled by the interface properties such as the clearance between the contact asperities and the diffusion properties of the porous debris layer. The dioxygen consumption rate is governed by the metal reactivity and the surface damage rate which could be qualified using the so-called “p.v” factor. Hence, the higher the “p.v” factor, the faster the degradation of the protective oxide layer, and the higher the fresh metal exposure, the faster the consumption of the available dioxygen molecules and therefore the faster the decreasing of the interfacial di-oxygen partial pressure “ P_{O_2} ”.

According to the given “contact oxygenation” concept [56], abrasive-oxidational wear is predominant in the condition of full contact oxygenation. This suggests that whatever the test duration and the contact position inside the fretted interface, the local P_{O_2} is higher than a threshold value $P_{O_2,th}$ above which the surface oxidation is guaranteed. Alternatively, composite abrasive-adhesive wear process is observed when P_{O_2} falls below this threshold value. Hence, there is a critical “oxygen distance d_O ” from the contact border above which P_{O_2} is no more sufficient so that seizure phenomena are activated (Figure 1.33).

1.13 Conclusion

This bibliographic analysis asserts that fretting wear is highly impacted by the fretting loading parameters which affect in turn the wear mechanisms such as abrasion, adhesion, oxidation, delamination, fatigue, etc. resulting in debris formation and ejection.

However, most of the previous investigations were conducted on Hertzian contacts such as sphere-on-flat and cylinder-on-flat which lead to modification of the contact pressure profile along the test duration due to wear extension and the associated growth in the contact area. Another drawback of these configurations is that both the contact pressure and contact area vary simultaneously with the normal force. This drives opposite effects on the contact oxygenation thus skewing the parametric analysis. Hence, decoupling the effects of the contact pressure, contact area and wear extension necessitates a flat-on-flat configuration where these aspects can be probed separately. Nevertheless, this configuration appears to be poorly addressed in literature due to alignment issues which makes it interesting to navigate this contact at different fretting solicitations.

So the objective of the current study is to use flat-on-flat configuration for three main objectives:

- Understanding the separate effect of fretting loading parameters on wear kinetics and wear mechanisms (third body flows, abrasion, adhesion and oxidation) (Chapter 3).
- Investigating adhesive wear extension in fretting interfaces by applying the contact oxygenation concept (Chapter 4).
- Modelling the adhesive wear extension in fretting interfaces by applying an advection-dispersion-reaction contact oxygenation approach (Chapter 5).

Chapter 2

Materials and experimental procedure

Contents

2.1	Material	41
2.1.1	Chemical composition	41
2.1.2	Microstructure	41
2.1.3	Mechanical properties	41
2.2	Contact configuration	42
2.2.1	Surface roughness	42
2.2.2	Plain flat-on-flat samples	43
2.2.3	Textured samples: access to smaller contact sizes	44
2.3	Numerical investigation of the pressure distribution in the studied flat contact	45
2.4	Fretting wear experimental set-up	47
2.5	Data acquisition	48
2.6	Experimental strategy	48
2.6.1	Plain samples	48
2.6.2	Textured samples test strategy	49
2.7	Damage characterization	50
2.7.1	Optical observation	50
2.7.2	Wear analysis	50
2.7.3	Scanning by electron microscopy (SEM)	52
2.7.4	Raman spectroscopy	53
2.7.5	Nano-indentation	54
2.8	Conclusion	56

2.1 Material

2.1.1 Chemical composition

The material used in this thesis is 34NiCrMo16 which is a nickel-chromium-molybdenum low-alloyed steel having a chemical composition shown in Table 2.1. Chromium is added to this steel to enhance its resistance to oxidation [111]. When added with chromium, nickel improves steel resistance to heat and corrosion. Besides, it contributes to high strength, ductility and excellent toughness (impact strength). By mixing with chromium-nickel austenitic steels, molybdenum improves resistance to localized pitting attack and crevice corrosion especially in sulfur and chlorides-containing environments [111].

Element	C	Si	Mn	P	S	Cr	Mo	Ni	Fe
% Weight	0.37	0.38	0.39	0.012	0.003	1.72	0.3	3.83	93

Table 2.1: Chemical composition of 34NiCrMo16 [112].

2.1.2 Microstructure

34NiCrMo16 displays a tempered martensitic structure (Figure 2.1a). It is obtained by several heat treatments starting by austenitization through which carbon steel is heated above a critical temperature (730° C). This leads to a phase transition [113] from a cubic body-centered (BCC) alpha iron (α -Fe or ferrite) to a cubic face-centered (FCC) gamma iron (γ -Fe) referred to as austenite (Figure 2.1a). This phase transition leads to dissolution of more carbon atoms due to the open structure of austenite. Following this, martensite is formed by quenching (rapid cooling) of the austenite at a rate that is sufficiently high to limit the time for carbon to diffuse out of the crystal structure of austenite. As a result, phase transition occurs from cubic face centered austenite to a highly strained tetragonal body-centered (BCT) martensite that is highly saturated with carbon [114]. This phase transformation results in a hard and brittle steel. To reduce brittleness, tempering is performed which is the process of heating steel to a high temperature so that it becomes more ductile through the segregation of carbon, the precipitation of carbides, the decomposition of retained austenite and the recovery and recrystallization of martensitic structure [114].

2.1.3 Mechanical properties

The mechanical properties of 34NiCrMo16 are shown in Table 2.2. Due to its high strength, superior cleanliness, elevated toughness, hardenability and its good dimensional stability, 34NiCrMo16 is used in a broad range of industrial applications such as aerospace, construction, heavy-duty machine parts, dies having thick sections and complex shapes submitted to high level of constraints.

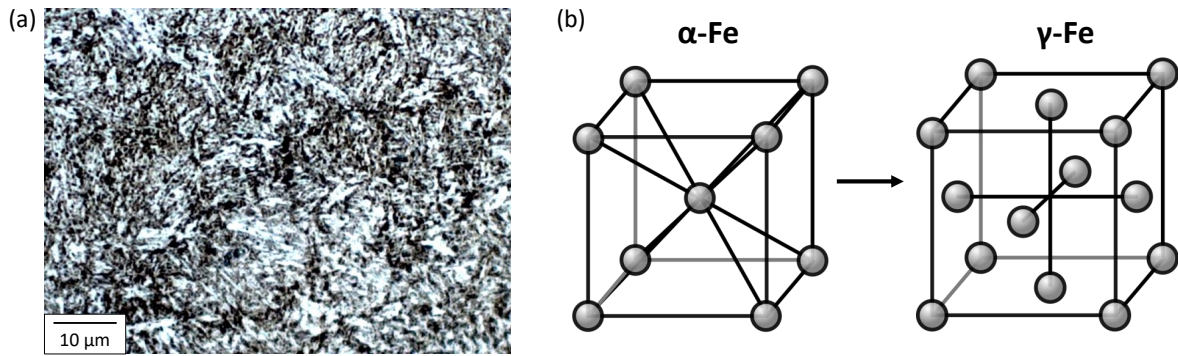


Figure 2.1: (a) Martensite structure of 34NiCrMo16 after chemical etching with nital; (b) phase transition from a cubic body-centered (BCC) alpha iron (α -Fe or ferrite) to a cubic face-centered (FCC) gamma iron (γ -Fe or austenite).

Young's modulus, E (GPa)	Poisson's ratio, ν	Yield stress (0.2%), $\sigma_{y,0.2\%}$ (MPa)	Ultimate stress, σ_u (MPa)
205	0.3	950	1130

Table 2.2: Mechanical properties of 34NiCrMo16 (obtained from the documentation of material supplier [115]).

2.2 Contact configuration

In this thesis, plain and textured homogeneous crossed flat-on-flat contacts will be investigated. The purpose behind using plain samples is to establish and calibrate empirical and numerical models for wear kinetics (Chapter 3) and contact oxygenation (Chapters 4 & 5). However, flat-on-flat contacts with textured bottom samples are used to study small contact areas, track debris flow, and validate the aforesaid models.

2.2.1 Surface roughness

The initial surface roughness of the samples (Figure 2.2) is measured by interference profilometry. The one-dimensional arithmetic mean height roughness Ra (Equation 2.1) is in the order of 0.25 μm . However, the maximum height of the profile Rz (Equation 2.2) which indicates the absolute vertical distance between the maximum peak height and the maximum valley depth along the sampling length " l " is in the order of 1.50 μm (Figure 2.2).

$$Ra = \frac{1}{l} \int_0^l |Z(x)| dX \quad (2.1)$$

$$Rz = \max [Z(X)]_{0 < X < l} + \min [Z(X)]_{0 < X < l} \quad (2.2)$$

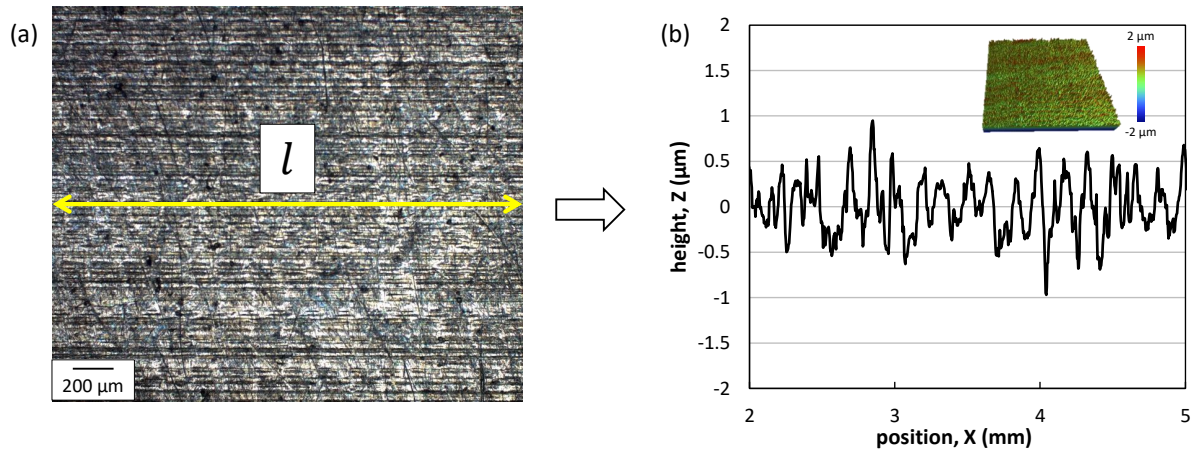


Figure 2.2: (a) Optical image of 34NiCrMo16 flat surface; (b) one-dimensional roughness profile along the sampling distance “ l ”.

2.2.2 Plain flat-on-flat samples

Figure 2.3a illustrates the homogeneous crossed plain flat-on-flat contact configuration. The fretted interface has a rectangular shape having a contact area “ $A = L_{\parallel\delta} \cdot L_{\perp\delta}$ ” where “ $L_{\parallel\delta}$ ” is the longitudinal contact length parallel to the sliding direction (δ) and “ $L_{\perp\delta}$ ” is the transverse contact length perpendicular to the sliding direction (δ).

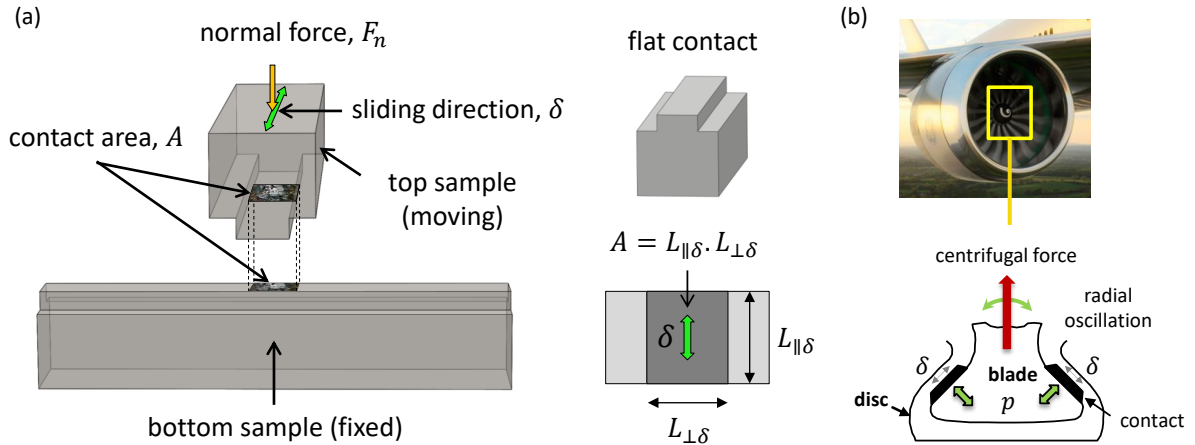


Figure 2.3: (a) Schematic presentation of the studied crossed flat-on-flat contact configuration; (b) flat-on-flat configuration in turbine engine dovetail blade/disk contact.

This configuration is selected as it allows a constant contact area and consequently a constant contact pressure during fretting wear test. This is not the case in Hertzian configurations such as punctual (sphere-on-flat) or linear (cylinder-on-flat) where contact area and contact pressure vary simultaneously during wear extension process. Although flat-on-flat configuration induces pressure discontinuities at the borders, it can still lead to a flat pressure profile such that wear tends to smooth these peak pressures as it will be detailed later using FEM surface modelling. Hence, although flat-on-flat contact implies a complex alignment procedure, this contact con-

figuration is evidently more convenient than Hertzian contacts in establishing constant pressure wear model, thus reliable wear rate.

In fact, former studies revealed a contact geometry dependence of wear kinetics [56, 81, 83–85]. It was proposed that increasing the contact area leads to an easier entrapment of debris particles in the interface resulting in lower wear rates due to the protective role of the third body particles in the contact as postulated by Godet in TBA [85]. On the other hand, increasing contact size leads to more difficult access of oxygen to the inner part of the surface shifting the contact from full abrasive-oxidative wear to a mixed abrasive-adhesive wear (Figures 1.16 & 1.33) [55, 56]. This transition, illustrated by the “contact oxygenation concept (COC)”, explains the decrease in the wear rate with the increase in the contact size as a result of adhesive wear extension since the adhesive wear rate is significantly lower than that detected in abrasive wear. Bearing these hypotheses in mind (i.e. TBA and COC), the reduction of the wear rate for larger contact sizes can be explained. From this viewpoint, the results obtained by spherical (punctual) or cylindrical (linear) contacts might overestimate wear rates if the real contacts are more likely flat-on-flat (planar).

Another point worth mentioning, flat contacts provide a better description of the real interfaces in some mechanical systems such as blade/disk interface (Figure 2.3b). Besides, this contact is highly adapted for studying many processes such as debris flows (Chapter 3) and contact oxygenation (Chapters 4 & 5) which are not simple to address using Hertzian contacts.

2.2.3 Textured samples: access to smaller contact sizes

To investigate third body flows and contact oxygenation at small contact sizes, macro-textured samples are used. The texturing strategy consists in machining rectangular grooves using Electrical Discharge Machining (EDM) on the flat surface of the bottom samples (Figure 2.4a). These grooves have the same initial roughness as the plain specimens. Note that this machining method has insignificant effect on the borders of the grooves which ensures uniform contact pressure profiles at the interface. The depth (D), and the thickness (L_t) of the grooves are kept constant (1 and 0.5 mm respectively) (Figure 2.4a). On the other hand, the spacing between grooves is varied to adjust the transverse length “ $L_{\perp\delta}$ ” which takes values between 0.5 and 2.25 mm while maintaining a constant $L_{\parallel\delta}=5$ mm (Figure 2.4b). However, by changing the orientation of textures with respect to the sliding direction (δ), the effect of the longitudinal contact length “ $L_{\parallel\delta}$ ” can be equally investigated. Hence, the spacing between grooves is varied to adjust “ $L_{\parallel\delta}$ ” which takes values between 0.75 and 2.25 mm while maintaining a constant $L_{\perp\delta}=5$ mm. It should be remarked that specimens having $L_{\parallel\delta} < 0.75$ mm are excluded from the analysis due to flexural fatigue failure of the textures. Note that in all cases, the normal force “ F_n ” is adjusted in a way to maintain a constant mean contact pressure at a desired value “ p ”.

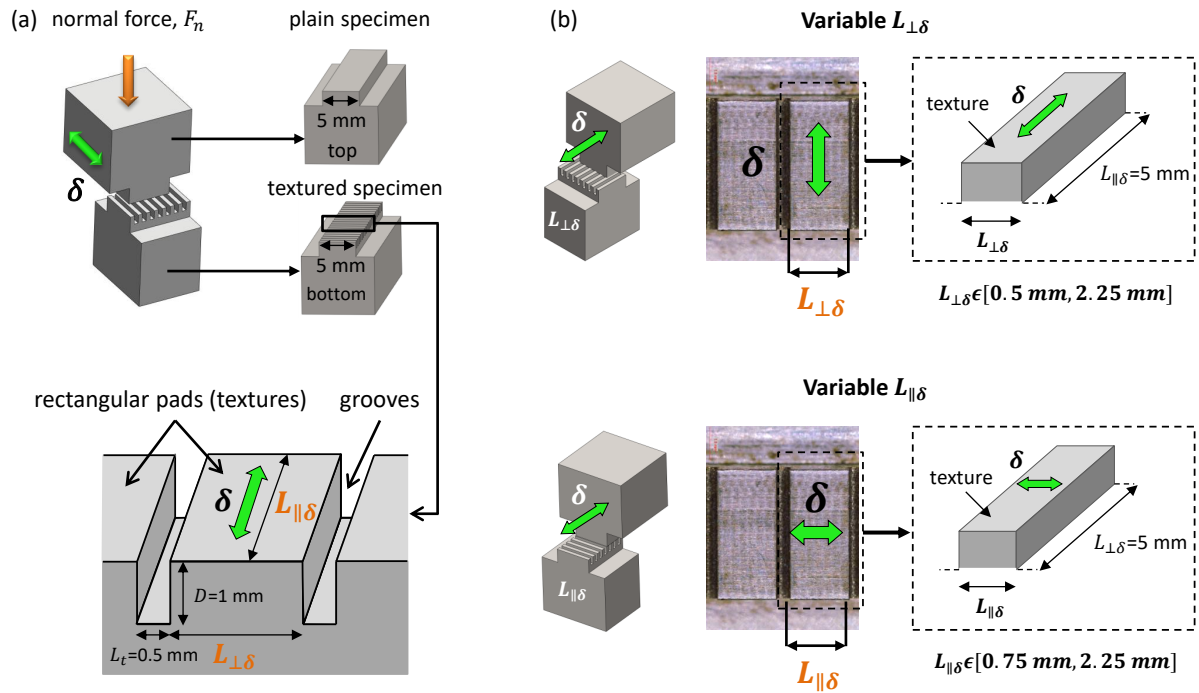


Figure 2.4: (a) Crossed flat-on-flat configuration with textured bottom samples; (b) geometrical description of the textures orientation with respect to the sliding direction.

2.3 Numerical investigation of the pressure distribution in the studied flat contact

One of the drawbacks of flat-on-flat contact configurations is the stress concentration existing at the borders of the contact which leads to a discontinuous pressure distribution at the interface. The objective of this study is to investigate wear process under constant and flat pressure condition. Hence, a key question is: does the current flat-on-flat contact converge to a flat pressure distribution with the surface wear extension?

To answer this question, numerical simulations of wear were done using a finite element code developed at LTDS (Laboratory of Tribology and Systems Dynamics) by Arnaud and co-workers (2017)[95]. This Matlab-Python-Abaqus code simulates the process of material removal from the interface leading to fretting wear. Besides, it permits computing contact pressure as a function of the fretting cycles. The 2D configuration of the flat-on-flat contact shown in Figure 2.5a is introduced in the model. Then, a so-called “Wear Box” is drawn around the contact zone (Figure 2.5b). The numerical procedure including $40 \mu\text{m}$ surface mesh size is fully detailed in [95]. Following this, the reference test parameters are injected in the model which are the energy friction coefficient $\mu_e = 0.7$, the contact pressure $p = 100 \text{ MPa}$, the sliding amplitude $\delta_g = \pm 100 \mu\text{m}$ and the energy wear rate $\alpha = 4.231 \times 10^{-5} \text{ mm}^3/\text{J}$.

Similar results were detected for the top and bottom samples. For the sake of simplicity, only results of the bottom samples will be shown in this part. The contact pressure at the edges is

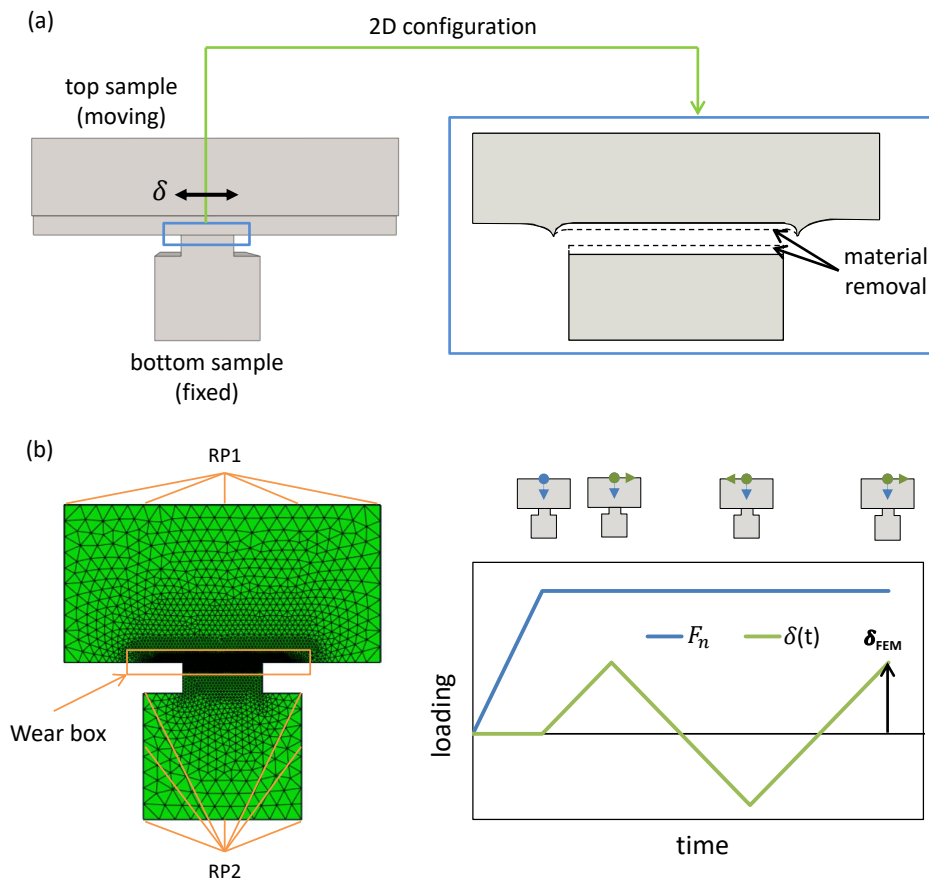


Figure 2.5: Illustration of the: (a) 2D contact configuration injected in the “wear box” model; (b) finite element flat-on-flat contact model and the loading criteria (after [95, 116]).

very high during the first 500 cycles for the bottom samples as can be shown in Figure 2.6a & b. The initial maximum contact pressure is four times higher than that found at the central part of the contact. However, after 500 cycles, the maximum pressure decreases by a factor of two and stabilizes around 200 MPa in the remaining test duration. This sharp decrease in the maximum contact pressure is directly related to the surface wear that smooths the contact edges. Away from the borders, the contact pressure is homogeneous along the interface and it has a constant value around 100 MPa with the number of cycles as reflected by the mean contact pressure (p mean) and the contact pressure at the center (p center) in Figure 2.6b. Hence, this allows us to conclude that, except for the edges, the contact pressure converges to a flat distribution after few fretting cycles. Besides, even at the contact borders, the peak pressure is drastically reduced which supports the assumption that a constant mean pressure condition can be considered. Another important remark is that the maximum contact pressure attained for the studied reference conditions is around 468 MPa which is lower than the yield stress (950 MPa). By increasing the contact pressure, it appears that yield stress is reached at the border for a mean contact pressure exceeding 175 MPa during the first few cycles. So, in what follows the studied contact pressures are kept less than or equal to 175 MPa to ensure that we are working systematically in elastic domain away from plastic yielding.

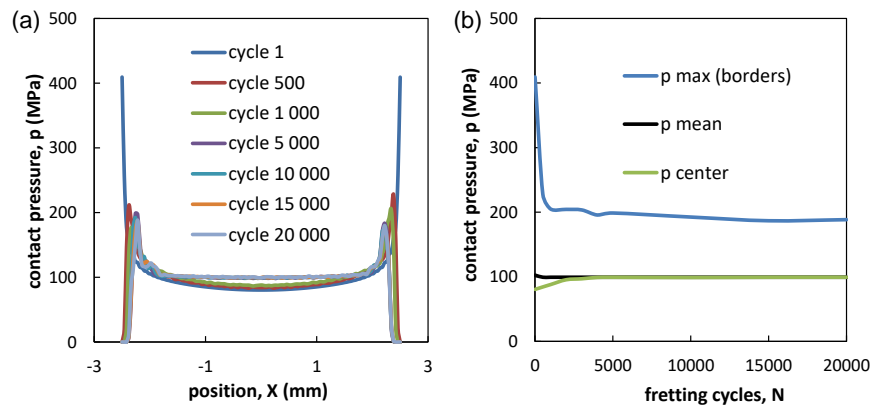


Figure 2.6: (a) Contact pressure distribution along the interface of the bottom sample; (b) evolution of the maximum, mean and central contact pressure versus the number of cycles for the bottom sample under the reference test conditions: $N=20000$ cycles, $p=100$ MPa, and $\delta_g=\pm 100$ μm .

2.4 Fretting wear experimental set-up

Fretting tests were performed on a hydraulic shaker (Figure 2.7) which is customized at LTDS Laboratory to investigate large horizontal crossed flat-on-flat configuration. The top sample is placed at the edge of an MTS (MTS Systems Corporation) hydraulic actuator used to impose displacement controlled cyclic loading. The bottom sample is fixed on a sample holder which can be adjusted in a way to obtain a good flat-on-flat alignment. Tests were performed at ambient temperature (25 $^{\circ}C \pm 5$ $^{\circ}C$) and relative humidity ($RH=40\% \pm 10\%$).

A fretting test consists of placing the samples in the holders then implementing a careful alignment using a goniometric system. Then, the contact is closed and a constant normal force is applied thanks to a spring system which can be adjusted during the test to compensate the loss in the normal load caused by fretting wear. After that, displacement controlled cyclic loadings are imposed until a desired number of cycles is reached. The relative displacement is measured by a high precision extensometer and the tangential and normal forces are recorded by high resolution force sensors.

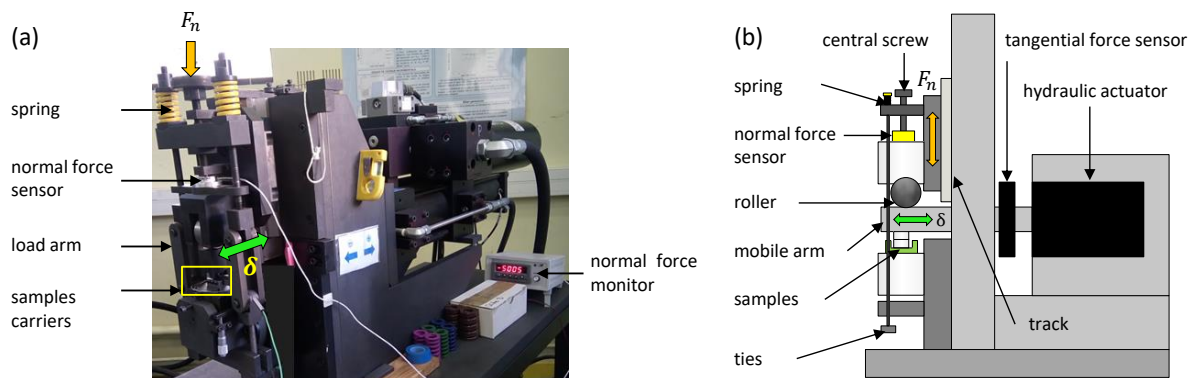


Figure 2.7: (a) Fretting wear experimental set-up at LTDS Laboratory; (b) schematic illustration of the experimental set-up.

2.5 Data acquisition

During the test, 200 values of the fretting displacement (δ), the tangential force (F_t) and the normal force (F_n) are recorded at each fretting cycle (Figure 2.8a). The evolution of “ F_t ” versus “ δ ” allows plotting the “ F_t - δ ” fretting cycle which has a quadrilateral shape under gross slip condition. Cumulating the fretting loops during the test gives birth to the so-called fretting log (Figure 2.8b) which permits checking the stability of the gross slip condition. The displacement amplitude (δ^*) is partly a function of the elastic accommodation of the test system which itself depends on the tangential force amplitude. To guarantee a given sliding amplitude, gross slip fretting tests were performed by monitoring the sliding amplitude δ_g , defined as the residual displacement when $F_t=0$. On the other hand, δ^* is continuously adjusted to keep constant δ_g at the required value.

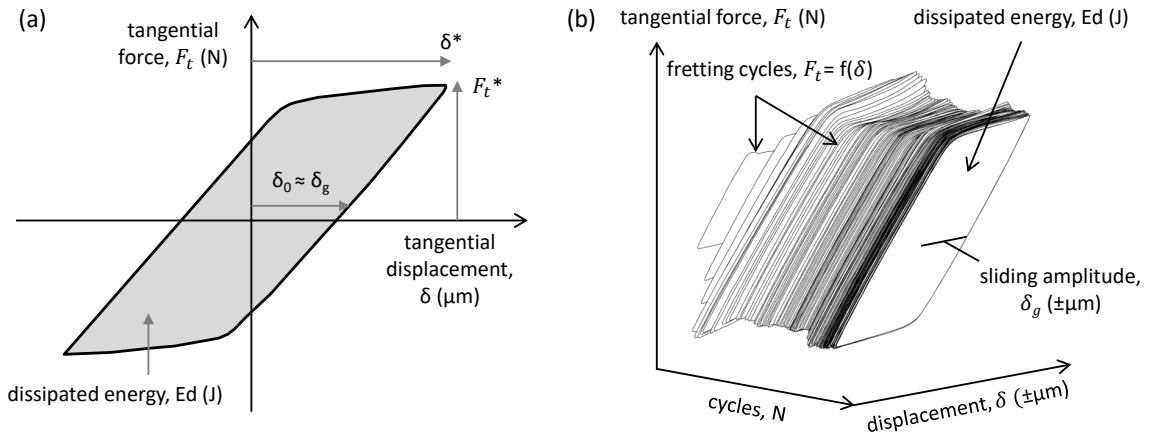


Figure 2.8: (a) Illustration of the parameters obtained from fretting cycle under gross slip condition; (b) fretting log with δ_g maintained constant by adjusting δ^* .

2.6 Experimental strategy

2.6.1 Plain samples

A multi-scale strategy (Figure 2.9) is followed to investigate plain flat-on-flat contact submitted to different loading parameters. Series of tests were carried out starting from a key reference experiment, repeated three times (denoted by O), having a number of cycles $N=20000$, contact pressure $p=100$ MPa, sliding amplitude $\delta_g = 100$ μm , sliding frequency $f=1$ Hz, and a square apparent contact area $A=25$ mm^2 ($L_{\parallel\delta}=L_{\perp\delta}=5$ mm where “ $L_{\parallel\delta}$ ” is the longitudinal contact length parallel to the sliding direction (δ) and “ $L_{\perp\delta}$ ” is the transverse contact perpendicular to the sliding direction (δ)).

A cross-test strategy is then applied where the contact pressure is varied from $p=10$ to 175 MPa (Figure 2.9a), the sliding amplitude from $\delta_g = \pm 25$ to ± 200 μm (Figure 2.9a), the frequency from $f=0.5$ to 10 Hz (Figure 2.9b), the number of cycles from $N=5000$ to 40000 cycles (Figure 2.9b),

and finally the contact area from $A=10$ to 25 mm^2 (Figure 2.9c). Note that the contact area is varied firstly by reducing the length “ $L_{\parallel\delta}$ ” along the sliding direction from 5 to 2 mm while maintaining a constant length “ $L_{\perp\delta}=5 \text{ mm}$ ”. Secondly, the contact area is varied by reducing the length “ $L_{\perp\delta}$ ” against the sliding direction from 5 to 2 mm while maintaining a constant length “ $L_{\parallel\delta}=5 \text{ mm}$ ”. The objective behind this contact geometry strategy is to evaluate the effect of contact orientation on both contact oxygenation and debris ejection.

In what follows, the extreme loading conditions will be denoted by: A and B for $p=10 \text{ MPa}$ and 175 MPa respectively, C and D for $\delta_g = \pm 25 \mu\text{m}$ and $\pm 200 \mu\text{m}$ respectively, E and F for $f=0.5 \text{ Hz}$ and 10 Hz respectively, G and H for $N=5000$ and 40000 cycles respectively, and finally I and J for $L_{\parallel\delta}=2 \text{ mm}$ and $L_{\perp\delta}=2 \text{ mm}$ respectively.

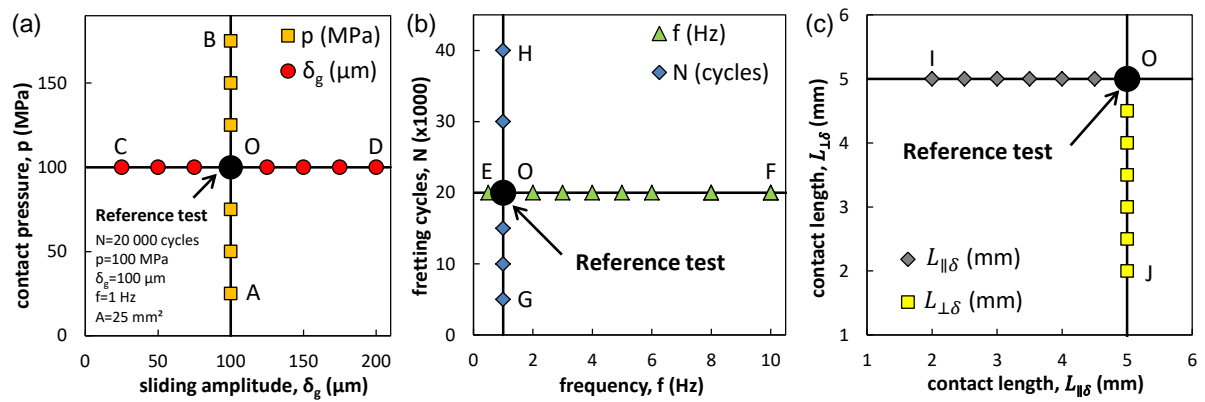


Figure 2.9: Multi-scale experimental strategy involving different loading conditions: (a) contact pressure versus sliding amplitude; (b) fretting cycles versus frequency; and (c) contact length ($L_{\perp\delta}$) versus contact length ($L_{\parallel\delta}$).

2.6.2 Textured samples test strategy

Since plain samples cannot allow investigating very small contact areas, textured samples are examined. Firstly, the length “ $L_{\perp\delta}$ ” against the sliding direction is tested (at the reference conditions) from 5 to 0.5 mm while maintaining a constant length “ $L_{\parallel\delta}=5 \text{ mm}$ ”. Secondly, the length “ $L_{\parallel\delta}$ ” along the sliding direction is tested from 5 to 0.75 mm while maintaining a constant length “ $L_{\perp\delta}=5 \text{ mm}$ ”.

Following the latter campaign, textured samples are examined at three loading conditions: pressure, sliding amplitude and sliding frequency (Figure 2.10) starting from the reference test. To simplify this experimental campaign, $L_{\parallel\delta}$ is kept constant equal to 5 mm. However, the contact length $L_{\perp\delta}$ ranging from 0.5 to 5 mm is tested at three contact pressures ($p=50, 100, \text{ and } 150 \text{ MPa}$), three sliding amplitudes ($\delta_g = \pm 50, \pm 100 \text{ and } \pm 150 \mu\text{m}$) and three frequencies ($f=0.5, 1 \text{ and } f=10 \text{ Hz}$). Note that when one loading condition is changed for a given $L_{\perp\delta}$, the other parameters are kept equal to the reference conditions.

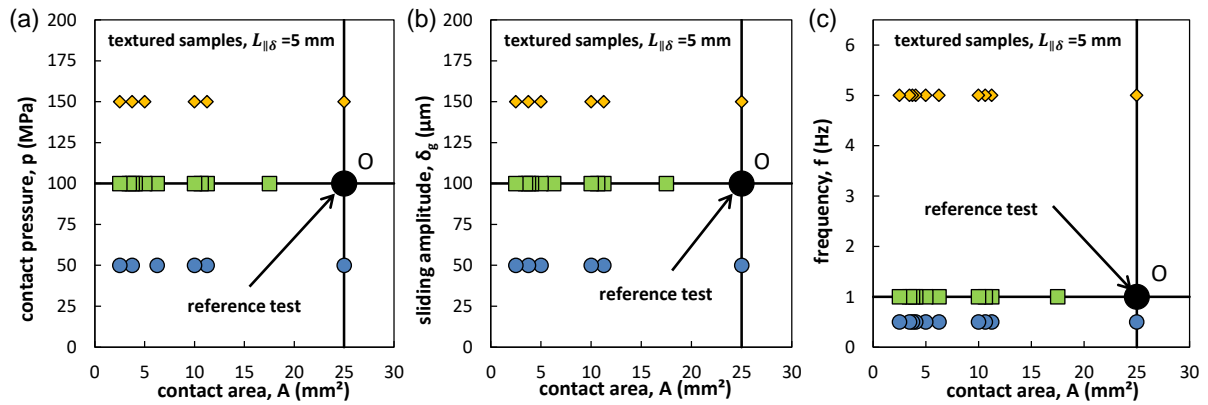


Figure 2.10: Experimental campaigns for textured samples at variable: (a) contact pressure (b) sliding amplitude, and (c) frequency.

2.7 Damage characterization

2.7.1 Optical observation

After each test, the samples are cleaned for 20 min in ultrasonic ethanol bath to remove the non-adhering oxide debris from the fretting scar. Samples are optically observed using Olympus SZ 61 microscope before and after cleaning to compare the ejected and the adhering debris particles at different loading conditions (Figure 2.11).

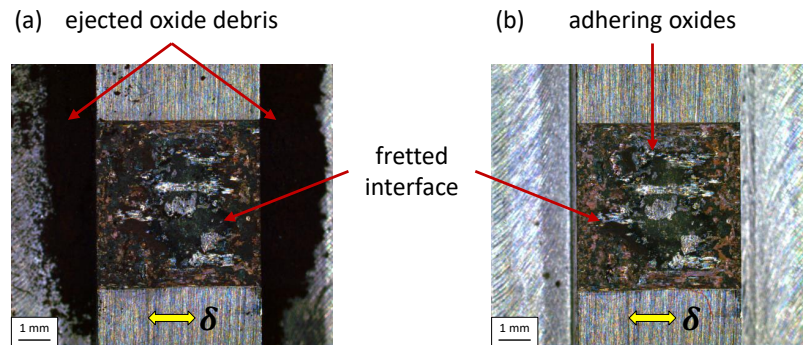


Figure 2.11: Optical observations of the fretting scar: (a) before and (b) after cleaning.

2.7.2 Wear analysis

Fretting scars are scanned using a 3D interferometric profilometry (VEECO Wyko NT9300) in Vertical Shift Interference mode (VSI) which allows mapping the topography of rough samples based on the principle of light wave interference [80]. This profilometer is equipped with three objectives: x2.5, x5 and x20. Since the contact sizes investigated in this thesis are relatively large, x2.5 objective is selected. Based on the chosen parameters, the vertical resolution is 0.3 nm and the lateral resolution is 3.68 μm which is highly sufficient regarding the large contact sizes investigated.

After 3D wear profiles are performed, wear volume is computed with respect to a reference plane corresponding to the intact surface outside the scar (Figure 2.12). 2D wear profiles can be obtained by averaging the 3D profiles on the transverse length ($L_{\perp\delta}$) for the top samples and the longitudinal length ($L_{\parallel\delta}$) for the bottom samples. Then, we determine the volume located below the reference plane which is V^- and the volume located above the reference plane which is V^+ . The volume V^- is associated with the quantity of matter removed from the rubbed surface whereas V^+ can be associated with the material transfer on the interface. The wear volume V_t is therefore expressed by Equation 2.3:

$$V_t = V^- - V^+ \quad (2.3)$$

The total wear volume V is calculated by summing the wear volumes of the top and bottom samples as expressed by Equation 2.4:

$$V = V_{t(top)} + V_{t(bottom)} \quad (2.4)$$

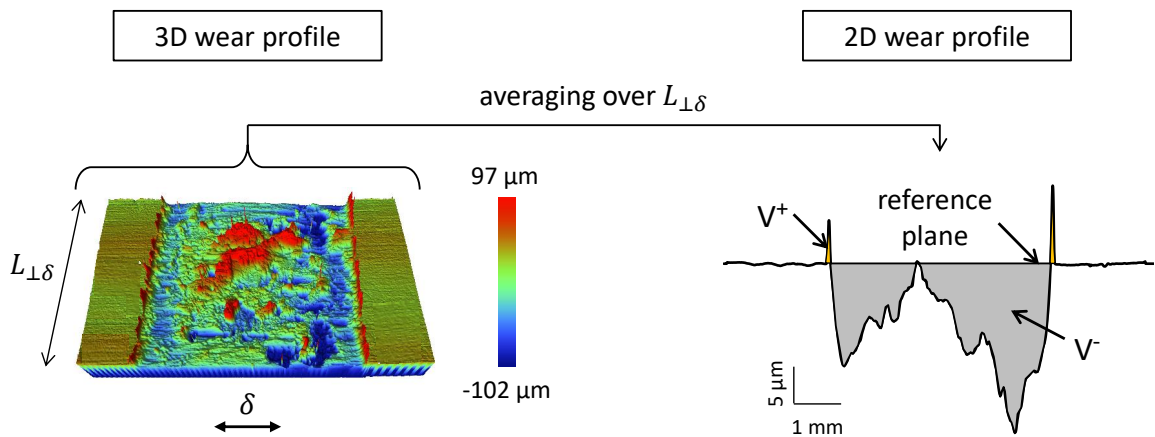


Figure 2.12: Illustration of the computation of the wear volume using 3D profilometry.

To provide an overall view of the fretting scar evolution, the 2D wear profiles (Figure 2.12 & 2.13) are calculated for the top and bottom samples by averaging their 3D profiles over the transverse length. Following this, an averaged 2D wear profile ($2D_{ave}$) is derived by averaging the sum of the 2D top and bottom wear profiles (Figure 2.13). This gives a qualitative description of the fretting scars for the tribo-couple in one single wear profile that allows comparing the test results for different loading conditions. Typically, this helps check if the wear process is mainly governed by abrasive wear leading to a “U-shape” fretting scar morphology or if a composite abrasive-adhesive wear is taking place inducing a “W-shape” fretting scar.

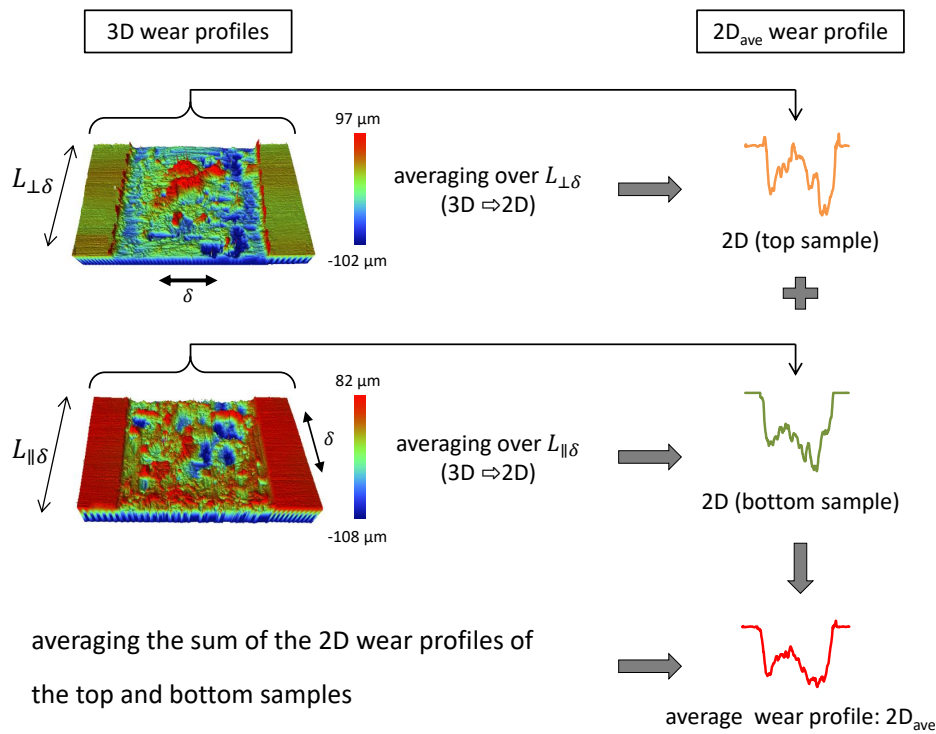


Figure 2.13: 3D profiles of the top and bottom samples and schematic illustration of the computation of the average 2D wear profiles ($2D_{ave}$).

2.7.3 Scanning by electron microscopy (SEM)

Qualitative non-destructive observations of the wear scars were obtained thanks to scanning by electron microscopy (TESCAN MIRA-3 FEG SEM). The latter allows scanning the samples with a focused beam of electrons that interact with atoms, producing various signals which contain information about the surface topography and the sample composition (Figure 2.14). Secondary electrons (SE) originate from the near surface regions giving information about the surface topography.

On the other hand, back scattered electrons (BSE) come from deeper regions to show compositional differences in the sample. They have high sensitivity to the differences in atomic number providing in turn distinct contrast such that regions of higher atomic number appear brighter than those with lower one.

SEM is also equipped with energy dispersive X-ray spectroscopy (EDX) detector (Oxford Instruments) which is used to semi-quantitatively determine the elemental composition of a zone of interest within the contact by gathering X-rays emitted from the sample and converting them to information about chemical elements constituting the sample. The scanned zones could be point, line or even a map of the whole surface. In the current study the voltage used for SEM-EDX analysis is 20 kV which helps obtain good inspection of the 34NiCrMo16 interface.

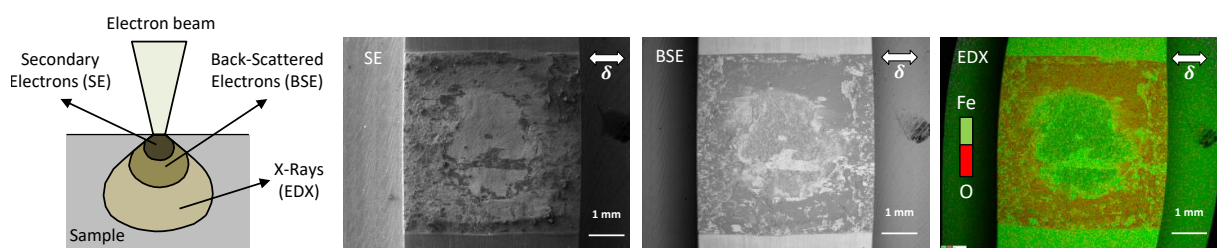


Figure 2.14: Different types of signals generated from electron-matter interaction and the resulting images for each signal (SE, BSE, EDX).

2.7.4 Raman spectroscopy

Although EDX analysis allows knowing the elemental composition of materials, it does not help identify the existing chemical structures such as oxides. One of the methods to find the structural fingerprint of molecules is Raman spectroscopy which is a non-destructive spectroscopic technique used to determine vibrational modes of molecules.

Raman spectroscopy consists in illuminating the top surface of the sample with a monochromatic beam of light having an incident energy $E_0 = h\nu_0$ with h being Planck's constant and ν_0 being photons' frequency (Figure 2.15a & b). When the light interacts with the surface molecules, most of the scattered photons will have the same energy as the incident photons E_0 . This is referred to as elastic or Rayleigh scattering. However, a very small number of these photons will scatter at a different frequency than the incident light. This process is called inelastic scattering, or the Raman effect from which the Raman spectra are extracted. The frequency of the scattered light could be lower than that of the incident light if the molecule is excited to a higher energy state than its basic vibrational state by absorbing part of the incident radiation energy. The resulting Raman frequency is called "Stokes" (or downshift) where the energy of the scattered Raman photons is given by $E_1 = h\nu_1 < E_0 = h\nu_0$. On the other hand, if the final state of the molecule is lower in energy, the frequency of the scattered light will be higher than the incident one due to the additional energy released by the molecules. The resulting Raman frequency is referred to as "Anti-Stokes" (or upshift) where the energy of the scattered Raman photon is given by $E_1 = h\nu_1 > E_0 = h\nu_0$.

The Raman Stokes and Anti-Stokes shifts are usually expressed in wavenumbers which are the inverse of the wavelengths and are expressed in cm^{-1} .

$$\Delta\tilde{\nu} = \frac{1}{c} (\nu_0 - \nu_1) = \frac{1}{\lambda_0} - \frac{1}{\lambda_1} \quad (2.5)$$

With c being the speed of light, λ_0 the excitation wavelength of the incident light and λ_1 is the Raman spectrum wavelength.

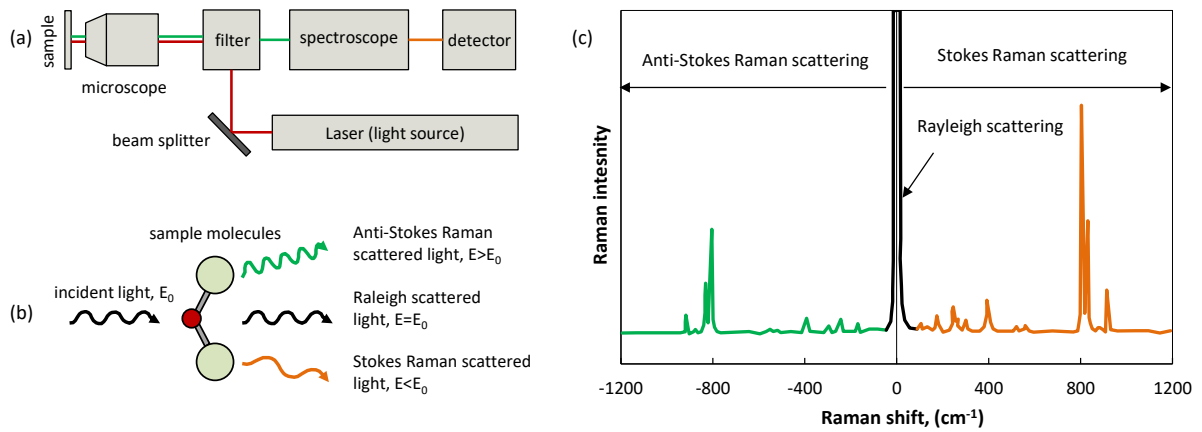


Figure 2.15: (a) Raman spectroscopy components; (b) scattering of light by the sample molecules; (c) illustration of the Raman spectrum [117].

Raman spectrum shows the evolution of the intensity (or the strength of activity) of the scattered light as a function of the Raman shifts (Figure 2.15c). The Rayleigh scattered light having the wavelength of the incident radiation has a very high intensity compared to Raman scattered light which is identified on both sides of the Rayleigh signal. Anti-Stokes shifts are detected on the shorter wavelengths whereas Stokes shifts are detected on the longer wavelengths. In general, Stokes lines are used in the analysis of Raman spectra.

In the current study, Raman analysis is performed using Horiba Xplora Raman microscope to determine the nature of oxides produced during the fretting wear of a low-alloyed steel contact. It was shown that steel particles detached from the fretting interface are transformed (Equation 2.6) firstly to magnetite (Fe_3O_4) and then into Hematite ($\alpha - Fe_2O_3$) (Equation 2.7) [85] which is the most stable iron oxides under ambient conditions [118] formed when the oxygen supply is relatively higher than that required to form magnetite [46].



2.7.5 Nano-indentation

To characterize the hardness of the superficial layers at the interface, for example tribologically transformed structures (TTS), nano-indentation¹ is used. It permits applying a normal load F_n to the surface of the material, using an indenter. Then, depending on the indenter geometry and its penetration depth different mechanical properties can be determined. These latter properties can be extracted from the load-displacement curve (Figure 2.16).

¹Thanks go for Dr. Gaylord GUILLONEAU for the training and discussion on nano-indentation.

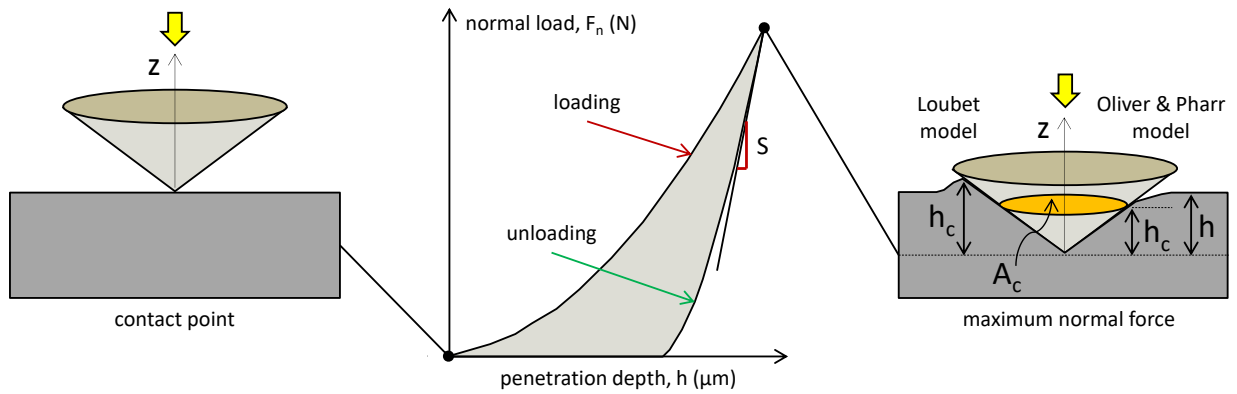


Figure 2.16: Illustration of the nano-indentation loading and unloading curves and the models applied for computing the projected contact area.

One of these parameters is the hardness of the material (H) which is defined as the ratio between the maximum normal load F_n and the residual projected indentation contact area (A_c) (Equation 2.8). Note that the value of the hardness, or the average contact pressure, is not an intrinsic property of the material, because it depends on the geometry of the indenter, and the test parameters [119]. In the current study, a CSM instruments Berkovich diamond indenter is used having a modulus of elasticity $E_i=1141$ GPa and a Poisson's ratio $\nu_i=0.07$.

$$H = \frac{F_n}{A_c} \quad (2.8)$$

The reduced contact area can be estimated as a function of the contact depth h_c depending on the shape of the indenter (Equation 2.9).

$$A_c = \pi \cdot \tan^2(\theta) \cdot h_c^2 \quad (2.9)$$

Where θ is the half-angle at the top of the equivalent cone representing the indenter (for Berkovich indenter $\theta = 70.32^\circ$; Cuber Corner indenter $\theta = 42.28^\circ$). The contact depth h_c in its turn depends on the penetration depth of the indenter which can be determined following two models:

-Oliver and Pharr model: the contact depth h_c is obtained from the following expression assuming that the subsidence around the indenter is purely elastic [120]:

$$h_c = h - \epsilon \cdot \frac{F_n}{S} + h_0 \quad (2.10)$$

Where $\epsilon=0.727$ is a constant obtained by the theory of elastic contact, S is the contact stiffness and h_0 is the defect of the indenter tip.

-Loubet model [119]: the contact depth is obtained by taking into account the material plastic deformation around the indenter:

$$h_c = \alpha \left(h - \frac{F_n}{S} + h_0 \right) \quad (2.11)$$

Where α is a constant depending on the geometry of the indenter (for Berkovich indenter $\alpha=1.2$ and for Cuber Corner indenter $\alpha=1.067$).

It is also possible to determine the reduced modulus of elasticity of the indentation contact (E_c), from the contact stiffness (S) corresponding to the slope of unloading curve and the reduced contact area A_c (Equation 2.12) [119]. This permits computing the plane strain modulus (E^*) and the specimen's modulus of elasticity (E) following Equation 2.13 by introducing the modulus of elasticity and the Poisson's ratio of the indenter (i.e. E_i and ν_i respectively).

$$E_c = \frac{S}{2} \sqrt{\frac{\pi}{A_c}} \quad (2.12)$$

$$\frac{1 - \nu^2}{E} = \frac{1}{E^*} = \frac{1}{E_c} - \frac{1 - \nu_i^2}{E_i} \quad (2.13)$$

2.8 Conclusion

The following chapter summarizes the experimental techniques and the test strategy used in this research work. The first section describes the chemical composition, the microstructure, and the mechanical properties of the tested material. The remaining parts describe the contact configuration, the fretting wear test set-up, the experimental strategy and finally the characterization techniques which will be used in the manuscript.

Chapter 3

Fretting wear kinetics of flat-on-flat contact

Contents

3.1	Introduction	59
3.2	Plain crossed flat-on-flat contact configuration	59
3.2.1	Friction analysis	59
3.2.2	Wear evolution	62
3.2.3	Wear volume prediction model	77
3.3	Results validation using textured samples: access to smaller contact sizes	83
3.3.1	Grooves' fill-up mechanism	84
3.3.2	Rheology of the third body particles	86
3.3.3	Qualitative validation of the contact size effect	89
3.3.4	Quantitative validation of experimental results	92
3.4	Stability of the composite-wear model using tests outside calibration domain	93
3.5	Wear depth prediction	94
3.6	Conclusion	97

3.1 Introduction

In this chapter, wear kinetics of plain and textured crossed flat-on-flat samples will be studied in details. The plain samples will be used to establish a wear kinetics prediction model that takes into account several loading parameters including number of cycles, contact pressure, sliding amplitude, frequency, and contact size as well as contact orientation with respect to the sliding direction. This model will be validated using textured samples which will be also used to investigate other features including the rheology and flows of the third body particles (i.e. wear debris).

3.2 Plain crossed flat-on-flat contact configuration

3.2.1 Friction analysis

3.2.1.1 Reference condition

Figure 3.1 shows the evolution of the coefficients of friction (μ and μ_e) with the test duration for the reference test. It is clear that the evolution of μ and μ_e is similar over the whole test duration with higher values of μ caused by ploughing effect. Four different stages can be distinguished in friction evolution. During the first 100 cycles (I), the coefficients of friction increase rapidly to reach maximum values corresponding to the ultimate metal-metal interaction. Beyond 100 cycles (II), the coefficients of friction decrease due to the formation of third body particles that tend to accommodate an important part of the applied loads by forming a screen layer which lowers metal/metal interaction. After 500 cycles (III), the debris bed tends to compact as a result of the applied fretting loading [82]. Being less accommodating compared to powdery debris particles, the compact debris bed exhibits higher friction values compared to the latter. Starting from cycle 5000 (IV), a stabilized friction behavior is detected which corresponds to a steady third body thickness at the interface.

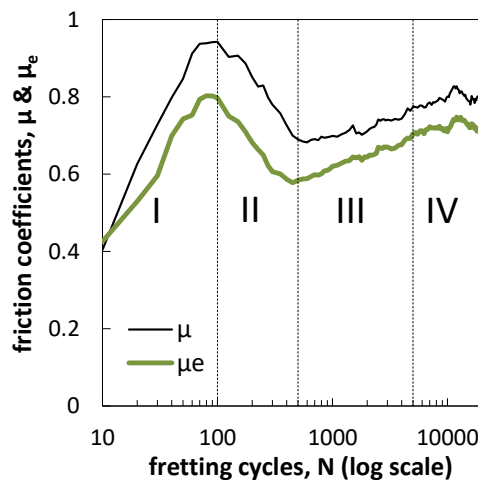


Figure 3.1: Variation of the friction coefficients (μ & μ_e) with test duration for the reference test (N=20000 cycles, p=100 MPa, $\delta_g = \pm 100 \mu m$, f=1 Hz and A=25 mm²).

3.2.1.2 Fretting cycles

In Figure 3.2a, experimental fretting cycle at the end of the reference test is plotted as a function of the displacement amplitude. As can be noticed, a quadrilateral shape of fretting cycle is obtained due to the stiffness of the machine which has a value $K_s=0.0132$ N/m. Since the sliding amplitude is monitored, which is equal to the cyclic aperture ($\delta_0=\delta_g$), it is then possible to compare an experimental fretting cycle to a numerical one by removing the influence of the machine stiffness. This can be obtained by plotting the tangential force as a function of the contact displacement amplitude δ_c (Equation 3.1).

$$\delta_c(t) = \delta(t) - \frac{1}{K_s} \cdot F_t(t) \quad (3.1)$$

Figure 3.2b compares the evolution of the experimental fretting cycles plotted against δ_c and the numerical fretting cycle obtained thanks to “Wear Box FEM” model [95]. By eliminating the impact of the machine stiffness and by maintaining constant sliding amplitude, a nearly similar shape of fretting cycles will be obtained experimentally and numerically. Note that the numerical cycle shows a friction plateau ($\mu=0.70$) corresponding to the averaged friction energy whereas the experimental cycle displays a smooth rising of the tangential force during the sliding plateau. The origin of this increase is not fully elucidated. Some authors suggest a ploughing effect within the contact asperities [121, 122] whereas others propose a kinematic hardening response of the debris layer as the detailed in the model [123].

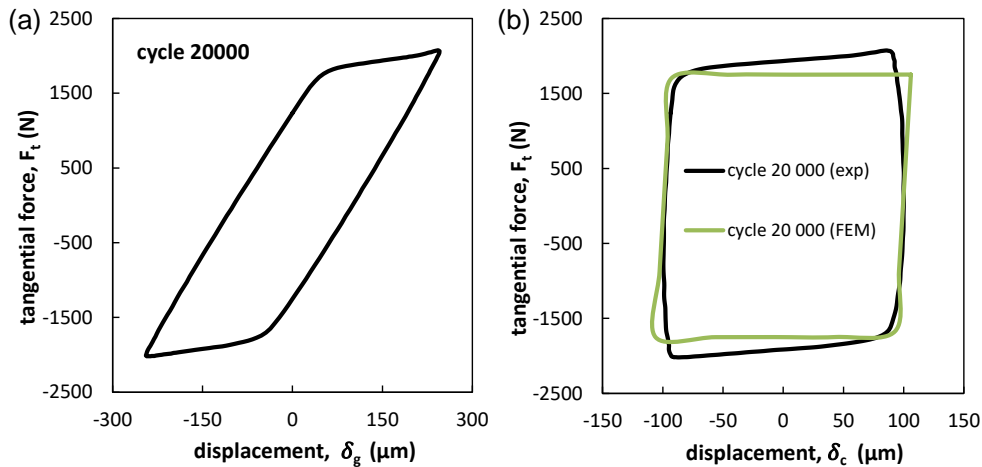


Figure 3.2: (a) Experimental fretting cycle at $N=20000$; (b) comparison between FEM and the corrected experimental fretting cycle using Equation 3.1 (test system compliance correction) under reference test conditions ($N=20000$ cycles, $p=100$ MPa, $\delta_g = \pm 100$ μm , $f=1$ Hz and $A=25$ mm^2).

3.2.1.3 Evolution of the energy friction coefficient versus the loading conditions

The influence of the loading condition on friction behavior is shown in Figure 3.3. The results show a stable coefficient of friction (around 0.7) by varying the number of cycles, contact pressure, sliding amplitude, frequency and contact lengths $L_{\parallel\delta}$ and $L_{\perp\delta}$. Hence the loading

conditions have a minor effect on the energetic coefficient of friction which has an average value equal to 0.7 ± 0.04 [55, 56]. This result is quite interesting such that it suggests that the coefficient of friction for the studied configuration is independent of the fretting loading conditions and the contact size. Former investigations focusing on dry AISI 52100 sphere-on-flat interfaces underlined, in contrast, a significant fluctuation of the friction coefficient with the contact size [81, 82] (See Chapter 1, Figure 1.23a). The difference between these latter results and the given investigation could be attributed to the fact Merhej et al. [81, 82] research work focuses on high pressure condition induced in sphere-on-flat contact which promotes a huge fluctuation of the friction coefficient. Hence, it can be admitted that shifting the contact from high plastic situation to low pressure condition generates a substantial variation of the contact pressure and the contact area which results in fluctuation of the friction coefficient. In the present investigation, constant low pressure conditions are imposed. Hence, taking into consideration this loading configuration, this result tends to confirm Amontons's law which states a constant friction coefficient whatever the contact loadings. One consequence of having a constant coefficient of friction is the equivalence between friction energy and Archard approaches. So for the sake of simplicity, the analysis in what follows will be carried out using friction energy approach.

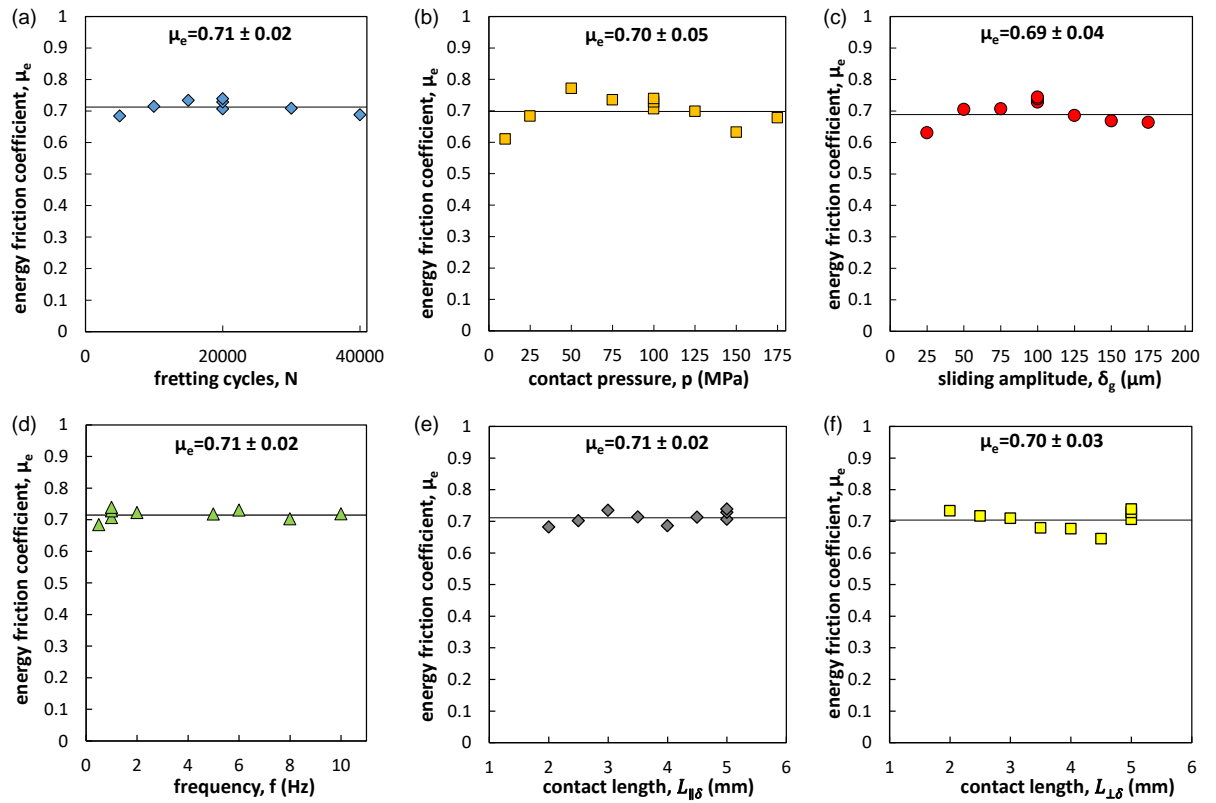


Figure 3.3: Variation of the average energy friction coefficient μ_e as a function of the (a) number of cycles; (b) contact pressure; (c) sliding amplitude; (d) frequency (e) contact length $L_{\parallel\delta}$; and (f) contact length $L_{\perp\delta}$.

3.2.2 Wear evolution

3.2.2.1 Fretting cycles

To assess the influence of test duration, the number of cycles (N) is varied from 5000 to 40000 cycles while maintaining the other parameters constant: $p=100$ MPa, $\delta_g=\pm 100$ μm , $f=1$ Hz and $A=25$ mm^2 . Figure 3.4a compares the evolution of the wear volume of the top and bottom sample versus the number of fretting cycles. It appears that both wear volumes increase linearly with the number of cycles. However, the disparity between the wear response of the top and bottom samples can be attributed to the transfer phenomenon where adhesive junctions are not homogeneously distributed between the top and bottom samples. On the other hand, a less dispersive linear increase is still observed in the total wear volume with the number of cycles (Figure 3.4b). Figure 3.4c displays the evolution of the total wear volume against the accumulated dissipated friction energy which permits computing the global energy wear rate ($\alpha=\alpha_{ref}$). It appears that there is a stable evolution of the energy wear rate ($\alpha=\alpha_{ref}=4.383 \times 10^{-5}$ mm^3/J) with the test duration which is compatible with both Archard and friction energy wear approaches.

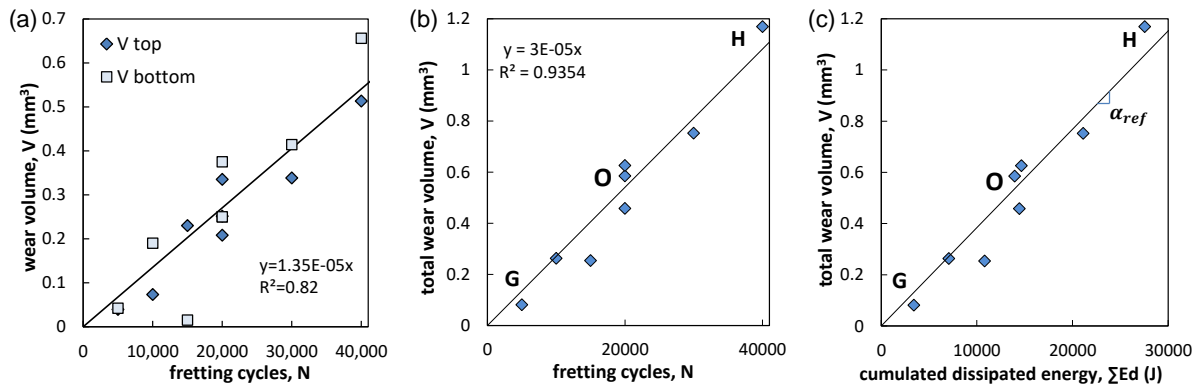


Figure 3.4: (a) Variation of the wear volumes of the top and bottom samples with the number of cycles; (b) evolution of the total wear volume with the number of cycles; and (c) variation of the total wear volume with the cumulated dissipated friction energy ($N=5000-40000$ cycles such that: $p=100$ MPa, $\delta_g=\pm 100$ μm , $f=1$ Hz and $A=25$ mm^2).

Concerning surface topography, 3D profiles of the top and bottom samples (Table 3.1) show that, for all the test durations, there is a mixed wear profile combining both abrasion and adhesion. Generally, one can notice that the adhesive wear is localized at the center of the contact and the abrasive wear is distributed at the borders. However, by comparing the $2D_{ave}$ profiles with the number of cycles, it can be noted that increasing the test duration leads to an increase in the wear depth along with a more homogeneous global wear profile. This is caused by the progressive elimination of adhesive transfers with the wear extension though adhesive wear is still present.

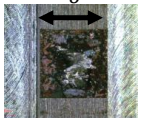
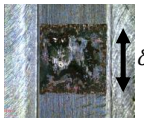
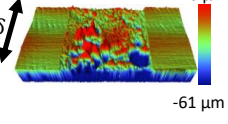
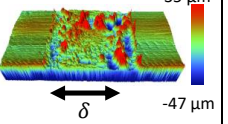
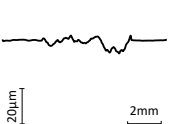
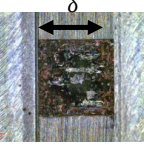
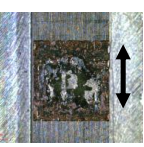
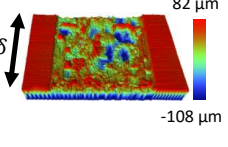
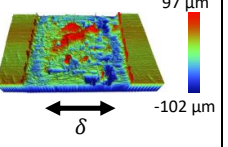
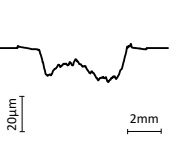
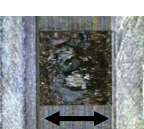
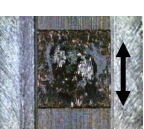
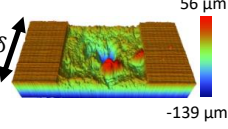
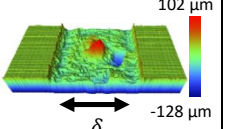
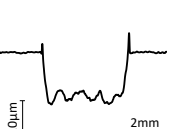
N	Bottom sample	Top Sample	Bottom 3D profile	Top 3D profile	$2D_{ave}$ wear profile
5 000 (G)					
20 000 (O)					
40 000 (H)					

Table 3.1: Evolution of the optical images, 3D fretting scars and $2D_{ave}$ wear profiles with the number of cycles for the top and bottom samples ($N=5000$, 20000 and 40000 cycles such that: $p=100$ MPa, $\delta_g = \pm 100$ μm , $f=1$ Hz and $A=25$ mm^2).

Figure 3.5 displays the micro-Raman analysis performed on the fretting scars of the bottom samples at three numbers of cycles $N=5000$, 20000 and 40000 cycles. To avoid further oxidation of debris particles due to laser-induced thermal effects, the density filters are adjusted in a way to maintain low laser power (0.35 mW) with an acquisition time of 150 seconds [124, 125]. The Raman spectra are compared with those obtained from pure hematite and magnetite powders and the resulting peaks are also confirmed by past studies [126, 127].

In all cases, it appears that two main different oxides are detected namely Hematite ($\alpha - Fe_2O_3$) that is reflected by its three intense characteristic peaks observed at 227 cm^{-1} , 293 cm^{-1} and 414 cm^{-1} , and Magnetite (Fe_2O_3) whose characteristic feature appears at 661 cm^{-1} . Additionally, in some spectra, there are traces of ferrihydrite ($\delta - FeOOH$) having Raman shifts detected at 400 cm^{-1} and 655 cm^{-1} [126]. This oxide is produced in humid environment or under high pressure condition. However, it was not present in all samples. Hence, It might be produced after the test as some samples were not analyzed directly right after the experiment or it might be created during the test due to humidity. Based on this investigation, it appears that similar oxides are detected at all number of cycles. However, the slight difference in Raman intensities at different fretting cycles can be associated with the difference in the distribution and the crystallization degree of the phases detected in the debris bed [128]. This allows concluding that number of cycles does not affect the nature of the oxides created during fretting.

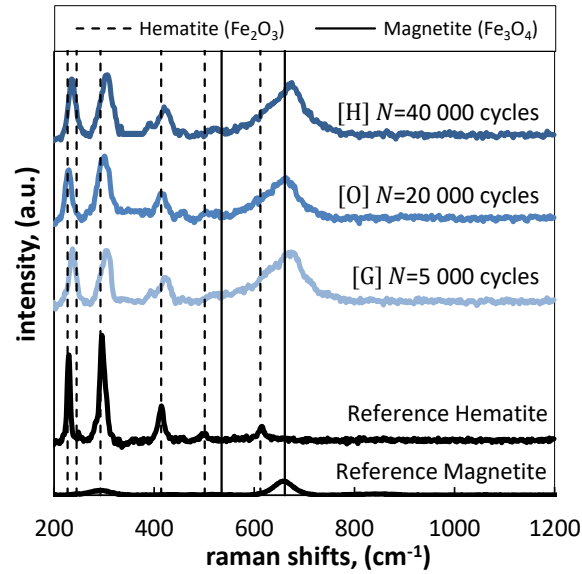


Figure 3.5: Raman spectra of the fretting scar (external abrasion corona) for $N=5000$, 20000 and 40000 cycles ($p=100$ MPa, $\delta_g = \pm 100$ μm , $f=1$ Hz and $A=25$ mm^2 , for Laser wavelength $\lambda = 785$ nm, Laser power= 0.35 mV, and acquisition time= 150 s).

3.2.2.2 Contact pressure

The influence of contact pressure is investigated by varying the latter from 10 to 175 MPa. Increasing the contact pressure causes a nonlinear increase in the wear volume (Figure 3.6a). The same trend is detected by plotting the total wear volume against accumulated dissipated friction energy (Figure 3.6b). Another interesting finding is the increase in the individual energy wear rates above 125 MPa (Figure 3.6c).

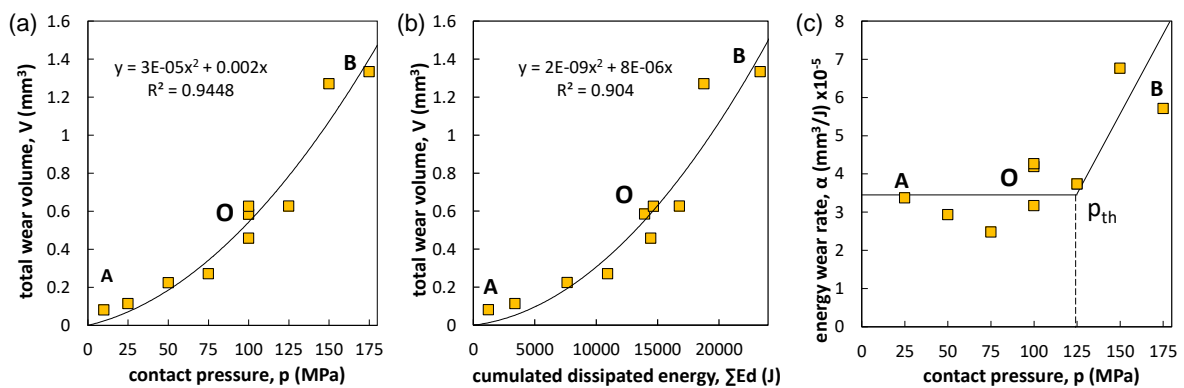


Figure 3.6: Variation of total wear volume with the (a) contact pressure and (b) cumulated friction energy; (c) variation of the individual energy wear rate α with the contact pressure ($p=10$ – 175 MPa such that $N=20000$ cycles, $\delta_g = \pm 100$ μm , $f=1$ Hz, and $A=25$ mm^2).

In fact, the influence of the contact pressure on fretting wear was discussed in many studies [35, 55, 56, 77, 129–134]. On one side, an increase in the contact pressure by shifting the

material response at the asperity scale from elastic to plastic shakedown may promote higher wear rate as suggested by K.L Johnson's pressure-friction coefficient shakedown maps [35]: the higher the accumulated plastic strain, the higher the wear rate. This hypothesis was ascertained by a previous investigation conducted by Burwell and Strang [131] who discerned two low and high-stress regions distinguished by a constant and steeply rising wear responses (Figure 3.7a). They suggested that in the low stress region (Figure 3.7b), the local welds are very small and isolated producing each a single wear particle. Hence, when the stress is increased, the number of welds and consequently wear particles increases linearly. So, the probability of wear particle removal or the Archard coefficient "K" remains constant. Therefore, in this low stress region the classical Archard or friction energy approaches still hold. The authors also proposed that in this region, there is no interaction between the removal processes such that when a particle is removed, it will be ejected freely without generating further particles. On the other hand, in the high stress region (Figure 3.7c), the individual welded areas are large and close to each other. Consequently, larger wear particles will be produced. Due to the increase in the true contact area with the pressure, there will be literally no room between the contacting surfaces for a single wear particle to escape the contact freely without scoring and generating further particles. In the same sense, the secondary wear particles will engender further particles in a self-accelerating process which may ultimately produce an avalanche of worn material. Viewed in this light, the wear rate increases faster than linearly hence the constant wear rate hypothesis assumed by Archard and energy wear models are no longer satisfied.

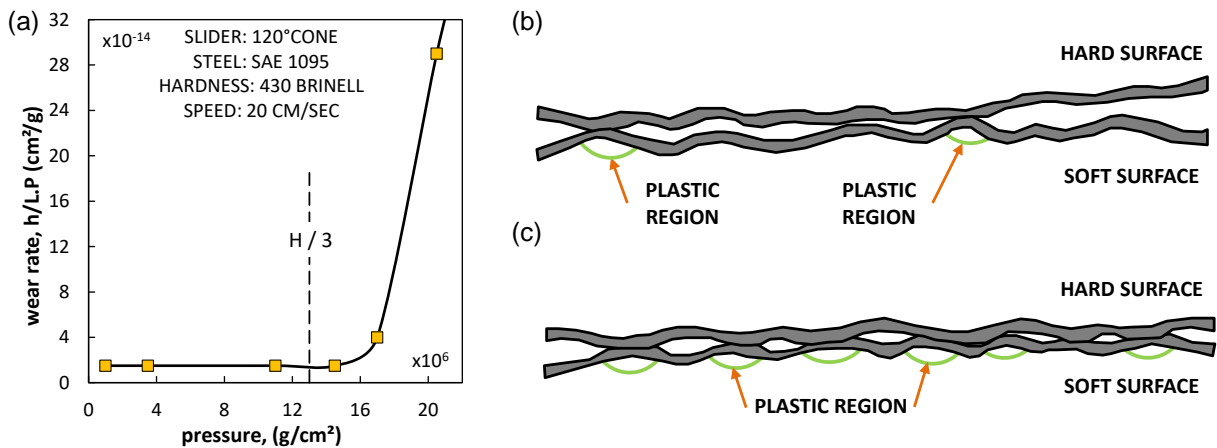


Figure 3.7: (a) Evolution of the ratio of the depth wear rate to the normal stress of a steel conical rider plotted against the normal stress [131]. Sketch of stress distribution in and around local asperities which are in contact: (b) at very low stress; (c) at stress equal to one third of the hardness [131].

Burwell and Strang [131] linked the inflection in the wear response to the plastic yielding of the material when a load higher than one-third of the indentation hardness is applied ($\sigma_y = H/3$). In the low-stress domain, the load is carried on the top of isolated asperities (Figure 3.7a) which in turn transmit the stress to its base where it eventually merges in the bulk. However, when the load rises, more asperities are brought into contact (Figure 3.7c), leading to further plastic deformation at the asperities' bases and ultimately interference of plastic flow. This generates

larger wear particles due to larger contact areas as well as greater removal of materials. The trend observed in the current study (Figure 3.6c) dovetails neatly with Burwell and Strang findings (Figure 3.7a) except with the fact that the threshold pressure ($p_{th}=125$ MPa) is far less than the yield strength of the steel alloy in question ($\sigma_y=950$ MPa). This discrepancy might be explained by Welsh [132–134] who found a more general trend of the wear response as a function of the normal load. While testing the dry wear of steel, Welsh noticed two inflections in the wear rate, mild to severe and severe back to mild at higher loads (Figure 3.8a).

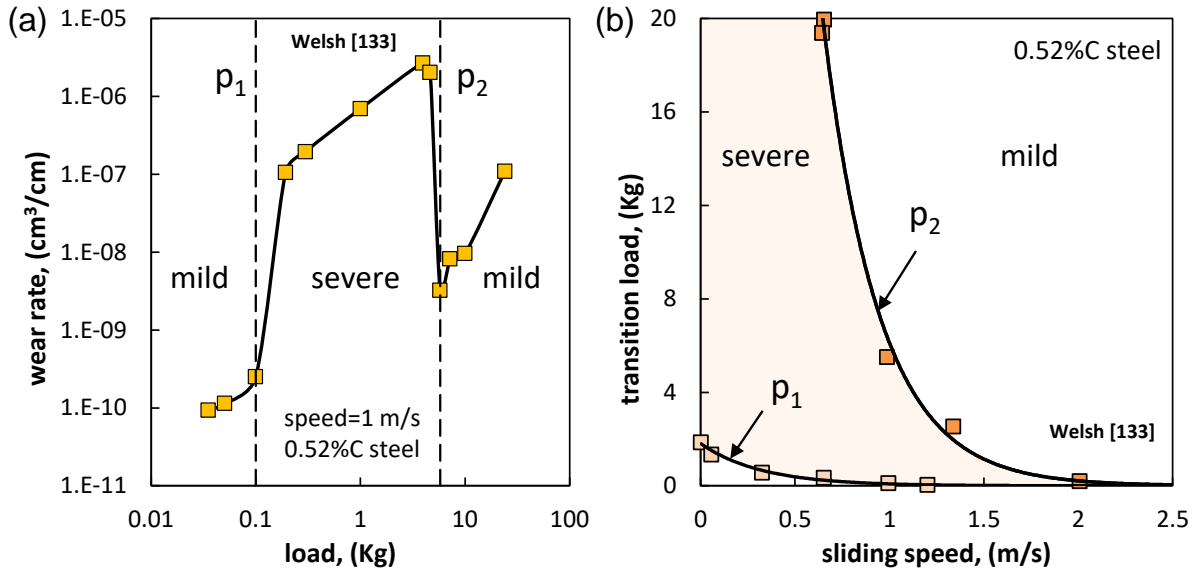


Figure 3.8: (a) Experimental results from Welsh [133] displaying load-dependent wear kinetics; (b) load-displacement map showing change of transition loads (p_1 and p_2) with the sliding speeds (after Welsh [133]).

Analogous load-dependent transitions are observed in both unidirectional and reciprocating sliding [135]. Welsh [132–134] suggested that the transition from mild to severe wear takes place when the combined rates of oxidation and strain-hardening can no longer outweigh the severe wear processes. However, the second transition from severe to mild wear takes place as a consequence of a new and intensive form of hardening referred to as “self-induced phase or quench-hardening”. This latter is chiefly produced by thermal heating which causes material transformation by local temperatures exceeding $\alpha - \gamma$ transition point. Welsh also highlighted that the transition loads p_1 and p_2 are strongly affected by the sliding speed illustrating the fact that at many speeds only one or even no transition is encountered. Figure 3.8b shows the influence of the sliding speed on the transition loads [133]. It appears that increasing the sliding speed shifts both p_1 and p_2 to lower values. Besides, p_1 changes more rapidly than does p_2 . Figure 3.8b also provides a convenient mapping for predicting wear transition such that a combination of load and sliding speed lying within the transition curves will induce continuous severe wear and any combination outside will give mild wear. Bearing this hypothesis in mind, it can be suggested that the chosen sliding speed and loads in this study exist in the domain where only mild to severe wear transition is activated.

The above hypotheses explained the transitions in the wear rate, but could not interpret the reason behind the composite adhesive-abrasive wear detected experimentally. Indeed, in the current case, 3D profiles (Table 3.2) reveal a mixed regime of adhesion and abrasion.


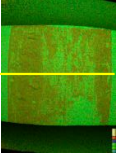
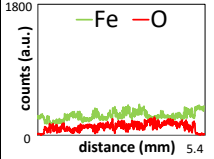
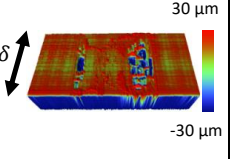
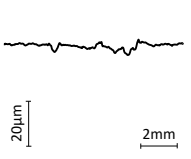

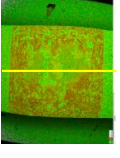
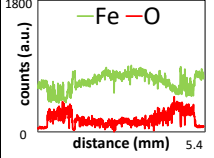
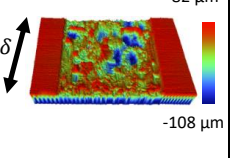
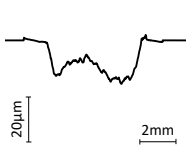

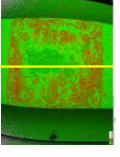
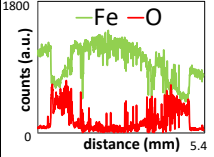
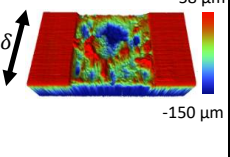
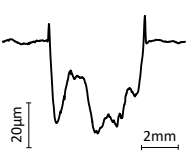
p (MPa)	Optical images	EDX maps	EDX line scans	3D profiles	$2D_{ave}$ wear profiles
10 (A)					
100 (O)					
175 (B)					

Table 3.2: Evolution of the optical images, EDX analysis, 3D fretting scars and $2D_{ave}$ wear profiles with the contact pressure for the bottom samples ($p=10, 100,$ and 175 MPa such that $N=20000$ cycles, $\delta_g = \pm 100 \mu m$, $f=1$ Hz and $A=25 \text{ mm}^2$).

At low contact pressure, wear is relatively very low and is mainly concentrated at the edges where pressure is high. However, adhesion becomes more severe with the increase in contact pressure. This result is confirmed by EDX analysis shown in Table 3.2. At low pressure, oxygen covers almost all the contact. Yet, a clear mixed regime is visible with the increase of pressure where oxygen content in the middle of the fretting scar decreases to be almost negligible at high normal loads. This fact also explains the reason for having nonhomogeneous $2D_{ave}$ wear profiles (Table 3.2). Considering the so-called “contact oxygenation concept” (COC), an increase in the contact pressure limits the oxygen access among interfacial asperities favoring the transition from abrasive to adhesive wear [55]. Adhesive wear was shown to induce lower wear rate than abrasive wear due to the high cohesive properties of the adhesive debris layer which reduce the debris ejection flow [56]. Note that using COC, the composite structure of fretting scars was explained where adhesive wear is observed in the inner part of the contact whereas abrasive wear is detected in the lateral zones [56]. Hence the interfacial oxygen concentration “COC” [56] which was established for titanium interface helps illustrate the given steel fretting scar evolution. However, it cannot explain the augmentation of the wear rate above a threshold contact pressure which seems more consistent with the plastic shakedown hypothesis [35, 73].

Figure 3.9 shows the micro-Raman analysis done on the fretting scars of the bottom samples at three contact pressures $p=10$, 100 and 175 MPa. Similar to the case of fretting cycles, two different oxides are detected which are Hematite ($\alpha - Fe_2O_3$) and Magnetite (Fe_3O_4). Hence, the contact pressure does not affect the nature of the oxides created during fretting but rather the wear mechanisms activated.

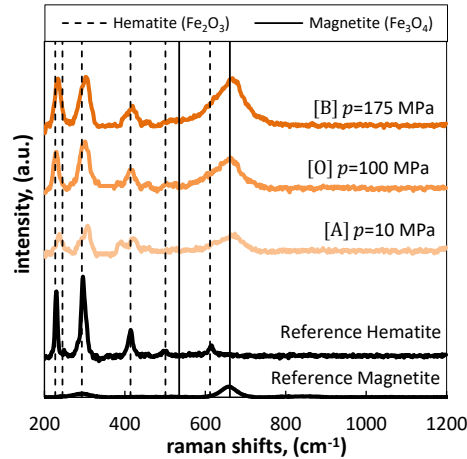


Figure 3.9: Raman spectra of the fretting scar (external abrasion corona) for $p=10$, 100, and 175 MPa ($N=20000$, $\delta_g = \pm 100 \mu m$, $f=1$ Hz and $A=25 mm^2$, for Laser wavelength $\lambda = 785$ nm, Laser power= 0.35 mV, and acquisition time= 150 s).

3.2.2.3 Sliding amplitude

The sliding amplitude is examined from ± 25 to $\pm 200 \mu m$ while setting the other parameters constant: $N=20000$ cycle, $p=100$ MPa, $f=1$ Hz and $A=25 mm^2$. Increasing the sliding amplitude triggers a nonlinear increase of the wear volume (Figure 3.10a). Similar evolution was obtained when the total wear volume is plotted as a function of the cumulated dissipated energy (Figure 3.10b) where a nonlinear growth of total wear volume is obtained. The analysis of the individual energy wear rate shows an increase in the wear rate with the sliding amplitude (Figure 3.10c). A past work stated by Ohmae and Tsukizoe (1974) [28] detected similar nonlinear increase in wear volume with the sliding amplitude in dry mild steel flat-on-flat contact. The authors hypothesized that such trend is associated with the different wear mechanisms taking place at smaller and larger slip amplitudes namely mild oxidation at smaller amplitudes, and abrasion, adhesion and oxidation at larger amplitudes. Equivalent impact of sliding amplitude was depicted in recent studies [77, 79, 136]. It is proposed that two main mechanisms might explain the increase in the wear rate versus sliding amplitude. Godet and co-workers [13, 50, 85, 94] postulated that increasing the sliding amplitude leads to an easier ejection of the debris particles and therefore promotes a higher energy wear efficiency [79]. A second hypothesis is the contact exposure to oxygen: an increase of the sliding amplitude enlarges the zone exposed to the outer environment causing higher wear rates [14]. This can be explained by the higher oxygen gas availability in the interface which increases oxidational-abrasive wear that has a higher wear rate than adhesive wear.

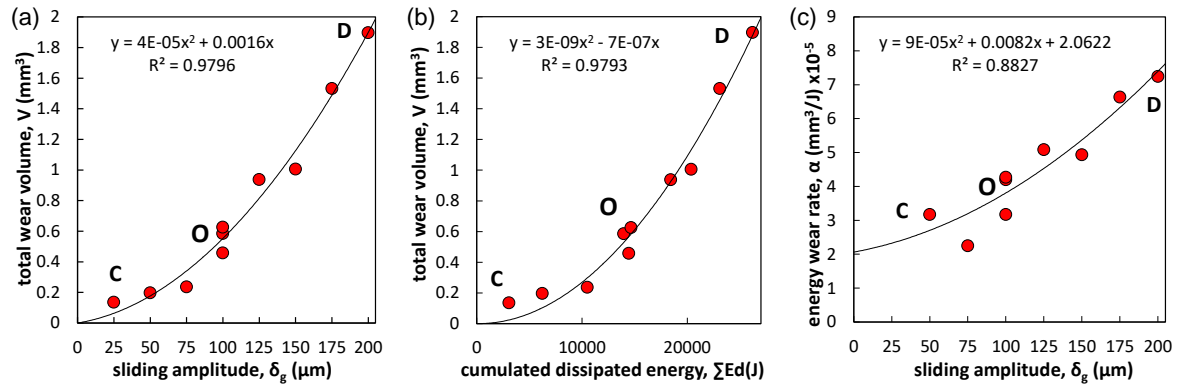


Figure 3.10: Variation of total wear volume with the: (a) the sliding amplitude and (b) cumulated friction energy; (c) variation of the individual energy wear rate with the sliding amplitude ($\delta_g = \pm 25 \pm 200 \mu m$ such that $N=20000$ cycles, $p=100$ MPa, $f=1$ Hz and $A=25 \text{ mm}^2$).

Observations of optical images, 3D wear profiles and EDX maps and line scans show a mixed regime of abrasion and adhesion at all sliding amplitudes (Table 3.3). This stems from the fact that the range of studied sliding amplitudes is very small compared to the contact size (<5%) so most of the interface remains hidden from the ambient air. On the other hand, the wear depth increases significantly with the sliding amplitude as reflected by the $2D_{ave}$ profiles despite the coexistence of abrasive and adhesive wear.

δ_g (μm)	Optical images	EDX maps	EDX line scans	3D profiles	$2D_{ave}$ wear profiles
25 (C)					
100 (O)					
200 (D)					

Table 3.3: Evolution of the optical images, EDX analysis, 3D fretting scars and $2D_{ave}$ wear profiles with the sliding amplitude for the bottom samples ($\delta_g = \pm 25, \pm 100$ and $\pm 200 \mu m$ such that $N=20\ 000$ cycles, $p=100$ MPa, $f=1$ Hz and $A=25 \text{ mm}^2$).

Figure 3.11 compares the micro-Raman analysis done on the fretting scars of the bottom samples at three sliding amplitudes $\delta_g = \pm 25, \pm 100$ and $\pm 200 \mu\text{m}$. Once again, two different oxides are detected which are Hematite ($\alpha - \text{Fe}_2\text{O}_3$) and Magnetite (Fe_3O_4). Hence, the sliding amplitude does not influence the nature of the oxides created during fretting but rather the wear mechanisms activated.

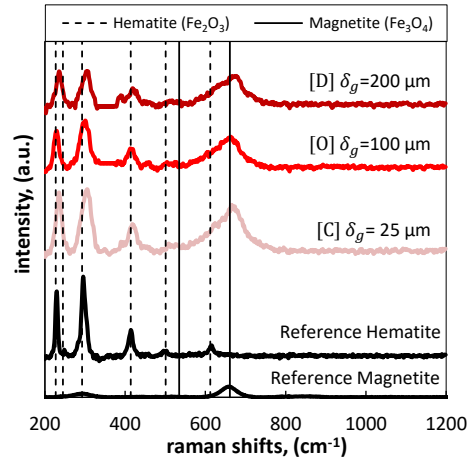


Figure 3.11: Raman spectra of the fretting scar (external abrasion corona) for $\delta_g = \pm 25, \pm 100$ and $\pm 200 \mu\text{m}$ ($N=20000$ cycles, $p=100$ MPa, $f=1$ Hz and $A=25 \text{ mm}^2$, for Laser wavelength $\lambda = 785$ nm, Laser power=0.35 mV, and acquisition time=150 s).

3.2.2.4 Frequency

In this section, the frequency is varied from 0.5 to 10 Hz while fixing the other parameters. A decrease in the total wear volume with the frequency is observed as can be seen in the Figure 3.12a. By plotting individual energy wear rates α with the frequency, one can notice a nonlinear decrease of the wear rates (Figure 3.12b).

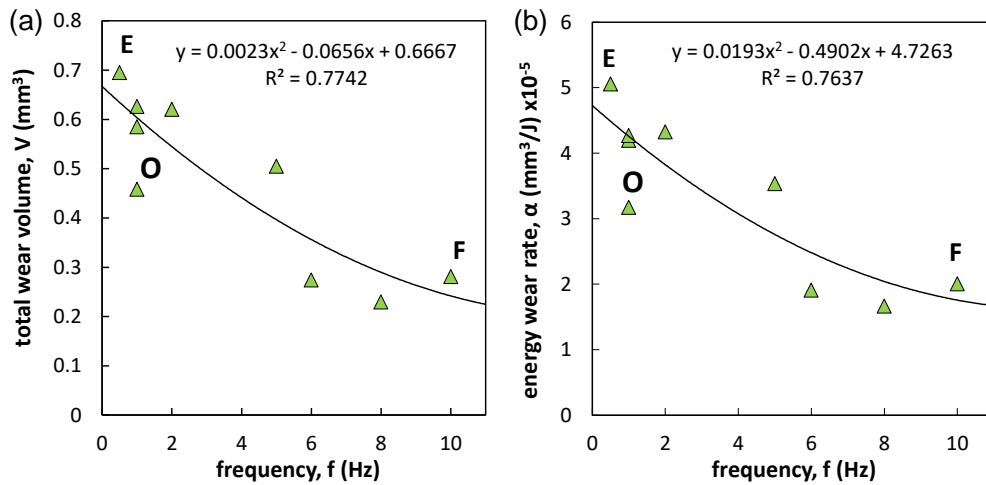


Figure 3.12: Variation of the (a) total wear volume and the (b) energy wear rate with frequency ($f=0.5$ -10 Hz such that $N=20000$ cycles, $p=100$ MPa, $\delta_g = \pm 100 \mu\text{m}$ and $A=25 \text{ mm}^2$).

The plausible explanation for this trend is that by increasing the sliding frequency, the friction power density inputted in the interface rises which promotes a faster fresh metal exposition and therefore a faster consumption of the available dioxygen molecules inducing a reduction of the abrasion zone. Besides, lower frequencies lead to a longer time given for oxygen to react with the native steel alloy. This causes build-up of thicker oxide layer on the surface and consequently a larger quantity of easily ejected oxide debris. According to Jin et al (2017) [109], an increase in the fretting frequency results in a reduction in the inter-pass time which is the time between asperity interactions for a given asperity. This in turn lessens the oxide formation per cycle which hence reduces abrasion and may also inhibit the formation of the debris bed at the same time. Similar test results were found also by Peteghem et al. (2011) [137], Fouvry et al. (2017) [56] and Dreano et al (2018) [77] who also explained the decrease in wear rate with the frequency considering a tribo-oxidation process and the ‘‘COC’’ concept. Regarding the 3D wear profiles (Table 3.4), it is noteworthy that a mixed abrasive-adhesive response is detected at all frequencies. However, the $2D_{ave}$ profiles tend to be less homogeneous with the increase in frequency, reflecting in turn a higher impact of adhesion over abrasion. Similar result is revealed by EDX analysis (Table 3.4), where both abrasion and adhesion are detected. At low frequency, oxygen is detected all over the interface indicating that abrasive wear is dominant. On the other hand, by increasing the frequency, adhesion becomes more pronounced until reaching a state where oxygen concentration at the central zone of the contact is almost negligible ($f=10$ Hz).

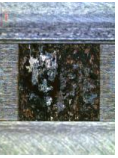
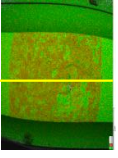
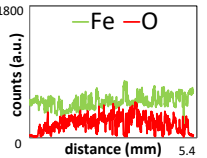
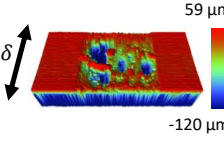
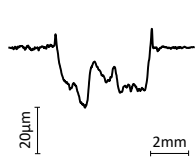
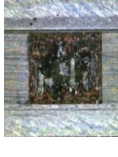
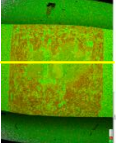
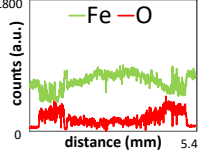
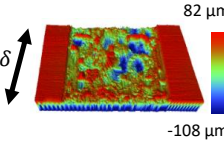
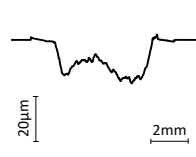

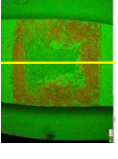
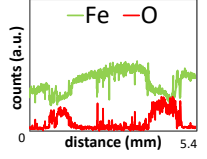
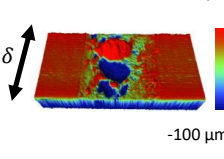
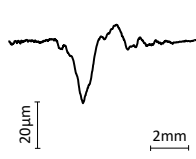
f (Hz)	Optical images	EDX maps	EDX line scans	3D profiles	$2D_{ave}$ wear profiles
0.5 (E)					
1 (O)					
10 (F)					

Table 3.4: Evolution of the optical images, EDX analysis, 3D fretting scars and $2D_{ave}$ wear profiles with the frequency for the bottom samples ($f=0.5, 1$ and 10 Hz such that $N=20000$ cycles, $p=100$ MPa, $\delta_g=\pm 100$ μm and $A=25$ mm^2).

Figure 3.13 displays the micro-Raman analysis done on the fretting scars of the bottom samples at three frequencies $f=0.5, 1$ and 10 Hz. Once again, two different oxides are detected which are Hematite ($\alpha - Fe_2O_3$) and Magnetite (Fe_3O_4). Hence, the sliding frequency does not affect the nature of the oxides created during fretting.

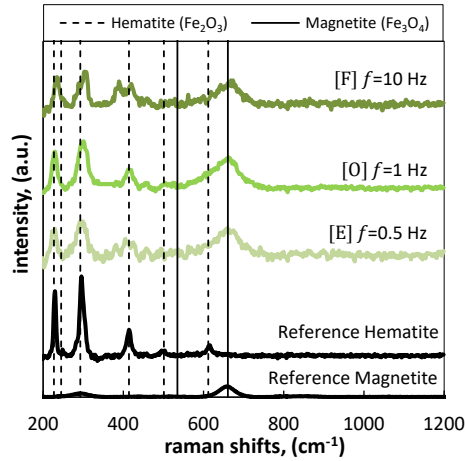


Figure 3.13: Raman spectra of the fretting scar (external abrasion corona) for three frequencies $f=0.5, 1$ and 10 Hz ($N=20000$ cycles, $p=100$ MPa, $\delta_g=\pm 100$ μm and $A=25$ mm^2 , for Laser wavelength $\lambda = 785$ nm, Laser power= 0.35 mV, and acquisition time= 150 s).

3.2.2.5 Contact length $L_{\parallel\delta}$

To investigate the effect of the contact size on both debris ejection and contact oxygenation the contact size parallel to the sliding direction “ $L_{\parallel\delta}$ ” is investigated. By changing the contact length and therefore the contact area, the wear extension cannot be compared as a function of the total wear volume. One alternative consists of dividing the half of the total wear volume V (assuming equal wear volumes of the top and bottom samples) by the contact area (A) which gives the mean wear depth h_{mean} such that:

$$h_{mean} = \frac{V}{2A} \quad (3.2)$$

Hence, regarding $L_{\parallel\delta}$ and $L_{\perp\delta}$ investigation, the mean wear depth parameter will be considered to formalize the wear extension. Figure 3.14a & b show the evolution of the mean wear depth and the energy wear rate with respect to $L_{\parallel\delta}$. By decreasing the latter from $L_{\parallel\delta}=5$ to 2 mm, the wear rate and the mean wear depth are multiplied by a factor of 3. This evolution could be possibly explained by two main hypotheses, namely the contact oxygenation concept [56] and the third body approach [85].

The contact oxygenation concept (COC) [55, 56] suggests that oxygen exclusion or interaction with the interface is a key factor of the wear mechanisms operating in the interface namely abrasion and adhesion. By decreasing the contact length $L_{\parallel\delta}$, the oxygen access within the interface is improved extending abrasive wear compared to adhesive transfers as reflected by

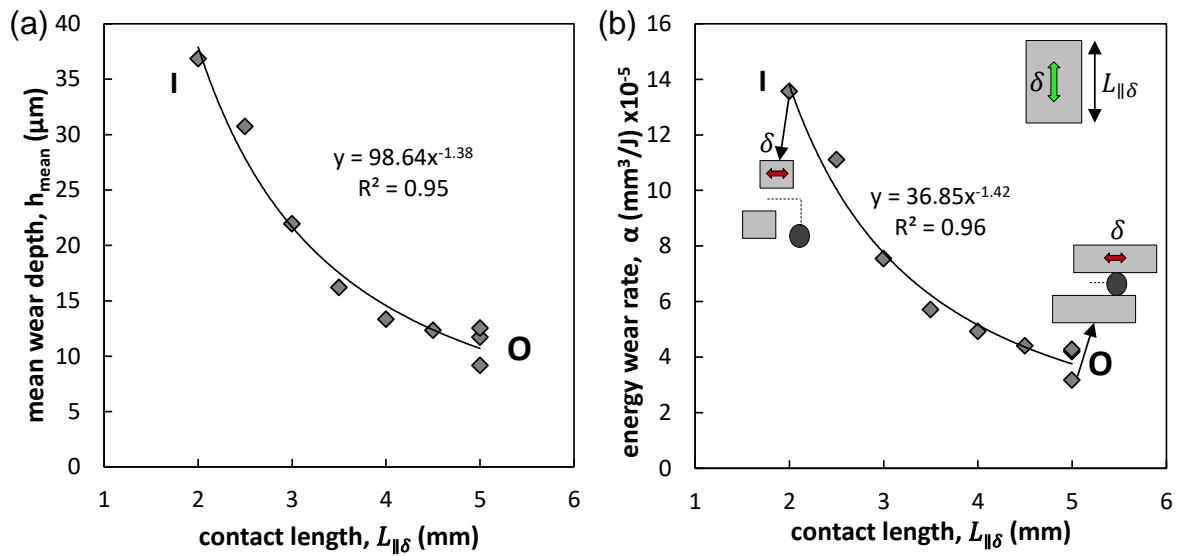


Figure 3.14: Evolution of the (a) mean wear depth and the (b) energy wear rate as a function of the contact length $L_{\parallel\delta}$ ($N=20000$ cycles, $p=100$ MPa, $\delta_g=\pm 100$ μm , $f=1$ Hz and $L_{\perp\delta}=5$ mm).

EDX maps (Figure 3.15). Because abrasive phenomena generate higher wear rates, the global increase in wear rate can be explained.

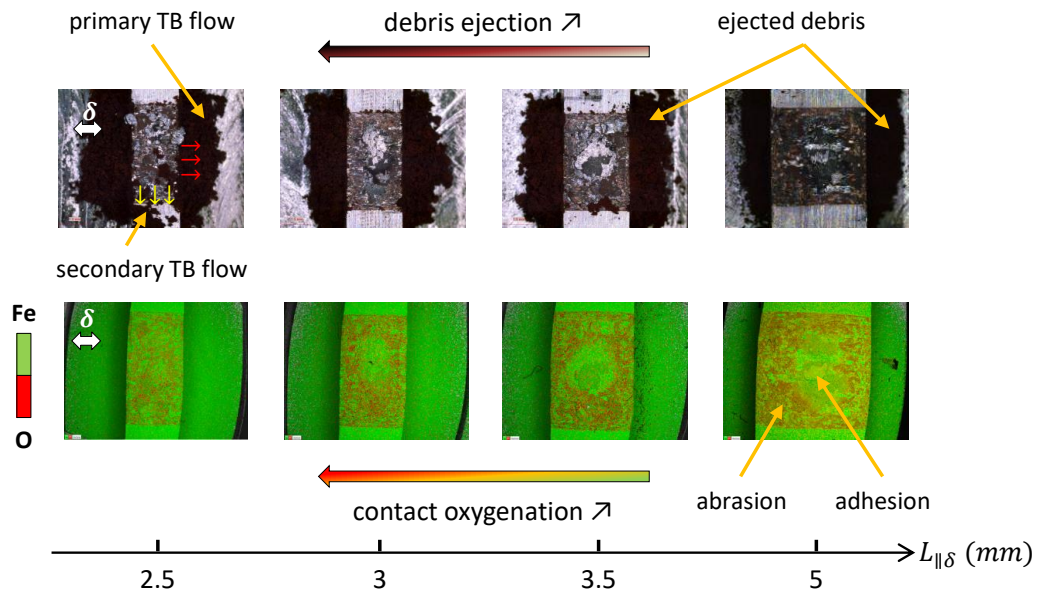


Figure 3.15: Evolution of the debris ejection (TBA) (optical images) and the contact oxygenation (COC) (EDX maps) as a function of the contact length $L_{\parallel\delta}$ ($N=20000$ cycles, $p=100$ MPa, $\delta_g=\pm 100$ μm , $f=1$ Hz and $L_{\perp\delta}=5$ mm).

The second probable explanation is the easier evacuation of debris particles by decreasing the contact size following the third body approach (TBA) (Figure 3.15). Based on the fundamental functions of the third body underlined by [13, 50, 60, 92], the applied stresses and displacements are not entirely handled on the expense of the bulk materials but rather accommodated by the

third body layer which by enduring the shear work reduces the first body degradation. Hence, eliminating third body from the contact signifies weaker protection of the first bodies against severe degradation. In the current case, by decreasing contact length $L_{\parallel\delta}$, the ejection path followed by debris particles along the sliding direction is reduced. Hence, the primary debris flow (Figure 3.15), defined as the third body flow along the sliding direction, increases. This leads to a faster evacuation of third body particles, a weaker shielding against wear and consequently a higher wear rate. Note that similar observation was detected recently by Zhu et al. [138] who showed that the instantaneous wear rate is inversely proportional to the wear scar width along the sliding direction in a cylinder-on-flat steel interface suggesting a contact size-dependence of fretting wear linked to third body expulsion.

3.2.2.6 Definition of $\delta_g/L_{\parallel\delta}$ parameter

Since both the contact size along the sliding direction “ $L_{\parallel\delta}$ ” and the sliding amplitude “ δ_g ” have similar impact on the ejection of the third body out of the contact in the direction of sliding, the ratio “ $\delta_g/L_{\parallel\delta}$ ” is introduced. By introducing “ $\delta_g/L_{\parallel\delta}$ ” (Figure 3.16), a single master curve combining both δ_g and $L_{\parallel\delta}$ can be defined to describe wear kinetics. Hence, by increasing $\delta_g/L_{\parallel\delta}$ either by increasing δ_g or reducing $L_{\parallel\delta}$, the elimination of the third body particles will be faster resulting in less protection of the counter bodies and consequently higher wear. This result is quite interesting as it suggests that the energy wear rate is inversely proportional to the number of sliding steps required to eliminate wear debris from the interface. In other words, the longer the debris path ($L_{\parallel\delta}$) and the smaller the sliding amplitude (δ_g), the higher the number of cycles (N_{TB}) required to eliminate the wear debris from the interface ($N_{TB} \propto L_{\parallel\delta}/\delta_g$).

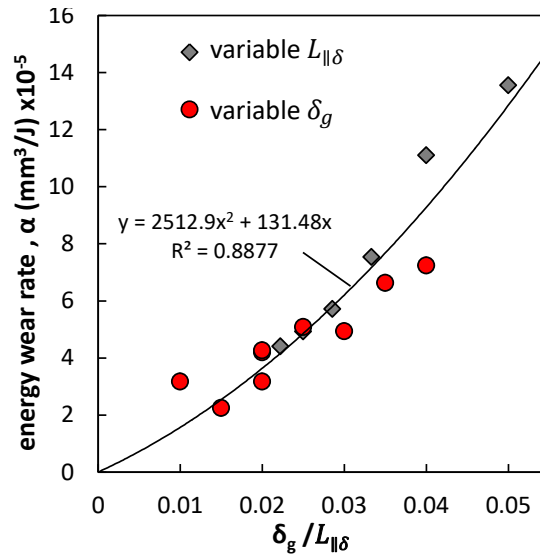


Figure 3.16: Evolution of the energy wear rate “ α ” versus $\delta_g/L_{\parallel\delta}$ ($N=20000$ cycles, $p=100$ MPa, $f=1$ Hz, and $L_{\perp\delta}=5$ mm).

3.2.2.7 Contact length $L_{\perp\delta}$

Figures 3.17a & b portray a systematic decreasing of the mean wear depth and the energy wear rate versus the contact size, as well as a significant difference between $L_{\perp\delta}$ and $L_{\parallel\delta}$ orientations.

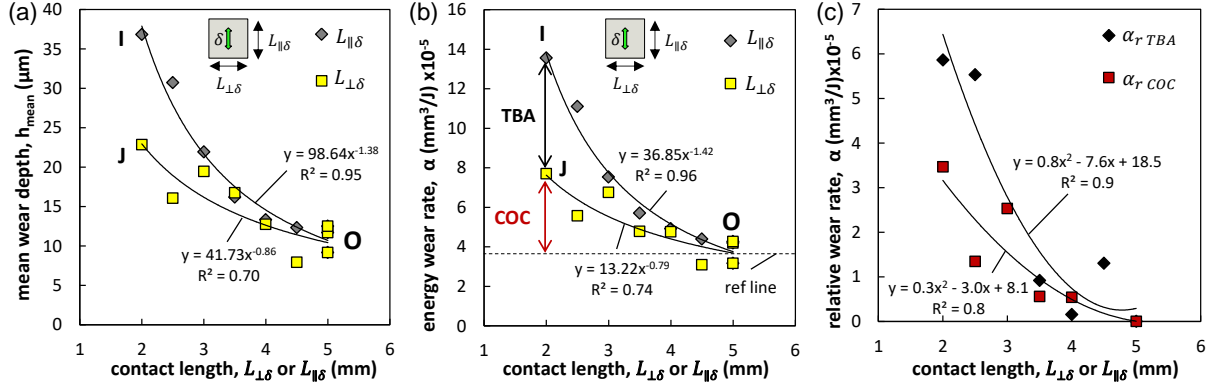


Figure 3.17: Comparison of the (a) mean wear depth; (b) energy wear rate and the (c) relative wear contributions of COC and TBA as a function of the contact lengths $L_{\parallel\delta}$ and $L_{\perp\delta}$ such that $L_{\parallel\delta}=5$ mm if $L_{\perp\delta}$ varies and $L_{\perp\delta}=5$ mm if $L_{\parallel\delta}$ varies ($N=20000$ cycles, $p=100\text{MPa}$, $\delta_g=\pm 100 \mu\text{m}$ and $f=1$ Hz).

Assuming iso-contact area condition, both $L_{\perp\delta}$ and $L_{\parallel\delta}$ contact lengths lead to a similar contact oxygenation condition. This is due to the fact the minimal distance “d” between the center of the contact and the open air is similar in both cases inducing similar oxygen access in both orientations and consequently iso-COC conditions. Hence, the major difference between the latter orientations is the way the third body is ejected out of the contact according to TBA. Keeping in mind that the debris travel for $L_{\parallel\delta}$ condition is shorter, thinner protective debris and consequently higher wear rates will be detected compared to the $L_{\perp\delta}$ situation where the debris travel along the sliding direction is nearly constant such that $L_{\parallel\delta}=5$ mm. This effect is significant as the wear rate $\alpha_{L_{\parallel\delta}}$ is nearly twice that of $\alpha_{L_{\perp\delta}}$ when $L_{\parallel\delta}=L_{\perp\delta}=2$ mm. Conversely, the wear rate difference decreases when the contact configuration converges to a square shape with $L_{\parallel\delta}=L_{\perp\delta}=5$ mm.

Hence, comparing the mean wear depths and the energy wear rates $\alpha_{L_{\parallel\delta}}$ and $\alpha_{L_{\perp\delta}}$ (Figure 3.17a & b), it is possible to consider a simplified decoupling analysis between third body flow and contact oxygenation effects on the wear rates (Figure 3.17b). Indeed, by neglecting the debris lateral secondary flow (compared to the longitudinal primary flow along the sliding direction (Figure 3.15)), it can be assumed, as a first approximation, that the wear difference between the reference base line (α_O) and $\alpha_{L_{\perp\delta}}$ is mainly related to a variation induced by the contact oxygenation process. Alternatively, the difference between $\alpha_{L_{\parallel\delta}}$ and $\alpha_{L_{\perp\delta}}$ should be thus attributed to a relative difference between third body ejection process (TBA). This could be better formalized considering a relative wear rate description assuming that:

$$\alpha_r \text{ COC} = \alpha_{L_{\perp\delta}} - \alpha_O \quad (3.3)$$

$$\alpha_r TBA = \alpha_{L_{\parallel\delta}} - \alpha_{L_{\perp\delta}} \quad (3.4)$$

Figure 3.17c compares the evolution of these two relative wear contributions. It's interesting to note that both TBA and COC have significant effect on wear kinetics which supports the idea that as TBA, COC consideration must be equally addressed to provide reliable wear rate predictions. It should be noted that the secondary TB flow decreases when the contact configuration converges to a square shape with $L_{\parallel\delta}=L_{\perp\delta}=5$ mm as reflected in Figure 3.15. However, this latter hypothesis should be considered with caution when the contact size becomes very small as the lateral TB flow will increase so its effect can no longer be neglected.

The TB contribution can be better illustrated by applying the TB flow approach proposed by Fillot et al. [93] (Figure 3.18). Since the contact oxygenation is nearly the same whatever the contact orientations for the same contact area, the particle detachment flow and therefore the source flow “ Q_s ” are assumed to be the same ($Q_s(L_{\parallel\delta})=Q_s(L_{\perp\delta})$). However, by decreasing the contact length “ $L_{\parallel\delta}$ ” along the sliding direction, the debris ejection flow will be faster by passing from variable $L_{\parallel\delta}$ to variable $L_{\perp\delta}$ contacts which can explain the higher $\alpha_{L_{\parallel\delta}}$ wear rates.

From this chart, it can be also deduced that the steady state debris layer thickness will be thinner by varying the contact length along the sliding direction compared to the case where the latter is varied perpendicular to δ (i.e. $(H_{ss}(L_{\parallel\delta}) < H_{ss}(L_{\perp\delta}))$).

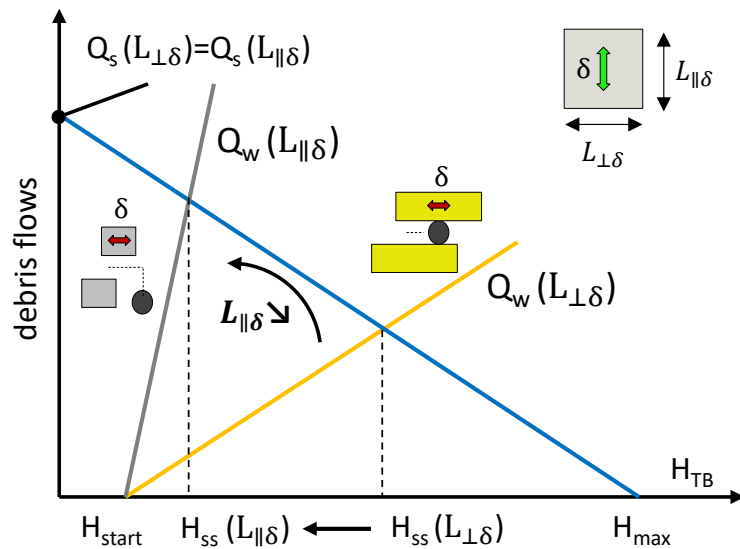


Figure 3.18: Reduction in the stabilized thickness of the third body caused by the faster ejection of debris particles (after [93]).

Figure 3.19 displays the micro-Raman analysis done on the fretting scars of the bottom samples at three contact configurations $L_{\parallel\delta}=L_{\perp\delta}=5$ mm (O), $L_{\parallel\delta}=2$ mm (I) and $L_{\perp\delta}=2$ mm (J). Once again, two different oxides are detected which are Hematite ($\alpha - Fe_2O_3$) and Magnetite (Fe_3O_4). As a result, it appears that in the studied ranges, the contact size as well as the

contact orientation has, qualitatively, very limited effect on the type of the ejected oxides. This might not be the case for smaller contact sizes where the oxide rheology might not be the same as will be shown in Section 3.3.3.2 when textured samples are considered.

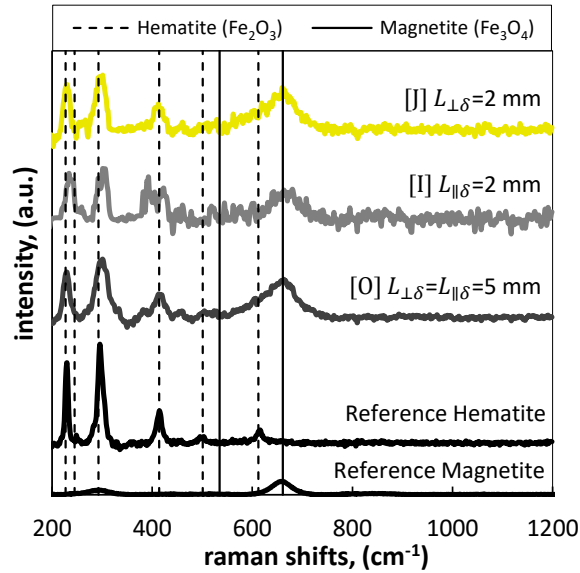


Figure 3.19: Raman spectra of the fretting scar (external abrasion corona) for three contact configurations $L_{\parallel\delta}=L_{\perp\delta}=5$ mm (O), $L_{\parallel\delta}=2$ mm & $L_{\perp\delta}=5$ mm (I) and $L_{\perp\delta}=2$ mm & $L_{\parallel\delta}=5$ mm (J) ($N=20000$ cycles, $p=100$ MPa, $\delta_g=\pm 100$ μm , and $f=1$ Hz, for Laser wavelength $\lambda = 785$ nm, Laser power= 0.35 mV, and acquisition time= 150 s).

3.2.3 Wear volume prediction model

3.2.3.1 Plain friction energy wear approach

Predicting wear volume of a contact under fretting wear is the overarching objective for many studies. So, the main thrust of this section is to establish a wear volume predictive model bearing in mind the impact of the aforementioned loading conditions. A first step towards the objective constitutes of applying the classical friction energy wear approach (Equation 3.5). The energy wear rate α is computed from the slope of the curve representing the variation of the total experimental wear volume (V) with the cumulated dissipated friction energy ($\sum Ed$) (Figure 3.4c): $\alpha=\alpha_{ref} = 4.383 \times 10^{-5} \text{ mm}^3/\text{J}$.

$$V_{pred} = \alpha_{ref} \cdot \sum Ed = \alpha_{ref} \cdot (4\mu_e F_n \delta_g N) \quad (3.5)$$

Figure 3.20 compares the total predicted wear volume ($V_{pred} = \alpha_{ref} \cdot \sum Ed$) with the experimental one (V_{exp}) for all the data collected at variable number of cycles, contact pressure, sliding amplitude, frequency, and contact area.

Note that to estimate the correlation between the experimental and the the predicted values for

a given quantity X which is here the wear volume V , a coefficient of determination R^2 is adopted henceforth such that:

$$R^2 = 1 - \frac{\sum (X_{pred} - X_{exp})^2}{\sum (X_{pred} - \bar{X}_{pred})^2} \quad (3.6)$$

It is worth mentioning that the plain energy approach seems to weakly predict the wear volume and hence is no longer reliable. A reason behind this is that the energy approach does not take into account the influence of third body and contact oxygenation along with other possible factors like tribo-oxidation, cyclic plastic strain and surface hardening that were shown to play an undeniable effect on wear kinetics.

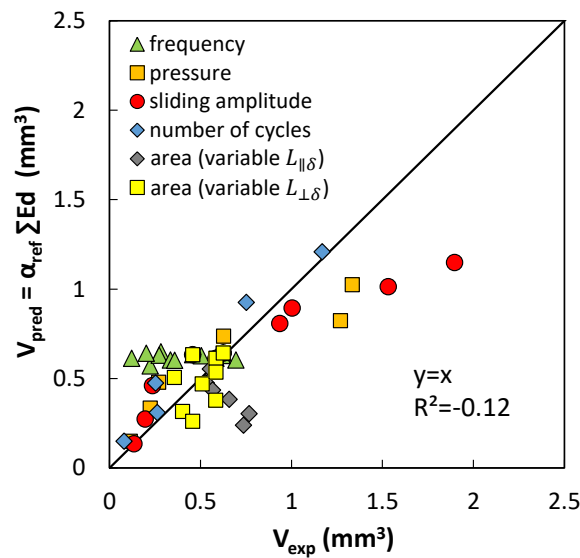


Figure 3.20: Variation of the total predicted wear volume ($V_{pred} = \alpha_{ref} \cdot \sum Ed$, Equation 3.5) as a function of the experimental wear volume (V_{exp}) considering all the tested loading conditions.

3.2.3.2 Friction power formulation

A second approach to better formalize the wear rate evolution is to consider the so-called friction power formulation. This approach, which better incorporates the influence of frequency, allows studying wear processes where adhesion and seizure are encountered [56]. Being equivalent to the so-called “pv” factor (i.e. the product of the contact pressure p and the sliding velocity v) at constant coefficient of friction, the friction power density φ^* (W/mm^2) can be introduced. This formulation was shown to well depict the Ti-6Al-4V fretting wear response for an iso cylinder-on-flat contact configuration [56]. Figure 3.21a plots the evolution of the individual energy wear rates as a function of the friction power density for the studied loading conditions. It appears that, except for the frequency loading condition, the results are very dispersive and do not exhibit a particular trend. However, the best fitting trend can be approximated by a power law (Equation 3.7):

$$\alpha_{\varphi^*} = 2.10^{-5} \cdot \varphi^*^{-0.27} \quad (3.7)$$

Figure 3.21b shows the total predicted wear volume ($V_{pred} = \alpha_{\varphi^*} \sum Ed$) plotted against the experimental wear volume (V_{exp}). As can be noticed, friction power density formulation is better than the classical friction energy approach (Figure 3.20) in predicting the experimental wear volume specifically at variable frequency. However, the friction power formulation does not predict well the wear volume as there is still dispersion in the latter when variable sliding amplitudes, contact pressures and contact areas are considered.

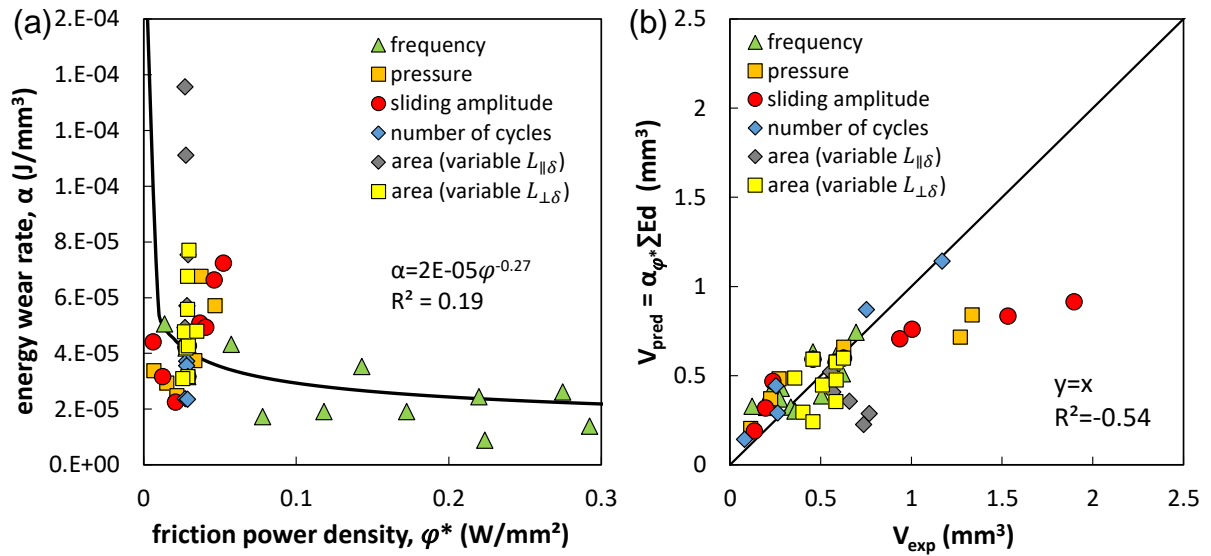


Figure 3.21: Compiling all the loading conditions to study the (a) variation of the energy wear rate as a function of the friction power density and (b) the evolution of the total predicted wear volume ($V_{pred} = \alpha_{\varphi^*} \sum Ed$) as a function of the experimental wear volume (V_{exp}).

The fact that this approach is not so efficient for the studied steel may be explained by different aspects. Firstly, steel is less influenced by adhesive wear than titanium alloy. Besides, the former investigation on titanium considers a cylinder-on-flat contact configuration which leads to extension of contact area during fretting. These two aspects might be a possible reason why the proposed energy wear rate formulation (α_{φ^*}) appears limited to quantify the wear volume extension for the studied flat-on-flat steel interface.

3.2.3.3 Weighted friction energy wear approach

The third strategy to predict wear volume constitutes of empirically extending the classical friction energy approach for flat-on-flat configuration of 34NiCrMo16 by taking into account the impact of all loading conditions (Equation 3.8). Based on the experimental test results, it is clear that wear volume is proportional to number of cycles (N), pressure (p), and $\delta_g/L_{\parallel\delta}$ parameter and is inversely proportional to frequency (f) and the contact length ($L_{\perp\delta}$). Hence we consider in the first approximation an additional contribution of all the loading conditions

such that the prediction model (V_{pred}) will have the form shown in Equation 3.9 where N_{ref} , p_{ref} , $\delta_{g,ref}$, f_{ref} , $L_{\parallel\delta,ref}$, and $L_{\perp\delta,ref}$ correspond to the reference test conditions being 20000 cycles, 100 MPa, $\pm 100 \mu m$, 1 Hz, 5 mm, and 5 mm respectively.

$$V_{pred} = \alpha \cdot F \left\{ \left(\frac{N}{N_{ref}} \right), \left(\frac{p}{p_{ref}} \right), \left(\frac{f}{f_{ref}} \right), \left(\frac{\delta_g/L_{\parallel\delta}}{\delta_{g,ref}/L_{\parallel\delta,ref}} \right), \left(\frac{L_{\perp\delta}}{L_{\perp\delta,ref}} \right) \right\} \cdot \sum Ed \quad (3.8)$$

$$V_{pred} = \alpha \cdot \left\{ \left(\frac{N}{N_{ref}} \right)^{n_N}, \left(\frac{p}{p_{ref}} \right)^{n_p}, \left(\frac{f}{f_{ref}} \right)^{n_f}, \left(\frac{\delta_g/L_{\parallel\delta}}{\delta_{g,ref}/L_{\parallel\delta,ref}} \right)^{n_{\delta_g/L_{\parallel\delta}}}, \left(\frac{L_{\perp\delta}}{L_{\perp\delta,ref}} \right)^{n_{L_{\perp\delta}}} \right\} \cdot \sum Ed \quad (3.9)$$

The unknowns of this model are the energy wear rate α , and the exponents n_N , n_p , n_f , $n_{\delta_g/L_{\parallel\delta}}$ and $n_{L_{\perp\delta}}$. The energy wear rate α is computed from the slope of the curve representing the variation of the total experimental wear volume with the cumulated dissipated friction energy (Figure 3.4c): $\alpha = \alpha_{ref} = 4.383 \times 10^{-5} \text{ mm}^3/J$. Following this, each exponent is obtained separately by minimizing the standard deviation between the experimental total wear volume (V_{exp}) and the predicted wear volume (V_{pred}) as shown in Equation 3.10 such that V_{ref} corresponds to the reference wear volume which is equal to 0.606 mm^3 . Note that the same method was used in a previous study and provided interesting results [139].

$$\text{Standard deviation (E\%)} = \frac{100}{V_{ref}} \sqrt{\frac{\sum_{i=1}^n (V_{exp} - V_{pred})^2}{n}} \quad (3.10)$$

$$\text{with } V_{pred} = \alpha_{ref} \cdot \left(\frac{X}{X_{ref}} \right)^{n_X} \cdot \sum Ed$$

Each exponent is calibrated using the experimental data corresponding to the studied loading parameter. By substituting each time the parameter X by N, p, f, $\delta_g/L_{\parallel\delta}$, and $L_{\perp\delta}$, the unknown exponents corresponding to each parameter are found to be: $n_N=0$, $n_p=0.6$, $n_f=-0.3$, $n_{\delta_g/L_{\parallel\delta}}=0.8$, and $n_{L_{\perp\delta}}=-0.5$ (Figure 3.22). However, $n_{\delta_g/L_{\parallel\delta}}=0.8$ differs slightly from the effect of the sliding amplitude alone ($n_{\delta_g} = 0.7$) supporting the stability of the approach.

It is worth mentioning that the obtained powers are in line with the experimental results in the sense that they describe well the weight possessed by each parameter during fretting wear process. In other words, the wear volume was linear with the number of cycles ($n_N=0$), nonlinearly proportional with the contact pressure ($n_p=0.6$), and $\delta_g/L_{\parallel\delta}$ parameter ($n_{\delta_g/L_{\parallel\delta}}=0.8$), and nonlinearly inversely proportional with the sliding frequency ($n_f=-0.3$) and the contact length ($n_{L_{\perp\delta}}=-0.5$). Hence, the final form of the extended energy wear approach is as follows:

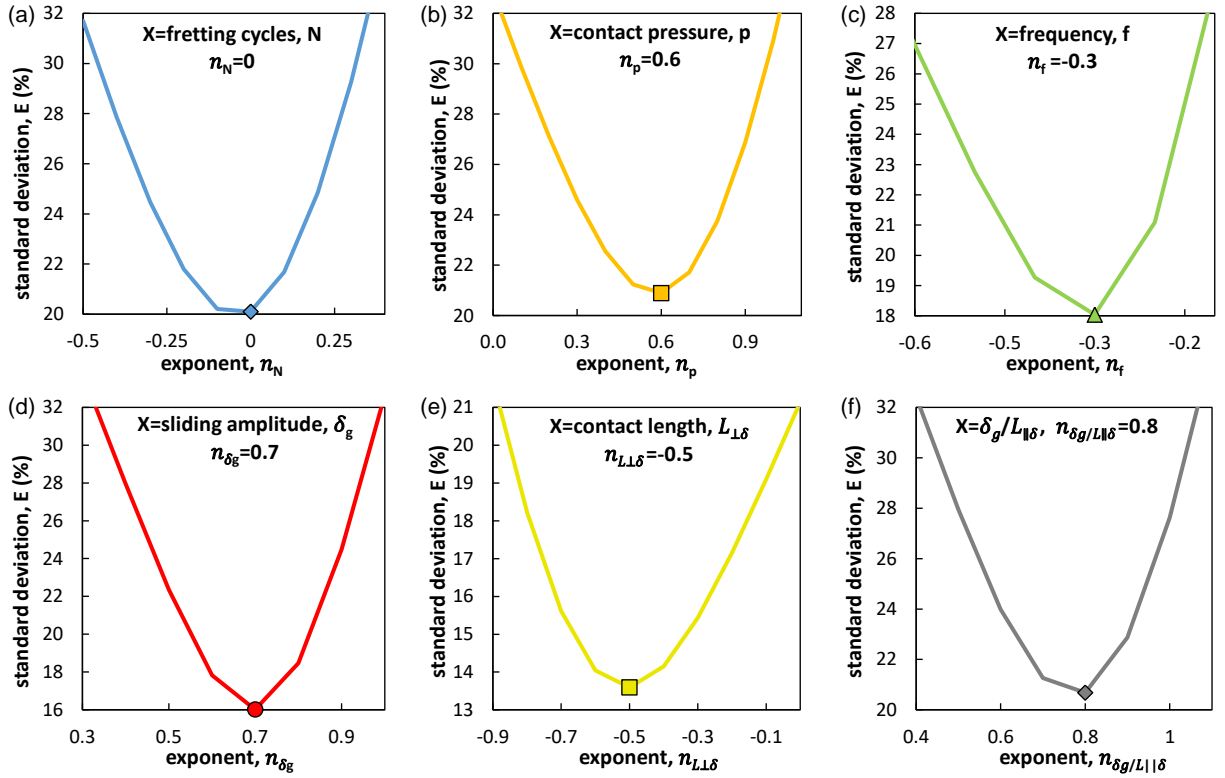


Figure 3.22: Variation of the standard deviation ($E\%$) for all the loading conditions versus the exponent corresponding to the studied parameters: (a) number of cycles, (b) contact pressure, (c) frequency, (d) sliding amplitude, (e) $L_{\perp\delta}$, and (f) $\delta_g/L_{\parallel\delta}$ parameter.

$$V_{pred} = \alpha^* \cdot \sum Ed$$

$$\alpha^* = \alpha_{ref} \cdot \left\{ \left(\frac{p}{p_{ref}} \right)^{0.6} \cdot \left(\frac{f}{f_{ref}} \right)^{-0.3} \cdot \left(\frac{\delta_g/L_{\parallel\delta}}{\delta_{g,ref}/L_{\parallel\delta,ref}} \right)^{0.8} \cdot \left(\frac{L_{\perp\delta}}{L_{\perp\delta,ref}} \right)^{-0.5} \right\} \quad (3.11)$$

$$\sum Ed = 4\mu_e N \delta_g F_n$$

By plotting the predicted wear volume ($V_{pred} = \alpha^* \cdot \sum Ed$) against the experimental one (V_{exp}) according to Equation 3.11, a linear relationship is obtained with a high $R^2=88\%$ (Figure 3.23a) which is higher than the classical energy wear approach and the friction power approach.

Since the friction coefficient is stable, Archard and energy approaches are equivalent. Hence, the obtained powers are applied for an extended Archard formulation having a reference Archard wear coefficient $K_{ref} = 3.030 \times 10^{-5} \text{ mm}^3/\text{J}$ (Equation 3.12). Once again, a nice correlation is obtained with a high coefficient of determination (R^2) being equal to 90% (Figure 3.23b).

$$V_{pred} = K^* \cdot \sum W$$

$$K^* = \alpha_{ref} \cdot \left\{ \left(\frac{p}{p_{ref}} \right)^{0.6} \cdot \left(\frac{f}{f_{ref}} \right)^{-0.3} \cdot \left(\frac{\delta_g/L_{\parallel\delta}}{\delta_{g,ref}/L_{\parallel\delta,ref}} \right)^{0.8} \cdot \left(\frac{L_{\perp\delta}}{L_{\perp\delta,ref}} \right)^{-0.5} \right\} \quad (3.12)$$

$$\sum W = 4N\delta_g F_n$$

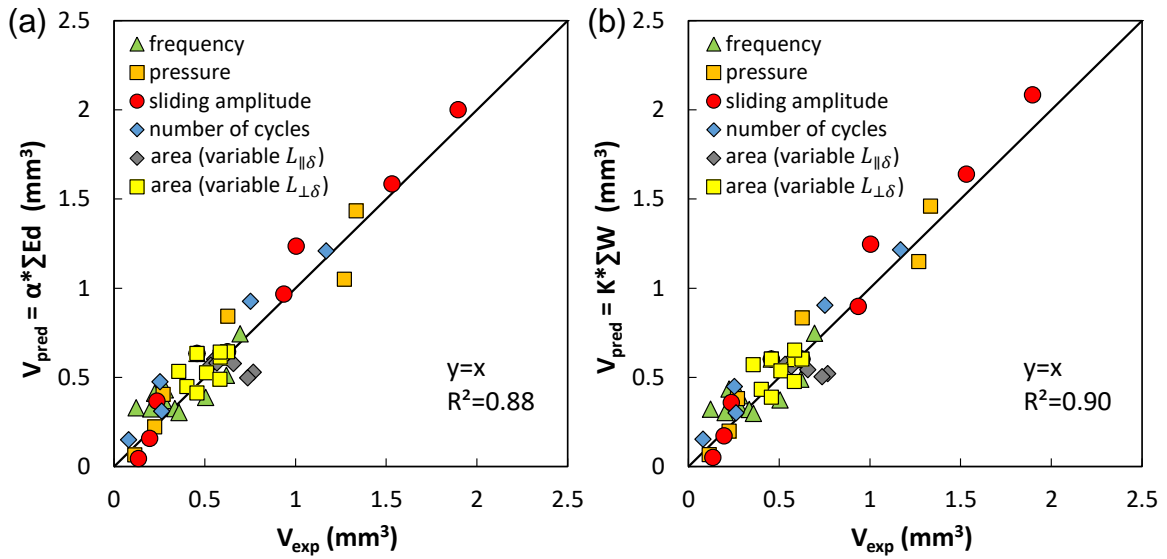


Figure 3.23: Variation of total wear volume versus the: (a) weighted cumulated friction energy (Equation 3.11) and (b) weighted Archard work for all the loading conditions (Equation 3.12).

In fact, the main objective of the above formulations is to try to understand the effect of fretting loading parameters from a global viewpoint. This would serve as a good starting step for deriving more general physical wear models in the future. It should be remarked that the obtained powers of the sliding amplitude and frequency are very close to those obtained by recent researches [65, 77–79]. Paulin et al. [78, 79], and Dreano et al. [77] detected $n_{\delta_g}=1$ and they presented many hypotheses to explain the latter including COC and TBA. However, none of these premises was proven analytically leaving the reason of the nonlinear increase of sliding amplitude an open question for future researches. On the other hand, Dreano et al. [77] found $n_f=-0.5$ and they proposed a physical interpretation of this tendency assuming a synergistic interaction between abrasion and tribo-oxidation processes. Hence, they suggested that the increase in frequency reduces the time between two sliding passes resulting in a thinner oxide film and consequently lower wear volume and wear rate. Note that the powers obtained in the current study slightly differ from those obtained by the former authors ($n_{\delta_g}=0.7$ instead of 1 for and $n_f=-0.3$ instead of -0.5).

This disparity might stem from different reasons. Firstly, the current study is conducted using large a flat-on-flat contact whereas the aforesaid studies use non-conformal crossed cylinders and cylinder-on-flat configurations. Since the contact configuration was shown to play undeniable role in debris entrapment and contact oxygenation, the difference of power might be clarified.

Warmuth et al. [84] showed that the effect of frequency is highly dependent on the contact geometry where the wear response seems less affected by frequency for more conforming contacts (as the current large crossed flat configuration). However, frequency has bigger influence on less conforming contacts where the wear rate is approximately 50% of that observed at low frequency. These authors proposed that more conforming contacts restrict oxygen access to the central regions of the contact where oxidation becomes limited. Indeed, frequency was shown to chiefly affect wear response through tribo-oxidation process [46, 140]. Besides, researches showed that frequency has very little effect in oxygen-starved environments [46, 140]. Combining these hypotheses, it can be deduced that the presence of composite abrasive-adhesive wear splits the interface into two regions: an external zone dominated by oxidational abrasive where frequency is effective and internal oxygen-deprived adhesion zone where frequency has insignificant effect. Thus the wear rate obtained at variable frequencies is nothing but an averaged response of frequency's small effect on adhesion internal zone and its big impact on the abrasion oxidized external zone. Since the previous models were derived in the condition of full abrasive-oxidational wear, higher frequency impact is obtained ($n_f = -0.5$).

The sliding amplitude, likewise, has smaller power than that obtained in the previous models which can be also attributed to the higher contact conformity driven by the studied flat configuration which leads to more debris entrapment and consequently lower wear. Besides, the presence of a composite abrasive-adhesive structure imparts its effects on the sliding amplitude as the quantity and quality of the wear particles ejected from the adhesion zone might not be of the same nature as those of external abrasion zone suggesting different wear rates.

Finally, the material studied in this thesis is 34NiCrMo16 steel alloy whereas the former studies were carried on titanium and cobalt alloys which have different oxidational and rheological properties that might possibly affect wear response.

In conclusion, the above discussion lends weight to the necessity of considering a composite adhesive-abrasive wear response of the interface instead of an averaged global wear behavior in order to better formalize wear kinetics.

3.3 Results validation using textured samples: access to smaller contact sizes

In this part, macro-textured samples will be examined firstly to validate the model and secondly to study the flows and the rheology of the third body at small contact sizes.

3.3.1 Grooves' fill-up mechanism

During fretting tests, series of images were taken to study the fill-up mechanisms of grooves with oxide debris. It appears that the first debris particles are ejected around 100 cycles. Besides, the grooves are completely filled between 1000-5000 cycles. However, debris particles undergo continuous compaction after 5000 cycles till the end of the test due to the continuous creation and ejection of debris particles to the grooves. Interestingly, whatever the orientation and widths of textures, the groove fill-up mechanism is generally the same and can be summarized by the following (1) to (9) steps as illustrated in Figures 3.24 & 3.25.

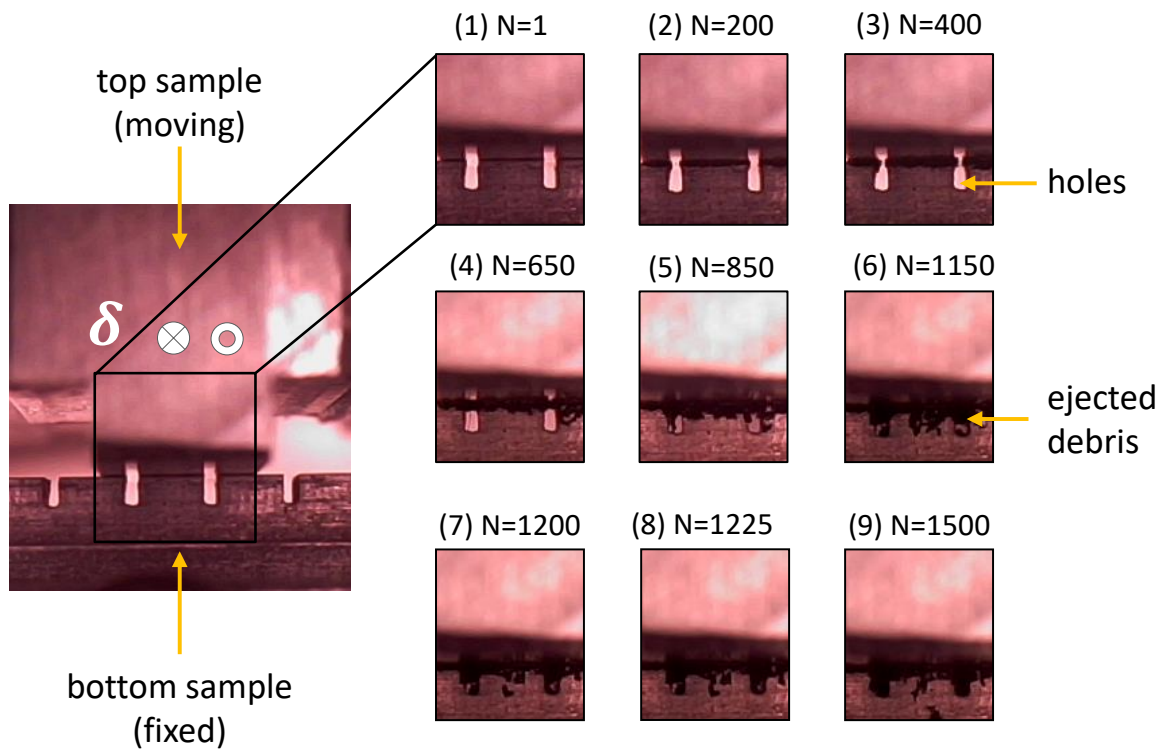


Figure 3.24: Grooves' fill-up mechanism obtained from textured samples with $L_{\perp\delta}=2$ mm, and $L_{\parallel\delta}=5$ mm, for $N=20000$ cycles, $p=100$ MPa, $\delta_g=\pm 100$ μm and $f=1$ Hz.

During the first few cycles, metal-metal interaction takes place leading to an increase in the coefficient of friction (1). Around the first 100 cycles, and once the metal-metal interaction becomes intense, the first debris particles are ejected out of the contact (2) leading to a decrease in the coefficient of friction due to the screen and accommodating effect of the first debris entrapped between the contacting first bodies. Then, the debris particles start to agglomerate on the topside of the groove from the edges towards the center (3) until clustering into a bridge which is detected between 278 and 698 cycles (4). Due to the applied normal load, the gravitational forces, and the powdery form of wear particles, the freshly formed debris will push the older conglomerates downside which will collapse into smaller particles that will occupy the bottom side of the grooves (5). Following this, debris particles start to accumulate on the bottom side of the grooves (6) until reaching a state where the latter form big clusters on the top and bottom

side of the groove (7). In step (8), the groove will be thoroughly filled with uncompact debris particles. Under the influence of applied loads and the continual production of debris particles, the groove will be entirely filled with continuously compacting conglomerates.

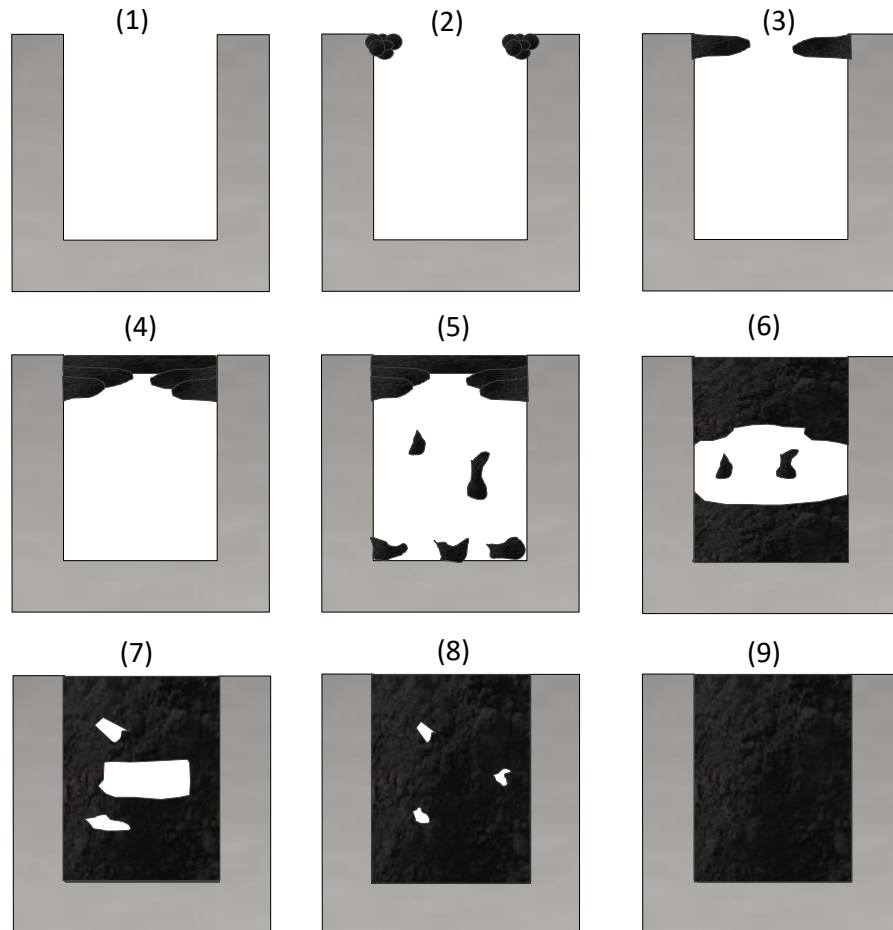


Figure 3.25: Schematic illustration of the grooves' fill-up mechanism: (1) initial stage; (2) ejection of debris particles; (3) agglomeration of debris particles on the top; (4) formation of a bridge of agglomerated debris on the top; (5) collapse and fall of some debris particles to the bottom; (6) accumulation of debris particles at the bottom; (7) clustering of debris particles on the top and bottom; (8) fill up of the hole with uncompact debris; (9) continuous compaction of the debris filling the hole.

This mechanism was confirmed whatever the textures sizes and orientations by more than 33 observations. Figure 3.24 illustrates the interest of image acquisition during the test underlining the relevance between the groove fill-up mechanism and the experimental observations. It is noteworthy that similar observations were reported for the stages (1) to (4) by a previous study [141] which was carried out on closed laser textured micro-pores. Since the grooves were closed and very small, the detected stages (1-4) were observed after opening the contact and could not be verified by on-line image acquisition like previously detailed. On the other hand, the fact of having opened and relatively large grooves was an advantage in the current study which helped construct a thorough continuation of the grooves' fill-up mechanism from stage (1) to (9).

3.3.2 Rheology of the third body particles

The SEM observations of grooves in both parallel and perpendicular orientations (Figure 3.26a & b) show that they contain third body particles with different morphologies ranging from powdery debris and platelets to very compact third bodies. This indicates that there are different mechanisms responsible for such discrepancy in the rheology of the ejected particles. Another plausible hypothesis is that these particles might be created and ejected at different stages. Hence, each morphology might be a reflection of a particular mechanism or a particular record in the timeline of debris creation and ejection. One interesting point one should shed the light on is that similar features are detected in both orientations which suggests that the mechanisms of creation and ejection of third body particles are independent of contact orientation with respect to the sliding direction.

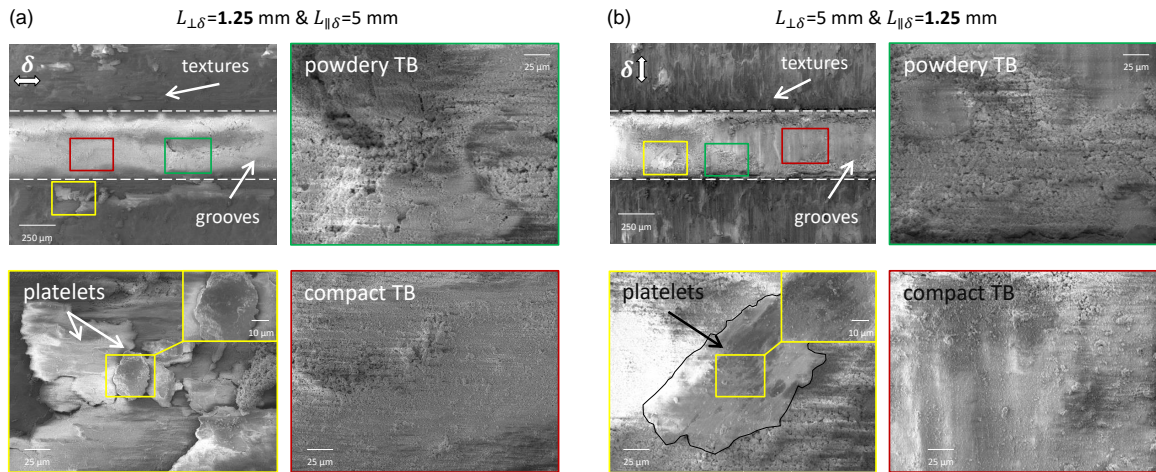


Figure 3.26: SEM observations of grooves in: (a) textured sample with $L_{\perp\delta}=1.25$ mm and $L_{\parallel\delta}=5$ mm (before cleaning with ethanol); and (b) textured sample with $L_{\perp\delta}=5$ mm and $L_{\parallel\delta}=1.25$ mm (before cleaning with ethanol) ($N=20000$ cycles, $p=100$ MPa, $\delta_g=\pm 100$ μm and $f=1$ Hz).

Figure 3.27 shows an example of plate-like sheet having a thickness of 2.53 μm embedded within the ejected particles. One of the possible origins of these flake-like sheets is the agglomeration of fine powder debris under the effect of fretting solicitations engendering thin platelets a few microns thick having a diameter that can reach several tens of microns. Similar observation was detected recently on high strength steel by Kirk et al. [51] who recognized pieces of debris with a size reaching 100 μm embedded in the ejected debris. Besides, they showed that most of the debris particles are made up of hematite crystallites of the order of 0.1 μm in diameter which were sintered to different levels. Kirk et al. [51] then hypothesized that such agglomeration and sintering processes can be the origin of different structures of third bodies ranging from vermicular to fully sintered glassy structures.

SEM observations of the ejected third body particles both in the grooves and outside the interface reveal presence of a significant amount of powdery particles (Figures 3.26 & 3.28). These particles might stem from different mechanisms. Firstly, the thin sheets might be the precu-

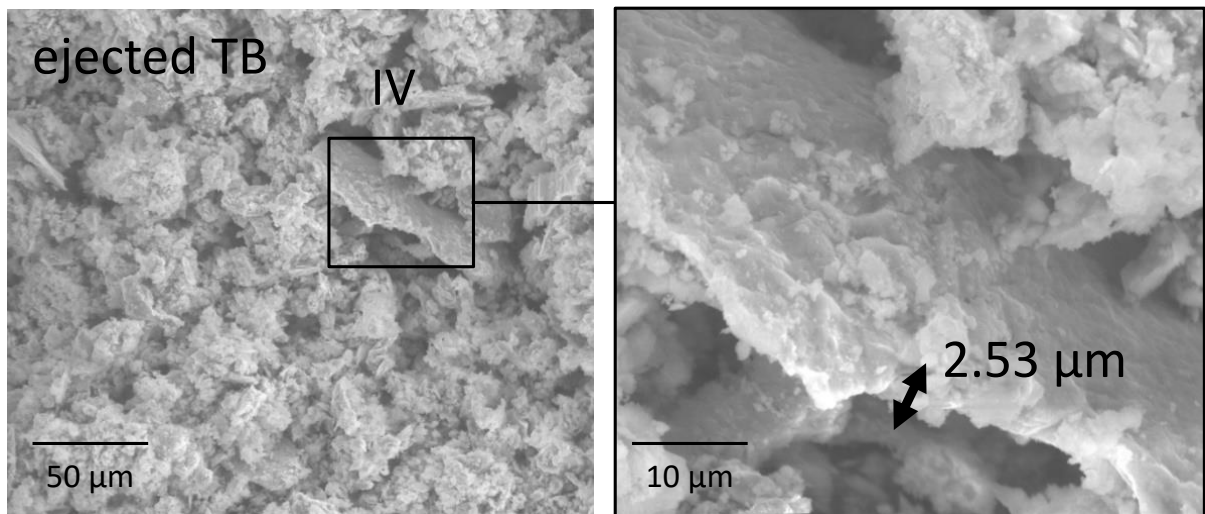


Figure 3.27: SEM and BSE observations of a thin wear sheet (platelet) embedded in the ejected third body outside the grooves in a textured sample with $L_{\perp\delta}=1.25$ mm, and $L_{\parallel\delta}=5$ mm, $N=20000$ cycles, $p=100$ MPa, $\delta_g=\pm 100$ μm and $f=1$ Hz (before cleaning with ethanol).

sor of smaller powdery particles as they get broken up and comminuted within the interface. Another mechanism is that these particles are created by plowing or micro-cutting of asperities resulting in debris particles. These powdery particles will agglomerate in the borders as reflected in Figure 3.28 which explains the bridge detected by camera observations in Figures 3.24 & 3.25. Additionally, these particles tend to fall in the holes and continuously accumulate in the contact giving birth to a compact third body which is also detected by online camera acquisitions.

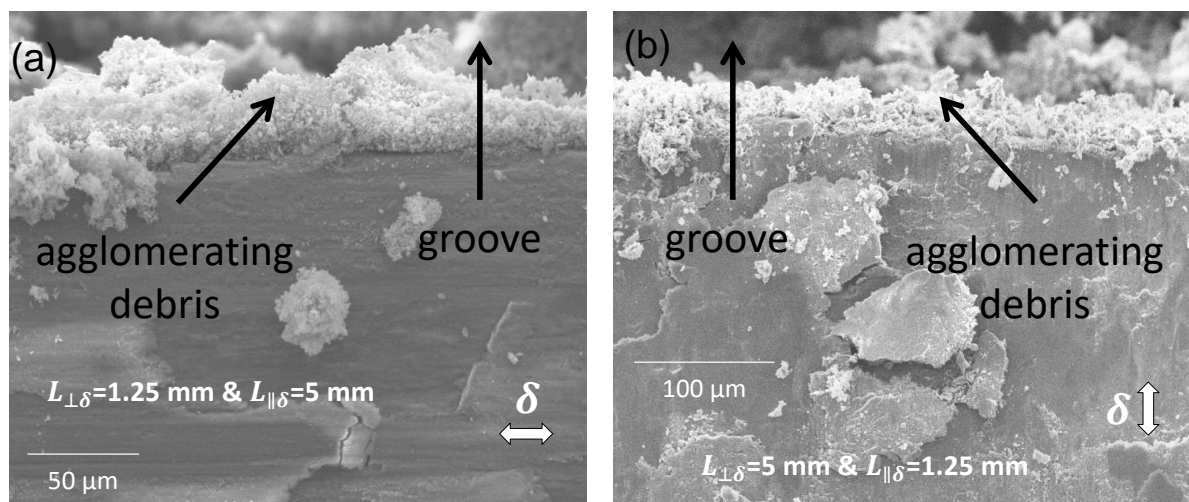


Figure 3.28: SEM observations of the agglomerated powdery debris at the borders of the contact in: (a) textured sample with $L_{\perp\delta}=1.25$ mm and $L_{\parallel\delta}=5$ mm (before cleaning with ethanol); and (b) textured sample with $L_{\perp\delta}=5$ mm and $L_{\parallel\delta}=1.25$ mm (before cleaning with ethanol) ($N=20000$ cycles, $p=100$ MPa, $\delta_g=\pm 100$ μm and $f=1$ Hz).

The comparison between contact orientations (Figure 3.29a & b) shows more compact third body either filling the grooves or ejected outside the grooves and the wear track. These particles are more homogeneous and exhibit smaller sizes in case of reducing $L_{\parallel\delta}$ compared to the case where $L_{\perp\delta}$ is reduced instead. This lends support to the hypothesis that more particles are ejected along the sliding direction so they tend to agglomerate and compact more than the case where particles are ejected against the latter.

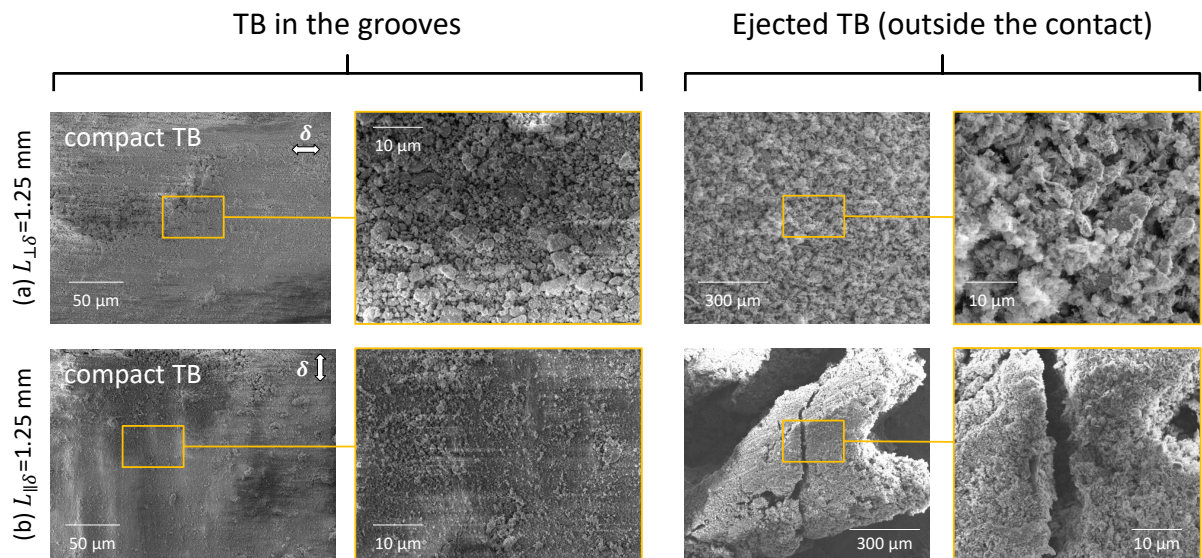


Figure 3.29: Comparison of the compaction of the third body ejected within the grooves and outside the contact for: (a) textured sample $L_{\perp\delta}=1.25$ mm and $L_{\parallel\delta}=5$ mm (before cleaning with ethanol); and (b) textured sample with $L_{\perp\delta}=5$ mm and $L_{\parallel\delta}=1.25$ mm (before cleaning with ethanol) ($N=20000$ cycles, $p=100$ MPa, $\delta_g=\pm 100$ μm and $f=1$ Hz).

The observation of the fretting scar (Figure 3.30) in both orientations (before cleaning with ethanol) reveals presence of bright exposed steel regions (i.e. bright zones in BSE images) with discontinuous patches of oxides (dark zones in BSE). In both cases, the steel furrows as well as the oxidized zones are oriented parallel to the sliding direction which may be explained by the plowing mechanism illustrated by [142]. The other exposed metallic zones detected might correspond to the zones where wear sheets and oxide particles were removed.

Another significant remark is that there is more adhering third body in case of reducing $L_{\perp\delta}$ compared to the case where $L_{\parallel\delta}$ is reduced. This comes in agreement with the fact that the longer the sliding direction, the more likely the particles will be entrapped in the interface and hence the slower they'll be ejected out of the contact. A closer look to the surface gives evidence of the secondary or lateral flow where particles are ejected against the sliding direction and the primary flow where particles are to be ejected in the direction of sliding (Figure 3.30b).

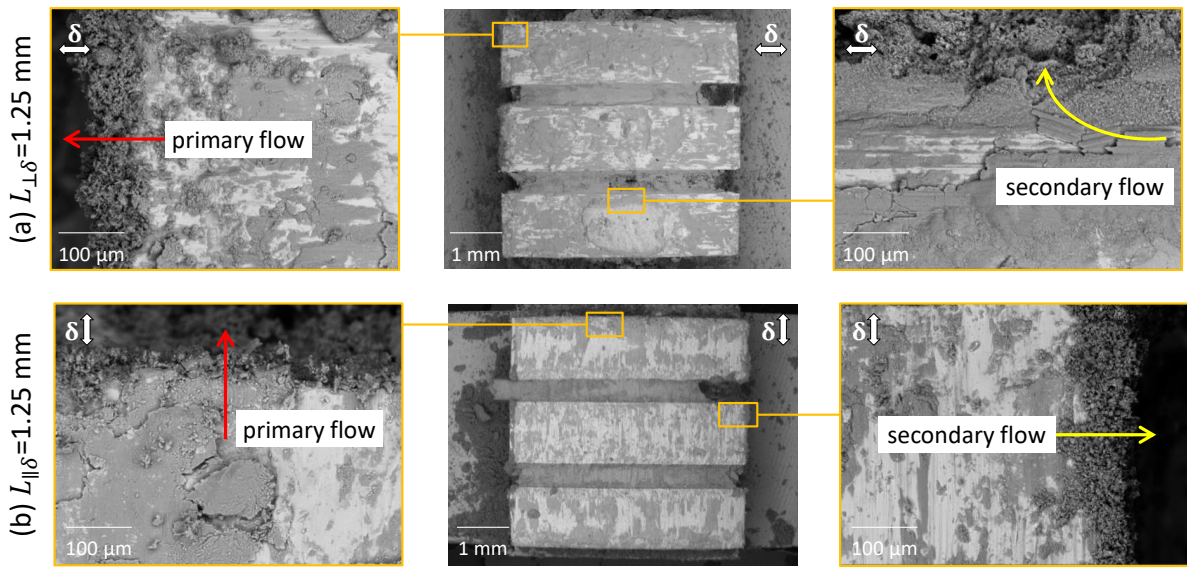


Figure 3.30: BSE observations of the (a) primary and secondary flows in a textured sample having $L_{\perp\delta} = 1.25$ mm and $L_{\parallel\delta} = 5$ mm (before cleaning with ethanol); and (b) primary and secondary flows in a textured sample having $L_{\perp\delta} = 5$ mm and $L_{\parallel\delta} = 1.25$ mm (before cleaning with ethanol) ($N = 20000$ cycles, $p = 100$ MPa, $\delta_g = \pm 100$ μm and $f = 1$ Hz).

3.3.3 Qualitative validation of the contact size effect

3.3.3.1 Wear track observations

Figure 3.31a compares the optical images of textured bottom samples of different orientations after cleaning with ethanol. For the same contact size per texture, remarkable bright scars are obtained for variable $L_{\parallel\delta}$, which is not the case for variable $L_{\perp\delta}$ where relatively darker fretting scars are detected. Additionally, it is obvious that a lower oxygen concentration is recognized at the EDX maps of the bottom samples in case of variable $L_{\parallel\delta}$ compared to those of variable $L_{\perp\delta}$ (Figure 3.31b). This is further confirmed by a semi-quantitative analysis of EDX maps where $[\text{O}]/[\text{Fe}]$ ratio is relatively higher in variable $L_{\perp\delta}$ than in variable $L_{\parallel\delta}$ (Figure 3.31c) especially when the contact size becomes smaller.

To further validate this result, BSE images of uncleaned top and bottom samples for the two orientations ($L_{\perp\delta} = 1.25$ mm and $L_{\parallel\delta} = 5$ mm) and ($L_{\perp\delta} = 5$ mm and $L_{\parallel\delta} = 1.25$ mm) were binarized. This allows estimation of the oxidized (in black) areas and exposed (or unoxidized) steel areas (in white) (Figure 3.32a). Following this, the ratio of oxidized to unoxidized areas is compared for both orientations in Figure 3.32b where textures width $L_{\perp\delta} = 1.25$ mm showed nearly double proportion of oxidized areas than in $L_{\parallel\delta} = 1.25$ mm textures. Besides, the binarization method is further compared with semi-quantitative analysis of EDX maps of uncleaned top and bottom samples where once again $[\text{O}]/[\text{Fe}]$ ratio is relatively higher in $L_{\perp\delta} = 1.25$ mm textures than in the case of $L_{\parallel\delta} = 1.25$ mm (Figure 3.32c).

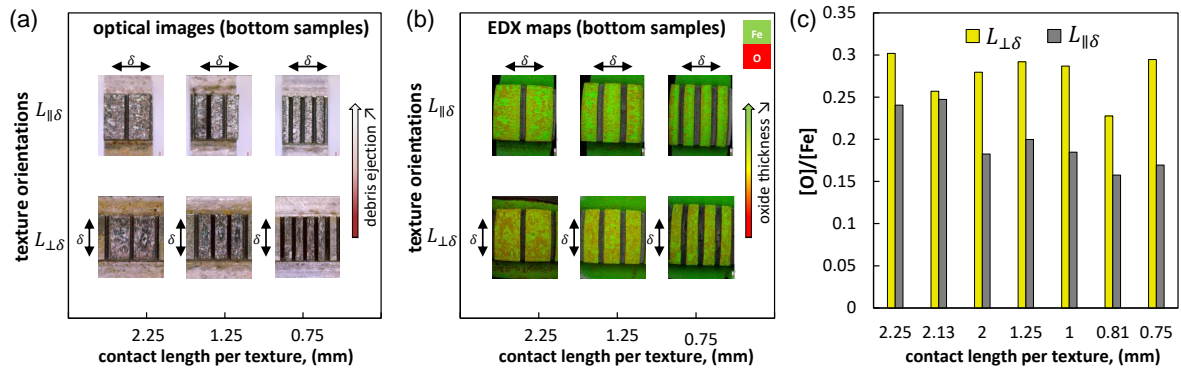


Figure 3.31: Comparison of the (a) optical observations, (b) EDX maps and (c) Oxygen to Iron ratio “[O]/[Fe]” of the bottom textured samples for both orientations with variable $L_{\perp\delta}$ and $L_{\parallel\delta}$ (after cleaning with ethanol) as a function of contact size per textures ($N=20000$ cycles, $p=100$ MPa, $\delta_g=\pm 100$ μm and $f=1$ Hz).

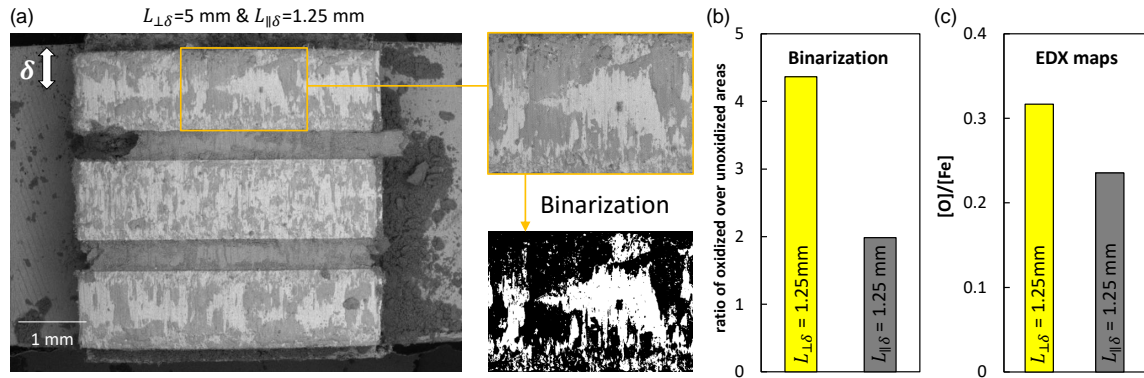


Figure 3.32: (a) Illustration of the binarization method used to estimate the ratio of oxidized area over unoxidized one for uncleaned top and bottom samples; (b) comparison of the ratio of oxidized area over unoxidized one for ($L_{\perp\delta}=1.25$ mm and $L_{\parallel\delta}=5$ mm) and ($L_{\perp\delta}=5$ mm and $L_{\parallel\delta}=1.25$ mm) orientations for both top and bottom samples (before cleaning with ethanol); (c) comparison of oxygen to iron ratio “[O]/[Fe]” of the top and bottom textured samples for ($L_{\perp\delta}=1.25$ mm and $L_{\parallel\delta}=5$ mm) and ($L_{\perp\delta}=5$ mm and $L_{\parallel\delta}=1.25$ mm) orientations (before cleaning with ethanol) ($N=20000$ cycles, $p=100$ MPa, $\delta_g=\pm 100$ μm and $f=1$ Hz).

3.3.3.2 XRD analysis of ejected debris

In addition to the fostered debris ejection detected in shorter $L_{\parallel\delta}$, a different color of oxide debris was detected by comparing both orientations where reddish brown color is detected for variable $L_{\perp\delta}$ and dark brown color is observed in variable $L_{\parallel\delta}$ (Figure 3.33a). The colors discrepancy appears clearly for contact areas falling below 12.5 mm^2 and becomes more pronounced with the decrease in the contact area.

To understand the reason behind this, X ray diffraction (XRD) was performed using ARL Equinox 100 (ThermoFisher scientific) diffractometer with cobalt radiation (Co- $K\alpha$, wave length (λ)=1.789010 \AA) in order to identify the phases existing in the ejected debris corresponding to

($L_{\perp\delta}=0.81$ mm and $L_{\parallel\delta}=5$ mm) and ($L_{\perp\delta}=5$ mm and $L_{\parallel\delta}=0.81$ mm) orientations¹. Note that for such condition, the interface is running under iso-contact oxygenation such that the minimum contact length is equal to 0.81 mm for the two situations. According to Figure 3.33b, it is clear that different diffraction patterns are detected for both orientations where three different phases are identified in both cases namely: Ferrite ($\alpha - Fe$), Hematite ($\alpha - Fe_2O_3$), and magnetite (Fe_3O_4).

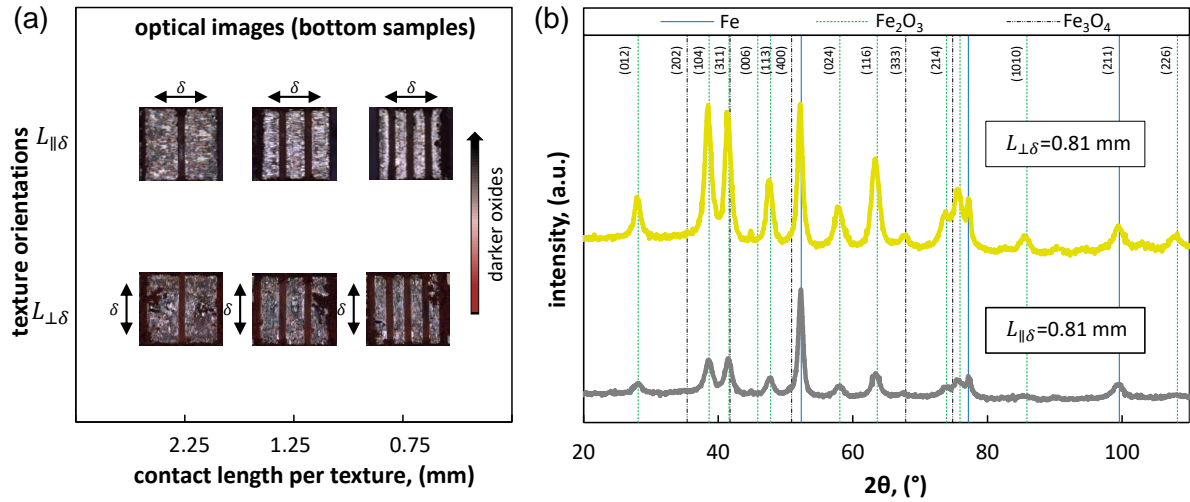


Figure 3.33: Evolution of the (a) debris color with the textures orientations by varying $L_{\perp\delta}$ and $L_{\parallel\delta}$ (before cleaning with ethanol); (b) XRD patterns of the ejected debris with the textures orientations for ($L_{\perp\delta}=0.81$ mm and $L_{\parallel\delta}=5$ mm) and ($L_{\perp\delta}=5$ mm and $L_{\parallel\delta}=0.81$ mm) orientations (N=20000 cycles, p=100 MPa, $\delta_g=\pm 100$ μm and f=1 Hz).

Table 3.5 shows the phase fractions in both orientations. It appears that bigger proportions of ferrite ($\alpha - Fe$) and magnetite (Fe_3O_4) are detected in $L_{\parallel\delta}=0.81$ mm compared to $L_{\perp\delta}=0.81$ mm. On the other hand, the fraction of hematite ($\alpha - Fe_2O_3$) in $L_{\perp\delta}=0.81$ mm is higher than that in $L_{\parallel\delta}=0.81$ mm. It is observed in fretting tests that once detached, the steel particles are transformed first into magnetite and then into hematite [11, 85]. Keeping this hypothesis borne in mind, the fact of having different oxides depending on the texture orientation may be clarified; when $L_{\perp\delta}$ is reduced, debris particles remain longer time in the contact which favors oxidation of iron and magnetite (Fe_3O_4) into hematite ($\alpha - Fe_2O_3$). In contrary, due to the fast ejection of debris particles in case of variable $L_{\parallel\delta}$, there will be no enough time for the majority of iron and magnetite particles to undergo further oxidation into Hematite so they are simply ejected in the form of iron and magnetite or hematite which explains the observed color difference in the two orientations. Another more plausible hypothesis is that the different degree of powders' compaction in grooves may be the reason why distinct colors are obtained especially that the difference in the phase fractions in both orientations is not sufficiently high. Indeed, it was reported that compacted hematite debris has black and iridescent color which turns into red when powdered [143]. The fact of having more compacted debris in the grooves when $L_{\parallel\delta}$

¹Thanks go for INEL S.A.S" and "Thermo Fisher Scientific" societies represented by Dr. Eric Berthier and Dr. Christophe Fontugne for performing XRD analysis using ARL Equinox 100 diffractometer

is reduced (Figures 3.29 & 3.30) supports this hypothesis where the oxides in this case have a rather black color. This result comes in agreement with the fact that textures orientations alter the ejection flow of debris particles, their compaction degrees in the grooves and consequently the color of the phase fractions.

Semi-quantitative analysis		
Orientation	$L_{\perp\delta}=0.81$ mm and $L_{\parallel\delta}=5$ mm	$L_{\perp\delta}=5$ mm and $L_{\parallel\delta}=0.81$ mm
% Hematite ($\alpha - Fe_2O_3$)	73	49
% Ferrite ($\alpha - Fe$)	20	38
% Magnetite (Fe_3O_4)	7	13

Table 3.5: Comparison of phase fractions in the ejected debris analyzed by XRD for ($L_{\perp\delta}=0.81$ mm and $L_{\parallel\delta}=5$ mm) and ($L_{\perp\delta}=5$ mm and $L_{\parallel\delta}=0.81$ mm) orientations (N=20000 cycles, p=100 MPa, $\delta_g=\pm 100$ μm and f=1 Hz).

3.3.4 Quantitative validation of experimental results

To quantitatively validate wear kinetics at small contact areas, Figure 3.34 is plotted to show the evolution of the energy wear rate as a function of the contact sizes ($L_{\perp\delta}$ and $L_{\parallel\delta}$) for different orientations in case of plain and textured samples. Obviously, one can see that both plain and textured samples fit on the same master curve for both orientations. Besides, the wear rate tendencies are very close from those predicted in the model in Equation 3.11 by considering variable ($L_{\perp\delta}$ and $L_{\parallel\delta}$) confirming the validity of the extended formulation at small contact sizes.

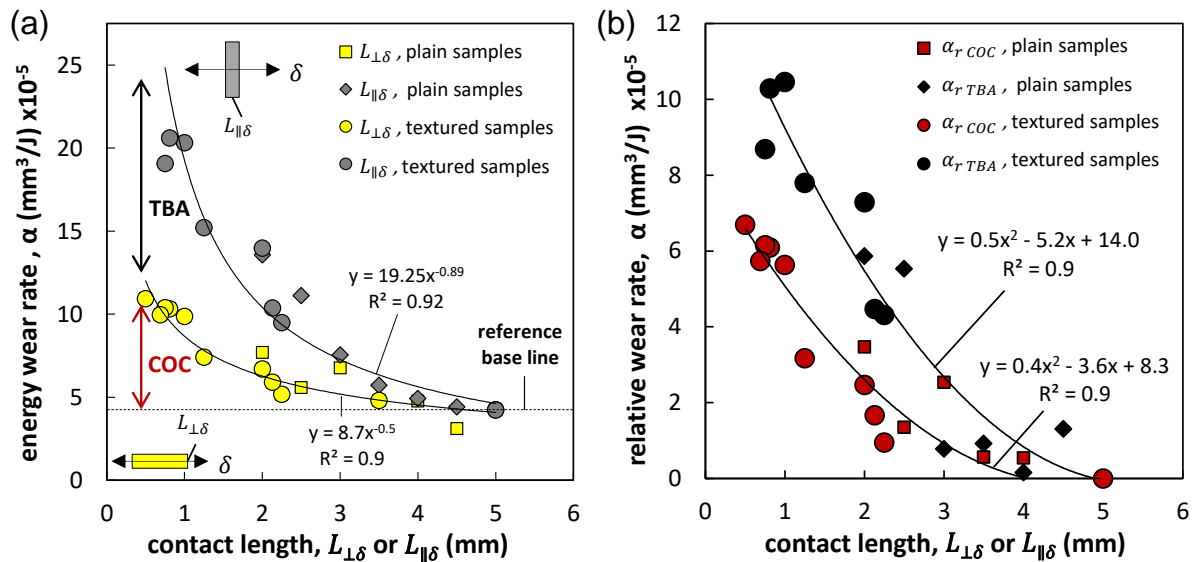


Figure 3.34: Evolution of the (a) energy wear rate and the (b) relative energy wear rate contributions of COC and TBA versus contact size for plain and textured samples.

This result is quite interesting. Indeed, the good correlation between the plain and macro-textured samples suggest that the secondary flow contribution, which is amplified using textured surface, has weak influence on wear kinetics. This indirectly backs the former hypothesis that the

TBA wear rate contributions is mainly driven by the primary debris flow and therefore governed by the $L_{\parallel\delta}$ length scale. Yet, it is still interesting to verify the limited effect of secondary lateral debris flow compared to the primary debris flow in future works by applying discrete element methods (DEM) for instance [144]. Hence, the relative wear rate description can be considered once again compiling both plain and textured fretting wear results (Figure 3.34b). It is worth mentioning that, regarding the contact size effect, TBA plays a major contribution compared to COC effect. Nonetheless, this result suggests that the COC approach needs to be also considered in variable contact size wear analysis.

3.4 Stability of the composite-wear model using tests outside calibration domain

To evaluate the stability of the extended wear model, quantitative cross-validation analysis should be considered (Figure 3.35) [80, 145]. This requires launching tests outside the calibration domain which consists of tests where only one parameter is varied with respect to the reference conditions (X_{ref}, Y_{ref}) with X and $Y \in [N, p, \delta_g, f, L_{\perp\delta}$ and $L_{\parallel\delta}]$. To simplify the validation analysis, for each loading combination (X, Y) , two loadings conditions are varied instead of one with respect to the reference conditions by considering both plain and textured samples.

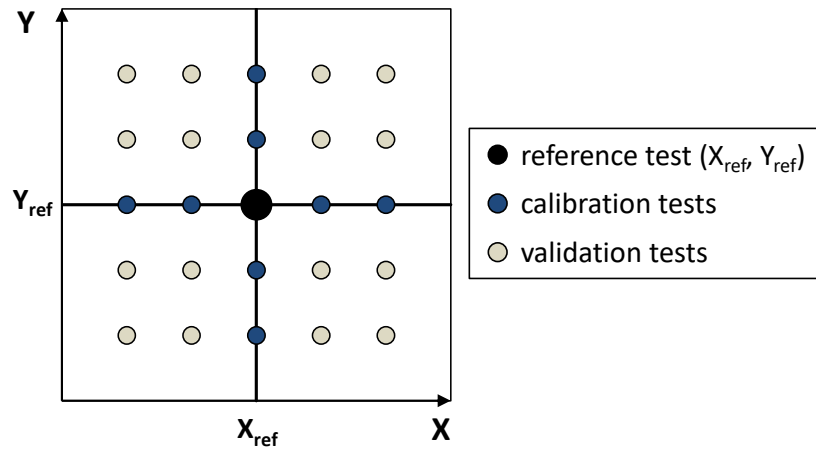


Figure 3.35: Illustration of the quantitative cross-validation strategy of the wear kinetics model with X and $Y \in [N, p, \delta_g, f, L_{\perp\delta}$ and $L_{\parallel\delta}]$ [80, 145].

Figure 3.36a compares the experimental and predicted wear volumes following Equation 3.11 using extended energy approach. By compiling the results of 120 tests (43 calibration tests with untextured plain bottom sample + 77 validation tests with plain and textured bottom samples), a nice correlation unfolds with a high coefficient of determination (R^2) equal to 0.86. Alternatively, applying the extended Archard formulation (Equation 3.12), a nice correlation is obtained once again with a high coefficient of determination (R^2) being equal to 0.88 (Figure 3.36b).

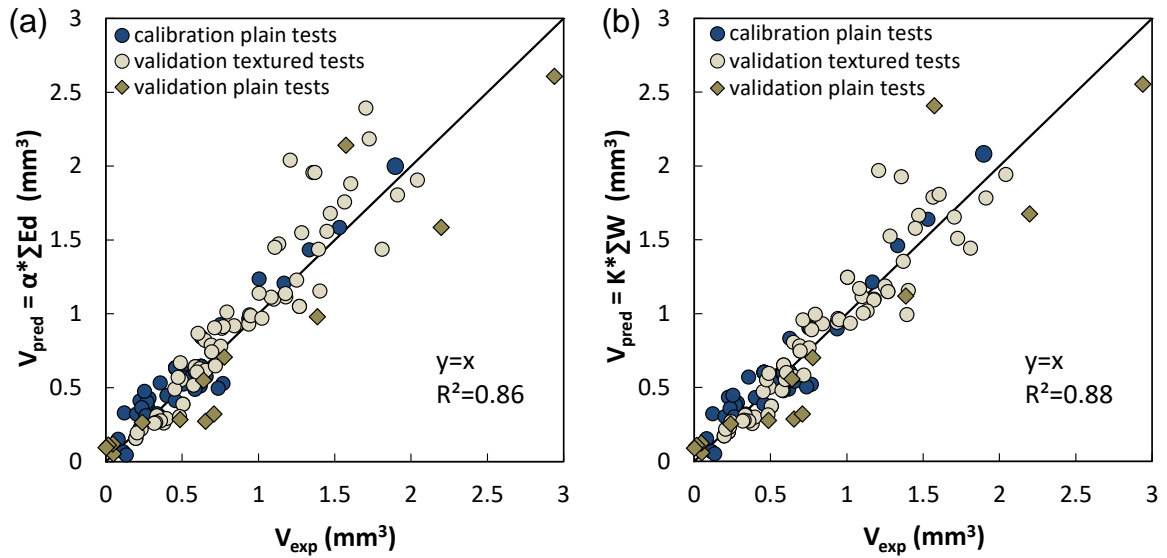


Figure 3.36: Correlation between the experimental and predicted fretting wear volumes by compiling all the tests inside and outside the calibration domain using: (a) extended friction energy wear approach (Equation 3.11) and (b) extended Archard approach (Equation 3.12).

3.5 Wear depth prediction

The former investigation introduces a global weighted friction energy wear model providing a reliable wear volume prediction. This approach suggests that the wear rate α is homogeneous along the whole fretted interface disregarding the wear mechanism involved such as abrasion and adhesion. However, the composite abrasive-adhesive structure of the wear scar suggests that the wear rate is not homogeneous along the interface leading to a nonhomogeneous wear depth.

In this section, the 2D averaged experimental and FEM wear profiles are compared (Figure 3.37). It is interesting to note that the lower the wear value, the higher the dispersion. The fact of having nonhomogeneous experimental $2D_{ave}$ profiles was previously detailed in Section 3.2.2. Indeed, more homogeneous flat wear profiles are envisioned when the abrasive wear is predominant (i.e. decreasing the frequency and contact pressure and increasing δ_g towards reciprocating sliding). This also depends on the wear volume extension and consequently the test duration (i.e. increasing N) and on the progressive elimination of adhesive structures. When the wear volume is important, the experimental wear profile converges to the flat wear profile given by the simulations (condition D, Figure 3.37i). At the beginning of the test, the significant adhesive transfer phenomenon alters the worn profiles (condition G, Figure 3.37a). However, when the wear extends, these local transfers are progressively eliminated and the wear profiles leads to a homogeneous quadrilateral shape despite the existence of adhesive wear (condition H, Figure 3.37c).

To quantify this aspect, the evolution of the experimental maximum wear depth measured on the 2D wear profile (h_{max}) is compared with that of the maximum wear depth derived from the

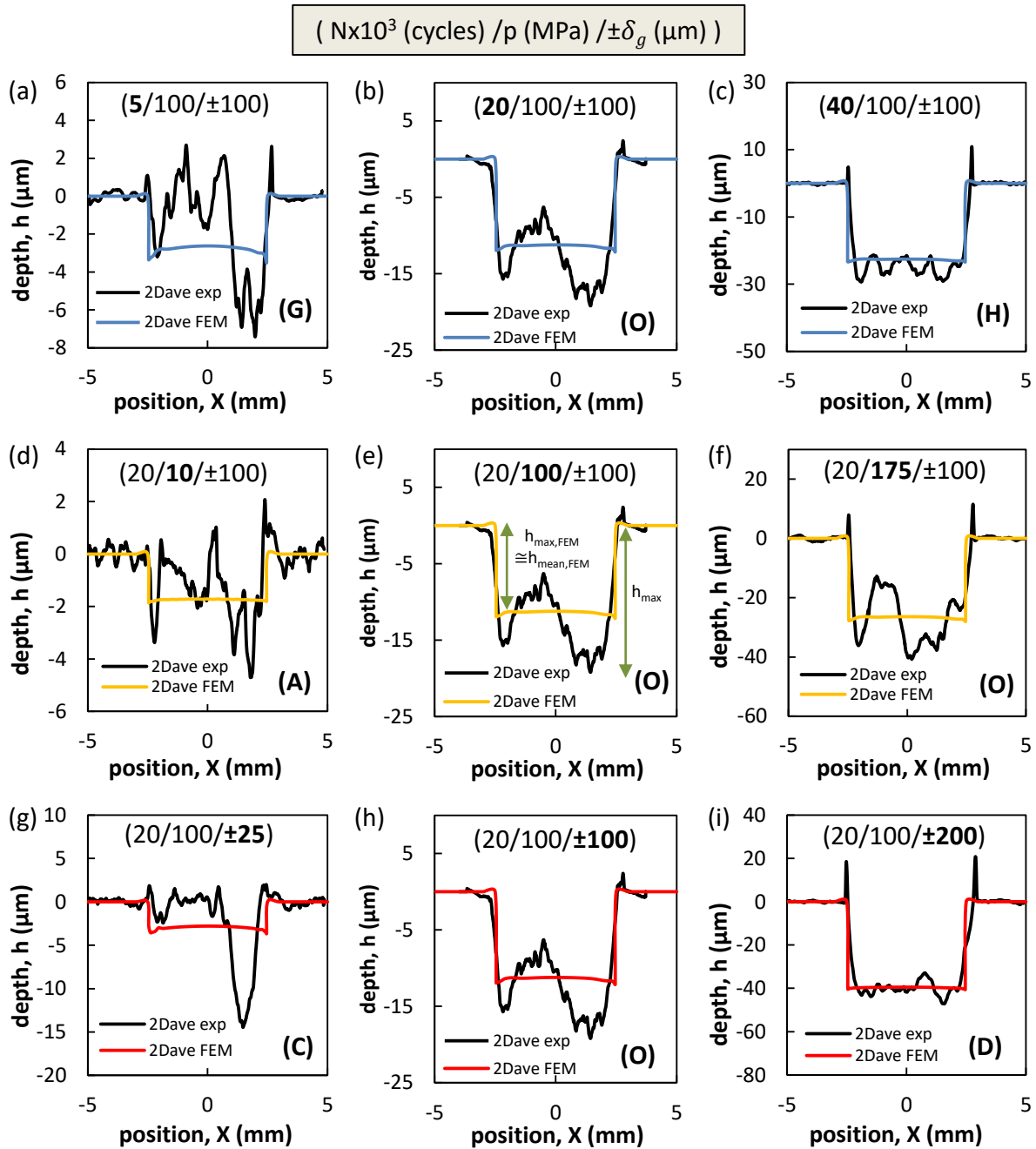


Figure 3.37: Comparison between the experimental and numerical $2D_{ave}$ wear profiles at $f=1$ Hz for the loading conditions: (a) $N=5\,000$ cycles (G), (b) $N=20\,000$ (O), (c) $N=40\,000$ (H), (d) $p=10$ MPa (A), (e) $p=100$ MPa (O), (f) $p=175$ MPa (B), (g) $\delta_g=\pm 25$ μm (C), (h) $\delta_g=\pm 100$ μm (O), and (i) $\delta_g=\pm 200$ μm (D).

FEM simulation ($h_{max,FEM}$) (details of FEM simulations are described in [95] and in Chapter 2). For the given flat-on-flat contact where the contact area remains constant as well as the contact pressure profile, the maximum simulated wear depth ($h_{max,FEM}$) is very close to the mean simulated value ($h_{mean,FEM}$) (Figure 3.37e). Alternatively, considering the wear depth volume correlation, the experimental mean wear depth (h_{mean}) should be identical to FEM

value ($h_{mean} = h_{max, FEM}$). Finally, a simple explicit formulation can be applied to determine $h_{max, FEM}$ by combining the energy wear rate, the friction energy and the contact area which is constant. Hence, the following expression (Equation 3.13) can be derived:

$$h_{max, FEM} = h_{mean, FEM} = h_{mean} = \frac{1}{2A} \alpha \sum Ed = \frac{V}{2A} \quad (3.13)$$

Figure 3.38a compares both experimental h_{max} and $h_{max, FEM}$. As expected, due to transfer phenomenon, the correlation is very poor for the low wear degradation. However, the higher the degradation (i.e. the deeper the wear depth), the better is the correlation. To formalize this aspect, $\Delta h_{max}\%$ ratio is considered (Equation 3.14):

$$\Delta h_{max}\% = \frac{h_{max} - h_{max, FEM}}{h_{max, FEM}} \quad (3.14)$$

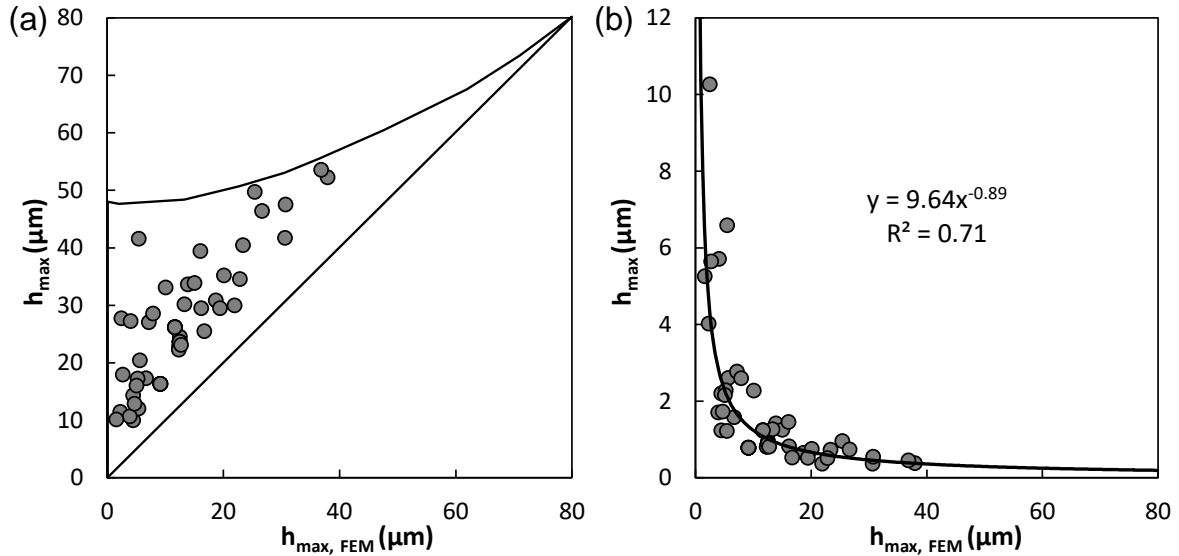


Figure 3.38: (a) Evolution of h_{max} versus $h_{max, FEM}$ by taking into account all the loading conditions; (b) evolution of $\Delta h_{max}\%$ versus $h_{max, FEM}$ by compiling all the test conditions.

Figure 3.38b shows that $\Delta h_{max}\%$ decreases with the increase of the wear depth. This analysis suggests that the given friction energy wear approach is acceptable to predict the wear depth for the high wear degradation conditions where abrasive wear and the progressive elimination of adhesive transfers induce a homogeneous flat wear profile. On the other hand, this analysis must be improved to consider the transfer phenomenon to predict lower wear depth where adhesive wear is significant resulting in a nonhomogeneous W-shaped wear profile. Additionally, more precise estimation of wear depth can be fulfilled by considering also the inherent evolution in the rheology of the TB with wear mechanisms which is a significant challenge for future studies.

3.6 Conclusion

This chapter aims at investigating the wear rate evolution of a steel alloy (34NiCrMo16) in a dry flat-on-flat contact configuration by varying several parameters including test duration, contact pressure, sliding amplitude, frequency, contact size and contact orientation with respect to sliding direction. Results of this parametric study manifested that wear rate highly depends on the aforesaid loading conditions. Hence, a wear volume prediction model was established using a single energy wear rate. By combining the impact of all loading parameters, a weighted energy wear formulation is introduced. Using this very basic power law approach, a reliable prediction of wear volume is obtained. The model was validated using experiments outside the model calibration domain. Hence, various contact sizes and loading conditions were remarkably predicted.

Another interesting finding of this work is that under all the studied loading conditions, a mixed regime of abrasion and adhesion is prevalent in the interface. The model, which demonstrates its suitability to predict the wear volume extension, was implemented in numerical simulations to provide the maximum wear depth. A large dispersion was observed which suggests that future developments need to consider adhesive transfer mechanisms by using a composite wear model with wear rate dependent on the wear mechanisms (abrasion and adhesion) and TB rheology than the current global approach involving constant wear rate along the interface.

To interpret such complex transition and the related wear rate evolution, both the contact oxygenation concept (COC) and third body approach (TBA) were discussed. Finally, by introducing a relative wear rate description considering both $\alpha_{L_{\parallel\delta}}$ and $\alpha_{L_{\perp\delta}}$ wear rate coefficients, it was possible to formalize and decouple the relative effect of COC and TBA regarding the contact size wear-rate fluctuations. Although TBA appears the dominating factor at least for the studied conditions, it appears that COC plays a significant effect. The next step of this research work will focus on this approach to better formalize and simulate COC phenomenon.

Chapter 4

Experimental investigation of adhesive wear extension in fretting interface

Contents

4.1	Introduction	100
4.2	Experimental procedure	101
4.2.1	Surface observation of abrasion and adhesion zones	102
4.2.2	Experimental estimation of oxygen distance “ d_O ” parameter from fretting scar expertise	104
4.3	Experimental results	106
4.3.1	Plain crossed flat-on-flat contact configuration	106
4.3.2	Textured crossed flat-on-flat contact	115
4.4	Discussion	120
4.4.1	Frequency effect	120
4.4.2	Contact pressure effect	120
4.4.3	Test duration effect	122
4.4.4	Sliding amplitude effect	122
4.4.5	Contact size and sliding orientation	123
4.4.6	Summary	124
4.5	Conclusion	124

4.1 Introduction

This chapter investigates the transition from abrasive to adhesive wear in gross-slip fretting assuming contact oxygenation concept (COC) which describes the evolution of the interfacial di-oxygen partial pressure “ P_{O_2} ” within fretting contacts and the associated partition of abrasion and adhesion zones under different loading parameters (Figure 4.1). Indeed, surface oxidation generated by fretting triggers the consumption of the diffusing dioxygen molecules from the outer environment and consequently the reduction of P_{O_2} towards the center of the interface. However, if the di-oxygen partial pressure exceeds a threshold value “ $P_{O_2, th}$ ” over the entire contact area, full contact oxygenation marked by abrasive-oxidational wear prevails. Alternatively, an abrasive-adhesive wear manifests itself in case of partial contact oxygenation such that adhesion and metal transfer are detected in the locations where the oxygen supply is below $P_{O_2, th}$ (Figure 4.1). Following this premise, “oxygen distance d_O ” parameter can be introduced as the distance from the interface boundaries to the frontiers of adhesion zone after which oxygen supply becomes very limited (Figure 4.1).

Assuming “ r ” the radial position from the center of a 3D contact and “ a ” the corresponding contact radius, the transition from a pure abrasive to a composite abrasive-adhesive wear may be expressed considering the following simple relationship:

$$\text{pure abrasive wear if whatever } r < a, P_{O_2}[r] > P_{O_2, th} \quad (4.1)$$

composite adhesive–abrasive wear :

$$\text{if } r > a - d_O, P_{O_2}[r] > P_{O_2, th} \Rightarrow \text{external abrasion zone} \quad (4.2)$$

$$\text{if } r < a - d_O, P_{O_2}[r] < P_{O_2, th} \Rightarrow \text{inner adhesion zone}$$

To experimentally demonstrate such “contact oxygenation” concept, the given research work investigates the evolution of “ d_O ” (i.e. the lateral width of abrasive zone) as a function of various contact loadings, contact size but also macro-textured surfaces. This is currently achieved thanks to a multi-scale experimental strategy applied on a flat-on-flat contact configuration where oxygen distance evolution can be easily tracked as detailed in Figure 4.1. The crossed flat configuration implies an (X,Y) description so that the former axisymmetric description is turned to a conjugate 2D approach:

$$\text{pure abrasive wear if whatever } X < L_{\parallel\delta}/2 \text{ and } Y < L_{\perp\delta}/2, P_{O_2} > P_{O_2, th} \quad (4.3)$$

composite adhesive–abrasive wear :

$$\text{if } X > L_{\parallel\delta}/2 - d_O \text{ or } Y > L_{\perp\delta}/2 - d_O, P_{O_2}[r] > P_{O_{2,th}} \Rightarrow \text{external abrasive wear} \quad (4.4)$$

Where $L_{\parallel\delta}$ and $L_{\perp\delta}$ are the longitudinal and transverse widths of the studied crossed flat contact interface.

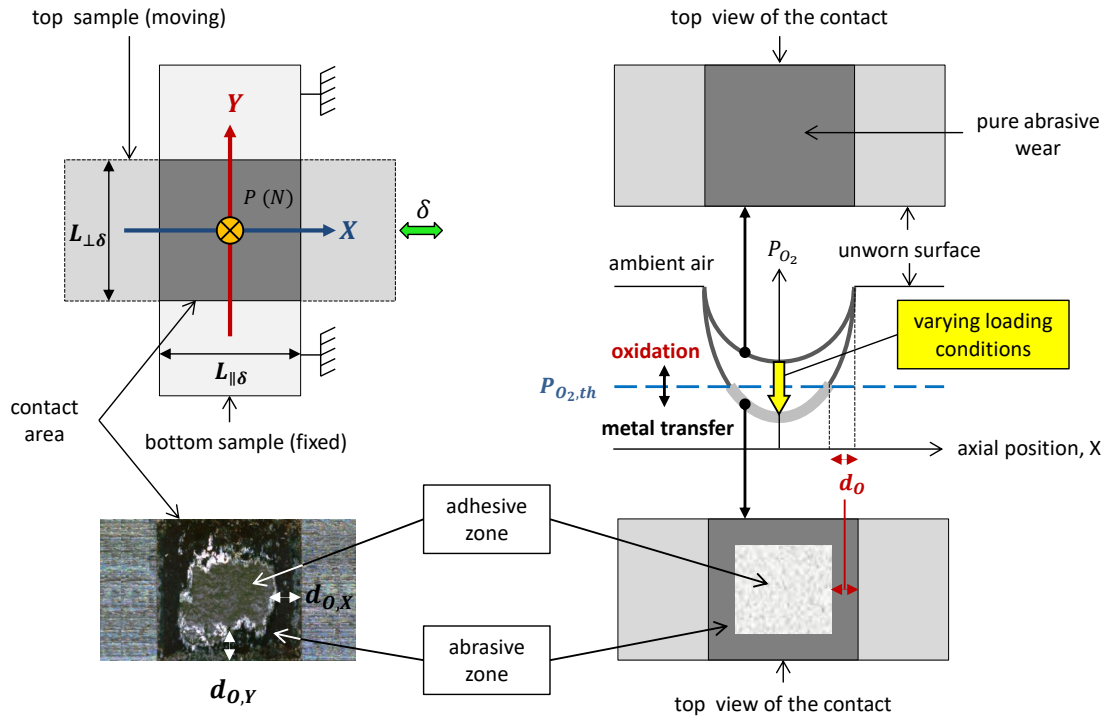


Figure 4.1: Schematic presentation of the transition of wear regimes from pure abrasive wear at high oxygen partial pressure ($P_{O_2} > P_{O_{2,th}}$) to a mixed abrasive-adhesive wear regime at low oxygen partial pressure ($P_{O_2} < P_{O_{2,th}}$), After [56].

4.2 Experimental procedure

The objective behind this part is to evaluate the effect of loading conditions on “ d_O ” parameter. Hence, a multi-scale experimental strategy (detailed in Chapter 2, Section 2.6) is applied whereby six loading parameters are varied starting from a key reference test namely the number of fretting cycles, contact pressure, sliding amplitude, sliding frequency, contact area and contact orientation with respect to sliding direction. Note that the minimum distance from the center of the contact to its borders is given by:

$$d = \text{minimum of } \left(\frac{L_{\parallel\delta}}{2}, \frac{L_{\perp\delta}}{2} \right) \quad (4.5)$$

4.2.1 Surface observation of abrasion and adhesion zones

Top view observations (BSE, EDX) of a mixed abrasive-adhesive wear regime (Figure 4.2) show a composite wear scar characterized by a central bright zone and an oxidized corona. Line EDX scans display very low oxide content in the central part compared to the borders. A marked difference in the third body morphology is detected inside and outside adhesive zone. In the central part of the contact where adhesion occurs, the poorly oxidized third body exhibits a bright round to angular shaped metallic protrusions whereas more homogeneous compacted oxide debris is detected in the abrasive zone. This observation is confirmed by cross section view. Thin oxide debris layers having $20\ \mu\text{m}$ thickness were observed on the lateral abrasive wear domain whereas partially transformed TTS structure with a thickness reaching $150\ \mu\text{m}$ was detected in the central adhesive wear zone. The inner TTS structure is characterized by micro-cracks (Figure 4.2 & 4.3) and a very poor oxygen content equivalent to the bulk as reflected by EDX and BSE analyses. Similar observations were detected by various authors for high strength steels [49, 51] and for titanium alloys [55, 56].

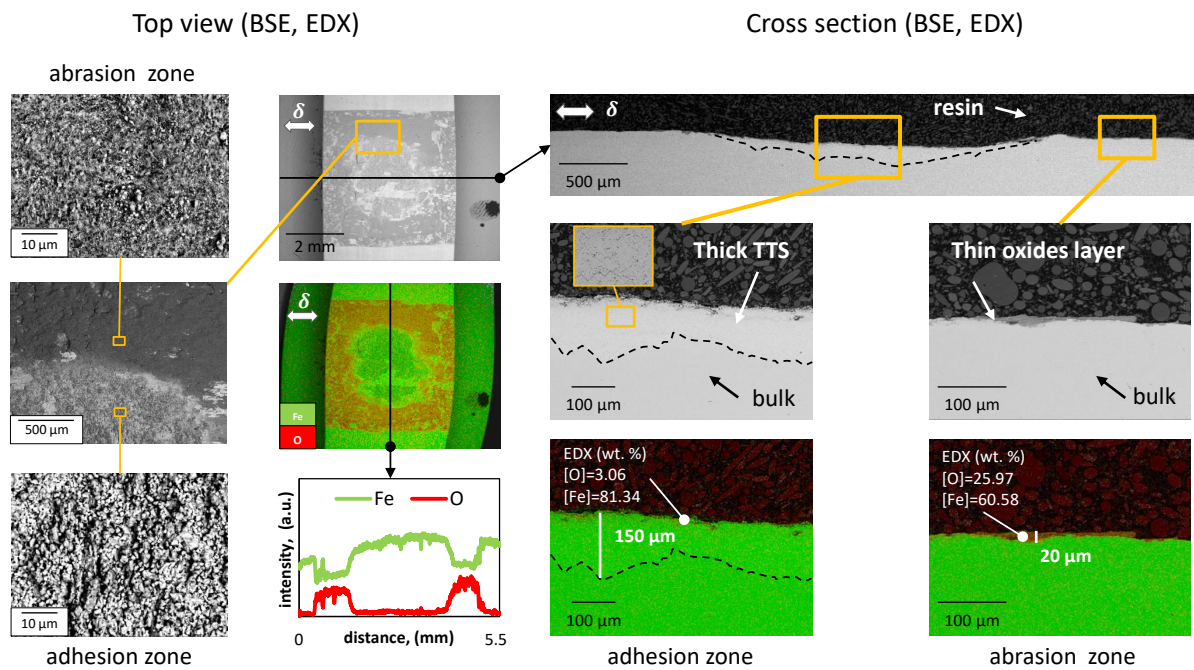


Figure 4.2: BSE and EDX observations of the top and cross section views of mixed abrasive-adhesive wear scar detected at the bottom sample ($N=20000$ cycles, $p=100$ MPa, $\delta_g = \pm 100\ \mu\text{m}$, $f=5$ Hz and $A=25\ \text{mm}^2$).

A closer observation of the TTS (Figure 4.3) reveals a clear limit between the latter and the bulk where TTS exhibits severe plastic deformations. However, what seems very interesting is that most of the cracks undergo zigzag propagation and have 45° orientation with respect to the horizontal plane. Several authors tried to explain this zigzag pattern in double slip systems including Neumann [146] and Proudhon et al. [147] based on short crack propagations dynamics.

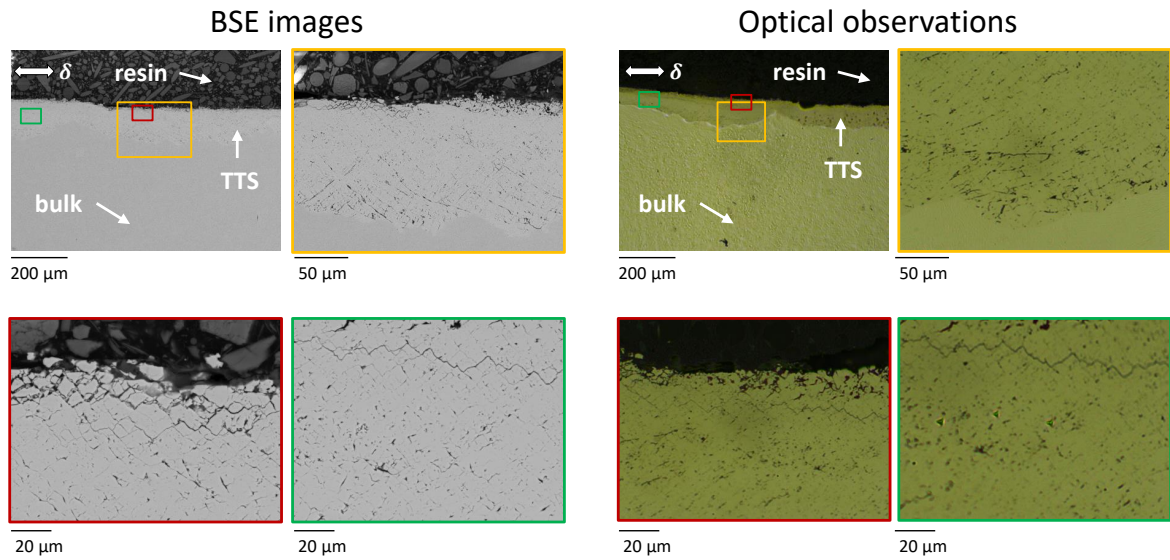


Figure 4.3: BSE and optical observations of the TTS structure ($N=20000$ cycles, $p=100$ MPa, $\delta_g = \pm 100$ μm , $f=5$ Hz and $A=25$ mm^2).

Additionally, force-controlled constant strain rate loading nano-indentation is performed by passing from the superficial tribologically transformed surface towards the bulk. This permits tracing hardness and Young's modulus profiles by averaging each time three measurements at the same depth with respect to the surface. Figure 4.4a & b reveal that TTS (964 ± 109 Hv) is two to three times harder than the base material (400 ± 25 Hv) which comes in agreement with previous studies conducted by Sauger et al. [49, 54], Tumbajoy-Spinel et al. [148, 149] and Shockley et al. [150] for different materials and contact conditions. However, TTS Young's modulus (Figure 4.4c) is lower than that of the bulk which can be explained by the presence of cracks and severe plastic deformations in the TTS compared to the uncracked bulk [151].

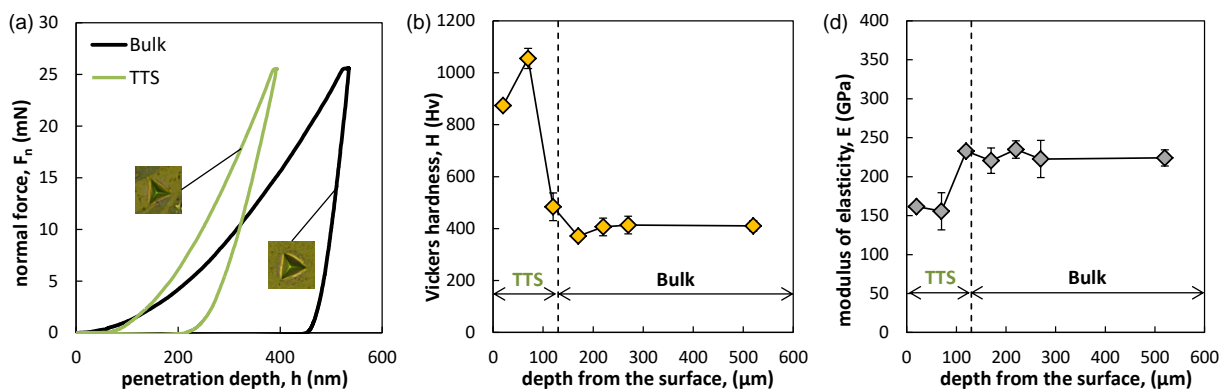


Figure 4.4: (a) Comparison of the nano-indentation force-displacement curve of the TTS and the bulk; (b) Evolution of the nano-scale Vickers hardness profile by passing from the superficial tribologically transformed surface towards the bulk; (c) Evolution of the modulus of elasticity profile by passing from the superficial tribologically transformed surface towards the bulk ($N=20000$ cycles, $p=100$ MPa, $\delta_g = \pm 100$ μm , $f=5$ Hz and $A=25$ mm^2). Force-controlled constant strain rate loading nano-indentation with acquisition rate=10 Hz, maximum normal load=25 mN, loading rate/load=0.10 s^{-1} , and pause=10 s).

4.2.2 Experimental estimation of oxygen distance “ d_O ” parameter from fretting scar expertise

A direct estimation of oxygen distance “ d_O ” parameter is not possible. This requires a local in situ analysis of the air composition which is currently technically unfeasible. However, it could be indirectly approximated by measuring the distance between the boundary marking the transition from abrasive to adhesive wear, and the contact borders (Figure 4.2). On the other hand, by the measuring the width of the abrasive corona d_{ab} we can indirectly estimate the oxygen distance d_O assuming that:

$$d_O \approx d_{ab} \quad (4.6)$$

The abrasive corona also corresponds to the high EDX oxygen concentration which indirectly supports the correlation between d_{ab} and d_O . To determine the representative “ d_O ” value, postmortem EDX oxygen profiles along the longitudinal sliding axis (X) and the transversal axis (Y) were performed (Figure 4.5). Using these two crossed oxygen profiles, the following parameters are estimated:

$$d_{O,X} = \frac{1}{2} \cdot (d_{O,X_1} + d_{O,X_2}) \quad (4.7)$$

$$d_{O,Y} = \frac{1}{2} \cdot (d_{O,Y_1} + d_{O,Y_2}) \quad (4.8)$$

$$d_O = \frac{1}{2} \cdot (d_{O,X} + d_{O,Y}) \quad (4.9)$$

Using the same concept, the adhesion area A_{ad} can be estimated from the regions where the oxygen intensity is relatively low:

$$A_{ad} = d_{ad,X} \cdot d_{ad,Y} \quad (4.10)$$

The abrasion area A_{ab} is deduced from the measured adhesion area A_{ad} so that:

$$A_{ab} = A - A_{ad} \quad (4.11)$$

The relative proportions of abrasion and adhesion areas are expressed by:

$$\%A_{ab} = \frac{A_{ab}}{A} \text{ and } \%A_{ad} = \frac{A_{ad}}{A} \quad (4.12)$$

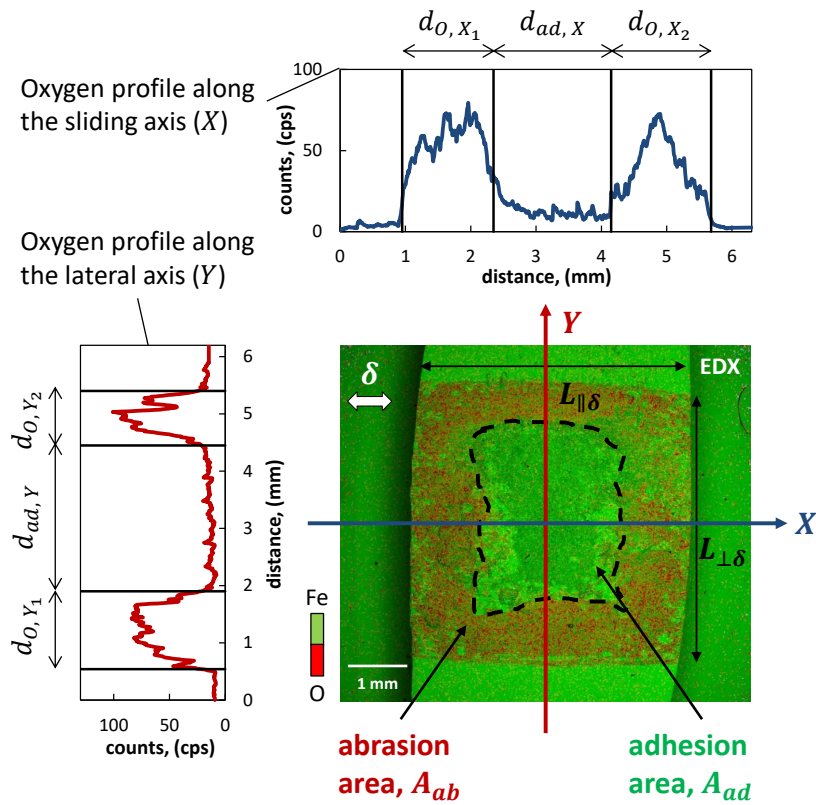


Figure 4.5: Computation of the oxygen distance “ d_O ” and the adhesion and abrasion areas by using crossed EDX oxygen line scans method.

Figure 4.6 plots the evolution of $d_{O,Y}$ as a function of the corresponding $d_{O,X}$ values. The results are quite dispersed which can be explained by the inherent experimental dispersions (small misalignments, dissymmetry of the tangential apparatus compliance, etc. . . .). To check the symmetry between the oxygen distances $d_{O,Y}$ and $d_{O,X}$ along the longitudinal sliding axis (X) and the transversal axis (Y) respectively, a median line ($y=x$) is traced. It is interesting to note that the data are symmetrically dispersed along the median curve. This suggests that the extension of the abrasive zone (i.e. well oxygenated interface so that $P_{O_2} > P_{O_{2,th}}$) is isotropic and non-dependent of the sliding direction and the related debris flow. Assuming such isotropic behavior, d_O which corresponds to the average value of four measurements (Equations 4.7-4.9) along X and Y directions, provides a representative value of the abrasive area extension.

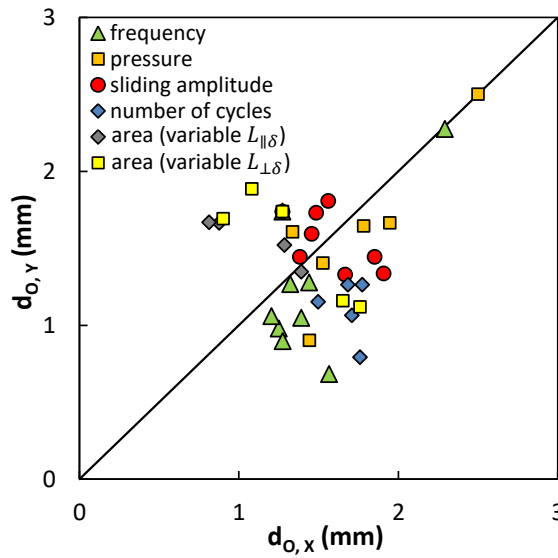


Figure 4.6: Variation of $d_{O,Y}$ versus $d_{O,X}$ by compiling all the loading conditions.

4.3 Experimental results

This section compiles the different results obtained from plain crossed flat-on-flat contact configuration then from the response of macro-textured samples which permit decreasing the mean distance from the inner part of the contact to the external open air allowing an easier investigation of the contact oxygen access.

4.3.1 Plain crossed flat-on-flat contact configuration

The following section assesses the influence of the studied parameters on the relative extension of abrasion and adhesion areas and the related evolution of oxygen distance d_O .

4.3.1.1 Effect of the frequency

Figure 4.7 compares wear scars using optical images and EDX maps and line scans for a frequency ranging from 0.5 to 10 Hz. It appears that inner adhesion area which is negligible at 0.5 Hz extends progressively with the frequency until it becomes significant at 10 Hz. It is interesting to note that at 10 Hz, this latter displays a well-defined square shape confirming the former hypothesis assuming that the oxygen distance d_O is equal in all directions.

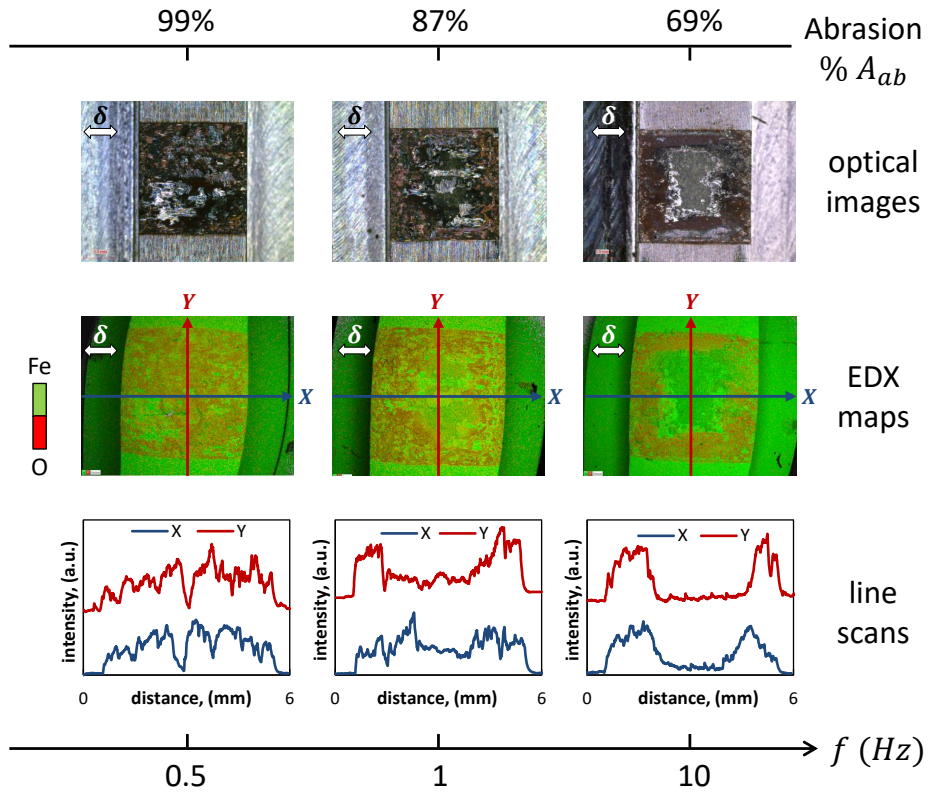


Figure 4.7: Optical images and EDX observations showing the recession of abrasive wear with the increase in frequency from 0.5 to 10 Hz ($N=20000$ cycles, $p=100$ MPa, $\delta_g = \pm 100 \mu m$, and $A=5 \times 5=25 \text{ mm}^2$).

Figure 4.8a plots the evolution of the relative proportion of abrasive wear as a function of the sliding frequency. An asymptotic decreasing evolution from nearly 100% at 0 Hz until a stabilized value around 69% for the highest frequency values is observed such that $\%A_{ab} = 0.88 \times f^{-0.12}$. Figure 4.8b displays the evolution of the corresponding d_O value defined from Equation 4.9. Considering the reference test condition ($f_{ref}=1$ Hz), the evolution d_O versus frequency may be expressed using a decreasing power law function so that:

$$d_O = K_f \times d_{O,ref} \times \left(\frac{f}{f_{ref}} \right)^{n_f} \quad (4.13)$$

With $d_{O,ref} = 1.51$ mm, the oxygen distance related to the reference test condition ($N=20000$ cycles, $p=100$ MPa, $\delta_g = \pm 100 \mu m$, $f=1$ Hz and $A=5 \times 5=25 \text{ mm}^2$), $n_f = -0.22$ the exponent marking the decreasing evolution of oxygen distance with frequency and $K_f=1.12$, which is an experimental constant defined by the best fitting of the global evolution of d_O from the chosen reference.

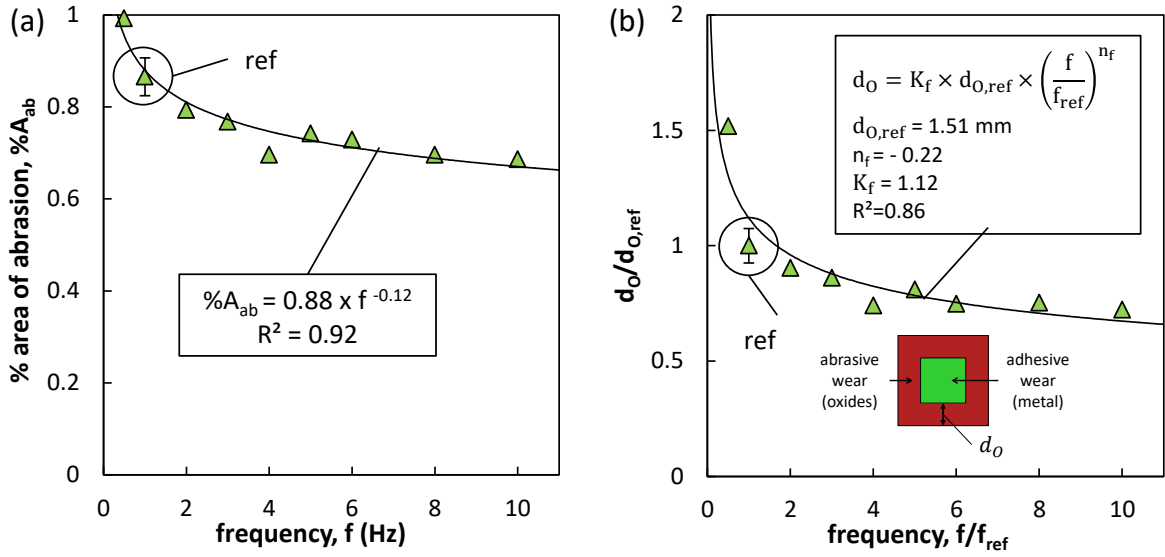


Figure 4.8: Evolution of the (a) percentage of abrasive wear area “ $\%A_{ab}$ ” and (b) the oxygen distance “ d_O ” as a function of the frequency ($N=20000$ cycles, $p=100$ MPa, $\delta_g = \pm 100$ μm , and $A=5 \times 5=25$ mm^2 with $f_{ref} = 1$ Hz and $d_{O,ref} = 1.51$ mm).

4.3.1.2 Effect of the contact pressure

The contact pressure is increased from 25 MPa to 175 MPa to detect its role on fretting wear regimes. Optical observations and EDX maps and line scans (Figure 4.9a) reveal a transition from nearly pure abrasive wear at low pressure ($p=25$ MPa) to a mixed abrasive-adhesive wear response at high pressure ($p=175$ MPa).

This is reflected in Figure 4.10a & b where the abrasion zone shrinks with the increase in contact pressure resulting in reduction of oxygen distance by 53% when the contact pressure is increased by 150 MPa such that $\%A_{ab} = 1.55 \times p^{-0.13}$.

Again the evolution of the oxygen distance parameter can be formalized using a simple power law function normalized as a function of the reference test condition so that:

$$d_O = K_p \times d_{O,ref} \times \left(\frac{p}{p_{ref}}\right)^{n_p} \quad (4.14)$$

With $n_p = -0.32$ the exponent marking the decreasing evolution of oxygen distance with the contact pressure and $K_p = 1.02$ the experimental correcting factor related to the best fitting of the global evolution of experimental data.

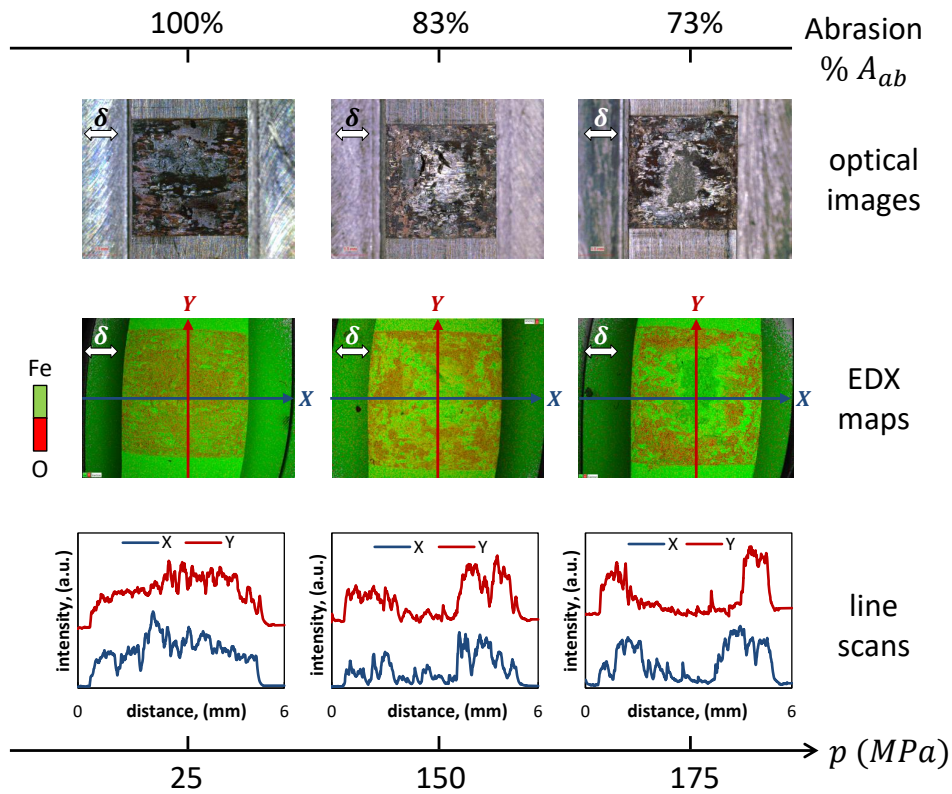


Figure 4.9: Optical images and EDX observations showing the extension of the inner adhesive zone with the increase in contact pressure from 25 to 175 MPa ($N=20000$ cycles, $\delta_g = \pm 100 \mu m$, $f=1$ Hz, and $A=5 \times 5=25 \text{ mm}^2$).

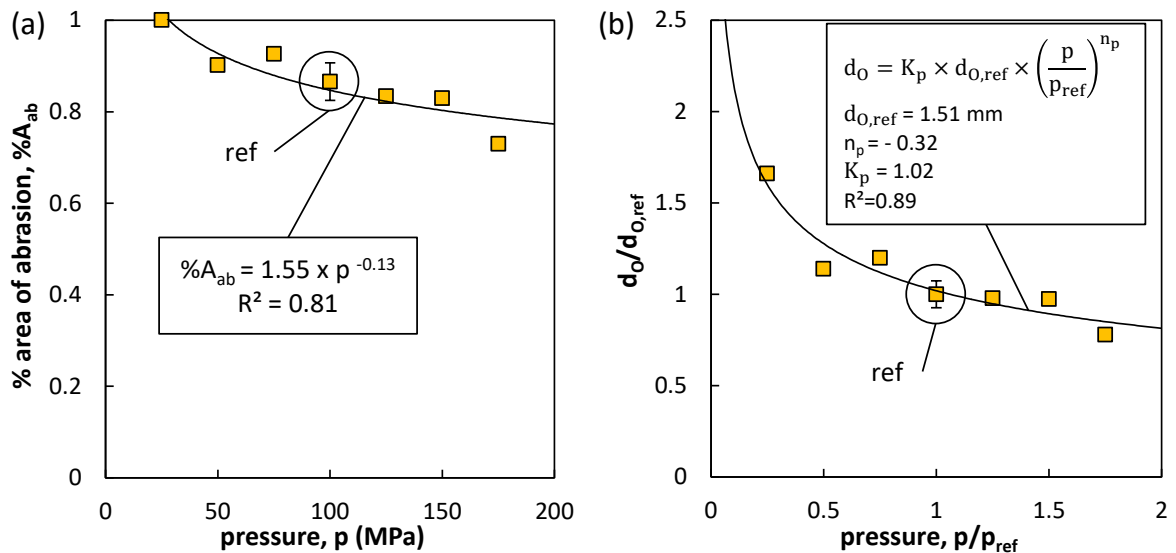


Figure 4.10: Evolution of the (a) percentage of abrasive wear area “ $\%A_{ab}$ ” and (b) the oxygen distance “ d_O ” as a function of the mean contact pressure ($N=20000$ cycles, $\delta_g = \pm 100 \mu m$, $f=1$ Hz, and $A=5 \times 5=25 \text{ mm}^2$ with $p_{ref} = 100 \text{ MPa}$ and $d_{O,ref}=1.51 \text{ mm}$).

4.3.1.3 Effect of the loading cycles

Figure 4.11 assesses the effect of the number of cycles by comparing wear scars using optical images and EDX maps and line scans at different test durations. No significant differences are observed.

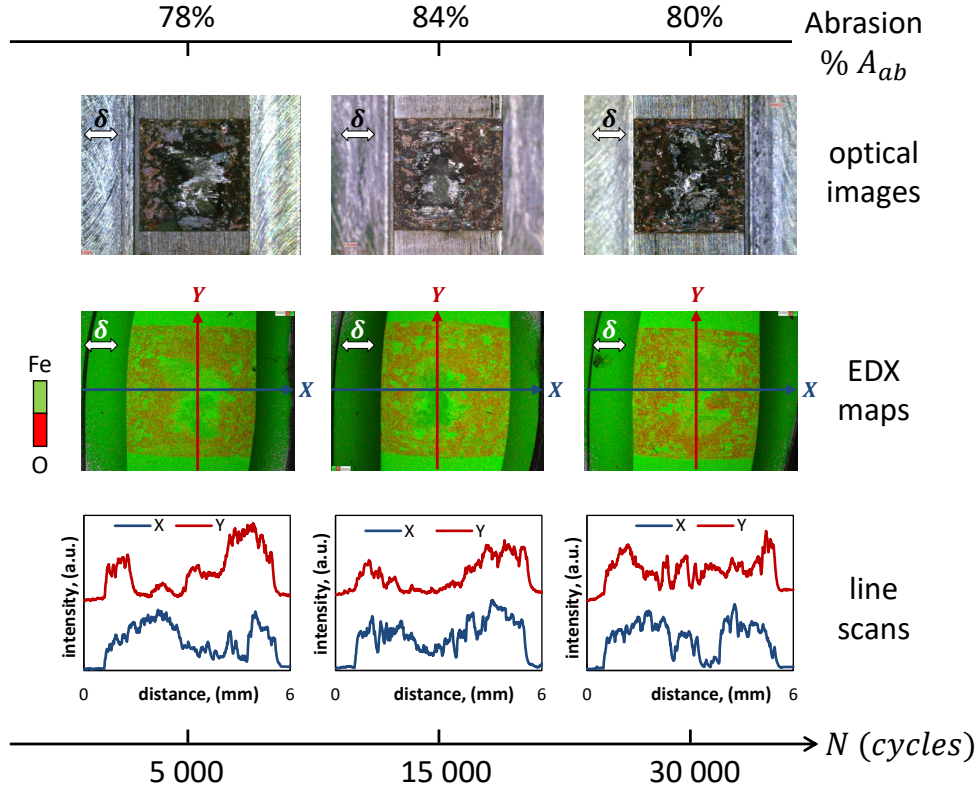


Figure 4.11: Optical images and EDX observations showing the evolution of abrasive wear with the increase in number of cycles from 5000 to 30000 cycles ($p=100$ MPa, $\delta_g = \pm 100$ μm , $f=1$ Hz, and $A=5 \times 5=25$ mm^2).

This is clarified in Figure 4.12a where the percentage of abrasive wear area remains constant ($\%A_{ab} = 0.83 \pm 0.03$) resulting in a constant d_O value (Figure 4.12b) so that:

$$d_O = K_N \times d_{O,ref} \approx 1.42 \text{ mm} \quad (4.15)$$

With $K_N = 0.94$ is a correcting factor of the mean value compared to the reference test condition ($d_{O,ref} = 1.51$ mm).

This suggests that the stabilized response of the interface is reached before 5000 cycles and the partition between adhesive and abrasive wear remains constant, independent of the test duration at least for the studied contact area conditions.

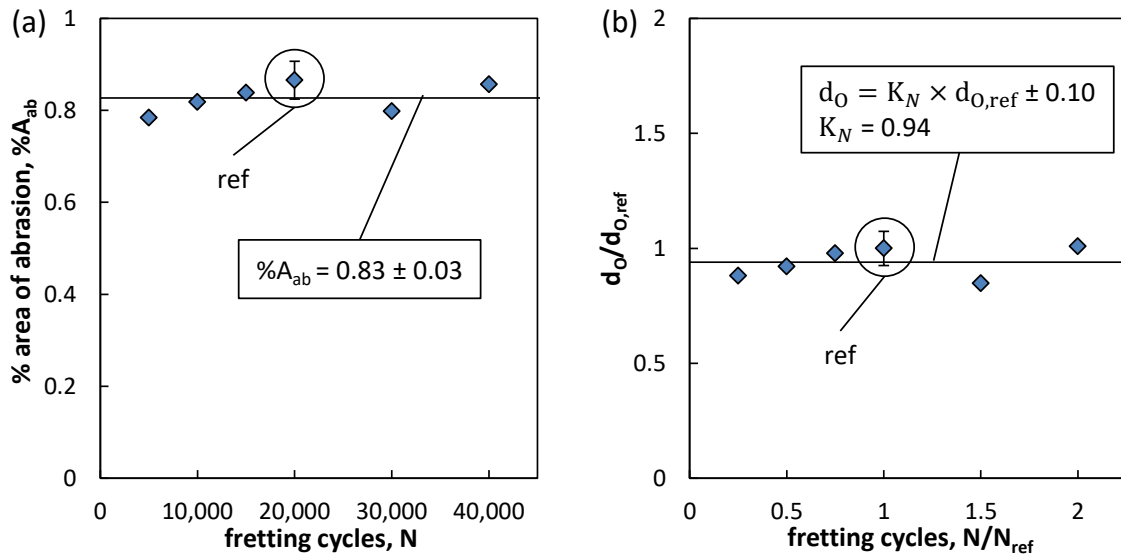


Figure 4.12: Evolution of the (a) percentage of abrasive wear area “ $\%A_{ab}$ ” and (b) the oxygen distance “ d_O ” as a function of fretting cycles ($p=100$ MPa, $\delta_g = \pm 100$ μm , $f=1$ Hz, and $A=5 \times 5=25$ mm^2 with $N_{ref} = 20000$ cycles and $d_{O,ref}=1.51$ mm).

4.3.1.4 Effect of the sliding amplitude

The effect of the sliding amplitude on abrasion and adhesion is investigated by comparing optical observations and EDX maps and line scans at different sliding amplitudes (Figure 4.13). No substantial differences are observed. Similar mixed abrasive-adhesive wear partitions are noticed suggesting that the sliding amplitude plays a minor role regarding the dioxygen diffusion processes within the interface.

This is quantified in Figure 4.14a where the percentage of abrasive wear remains constant ($\%A_{ab} = 0.87 \pm 0.03$) suggesting that the sliding amplitude plays a minor role regarding the dioxygen diffusion processes within the interface.

This is also reflected in Figure 4.14b where the oxygen distance stabilizes at $d_O=1.57$ mm whatever the applied sliding amplitude which implies:

$$d_O = K_\delta \times d_{O,ref} \approx 1.57 \text{ mm} \quad (4.16)$$

With $K_\delta=1.04$ being an experimental correcting factor of the mean value related to the sliding amplitude analysis.

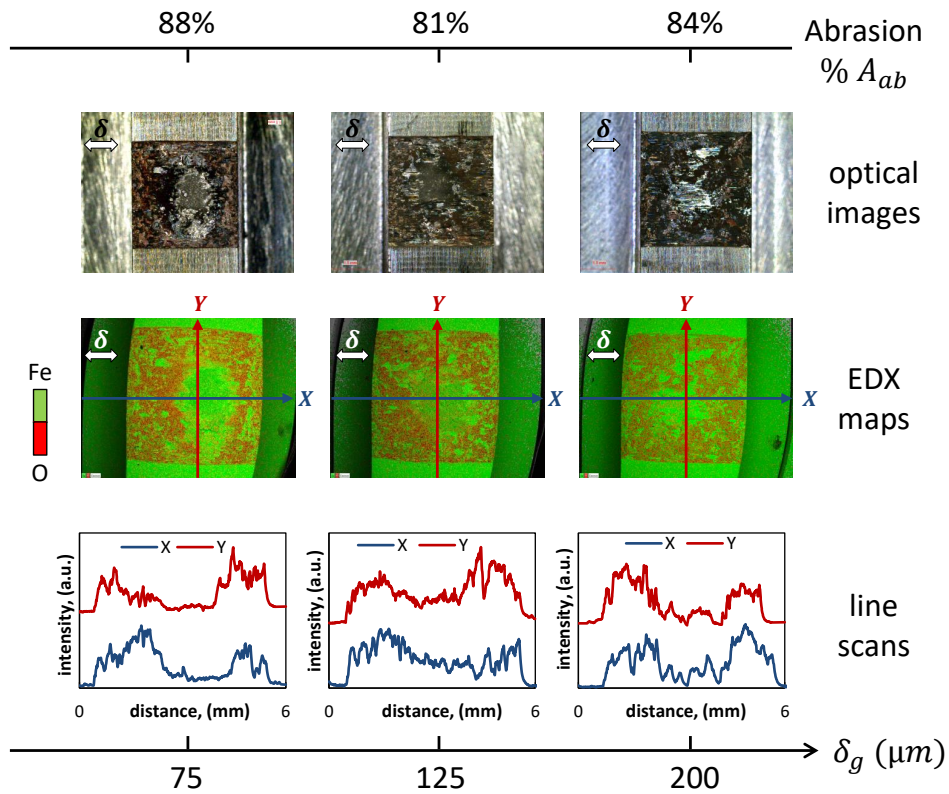


Figure 4.13: Optical images and EDX observations showing the evolution of abrasive wear with the increase in sliding amplitude from ± 75 to $\pm 200 \mu\text{m}$ ($N=20000$ cycles, $p=100$ MPa, $f=1$ Hz, and $A=5 \times 5=25 \text{ mm}^2$).

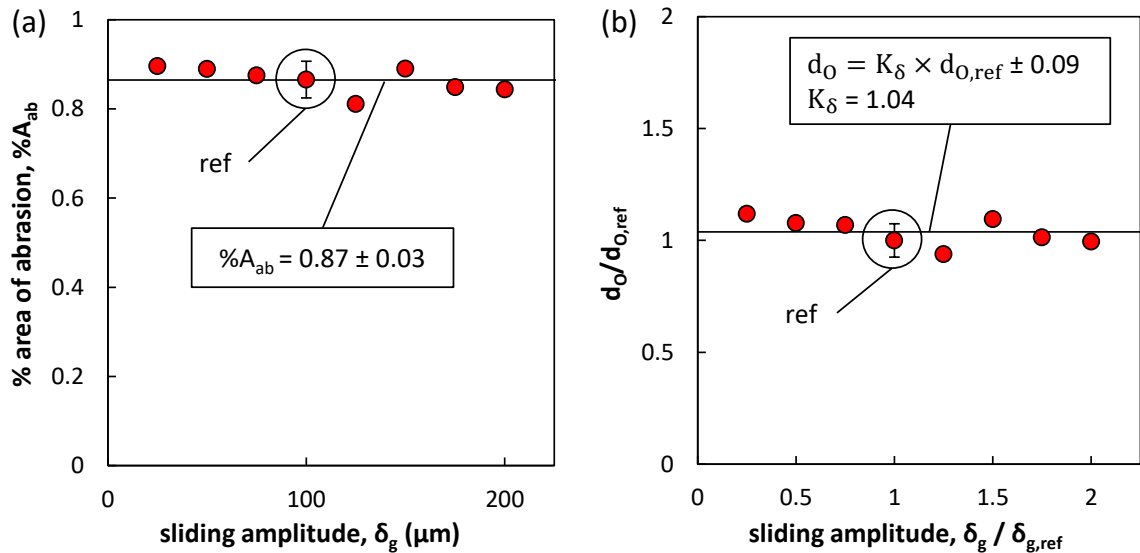


Figure 4.14: Evolution of the (a) percentage of abrasive wear area “ $\%A_{ab}$ ” and (b) the oxygen distance “ d_o ” as a function of the sliding amplitude ($N=20000$ cycles, $p=100$ MPa, $f=1$ Hz, and $A=5 \times 5=25 \text{ mm}^2$ with $\delta_{g,ref} = \pm 100 \mu\text{m}$ and $d_{O,ref}=1.51 \text{ mm}$).

4.3.1.5 Effect of the contact area and the contact orientation

In this section, the evolution of the oxygen distance is investigated as a function of both the contact area and the contact orientation. The contact area is decreased from 25 to 10 mm^2 by reducing firstly the length “ $L_{\parallel\delta}$ ” along the sliding direction from 5 to 2 mm while maintaining constant “ $L_{\perp\delta}=5$ mm”, then by reducing the length “ $L_{\perp\delta}$ ” against the sliding direction from 5 to 2 mm while maintaining constant “ $L_{\parallel\delta}=5$ mm”.

Decreasing the contact area either by reducing $L_{\perp\delta}$ (Figure 4.15a) or $L_{\parallel\delta}$ (Figure 4.15b) promotes a remarkable regression in the adhesive wear area until it completely vanishes when the contact area is less than or equal to 12.5 mm^2 . This is confirmed by comparing optical images and EDX lines scans and maps for both orientations.

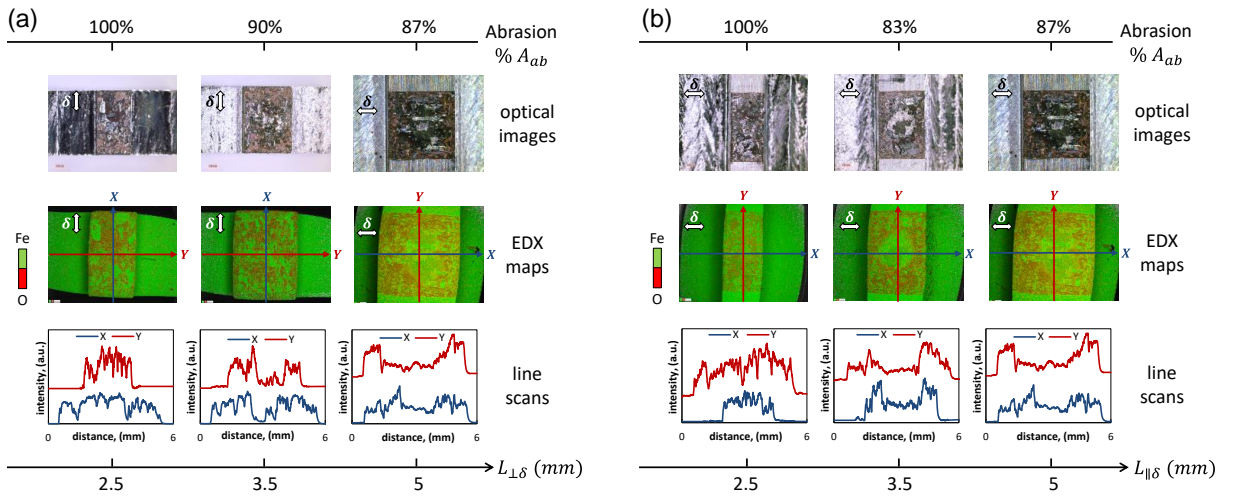


Figure 4.15: Optical images and EDX observations showing the recession of adhesive wear with the decrease of the contact area from 25 to 12.5 mm^2 ($N=20000$ cycles, $p=100$ MPa, $\delta_g = \pm 100$ μm , and $f=1$ Hz): (a) variable $L_{\perp\delta}$ and (b) variable $L_{\parallel\delta}$.

Such transition in wear regimes from a mixed abrasive-adhesive to a pure abrasive wear is confirmed in Figure 4.16a where the percentage of abrasion area increases from 87% at 25 μm to 100% for contact areas less than or equal to 12.5 μm . Another significant remark is that no substantial difference is detected by varying the contact orientation with respect to the sliding direction for the same contact area. On the other hand, if the adhesive wear area decreases with the contact size, the oxygen distance remains constant and stabilizes around $d_O = 1.37$ mm (Figure 4.16b) so that:

$$d_O = K_A \times d_{O,ref} \approx 1.37 \text{ mm} \quad (4.17)$$

Where $K_A=0.91$ is an experimental correcting factor of the mean value compared to the reference test condition.

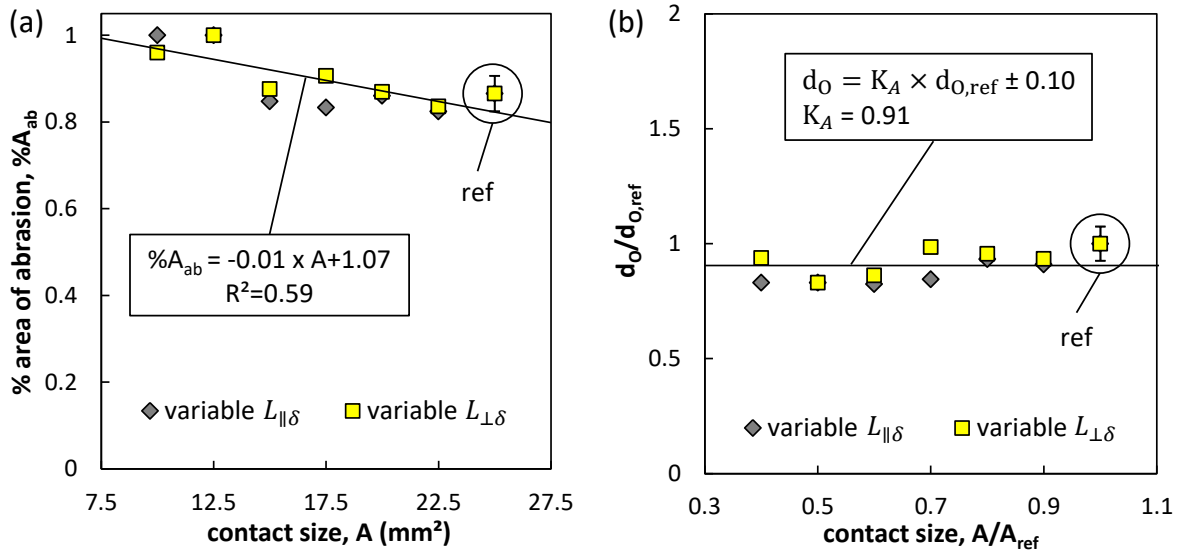


Figure 4.16: Evolution of the (a) percentage of abrasive wear area “%A_{ab}” and (b) the oxygen distance “d_O” as a function of the contact size by varying either the longitudinal length (L_{∥δ}) or the transverse width (L_{⊥δ}) (N=20000 cycles, p=100 MPa, δ_g = ±100 μm, and f=1 Hz with A_{ref}=5×5=25 mm² and d_{O,ref}=1.51 mm).

4.3.1.6 A parametric “oxygen distance” modeling

The objective of the following part is to formalize the oxygen distance evolution as a function of the fretting parameters. The given experimental results suggest that the fretting cycles, contact area and sliding amplitude have a weak impact on oxygen distance d_O at least for the studied interfaces. On the other hand, oxygen distance appeared to be significantly affected by the contact pressure and frequency. By combining Equations 4.13, 4.14, 4.15, 4.16 & 4.17, the oxygen distance “ d_O ” can be estimated using a very simple power law function:

$$d_{O,pred} = d_O = d_{O,ref} \times (K_N \times K_\delta \times K_A \times K_f \times K_p) \times \left(\frac{f}{f_{ref}}\right)^{n_f} \left(\frac{p}{p_{ref}}\right)^{n_p} \quad (4.18)$$

$$\frac{d_{O,pred}}{d_{O,ref}} = K_N \times K_\delta \times K_A \times K_f \times K_p \times \left(\frac{f}{f_{ref}}\right)^{n_f} \left(\frac{p}{p_{ref}}\right)^{n_p}$$

The correlation between the “K” coefficients leads to:

$$K_N \times K_\delta \times K_A \times K_f \times K_p \approx 1.0 \quad (4.19)$$

Hence, the predicted oxygen distance can be expressed using the simplified relationship:

$$d_{O,pred} = d_O = d_{O,ref} \times \left(\frac{f}{f_{ref}} \right)^{n_f} \left(\frac{p}{p_{ref}} \right)^{n_p} \quad (4.20)$$

with $d_{O,ref}=1.51$ mm, $n_f=-0.22$, $n_p=-0.32$, $p_{ref}=100$ MPa, and $f_{ref}=1$ Hz for a given contact pressure (p) and sliding frequency (f).

Figure 4.17 compares the experimental and the predicted oxygen distance d_O derived from Equation 4.20. A good correlation is observed which suggests that the given formulation of d_O value is able to formalize not only the transition from pure abrasive wear to a composite abrasive-adhesive fretting wear response but also to express the partition between the abrasive and adhesive wear domains inside the fretting scar.

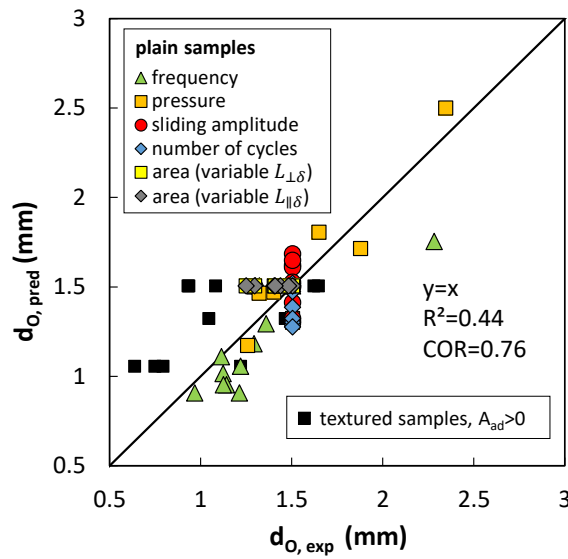


Figure 4.17: Comparison between the predicted and experimental oxygen distance using Equation 4.20 applied on plain and textured samples at different loading conditions and contact geometries.

4.3.2 Textured crossed flat-on-flat contact

The significance of predicting oxygen distance is that it permits not only detecting the nature of the wear regime (i.e. pure abrasive or mixed abrasive-adhesive wear), but also helps forecasting the transition between these regimes at different loading conditions. To check this aspect outside the calibration domain, textured bottom samples are tested. One interest of macro-textured surfaces is the possibility of investigating a broad range of “d” values (i.e. minimum distance from the contact center to the external air, (Equation 4.5)) while keeping constant the longitudinal length “ $L_{\parallel\delta}$ ”.

4.3.2.1 Experimental strategy

The texturing strategy is detailed in Chapter 2 Section 2.6 (Figure 4.18) and will be briefly reminded here. In the current case, the rectangular pads are systematically parallel to the

sliding direction (δ) where " $L_{\perp\delta}$ " ranges from 0.5 to 5 mm, the contact pressure (p), the sliding amplitude (δ_g) and the frequency (f) are varied while maintaining a constant number of cycles $N=20000$. Three mean contact pressures $p=50, 100$ and 150 MPa were investigated along with three different sliding amplitudes $\delta_g=\pm 50, \pm 100$ and ± 150 μm and three distinct frequencies $f=0.5, 1$ and 5 Hz. For each contact pressure value, the normal load (F_n) is adjusted to keep the desired contact pressure constant within textures' widths ($L_{\perp\delta}$). Note that for a given textured sample, oxygen distance is estimated separately for each rectangular pad, and then an average oxygen distance value is estimated for the whole sample. Oxygen distance is generally the same for all pads in the same textured sample; however very slight dispersion among pads might be detected for the same reasons discussed in Section 4.2.2 (i.e. small misalignments, dissymmetry of the tangential apparatus compliance, etc. ...).

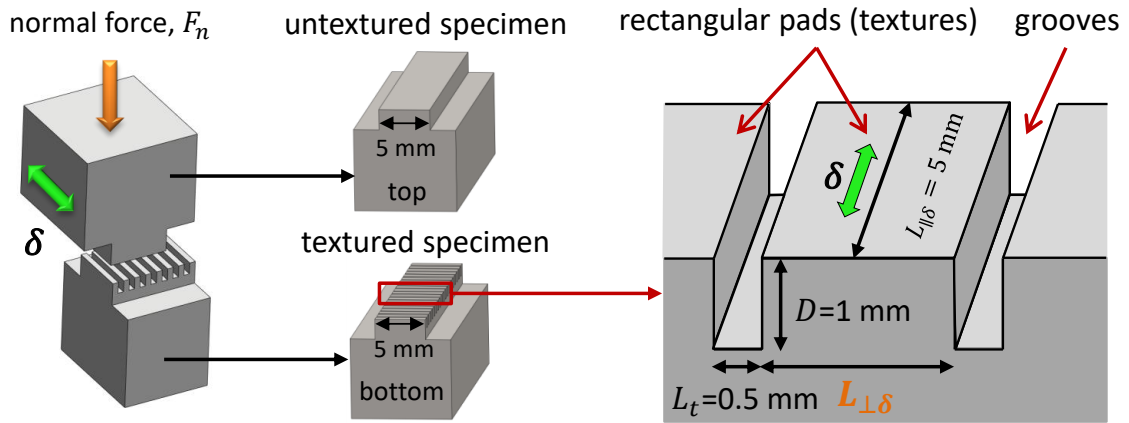


Figure 4.18: Crossed flat-on-flat configuration with textured bottom sample.

4.3.2.2 Qualitative validation of the model

-Influence of the contact size and the sliding amplitude:

Figure 4.19 shows the evolution of wear scars at different textures' width $L_{\perp\delta}$ ranging from 0.5 to 5 mm (i.e. different areas, A) applying the reference test conditions. According to Equation 4.20, the predicted oxygen distance marking the transition from pure abrasive to mixed abrasive-adhesive response is equal to $d_{O,pred}=d_{O,ref}=1.51$ mm. After this consideration, when $L_{\perp\delta} > 2 \cdot d_{O,pred}=3$ mm, a mixed regime is expected and below this value, we should observe pure abrasive wear. Careful observations of EDX maps reveal a mixed regime of abrasion and adhesion at $L_{\perp\delta}=5$ mm and a dominant abrasive wear for $L_{\perp\delta} \leq 3$ mm which indirectly confirms the theoretical d_O boundary. Note that like for mono-plain contact configuration, the sliding amplitude plays a minor role as a constant transition is observed (Figure 4.19a to c).

-Influence of the frequency and the contact pressure:

The capacity of predicting wear transitions of textured surfaces is also tested for variable contact pressure and frequency as displayed in Figure 4.20. By reducing the contact pressure, it is

expected to have transition of wear regimes at larger textures' width which is the case detected experimentally where the oxygen distance decreases by passing from $p=50$ to 150 MPa (Figure 4.20a & b). This transition is even clearer with the increase in frequency where a marked shift in the oxygen distance is noticed by comparing EDX maps at 0.5 and 5 Hz (Figure 4.20c & d).

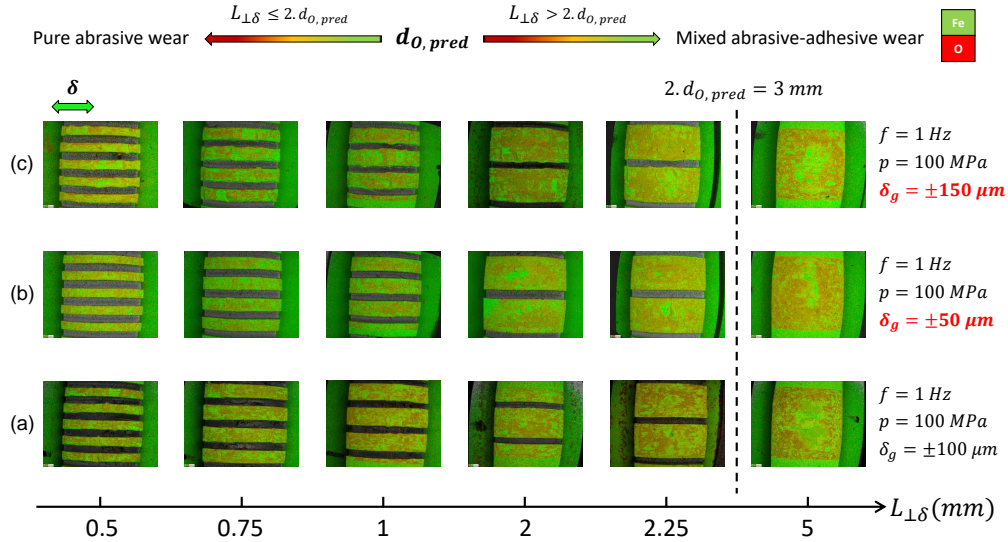


Figure 4.19: Prediction of the transition of wear regime by using the predicted threshold oxygen distance (Equation 4.20) for: (a) variable contact area under reference loading conditions; (b) variable contact area at low sliding amplitude, $\delta_g = \pm 50 \mu m$; and (c) variable contact area at high sliding amplitude, $\delta_g = \pm 150 \mu m$.

Note that textured samples lead to smaller oxygen distance and consequently bigger adhesion zone than that predicted by the model as noticed at high frequency especially in regions close to the grooves (Figure 4.20 & 4.21). This can be explained by the fact that the oxygen access to the interface near to the grooves is less than that in the borders exposed to air due to the presence of debris particles filling the holes. This results in axisymmetric oxygen distance as the latter is lower in the regions close to the internal grooves compared to the regions exposed to the outer air (i.e. $d_{O,X} > d_{O,Y}$ Figure 4.21).

4.3.2.3 Validation of the parametric “oxygen distance” model

The parametric “oxygen distance” model (Equation 4.20) is now considered to predict the extension of the d_O oxygenation length scale for the studied textured samples. Note that when the lateral width is smaller than the full oxygenation condition ($L_{\perp\delta} < 2 \cdot d_O$), so that the adhesion area is zero (i.e. $A_{ad}=0$), the corresponding data points are not considered in the analysis. Figure 4.17 compiled both plain and textured crossed flat-on-flat contact results. A good correlation is still observed which confirms the stability of the approach to formalize the extension of abrasion domain within the fretting wear interface whatever the fretting loading condition and the contact morphology.

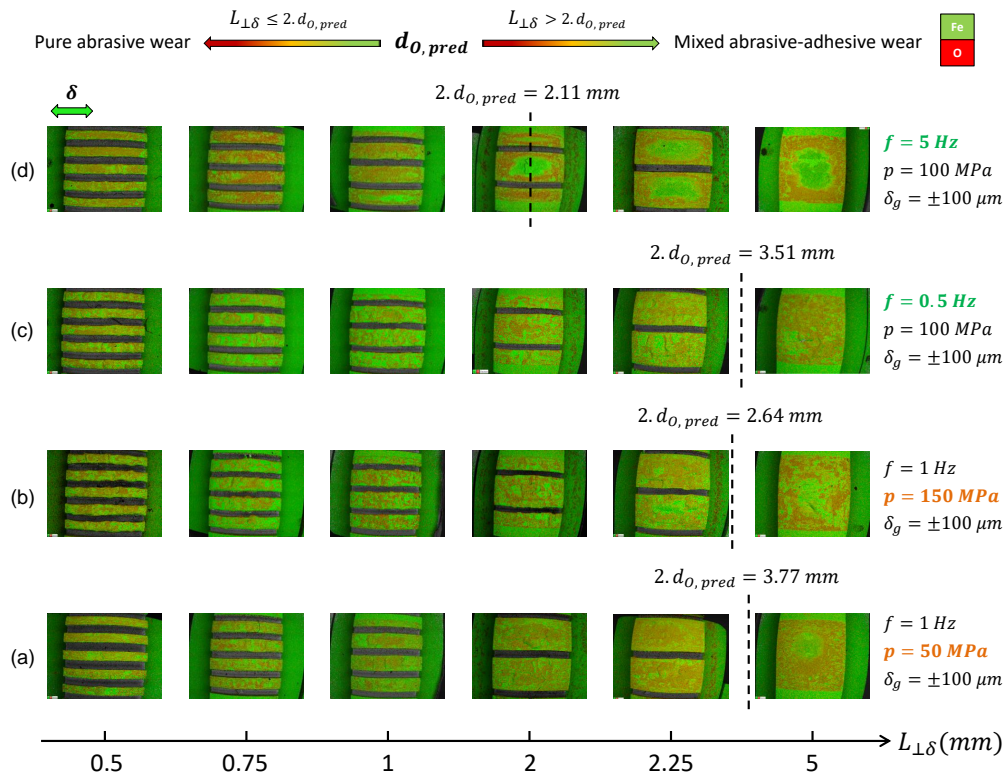


Figure 4.20: Prediction of the transition of wear regime by using the predicted threshold oxygen distance (Equation 4.20) for: (a) variable contact area at low contact pressure, $p=50$ MPa; (b) variable contact area at high contact pressure, $p=150$ MPa; (c) variable contact area at low frequency, $f=0.5$ Hz; and (d) variable contact area at high frequency, $f=5$ Hz.

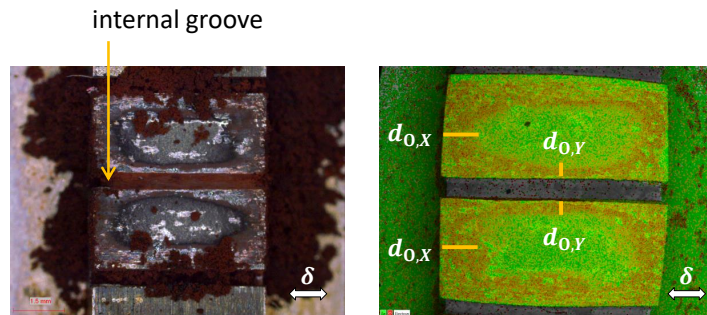


Figure 4.21: Illustration of the effect of internal grooves on the oxygen distance sample ($N=20000$ cycles, $p=100$ MPa, $\delta_g = \pm 100$ μm , $f=5$ Hz, $L_{\perp\delta}=2.25$ mm and $L_{\parallel\delta}=5$ mm).

Now, assuming that the oxygen distance is equal in all directions and the inner adhesive wear is equivalent to a homothetic rectangular region (Figure 4.22), the adhesive and abrasive wear areas “ A_{ad} & A_{ab} ” as well as the proportions of the adhesive and abrasive wear areas “ $\%A_{ad}$ & $\%A_{ab}$ ” can be expressed as a function of the d_O formulation (Equations 4.21) such that:

$$\begin{aligned}
& \text{if } d = \min\left(\frac{L_{\parallel\delta}}{2}, \frac{L_{\perp\delta}}{2}\right) > d_O, \\
& A_{ad} = (L_{\perp\delta} - 2.d_O).(L_{\parallel\delta} - 2.d_O) = L_{\perp\delta}.L_{\parallel\delta} - 2.d_O(L_{\perp\delta} + L_{\parallel\delta}) + 4.d_O^2 \\
& \Rightarrow A_{ad} = A - 2.d_{O,ref} \times \left(\frac{f}{f_{ref}}\right)^{n_f} \left(\frac{p}{p_{ref}}\right)^{n_p} \times (L_{\perp\delta} + L_{\parallel\delta}) + 4.d_{O,ref}^2 \times \left(\frac{f}{f_{ref}}\right)^{2n_f} \left(\frac{p}{p_{ref}}\right)^{2n_p} \\
& \Rightarrow A_{ab} = A - A_{ad} = 4.d_{O,ref}^2 \times \left(\frac{f}{f_{ref}}\right)^{2n_f} \left(\frac{p}{p_{ref}}\right)^{2n_p} - 2.d_{O,ref} \times \left(\frac{f}{f_{ref}}\right)^{n_f} \left(\frac{p}{p_{ref}}\right)^{n_p} \times (L_{\perp\delta} + L_{\parallel\delta}) \\
& \text{if } d = \min\left(\frac{L_{\parallel\delta}}{2}, \frac{L_{\perp\delta}}{2}\right) \leq d_O \text{ then } A_{ad} = 0 \text{ and } A_{ab} = A
\end{aligned} \tag{4.21}$$

The relative proportions of abrasion ($\%A_{ab}$) and adhesion ($\%A_{ad}$) areas are expressed by Equation 4.12.

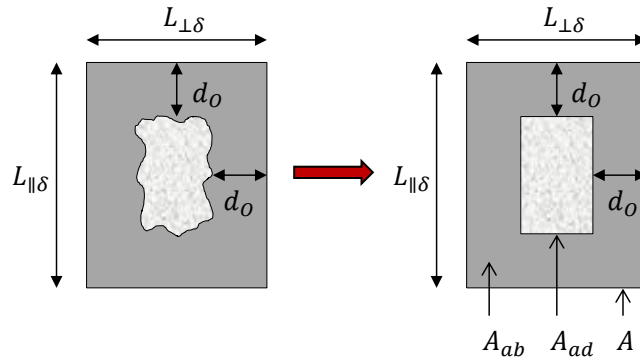


Figure 4.22: Illustration of the simplified partition of the abrasive and adhesive wear areas.

The prediction of the corresponding effective adhesive (A_{ad}) and abrasive (A_{ab}) areas along with the relative abrasive wear areas ($\%A_{ab}$) achieved using Equations 4.12, 4.20 & 4.21 are compared versus the experimental data in Figure 4.23a, b & c respectively. By compiling the results of 104 tests (49 calibration tests with untextured plain bottom sample + 55 validation tests with textured bottom samples), very good correlations emerge especially for the prediction of abrasive and consequently adhesive wear areas where $R^2=0.98$ and 0.88 correlation factors are observed respectively. Hence, it can be concluded that the given formulation of d_O (Equation 4.20) and the consequent expressions of the abrasive and adhesive wear areas “ $\%A_{ab}$ ” and “ $\%A_{ad}$ ” are very reliable and may be considered to formalize the fretting scar morphology at least for the studied crossed flat contact configurations inducing constant contact areas and nearly constant mean pressure during the test.

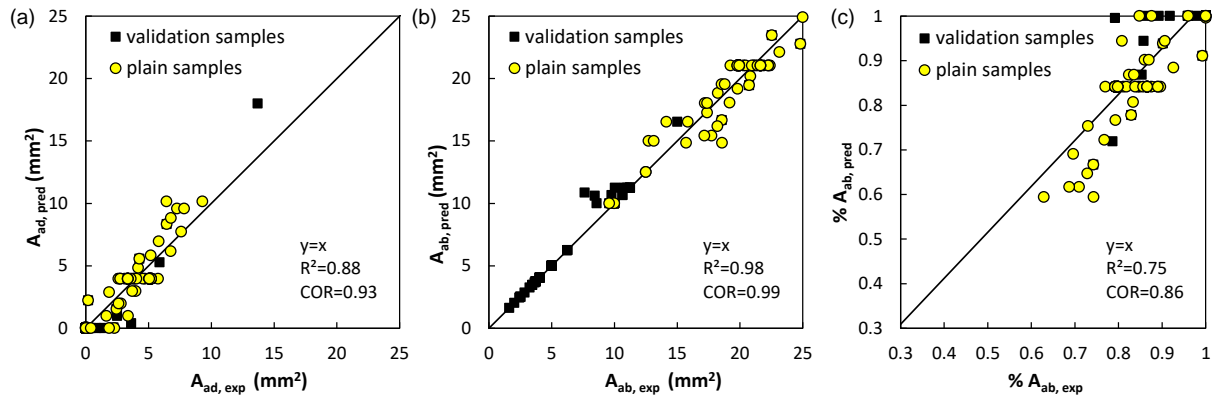


Figure 4.23: Correlation between the experimental and the predicted results (Equations 4.12, 4.20 & 4.21) for (a) the adhesion area “ A_{ad} ”; (b) the abrasion area “ A_{ab} ” and (c) the relative proportion of abrasion area “ $\%A_{ab}$ ” by compiling all the tests for plain and textured samples.

4.4 Discussion

The former investigation allows us to quantify and formalize the relative extension of abrasive and adhesive wear areas within a flat-on-flat fretting interface. A simple parametric formulation was extracted taking into account most of the fretting loading parameters such as the sliding frequency, the mean contact pressure, the sliding amplitude, the test duration and also the contact size and contact morphology including complex macro-textured interfaces. There is however a crucial interest to interpret in a physical point of view the relative influence of each of these parameters. To do this, we consider the COC concept previously introduced in [56].

4.4.1 Frequency effect

The asymptotic decreasing of d_O versus frequency (Figure 4.8) is consistent with the “contact oxygenation” concept [56] (Figure 4.24). Indeed by increasing the sliding frequency, the friction power density inputted in the interface rises which promotes a faster fresh metal exposure and therefore a faster consumption of the available dioxygen molecules within the fretting interface and therefore a reduction of d_O . Moreover, it reduces the time allowed to the dioxygen molecule to diffuse inward the inner part of the fretting contact. These combined effects tend to decrease the interface dioxygen partial pressure which can explain the reduction of the well oxygenated lateral abrasive domain d_O and the corresponding extension of the inner oxygen-deprived adhesive wear area. However, it is difficult to determine which of the above effects is preponderant in the absence of available experimental tools indispensable for quantifying the dioxygen diffusion, rate of di-oxygen consumption, etc.,...

4.4.2 Contact pressure effect

Like frequency, an increase of the contact pressure promotes a rising of the friction power density and consequently a faster consumption of the dioxygen molecule available within the fretting

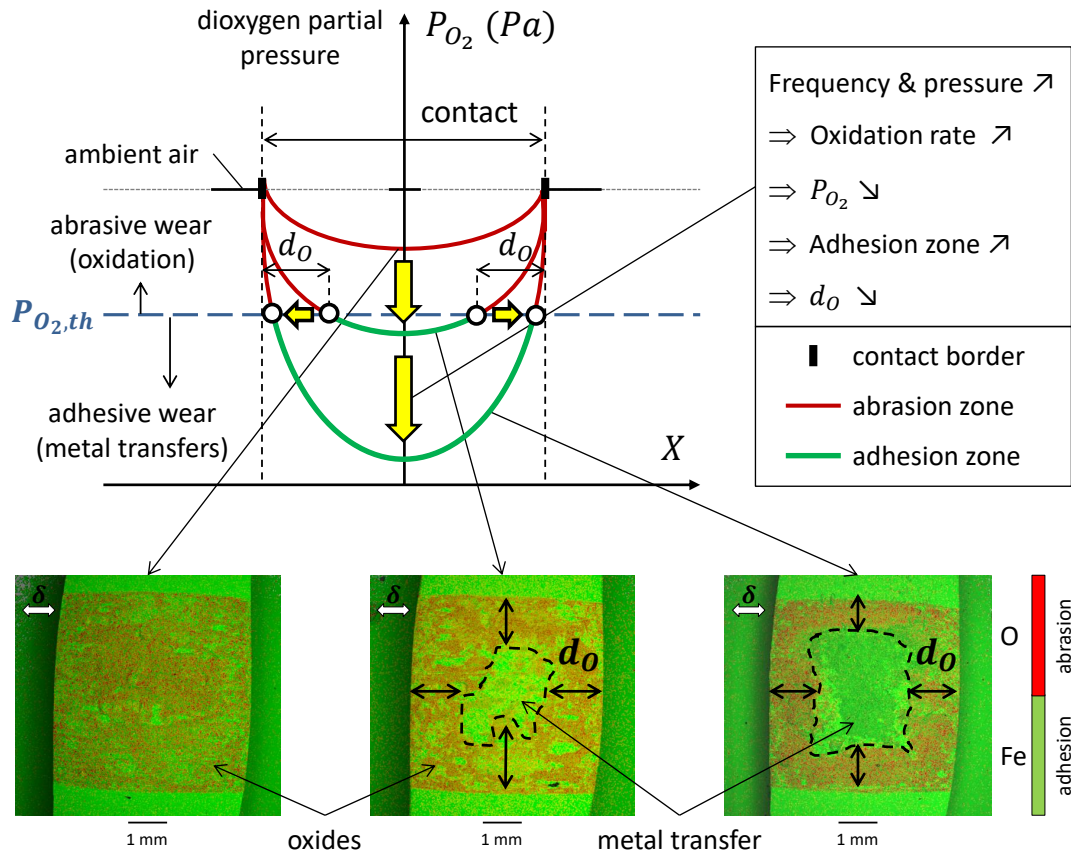


Figure 4.24: Illustration of the contact oxygenation concept to interpret the effect of contact pressure and sliding frequency regarding the evolution of d_O and the related partition between adhesive and abrasive areas.

interface. Moreover, an increase of contact pressure, by compacting the surface roughness and the debris layer, tends to reduce the diffusion of dioxygen molecules from the open air toward the inner part of the contact. These two combined effects drastically reduce the interfacial dioxygen partial pressure (Figure 4.24) which indirectly explains the fast reduction of d_O versus contact pressure observed in Figure 4.10 (Equation 4.14). It is noteworthy to mention the larger n_p pressure exponent compared to the corresponding frequency value (i.e. $|n_p|/|n_f| \approx 1.5$). This suggests a dominant effect of contact pressure regarding the partition between abrasive and adhesive wear compared to the frequency effect. This dominant effect might come from the fact that increasing the contact pressure causes an increase in the reaction rate with the dioxygen molecules in addition to the compaction of the debris bed which reduces the porosity and hence the permeability of the latter. This particular effect might not be significant when the frequency is increased, a possible reason why it has smaller exponent compared to the contact pressure.

4.4.3 Test duration effect

It is interesting to underline the very fast convergence of the interface toward a stabilized partition between abrasive and adhesive wear zone (Figure 4.12). The d_O length scale stabilized before 5000 fretting cycle and then remained constant. This suggests a constant interfacial dioxygen partial pressure profile (P_{O_2}) (i.e. boundary between well-oxygenated abrasive domains and under-oxygenated adhesive domains) whatever the surface wear extension. This tendency is coherent with the contact oxygenation concept in the sense that the studied crossed flat configuration imposes constant contact area, constant mean pressure and therefore constant friction work density. A different behavior should be observed if a Hertzian contact configuration was investigated. Indeed, a Hertzian contact, which displays a huge extension of the worn contact area, is expected to induce a significant increase of the d_O length scale with the fretting cycles and potentially an evolution from a composite adhesive-abrasive wear response toward a pure abrasive wear process. Unfortunately it was not possible in the frame of this investigation to study different contact geometries. The given stable evolution of d_O needs however to be considered with caution for very long test conditions where the progressive surface wear could eventually modify the dioxygen diffusion rate within the interface and therefore change the partition between abrasive and adhesive wear domains.

4.4.4 Sliding amplitude effect

It is surprising to notice a quasi-constant evolution of the d_O length scale versus the studied ± 25 to $\pm 200 \mu m$ sliding amplitude range (Figure 4.14). Longer sliding amplitudes increase the contact exposure to the outer environment ($e = \delta_g/a$) causing recession of adhesive zone [14, 77, 152, 153]. This was observed in many studies especially for very large fretting sliding amplitudes equivalent for instance to the reciprocating sliding case ($e \geq 1$). However, in the present situation the sliding amplitude remains smaller than 8% compared to the half contact width. This implies that most of the interface remains hidden from the outer environment which may explain the rather small influence of the studied sliding amplitude regarding the d_O parameter.

To interpret such constant evolution of d_O , the “contact oxygenation” concept will be considered again. An increase in the sliding amplitude causes a proportional increase in the friction power density (i.e. $\mu \cdot p \cdot v$ with μ being the friction coefficient) and therefore acceleration in the dioxygen reaction rate with fresh metal surfaces exposed by the tribological processes. This implies a decreasing of the P_{O_2} profile and consequently a reduction of the abrasive domain. The fact that d_O remains constant suggests that another mechanism is counterbalancing such effect. One hypothesis could be that an increase of the sliding amplitude also enhances debris flow and consequently the open access between interlocked asperities favoring in turn the diffusion of dioxygen molecules inward the fretted interface. These two opposite effects (increase of dioxygen consumption rate and easier diffusion of dioxygen molecule from outer ambient air) could explain the constant evolution of d_O with the sliding amplitude at least for the studied

condition. However, proving experimentally the validity of these hypotheses remains a scientific challenge. It is clear that the application of longer sliding amplitude may shift the balance between the two processes and consequently modify the oxygen distance parameter extending progressively the abrasive wear area when the sliding amplitudes approach the reciprocating sliding condition.

4.4.5 Contact size and sliding orientation

Contact oxygenation concept (COC) and the related P_{O_2} profiles [56] suggest that the extension of d_O (i.e. lateral abrasive wear domain) is a function of the balance between the dioxygen molecule diffusion rate from the external contact borders and the rate of oxygen consumption related to the oxidation process of fresh metal surface and metal debris induced by the friction work. Assuming constant friction work density condition (i.e. constant pressure and frequency for the studied flat-on-flat interface), contact size is not involved in such description and therefore d_O should be independent of contact area. This conclusion is confirmed experimentally in Figure 4.16b. Obviously, when the minimum distance between the contact border and the contact center becomes smaller than d_O , the interface shifts towards a pure abrasive wear interface: $d < d_O \Rightarrow \% \text{ abrasive area} = 100\%$. Alternatively, if d_O remains constant, an increase of the contact size tends to increase the inner adhesive area, promoting a reduction of the relative abrasive area ($\%A_{ab}$) as confirmed in Figure 4.16a.

The isotropic distribution of d_O around the fretted scar whatever the contact size and orientation (i.e. $d_{O,L_{\parallel\delta}} \approx d_{O,L_{\perp\delta}}$) can be explained by the isotropic diffusion of dioxygen molecules (i.e. $d_{O,X} \approx d_{O,Y}$ in Figure 4.6). Such isotropic response is not so obvious. Indeed, the studied crossed flat contact allows homogeneous friction power density dissipation over the whole fretted interface. Therefore, homogeneous dioxygen consumption rate is expected. However, it could be assumed that the longitudinal abrasive grooves along the sliding direction will allow easier oxygen diffusion inward the center of the fretted interface. In contrast, focusing on the transverse direction, dioxygen molecules need to overpass the perpendicular roughness barriers related to the longitudinal grooves. From this topographic consideration, it might be expected larger $d_{O,X}$ than $d_{O,Y}$ values.

The fact that similar $d_{O,X}$ and $d_{O,Y}$ distances are observed suggests that isotropic diffusion conditions, (i.e. independent of the sliding and roughness directions) are ensured within the fretted contact. This result could be explained by assuming that the interfacial dioxygen diffusion process is mainly driven by the isotropic $10 \mu m$ thick porous debris layer rather than by $1 \mu m$ anisotropic fluctuation of fretting scar roughness.

4.4.6 Summary

To conclude, it can be stated that the proposed COC concept and the related di-oxygen partial pressure distribution approach appear as a pertinent strategy to explain the typical abrasive-adhesive composite structure observed in large fretting wear interface. Using such simple concept, it is possible to explain the relative influence of frequency, pressure, loading cycles, sliding amplitude and contact size effects regarding the extension of the inner adhesive zone in fretting contact. A basic formulation is also introduced allowing the formalization of the d_O length scale (i.e. surrounding “well oxygenated” lateral band of the fretted interface) as well as the corresponding adhesive and abrasive areas. The very good correlation with the experiments confirms the proposal and was even able to formalize the fretting wear response of complex macro textured interfaces. This formalization of the composite adhesive-abrasive fretting wear interface will permit a better description of the global wear rate such that different wear rates should be expected in the distinct adhesion and abrasion zones. It will also permit a better prediction of the fretting cracking process observed in large and low pressure interfaces where adhesive interface can localize contact stressing favoring fretting crack nucleation process [154, 155]. Future works will be undertaken to investigate the influence of the contact geometry studying for instance various Hertzian contact configurations. Another aspect will concern the investigation of various materials like bronze, aluminum and titanium alloys displaying various oxidation rates and adhesive wear properties. Hence by tuning the balance between di-oxygen diffusion and di-oxygen depletion it will be possible to establish a more physical formulation of the d_O length scale. However, the main objective of the current development consists of the establishment of an explicit formulation of the di-oxygen partial pressure profile thus to provide a robust prediction of d_O and the related partition between adhesive and abrasive wear zones in fretting interfaces. This approach, though being fundamental, might be profitable for industrial practice as it allows better prediction of wear kinetics and wear depth by taking into account mixed abrasive-adhesive wear which is highly encountered in many industrial applications especially those operating in oxygen-starved environments like large press-fitted assemblies where seizure may occur. Note that seizure phenomenon can favor crack nucleation and fretting fatigue failures [156]. Therefore, the prediction of adhesive wear zone is a key issue to establish safe fretting fatigue interface.

4.5 Conclusion

This chapter aims at investigating the evolution and transition of wear mechanisms (abrasion and adhesion) for a 34NiCrMo16 dry flat-on-flat interface. This is achieved by introducing the “oxygen distance, d_O ” defined as the distance between the contact extremities and the limits of adhesion domain. Then, a multi-scale experimental strategy is applied where the number of cycles, contact pressure, sliding amplitude, frequency, and contact area and geometry are varied.

Results showed that oxygen distance depends mainly on pressure and frequency. This is due to higher dissipated friction energy which leads to high plastic deformations and decrease in the

time given for the oxidation to take place (in case of frequency). On the other hand, oxygen distance was shown to be stable with the number of cycles, sliding amplitude and contact area. Taking these results into account, an oxygen distance prediction model was proposed which depends on pressure and frequency. This model was validated by using textured samples with variable textures' width. In addition, to predicting abrasion area, this model helped detect the transition of wear mechanisms from full abrasion to a mixed abrasive-adhesive wear under coupled loading conditions.

Chapter 5

ADR Modelling of adhesive fretting wear extension

Contents

5.1	Introduction	128
5.2	ADR model	129
5.2.1	Gas transport in debris bed	130
5.2.2	Reaction term	133
5.2.3	ADR continuity equation	134
5.3	Numerical solution of the ADR continuity equation	134
5.3.1	Finite difference scheme	134
5.3.2	Solution method	136
5.3.3	Steady-state solution	136
5.4	Parameters identification and model calibration	137
5.4.1	Illustration of the studied interface	137
5.4.2	Properties of the debris layer porous medium	139
5.4.3	Threshold partial pressure ($P_{O_2, th}$)	141
5.4.4	Identification of the reaction rate coefficient (r_{O_2})	142
5.4.5	Qualitative comparison with fretting experiments	143
5.5	Model validation	145
5.5.1	Test strategy	145
5.5.2	Effect of sliding frequency (f)	145
5.5.3	Effect of contact pressure (p)	148
5.5.4	Archard power density factor formulation	149
5.5.5	Effect of contact area (A)	150
5.5.6	Quantitative validation of ADR approach	152
5.6	Discussion	154
5.7	Conclusion	158

5.1 Introduction

In the previous chapter, it was shown that “oxygen distance d_O ” is highly dictated by the operating loading conditions in the interface namely the sliding frequency and contact pressure [157]. In fact, when the latter are relatively low, abrasive-oxidational wear dominates. In contrary, when the contact pressure and sliding frequency are high, composite adhesive-abrasive wear is triggered. However, the other loading conditions such as number of cycles, sliding amplitude, contact size and contact orientation appeared to have no substantial effect on oxygen distance at least in the studied ranges. Hence, a parametric model linking oxygen distance evolution to the contact pressure and frequency was proposed. Although the aforesaid model was highly predictive, it remained parametric in essence, hence more physical interpretation is sought.

In the light of the former results, the purpose of this chapter is to explain and model contact oxygenation and the evolution of oxygen distance observed in fretting contacts. This is achieved by modelling oxygen transport using an Advection-Dispersion-Reaction (ADR) [158] approach by considering debris bed as compact powdery porous medium traversed by atmospheric gases. Figure 5.1 illustrates the principle of this model which is based on establishing the balance between the di-oxygen flow coming from the external part of the contact through an advection-dispersion process within the porous debris layer, and the oxygen consumption rate induced by the oxidation reaction of the fresh metal surface exposed by the friction process (i.e. removing the protective oxide layer through asperities interactions).

As detailed previously, abrasive-oxidational wear dominates the regions where oxygen concentration is sufficiently high (i.e., $P_{O_2} \geq P_{O_2, th}$) whereas adhesive wear is detected whenever oxygen access becomes restricted such that $P_{O_2} < P_{O_2, th}$. The oxygen distance “ d_O ” marks the transition between these two wear phenomena. Hence, this chapter will detail the basics of the model, the various hypotheses involved and the related numerical scheme to predict the relative partition between abrasive and adhesive wear zones (i.e. oxygen distance d_O). The given predictions are discussed regarding the corresponding experiments thus establishing the potential but also the limits of this multi-physics strategy to predict wear processes partition within fretting interfaces.

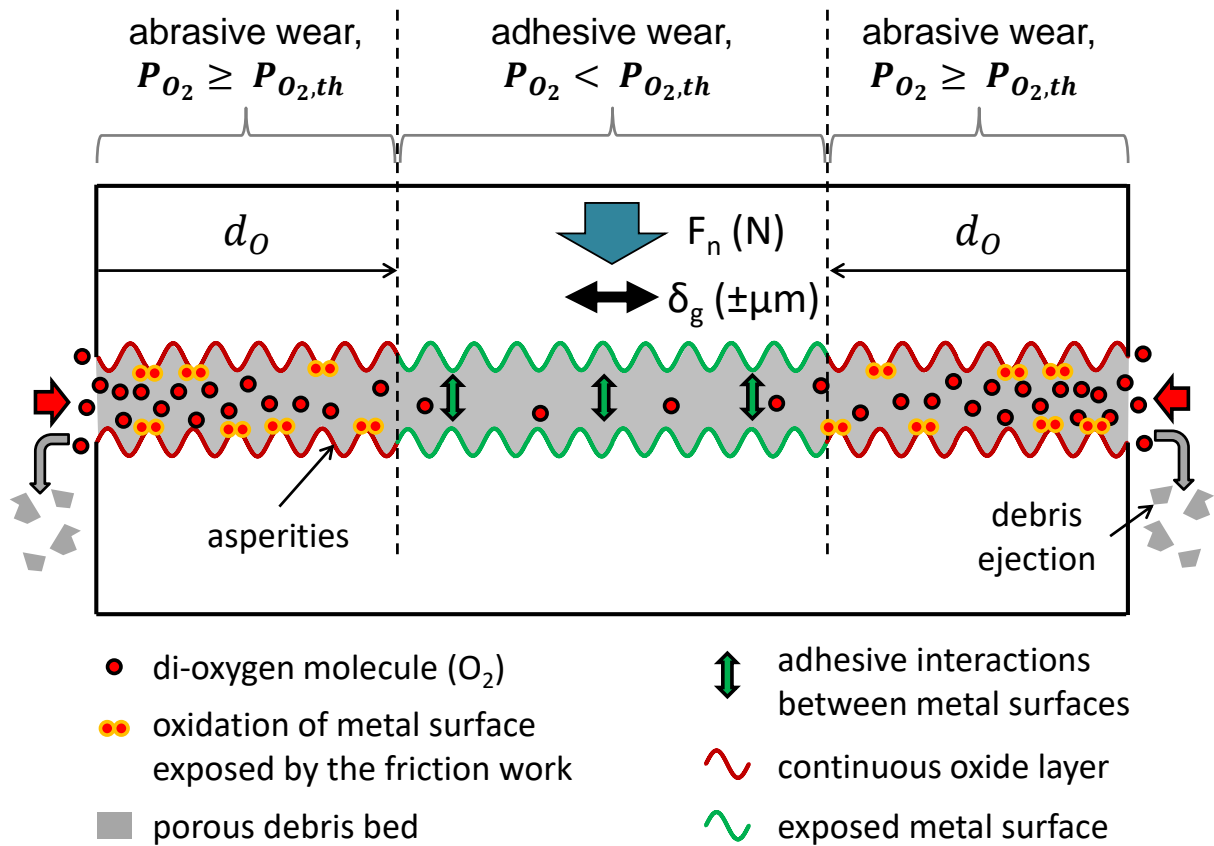


Figure 5.1: Illustration of the ADR model to predict the extension of adhesive / abrasive wear distribution within a fretting interface.

5.2 ADR model

In advection-dispersion-reaction ADR model, debris bed is considered to be a dry compact powdery porous medium allowing transport of gases (Figure 5.2). This model includes only two gas components which are nitrogen and oxygen. The other gases in the atmosphere (mainly argon, water vapor, and carbon dioxide) are neglected firstly because they present around 1% of the atmospheric air which is nearly negligible compared to other gas constituents. Thus, whenever oxygen concentration is relatively high, these gases do not play a significant role in oxidation and consequently contact oxygenation. This is confirmed by previous studies showing that high temperature oxidation of steel in gases containing free oxygen is chiefly governed by the oxygen gas which is the main oxidizing agent and that the additions of CO_2 and H_2O (with relatively high percentages compared to the air composition) had little effect on the magnitude of the initial oxidation rates [159]. Besides, the overall oxidation in atmospheres containing higher free oxygen content ($>15\%$) was shown to be unaffected by changing the concentration of H_2O or CO_2 [160]. This is further confirmed by fretting wear tests of steel alloy where water vapor and carbon dioxide seemed to have negligible effect on the oxidized debris whenever the oxygen concentration is sufficient ($>2\%$) [161].

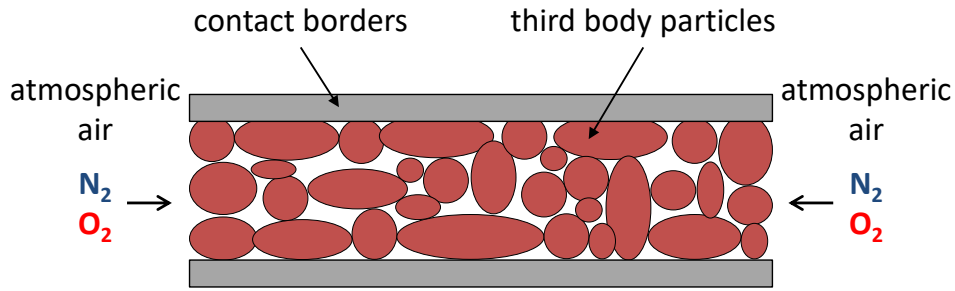


Figure 5.2: Schematic presentation of the powdery porous debris bed allowing gas transport.

5.2.1 Gas transport in debris bed

Gas transport in porous media is chiefly controlled by dispersion and advection [162]. Hence, for a gas component “i” the general flux equation is given by:

$$J_i = J_{a,i} + J_{d,i} \quad (5.1)$$

With J_i being the general molar flux of gas component i ($mol.m^{-2}.s^{-1}$), $J_{a,i}$ the advective flux of gas component i ($mol.m^{-2}.s^{-1}$) and $J_{d,i}$ the dispersive flux of gas component i ($mol.m^{-2}.s^{-1}$).

5.2.1.1 Advective transport

The advection (bulk flow) (Equation 5.2) is the transport of the entire gas mixture by bulk motion due to gradients in the total pressure of the gas mixture.

$$J_{a,i} = vC_i \quad (5.2)$$

With C_i being the molar concentration of a component i ($mol.m^{-3}$), and v being the advection velocity of the gas mixture in the debris bed ($m.s^{-1}$).

Gas advection in porous media is investigated using Darcy’s law [163] which defines gas advection velocity “v” as being directly proportional to the gas phase pressure gradients [164]. The pressure gradients are caused by compositional changes in the gas mixture which, in fretting wear, are caused by the consumption of oxygen during oxidation reaction of freshly exposed metal. Darcy’s law is given by:

$$v = -\frac{k}{\mu} \nabla P \quad (5.3)$$

With μ being the gas mixture viscosity ($kg.m^{-1}.s^{-1}$), k the intrinsic permeability of the debris bed (m^2), and P being the total pressure of the gas mixture (Pa).

The total pressure P of a gas mixture of “m” gases is equal to the sum of the partial pressures of the individual gases (P_i) according to Dalton’s law [165]:

$$P = \sum_{i=1}^m P_i \quad (5.4)$$

The viscosity (μ) of the entire gas mixture is estimated using Wilke model [166] through applying a mixing rule for the viscosities of the individual gases based on kinetic gas theory.

$$\mu = \sum_{i=1}^m \frac{\mu_i}{1 + \sum_{j=1, j \neq i}^m \theta_{i,j} \frac{y_j}{y_i}} \quad (5.5)$$

$$\theta_{i,j} = \frac{\left[1 + \left(\frac{\mu_i}{\mu_j} \right)^{1/2} \times \left(\frac{M_j}{M_i} \right)^{1/4} \right]^2}{\sqrt{8} \left(1 + \frac{M_i}{M_j} \right)^{1/2}} \quad (5.6)$$

$$y_i = \frac{n_i}{\sum_{i=1}^m n_i} = \frac{P_i}{\sum_{i=1}^m P_i} \quad (5.7)$$

With μ being the viscosity of the gas mixture ($kg.m^{-1}.s^{-1}$), μ_i the viscosity of the gas component “i” ($kg.m^{-1}.s^{-1}$), y_i the mole fraction of gas component “i”, n_i the number of moles of gas component “i”, $\theta_{i,j}$ is expressed in Equation 5.6, and M_i is the molar mass of gas component “i” ($kg.mol^{-1}$).

The intrinsic permeability can be estimated using Carman-Kozeny equation [167, 168]:

$$k = \frac{d_p^2 a^3}{180(1-a)^2} \quad (5.8)$$

With d_p being the average particle size in the debris bed (m) and a is the porosity of the debris bed (dimensionless).

5.2.1.2 Dispersive transport

Dispersion of gases consists of diffusive and mechanical mixing processes [169]. Diffusive flux is governed by molecular diffusion which is defined as the random spreading of a gas component “i” in a mixture of gases due to concentration gradients [169]. Mechanical mixing is a solute-independent constituent of dispersion controlled by the physical characteristics of the porous medium and the carrier gas velocity [169]. Mechanical mixing and dilution of gases result from velocity variations that originate from non-uniform velocity profiles within a single pore due to wall-effects, pore size distributions (large pores induce higher velocities than smaller ones), and the tortuosity effects [169].

Dispersion is analyzed using Fick's law [170] which relates the dispersive flux of gases to the concentration gradients:

$$J_{d,i} = -D_i \nabla C_i \quad (5.9)$$

The dispersion coefficient of a gas component "i" (D_i) is given by [169]:

$$D_i = D_{mechanical\ mixing} + D_{diffusion, i} \quad (5.10)$$

The molecular diffusion term of dispersion is solute dependent and is given by [169]:

$$D_{diffusion, i} = \tau D_{im} \quad (5.11)$$

The diffusion coefficient of a gas component "i" diffusing in a homogeneous mixture of "m" gases [162] is given by Wilke model [171] such that:

$$D_{im} = \frac{1 - y_i}{\sum_{j=1, j \neq i}^m \frac{y_j}{D_{ij}}} \quad (5.12)$$

Where D_{ij} is the diffusion coefficient for a binary mixture of gas components "i" and "j" ($m^2.s^{-1}$) which can be estimated using a semi-empirical model proposed by Chen and Othmer [172]:

$$D_{ij} = \frac{0.604 \times 10^{-8} \times T^{1.81} \times \left(\frac{M_i + M_j}{M_i \times M_j}\right)^{0.5}}{P \times (T_{C,i} \times T_{C,j})^{0.1405} \times (V_{C,i}^{0.4} + V_{C,j}^{0.4})^2} \quad (5.13)$$

With M_i being the molar mass of a gas component "i" ($kg.mol^{-1}$), $T_{C,i}$ the critical temperature (K), $V_{C,i}$ the critical volume ($m^3.kmol^{-1}$), T the desired air temperature (K), and P being the air pressure (bar).

The product of the diffusion coefficient and the tortuosity " τ " is referred to as "effective diffusion coefficient, $D_{diffusion, i}$ " [169]. The tortuosity is an intrinsic property of a porous medium estimated from the ratio of the actual length of the flow path to the straight-line distance between its ends [173]. Indeed, in porous media the diffusion coefficient of a given gas is less than that in free air due to the presence of the solid phase which decreases the cross-sectional area allowing diffusion in addition to the tortuosity effects [162, 169]. Several authors attempted to empirically and semi-empirically express tortuosity " τ " as a function of the porosity " Φ " and the volumetric air content " a ". Moldrup et al. [174] model (Equation 5.14) will be considered in this investigation. This latter diffusion-based model is widely used in literature and is selected

here as it was shown to most accurately predict tortuosity for both dry and moist porous media [175–177].

$$\tau = 0.66\Phi \left(\frac{a}{\Phi}\right)^2 \quad (5.14)$$

In case of dry porous medium the porosity is assumed to be equal to the volumetric air content ($\Phi = a \Rightarrow \tau = 0.66a$).

The mechanical mixing term of dispersion is solute independent and is given by [169]:

$$D_{mechanical\ mixing} = \alpha_L |v| \quad (5.15)$$

Where v is Darcy's velocity ($m.s^{-1}$) and α_L is the longitudinal dispersivity of the gas mixture which is a measure of the physical heterogeneity of the porous medium (in m) [169]. The variable α_L can be empirically correlated to the scale length or the distance travelled by the gas which is, in the current case, equal to the contact size “ L ” expressed in meters. One of the aforesaid empirical relations is that proposed by Pickens and Grisak [178] as follows:

$$\alpha_L = \frac{L}{10} \quad (5.16)$$

Note that transverse dispersion is also observed in porous media and is expressed by transverse dispersivity coefficient “ α_T ”. Nevertheless, transverse dispersion is very small compared to the longitudinal dispersion (by factor 10) for this reason it will be neglected in the current study (i.e. $\alpha_T \approx 0$) [169].

5.2.2 Reaction term

In fact, the oxidation of Iron (Fe) during fretting wear presents a cardinal sink for oxygen gas. Di-oxygen molecules react with iron (Fe) element to form hematite (Fe_2O_3) and magnetite (Fe_3O_4) oxides. This oxidation reaction (i.e. consumption of O_2) depends on the concentration of di-oxygen molecules (C_{O_2}) but also on the material properties and the contact sliding conditions which monitor the progressive elimination of the protective oxide layer exposing new fresh metal surfaces to react with the available di-oxygen molecules. For simplicity and as a first approach, a first-order decay rate of oxygen gas is assumed such that:

$$R_{O_2} = r_{O_2} \times C_{O_2} \quad (5.17)$$

where r_{O_2} (s^{-1}) is the oxidation rate coefficient which expresses the reaction rate between the fresh metal surface and the available dioxygen molecules in the interfacial air. It depends on the fretted material and its avidity to react with oxygen but also on the formed protective oxide layer

(i.e. limiting the oxidation of the metal) and its endurance regarding friction processes. The r_{O_2} reaction rate coefficient mainly depends on tribological parameters like the contact pressure, sliding amplitude, and frequency. The explicit formulation of r_{O_2} is quite complex. However, stating that the higher the friction power dissipated in the interface, the faster the metal reaction with the available oxygen gas, a simple phenomenological empirical expression based on the so-called “p.v” power factor (with “p” being the pressure and “v” being the sliding speed) will be considered. The proposed formulation and its calibration are detailed later in Section 5.4. Note that the given formulation neglects the reactivity with nitrogen gas (i.e. $r_{O_2} \approx 0$) although some nitriding processes could be observed [56, 70] as detailed in the following discussion (Section 5.6).

5.2.3 ADR continuity equation

The continuity equation of the advection-dispersion-reaction (ADR) process of a gas constituent “i” is therefore given by:

$$a \frac{dC_i}{dt} = -\nabla \cdot (J_i) + R_i = -\nabla \cdot (-D_i \nabla C_i + v C_i) + R_i \quad (5.18)$$

By multiplying Equation 5.18 by “ $R.T$ ” following ideal gas law [179] (Equation 5.19), continuity equation can be expressed in terms of the partial pressure of individual gas components instead of the molar concentrations (Equation 5.20).

$$P_i = C_i \cdot R \cdot T \quad (5.19)$$

$$a \frac{dP_i}{dt} = -\nabla \cdot (-D_i \nabla P_i + v P_i) + R_i \quad (5.20)$$

with R being the universal gas constant ($8.314 \text{ J.mol}^{-1} \cdot \text{K}^{-1}$) and T being the temperature (K).

5.3 Numerical solution of the ADR continuity equation

5.3.1 Finite difference scheme

ADR model does not take into account the effect of contact orientation with respect to the sliding direction which was shown to have insignificant effect on the oxygen distance (see Chapter 4). Hence, in the current chapter, to facilitate the numerical description of the model, L_x and L_y will be used interchangeably to denote $L_{\parallel\delta}$ and $L_{\perp\delta}$ respectively. The ADR continuity equation is solved numerically by applying a finite difference scheme which was previously described by Stein and co-authors [162]. The nominal contact area “ $A = L_x \cdot L_y$ ” is discretized into equal number of nodes ($n_x = n_y$) in both directions such that gas partial pressures vary linearly between these nodes. Hence, the contact sizes L_x and L_y are respectively divided into p and q

segments centered at the nodes. Following this, a central difference approximation is applied for the general flux gradient yielding the continuity equation below:

$$a_{(p,q)} \frac{dP_{i(p,q)}}{dt} = \frac{J_{i(p-\frac{1}{2},q)} - J_{i(p+\frac{1}{2},q)}}{\Delta x} + \frac{J_{i(p,q-\frac{1}{2})} - J_{i(p,q+\frac{1}{2})}}{\Delta y} + R_i \quad (5.21)$$

The discretization of the time domain consists of applying a forward difference approximation such that:

$$\frac{P_{i(p,q)}^{j+1} - P_{i(p,q)}^j}{\Delta t} = \frac{J_{i(p-\frac{1}{2},q)} - J_{i(p+\frac{1}{2},q)}}{\Delta x \cdot a_{(p,q)}} + \frac{J_{i(p,q-\frac{1}{2})} - J_{i(p,q+\frac{1}{2})}}{\Delta y \cdot a_{(p,q)}} + \frac{R_i}{a_{(p,q)}} \quad (5.22)$$

$$P_{i(p,q)}^{j+1} = P_{i(p,q)}^j + \Delta t \cdot \left(\frac{J_{i(p-\frac{1}{2},q)} - J_{i(p+\frac{1}{2},q)}}{\Delta x \cdot a_{(p,q)}} + \frac{J_{i(p,q-\frac{1}{2})} - J_{i(p,q+\frac{1}{2})}}{\Delta y \cdot a_{(p,q)}} + \frac{R_i}{a_{(p,q)}} \right) \quad (5.23)$$

$$P_{i(p,q)}^{j+1} = P_{i(p,q)}^j + \Delta t \cdot f_{i(p,q)}^j \quad (5.24)$$

$$\text{for } i \in [1, m], p \in [1, n_x], q \in [1, n_y], j \in [0, n_t]$$

The general flux of a gas component “i” is discretized through the lower boundaries (Equations 5.25 & 5.27) and the upper boundaries (Equations 5.26 & 5.28) of segments p and q respectively.

$$J_{i(p-\frac{1}{2},q)} = - \left[D_{i(p-\frac{1}{2},q)} \cdot \frac{P_{i(p,q)} - P_{i(p-1,q)}}{\Delta x} \right] - \left[\frac{k_{(p-\frac{1}{2},q)}}{\mu_{(p-\frac{1}{2},q)}} \cdot \frac{P_{(p,q)} - P_{(p-1,q)}}{\Delta x} \cdot \frac{P_{i(p,q)} + P_{i(p-1,q)}}{2} \right] \quad (5.25)$$

$$J_{i(p+\frac{1}{2},q)} = - \left[D_{i(p+\frac{1}{2},q)} \cdot \frac{P_{i(p+1,q)} - P_{i(p,q)}}{\Delta x} \right] - \left[\frac{k_{(p+\frac{1}{2},q)}}{\mu_{(p+\frac{1}{2},q)}} \cdot \frac{P_{(p+1,q)} - P_{(p,q)}}{\Delta x} \cdot \frac{P_{i(p+1,q)} + P_{i(p,q)}}{2} \right] \quad (5.26)$$

$$J_{i(p,q-\frac{1}{2})} = - \left[D_{i(p,q-\frac{1}{2})} \cdot \frac{P_{i(p,q)} - P_{i(p,q-1)}}{\Delta x} \right] - \left[\frac{k_{(p,q-\frac{1}{2})}}{\mu_{(p,q-\frac{1}{2})}} \cdot \frac{P_{(p,q)} - P_{(p,q-1)}}{\Delta x} \cdot \frac{P_{i(p,q)} + P_{i(p,q-1)}}{2} \right] \quad (5.27)$$

$$J_{i(p,q+\frac{1}{2})} = - \left[D_{i(p,q+\frac{1}{2})} \cdot \frac{P_{i(p,q+1)} - P_{i(p,q)}}{\Delta x} \right] - \left[\frac{k_{(p,q+\frac{1}{2})}}{\mu_{(p,q+\frac{1}{2})}} \cdot \frac{P_{(p,q+1)} - P_{(p,q)}}{\Delta x} \cdot \frac{P_{i(p,q+1)} + P_{i(p,q)}}{2} \right] \quad (5.28)$$

5.3.2 Solution method

The partial differential equation (PDE) of the ADR model is solved using Runge-Kutta method with order 4 (RK4) which provides more stable and accurate solution than the explicit Euler scheme even when a higher time step Δt (by factor 10) is considered. According to RK4, the initial value problem is firstly defined in Equations 5.29 & 5.30 as follows:

$$\frac{dP_{i(p,q)}}{dt} = P_{i(p,q)}^j = f\left(t_j, P_{i(p,q)}^j\right) \quad (5.29)$$

$$P_{i(p,q)}^{j=1} = P_{i(p,q)}^0 \quad (5.30)$$

Secondly, the four Runge-Kutta increments are determined following the equations below:

$$K_1 = \Delta t \times f\left(t_j, P_{i(p,q)}^j\right) \quad (5.31)$$

$$K_2 = \Delta t \times f\left(t_j + \frac{\Delta t}{2}, P_{i(p,q)}^j + \frac{K_1}{2}\right) \quad (5.32)$$

$$K_3 = \Delta t \times f\left(t_j + \frac{\Delta t}{2}, P_{i(p,q)}^j + \frac{K_2}{2}\right) \quad (5.33)$$

$$K_4 = \Delta t \times f\left(t_j + \Delta t, P_{i(p,q)}^j + K_4\right) \quad (5.34)$$

Thirdly, the partial pressure of gas “i” at node “(p, q)” can be estimated for a time step “j+1” by adding the gas pressure at the previous time step “j” to the weighted average of the four Runge-Kutta increments:

$$P_{i(p,q)}^{j+1} = P_{i(p,q)}^j + \frac{1}{6} (K_1 + 2K_2 + 2K_3 + K_4) \quad (5.35)$$

$$t_{j+1} = t_j + \Delta t \quad (5.36)$$

5.3.3 Steady-state solution

The steady-state solution is defined by a stopping criterion such that if the difference between the pressure profiles between two consecutive instants of time falls below a certain predefined value “ ε ”, then the steady state is reached.

$$|P_i^{j+1} - P_i^j| < \varepsilon \Rightarrow \text{steady state is reached} \quad (5.37)$$

5.4 Parameters identification and model calibration

The input parameters related to the air conditions, gases physical properties, spatial and temporal discretization applied for the simulation of the steady-state condition are compiled in Table 5.1.

Air conditions	T= 25° C=298 K		P=1 atm=1.01325 bar=101325 Pa			R=8.314 J/K.mol
Gas physical properties	Oxygen, O_2	$T_{C,O_2} = 154.4$ K	$P_{C,O_2} = 50.43$ bars	$V_{C,O_2} = 0.08$ m ³ /kmol	$M_{O_2} = 32$ g/mol	$\mu_{O_2} = 20.8e^{-6}$ kg/m.s
	Nitrogen, N_2	$T_{C,N_2} = 126$ K	$P_{C,N_2} = 34$ bars	$V_{C,N_2} = 0.089$ m ³ /kmol	$M_{N_2} = 28$ g/mol	$\mu_{N_2} = 17.9e^{-6}$ kg/m.s
Spatial discretization	$n_x = 50$	$n_y = 50$	Temporal discretization	$\Delta t = 0.00001$ s	Steady state condition	$\varepsilon = 1e^{-5}$ Pa

Table 5.1: Input parameters of the ADR model.

Figure 5.3 illustrates a global overview of the ADR flow chart. It also considers the necessity to develop an adequate strategy combining literature analysis and well-calibrated fretting experiments to identify the unknown parameters required by the model (Equation 5.18) which are respectively:

- $P_{O_2, th}$: The threshold partial pressure below which the steel oxidation is no more possible and adhesive wear is activated.

d_p , a , k , and α_L : The intrinsic properties of the porous debris layer.

- r_{O_2} : The dioxygen reaction rate coefficient with fresh steel metal exposed by the friction process consuming the available dioxygen molecules present within the interface to generate metal oxides.

5.4.1 Illustration of the studied interface

Three frequencies ($f=0.5, 1, \& 10$ Hz) of plain crossed flat samples are investigated to calibrate the model while keeping constant the fretting cycles $N=20000$ cycles, contact pressure $p=100$ MPa, sliding amplitude $\delta_g = \pm 100$ μm , and the apparent contact area $A=25$ mm². Note that the number of fretting cycles was fixed at 20000 cycles to achieve a steady state friction regime which is reached after 5000 fretting cycles as shown in Chapter 3. Former investigations in Chapter 4 confirmed insignificant changes regarding the partition between abrasive and adhesive wear areas between 5000 to 40000 cycles. However, very long test durations could eventually modify the dioxygen diffusion rate within the interface due to the progressive surface wear which can therefore change the distribution between abrasive and adhesive wear domains. Unfortunately, this is not investigated in the current study and it will be addressed in future work.

The oxygen distance parameter “ d_O ” is defined experimentally using crossed EDX line scans as detailed in Chapter 4.

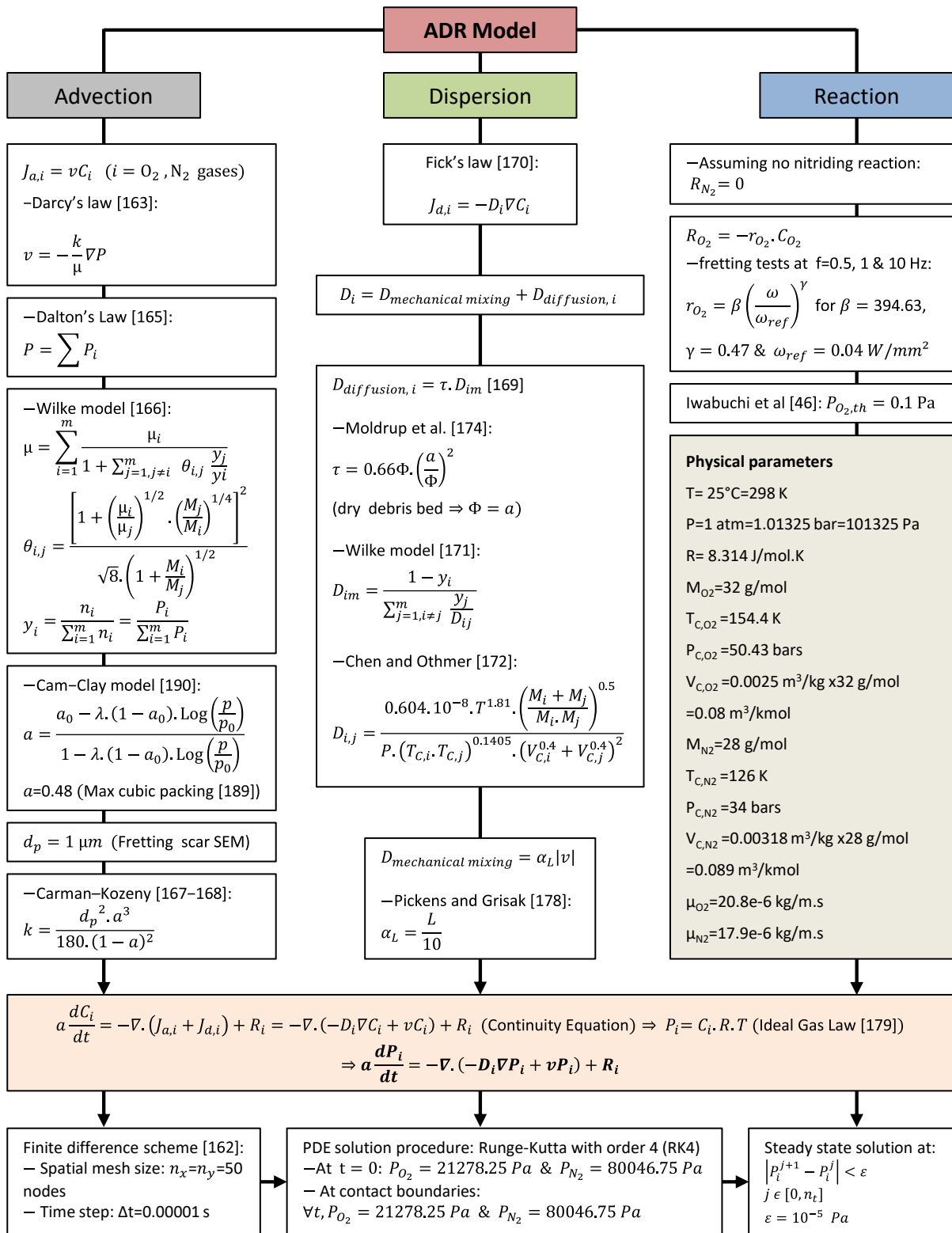


Figure 5.3: Flow chart summarizing the input data, models and the numerical solution of the ADR model.

5.4.2 Properties of the debris layer porous medium

5.4.2.1 Longitudinal dispersivity (α_L)

The longitudinal dispersivity can be estimated from the contact sizes L_x and L_y following Pickens and Grisak relationship [178] such that:

$$\alpha_{L,x} = \frac{L_x}{10} \quad (5.38)$$

$$\alpha_{L,y} = \frac{L_y}{10} \quad (5.39)$$

5.4.2.2 Particle size (d_p)

Particle size can be obtained from the SEM-BSE analysis of the wear scar of the fretting tests and is found to have an average value around $d_p=1 \mu m$ (Figure 5.4). Former studies showed that the ejected debris is heterogeneous in nature consisting of loose and fine particles where only some plate-like fragments are occasionally present [180]. Shima and co-workers [181] revealed, through extensive investigation of particle size and morphology, that most of oxidized debris particles formed between steel surfaces have a diameter below $1 \mu m$ in addition to the presence of some oxide-coated large platelets. However, several studies demonstrated that debris particles formed in steel alloys have a size ranging from 0.01 to $1 \mu m$ [9, 11, 161, 182–184] and some others reported a size ranging from 1 to $10 \mu m$ [185, 186]. By combining the current SEM observations (Figure 5.4) with the aforesaid literature investigations, it can be proposed that $d_p=1 \mu m$ is an appropriate assumption in the ADR model which will be backed by sensitivity analysis of particle size ranging from $d_p=0.01$ to $10 \mu m$ in the following discussion (Section 5.6).

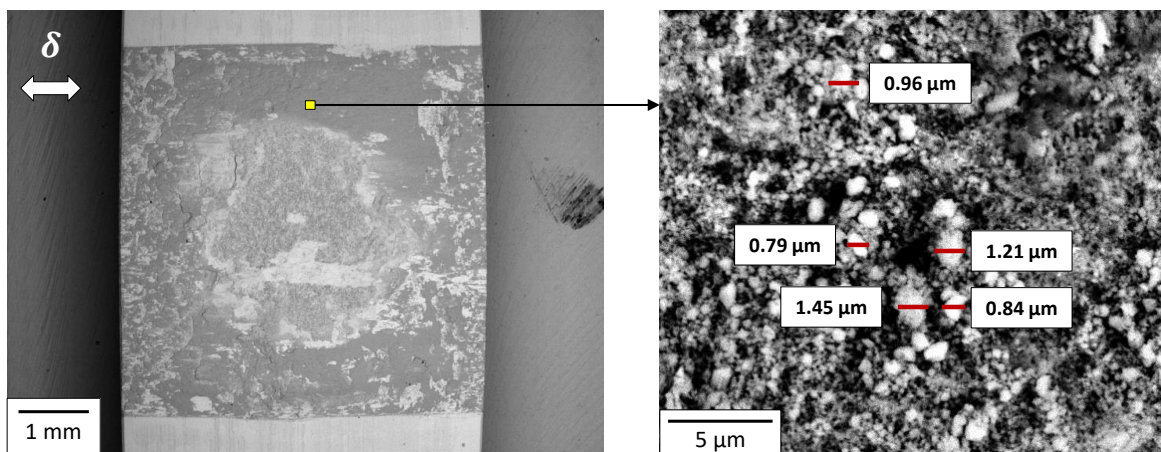


Figure 5.4: SEM-BSE images showing the size of the particles constituting the debris bed after a fretting test ($N=20000$ cycles, $p=100$ MPa, $\delta_g = \pm 100 \mu m$, $f=5$ Hz and $A=25 \text{ mm}^2$).

5.4.2.3 Porosity of the debris bed (a)

One of the most challenging parameters in the ADR model is the estimation of the porosity parameter “ a ” of the debris layer related to a fretting wear interface. In fact porosity is influenced by many factors including particles’ size, shape, and distribution [187, 188], in addition to the contact pressure and contact configuration. However, in the current study due to the lack of information about the aforesaid parameters, porosity is computed by assuming that the debris bed is made up of spherical particles of identical size, packed in a cubic manner [189] (Figure 5.5).

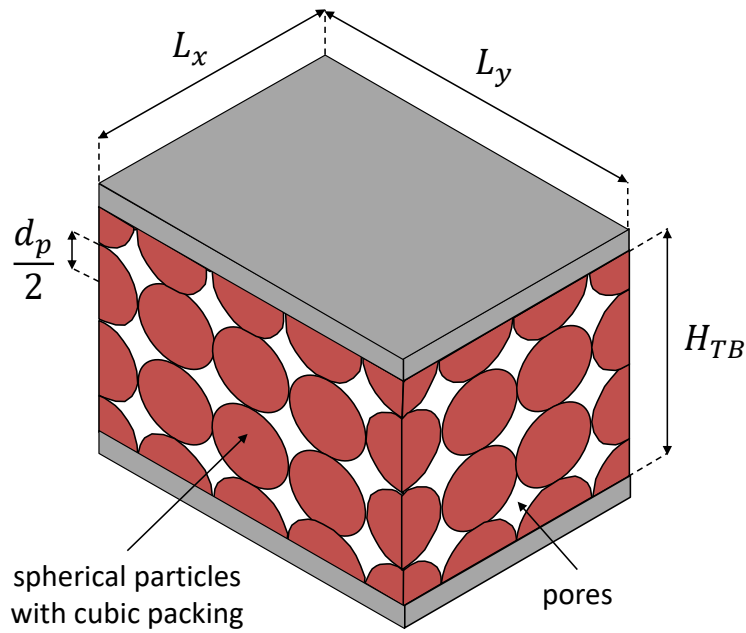


Figure 5.5: Porosity estimation by assuming cubic packing of identical spheres in the debris bed.

Using these hypotheses, porosity can be approximated assuming a debris bed “bulk volume” (Figure 5.5) such that $V_{bulk} = L_x \cdot L_y \cdot H_{TB}$ where the number of spheres constituting the debris bed is given by:

$$n = \left(\frac{L_x}{d_p}\right) \cdot \left(\frac{L_y}{d_p}\right) \cdot \left(\frac{H_{TB}}{d_p}\right) \quad (5.40)$$

where H_{TB} is the thickness of the third body (debris bed). Thus the total volume of the matrix of solid particles is equal to the number of spheres (n) multiplied by the volume of one sphere:

$$V_{solid\ matrix} = n \cdot \left(\frac{\pi}{6} \cdot d_p^3\right) = \frac{\pi}{6} (L_x \cdot L_y \cdot H_{TB}) = \frac{\pi}{6} V_{bulk} \quad (5.41)$$

Consequently, the porosity of the debris bed is estimated by:

$$a = \frac{V_{pores}}{V_{bulk}} = \frac{V_{bulk} - V_{solid\ matrix}}{V_{bulk}} = 1 - \frac{\pi}{6} = 0.48 \quad (5.42)$$

This approximation of the porosity parameter “ a ”, leading to a constant $a=0.48$ value, is based on a rough geometrical description of the debris layer which does not consider any loading parameter as the contact pressure for instance. Changing the contact pressure highly affects the debris bed porosity which influences in turn the permeability and consequently gas diffusion and oxygen distance. Hence, the effect of the contact pressure on powder porosity should be carefully addressed. Critical state soil mechanics (CSSM) and powder metallurgy (PM) have provided many models relating pressure to porosity like Cam-Clay model [190] which is usually applied to model powder compaction [191] (Equation 5.43).

$$a = \frac{a_0 - \lambda \cdot (1 - a_0) \cdot \text{Log}\left(\frac{p}{p_0}\right)}{1 - \lambda \cdot (1 - a_0) \cdot \text{Log}\left(\frac{p}{p_0}\right)} \quad (5.43)$$

With p_0 being the yield pressure of the particles (Pa), a_0 the initial porosity at p_0 , and λ being the loading slope of the yield surface (Pa^{-1}) by neglecting the initial stage of elastic deformation of grains.

This more complete description requires the identification of “ λ ” variable which unfortunately cannot be addressed in the frame of this investigation. Therefore, and as a first approximation, the porosity variable “ a ” is set at 0.48.

5.4.2.4 Intrinsic permeability of debris layer (k)

The intrinsic permeability can be found through Carman-Kozeny equation (Equation 5.8) [167, 168] by using the particle size (d_p) and the porosity (a) values defined in the previous sections. Doing so, the intrinsic permeability of debris bed is found to be equal to $k = 2.27 \times 10^{-15} m^2$.

5.4.3 Threshold partial pressure ($P_{O_2, th}$)

Based on thermodynamic considerations, an oxide is produced on a metal surface whenever the oxygen potential in the environment is higher than the oxygen partial pressure in equilibrium with the oxide [192]. Below this equilibrium oxygen pressure, which is also referred to as oxide dissociation pressure, metal oxidation is not likely to take place. Iwabuchi and co-workers [46] showed that oxidative wear of an iron-based alloy is significant when oxygen partial pressure is above $P_{O_2, th}=0.1$ Pa where magnetite and hematite are detected, and adhesive transfer of metallic debris prevails below 0.1 Pa. They obtained these results by conducting gross slip fretting tests of S45C steel under oxygen-controlled environments at room temperature ($23^\circ \pm 5^\circ$). The studied low alloyed steel displays a quite similar composition as S45C. So, an equivalent $P_{O_2, th}$ can be considered.

Besides, the micro-Raman analysis of the external abrasive corona (Figure 5.6), like the former Iwabuchi investigations, shows that the external oxide debris layer consists mainly of magnetite and hematite which again supports the chosen $P_{O_2, th}$ threshold value.

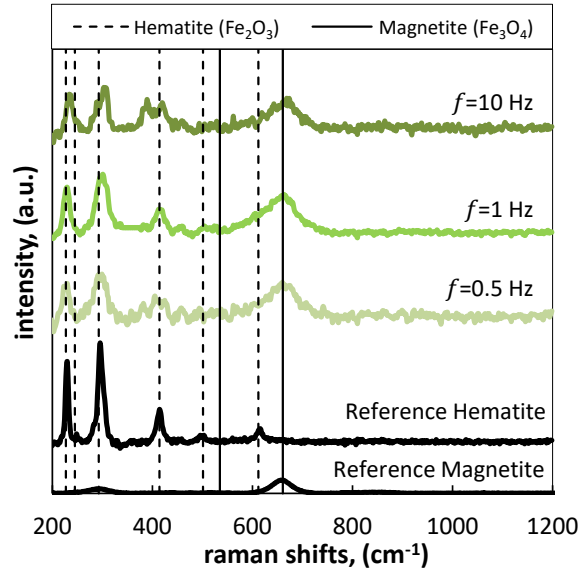


Figure 5.6: Raman spectra of the oxide debris layer (external abrasive corona) related to the calibration tests (Table 5.1): $f=0.5, 1$ and 10 Hz ($N=20000$ cycles, $p=100$ MPa, $\delta_g=\pm 100$ μm and $A=25$ mm^2 , for Laser wavelength $\lambda = 785$ nm, Laser power= 0.35 mV, and acquisition time= 150 s).

5.4.4 Identification of the reaction rate coefficient (r_{O_2})

Former investigations confirm that increasing the frequency and contact pressure tend to decrease the oxygen distance d_O [157]. Indeed, a higher friction power input in the fretted interface increases the reaction rate coefficient r_{O_2} between the fresh metal and the available dioxygen molecules which decreases in turn the oxygen partial pressure extending the inner adhesive wear domain and consequently decreasing the lateral d_O length scale. As mentioned previously, the reaction rate may depend on material properties as well as the contact loading parameters. Wear rate is usually formalized through the Archard theory expressing the wear volume extension as a function of the accumulated Archard factor $\sum W$ ($N.m$) defined as the product of the normal force multiplied by the sliding distance [72]. This wear process description is indirectly supported by the Bowden and Tabor theory suggesting that surface degradations occur through local interactions between rough surfaces where plastic deformations of contacting high spots (asperities) occurred [193]. They demonstrated that the real area of contact is proportional to the normal loading divided by the metal hardness which indirectly justifies that the wear rate is also proportional to the normal load. The local Archard's density parameter " w " ($N.m/mm^2$) was successively considered to predict the wear depth extension whereas the related Archard's power density factor " ω " ($N.m/mm^2/s$), also related to the so-called "pv" factor, is commonly adopted to describe metal seizure phenomena. This latter variable is very interesting as it de-

scribes the local friction work rate inputted within the interface to damage the surfaces. In a first approximation, the reaction rate coefficient monitoring the di-oxygen reaction is therefore expressed as a function of the Archard power density factor ω ($N.m/mm^2/s$ or W/mm^2) given for the studied fretting sliding condition:

$$\omega = p \times v = \left(\frac{F_n}{A} \right) \times (4.\delta_g.f) = 4.p.\delta_g.f \quad (5.44)$$

Former experimental investigations [55] underlined a power-law decreasing evolution of the oxygen distance d_O with the increase in the sliding frequency and the contact pressure. So, as a first approximation, the sink term “ r_{O_2} ” is assumed, by heredity, to have a power-law growth with the Archard power density factor such that:

$$r_{O_2} = \beta \left(\frac{\omega}{\omega_{ref}} \right)^\gamma \quad (5.45)$$

ω_{ref} is the Archard power density factor at the reference conditions ($N=20000$ cycles, $p=100$ MPa, $F_n=2500$ N, $\delta_g = \pm 100 \mu m$, $f=1$ Hz, $L_x=L_y=5$ mm, and $A=25 \text{ mm}^2$) so that $\omega_{ref}=0.04 \text{ W/mm}^2$. β and γ coefficients can be calculated by simulating only three calibration tests varying the frequency at $f=0.5$, 1 and 10 Hz but keeping constant the other parameters ($N=20000$ cycles, $p=100$ MPa, $F_n=2500$ N, $\delta_g = \pm 100 \mu m$, $L_x=L_y=5$ mm, and $A=25 \text{ mm}^2$). Both β and γ are tuned in order to minimize the error between the experimental d_O values ($d_{O,exp}$) measured in the fretting scars and the predictions given by the ADR approach ($d_{O,ADR}$) assuming the former hypotheses for the other variables of the model. The best fitting is achieved with $\beta=394.63$ and $\gamma=0.47$ (Table 5.2).

Frequency, f (Hz)	Archard power density factor, ω (W/mm^2)	Experimental oxygen distance, $d_{O,exp}$ (mm)	Numerical oxygen distance, $d_{O,ADR}$ (mm)	Relative error, (%)
0.5	0.0	2.3	2	13
1	0.04	1.5	1.7	13
10	0.4	1.1	1.1	0

Table 5.2: Calibration of the reaction rate coefficient (r_{O_2}) (Equation 5.45) ($\beta=394.63$ and $\gamma=0.47$) for 34NiCrMo16 interface with $N=20000$ cycles, $p=100$ MPa, $\delta_g = \pm 100 \mu m$ and $A=25 \text{ mm}^2$.

5.4.5 Qualitative comparison with fretting experiments

Figures 5.7a & b compare the evolution of the steady state total pressure (P) and the oxygen gas partial pressure (P_{O_2}). Although the dioxygen partial pressure drastically decreases from 21278.2 Pa to 3.06×10^{-9} Pa at the center of the contact, the total pressure displays a small diminution of about 10%. This tendency is explained by the fact that nitrogen gas compensates the elimination of oxygen gas inducing a 10% increase in N_2 partial pressure in the inner part of the interface. This pressure balance is driven by the advection process of the entire gas mixture (i.e. bulk flow) activated by the total pressure gradients. The target of the model, which is

to predict the adhesive versus abrasive wear extension, is illustrated in Figures 5.7c & d where the 2D EDX map of the fretting scar is compared to the 2D simulation of the dioxygen partial pressure in the fretted interface. By considering $P_{O_2, th}=0.1$ Pa, the limit between the adhesion and abrasion zones can be established. A very good correlation is observed with the experiments where pure metal interactions are observed in the inner part of the fretting scar (green=very poor oxygen concentration) whereas abrasive-oxidational processes are occurring in the d_O width corona (brick red=high oxygen concentration).

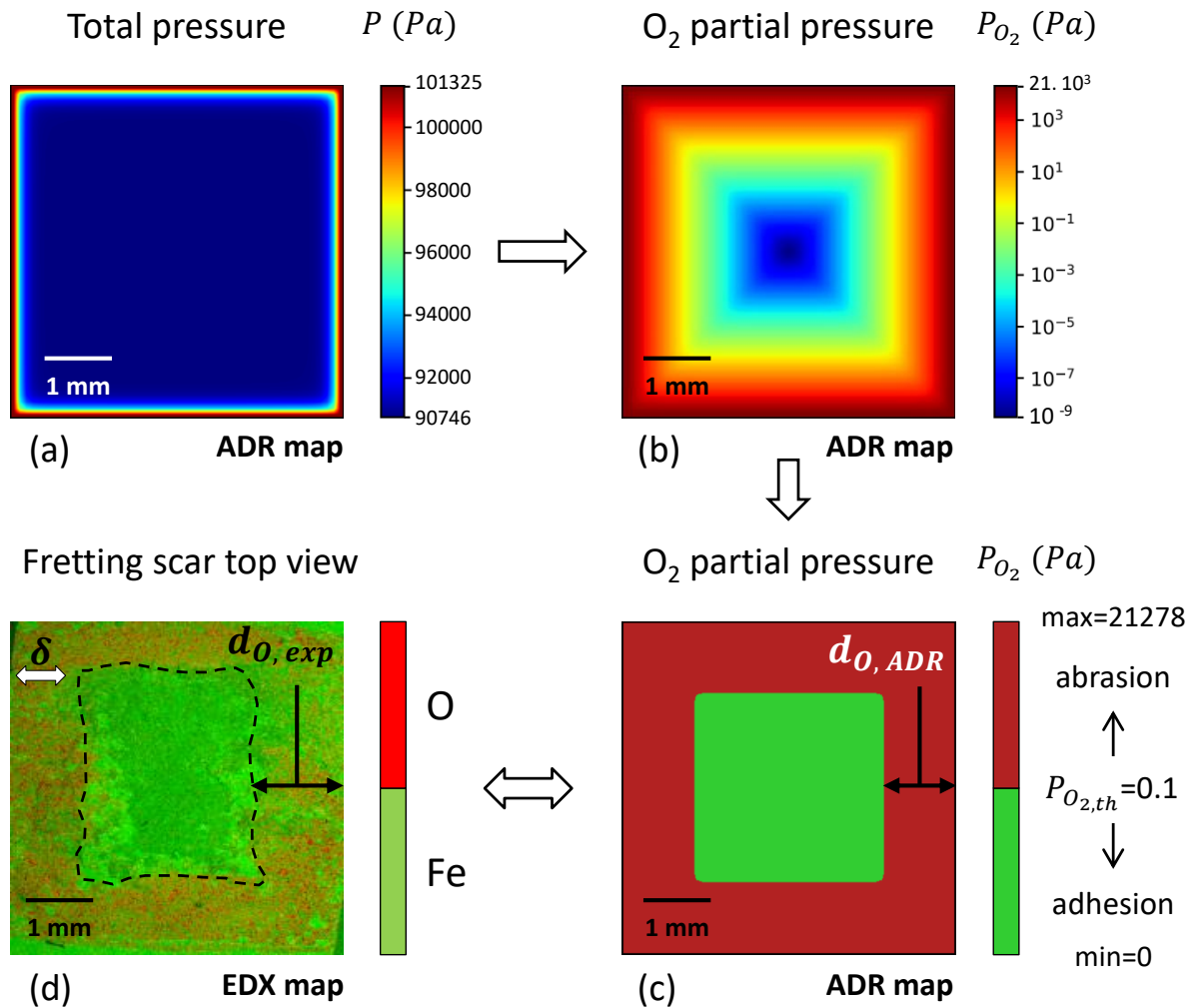


Figure 5.7: Comparison between the 2D simulation of the dioxygen partial pressure at steady state ($r_{O_2} = \beta(\omega/\omega_{ref})^\gamma$ with $\beta=394.63$ and $\gamma=0.47$, $\omega_{ref}=0.04$ W/mm², $P_{O_2, th}=0.1$ Pa, $a=0.48$, $d_p=1$ μ m, $k=2.27 \times 10^{-15}$ m², and $\alpha_{L,x}=\alpha_{L,y}=0.0005$ m) and EDX mapping of the studied fretting scar (34NiCrMo16 / 34NiCrMo16, N=20000 cycles, p=100 MPa, $\delta_g = \pm 100$ μ m, f=10 Hz and A=25 mm²) with: (a) ADR map showing the evolution of the total pressure; (b) ADR map showing the evolution of dioxygen partial pressure (log scale); (c) ADR map representing the partition between abrasion and adhesion; (d) EDX map showing the fretting scar top view.

This multiphysics ADR model of the adhesive/abrasive wear extension in fretting appears as a real opportunity to predict fretting processes. Based on a physical description of wear and dioxygen diffusion processes within the debris layer, ADR requires a limited number of variables and can be calibrated using a limited number of fretting experiments. However, to validate this approach, the given model will be compared versus various sliding frequencies, contact pressures and contact sizes.

5.5 Model validation

5.5.1 Test strategy

To check the validity of ADR model, former experimental results (detailed in Chapter 2) outside the current calibration conditions are simulated. The main results of this experimental work are presently recalled. A reference test (repeated three times) having a number of cycles $N=20000$ cycles, contact pressure $p=100$ MPa, sliding amplitude $\delta_g = \pm 100 \mu\text{m}$, frequency $f=1$ Hz, and a square contact area $A=25 \text{ mm}^2$ ($L_x=L_y=5 \text{ mm}$) is considered (Figure 5.8). Following this, a cross-experimental scheme is performed such that the sliding frequency “ f ” is examined from 0.5 to 10 Hz, the contact pressure “ p ” from 25 to 175 MPa and the apparent contact area “ A ” is varied from 10 to 25 mm^2 .

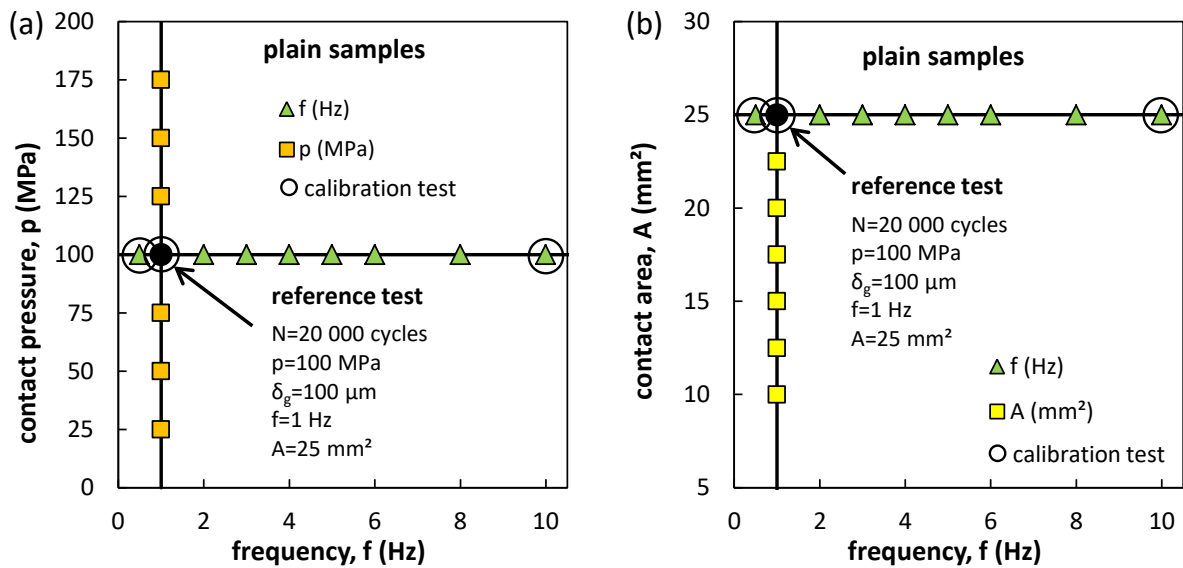


Figure 5.8: Cross-experimental strategy to validate the ADR approach for plain crossed flat-on-flat samples: (a) contact pressure versus frequency; and (b) apparent contact area versus frequency.

5.5.2 Effect of sliding frequency (f)

Figure 5.9 displays the evolution of the dioxygen partial pressure profile along the median axes L_x and L_y (equivalently $L_{\parallel\delta}$ and $L_{\perp\delta}$) as a function of the applied frequency from 0.5 to 10 Hz. As previously mentioned, increasing frequency leads to growth of the inner zone where $P_{O_2} <$

$P_{O_2, th}$ resulting in expansion of the adhesion area and consequently lower oxygen distance. This is due to the fact that for higher frequencies the metal exposure rate and therefore the rate of oxidation reaction with the existing interfacial dioxygen molecules are increased [56]. Hence, a high oxygen consumption rate at the borders limits oxygen gas availability towards the center of the contact.

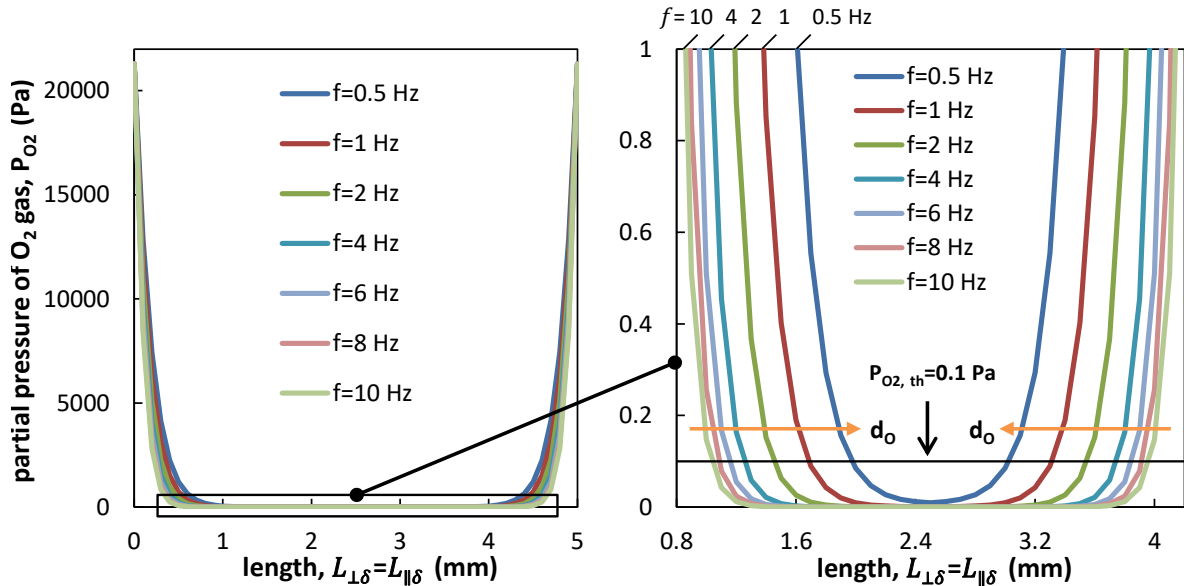


Figure 5.9: Evolution of the oxygen partial pressure with the increase in frequency from 0.5 to 10 Hz ($N=20000$ cycles, $p=100$ MPa, $\delta_g=\pm 100$ μm , and $A=5\times 5=25$ mm^2).

Figure 5.10 shows the evolution of the EDX maps and line scans with the increase in frequency compared with those predicted numerically by ADR approach. Note that numerical line scans are constructed by giving two arbitrary high and low constant intensities for $P_{O_2} \geq P_{O_2, th}$ and $P_{O_2} < P_{O_2, th}$ respectively. A rather good correlation is observed between numerical ADR simulations and experimental results. Indeed, both of them show extension of the inner adhesion area with the increase of the frequency from 0.5 to 10 Hz. It is worth mentioning that the latter exhibits an evident square shape (especially at 10 Hz) which is also captured by the simulations validating the hypothesis of oxygen distance isotropic distribution in case of square contact area.

Figure 5.11 compares the evolution of the experimental and numerical oxygen distance values d_O for frequencies ranging from 0.5 to 10 Hz. Established from only three calibration tests ($f=0.5$, 1 & 10 Hz), this analysis confirms that the ADR approach is able to capture the decreasing trend of the oxygen distance obtained experimentally with a correlation coefficient reaching 99%.

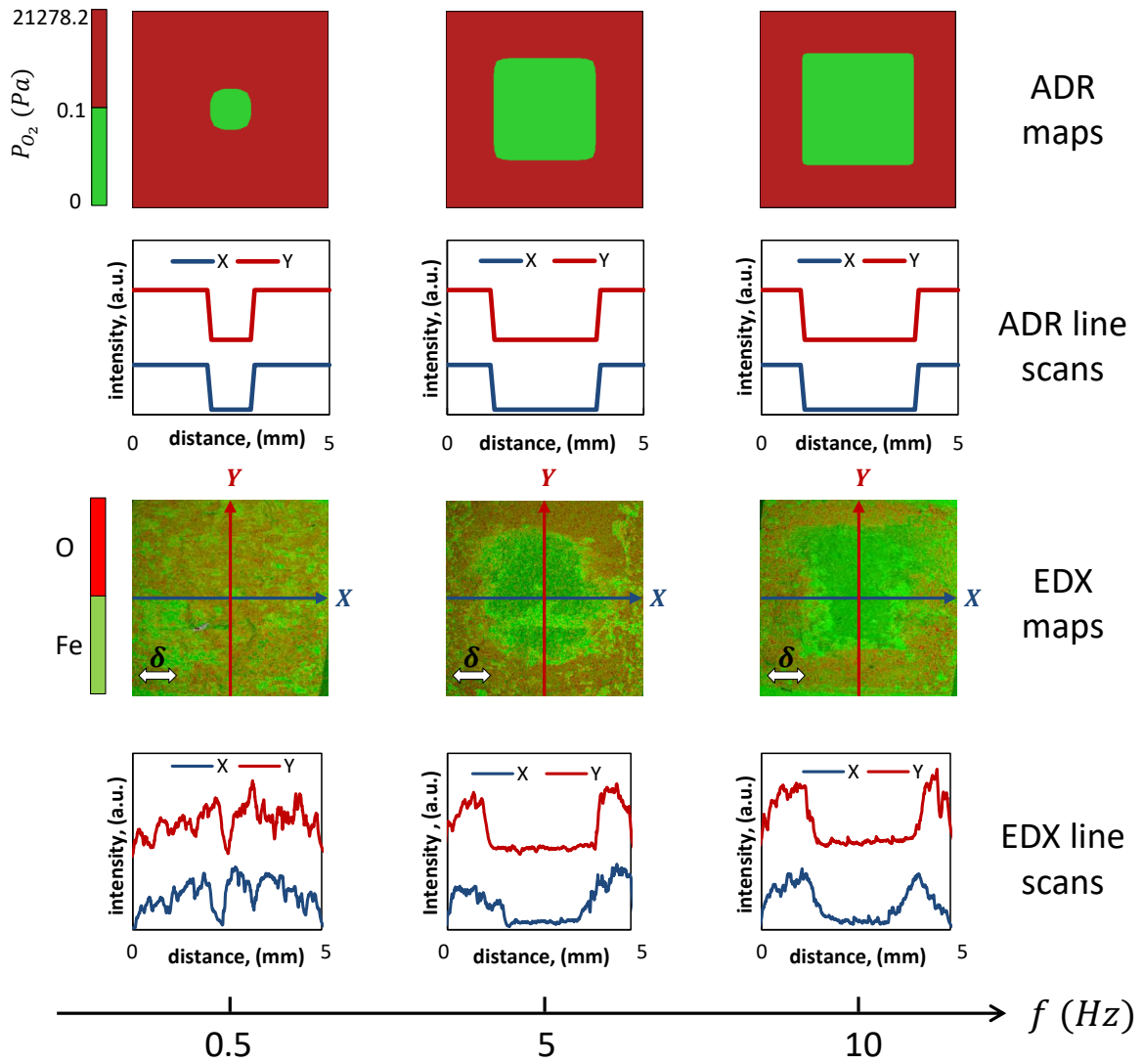


Figure 5.10: Correlation between EDX and numerical ADR maps and the corresponding line scans revealing the growth of adhesion zone with the increase in the sliding frequency from 0.5 to 10 Hz ($N=20000$ cycles, $p=100$ MPa, $\delta_g=\pm 100$ μm , and $A=5 \times 5=25$ mm^2).

From the ADR simulation 5.11, a simplified power law can be extracted such that:

$$d_O = 1.72 \times f^{-0.21} \quad (5.46)$$

This result is very interesting as it shows that using the ADR physical modelling of the COC, it is possible to demonstrate the empirical power law formulation previously introduced in Chapter 4 to formalize the evolution of d_O as a function of the applied frequency.

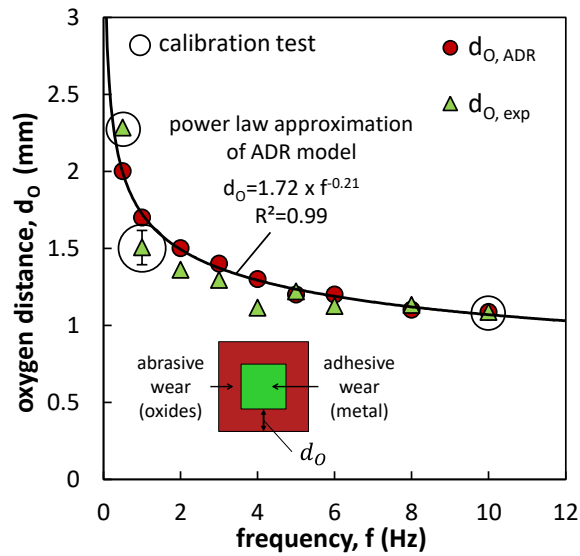


Figure 5.11: Correlation between the experimental ($d_{O,exp}$) and the predicted oxygen distance from ADR approach ($d_{O,ADR}$) as a function of the sliding frequency ($N=20000$ cycles, $p=100$ MPa, $\delta_g=\pm 100$ μm , and $A=5 \times 5=25$ mm^2).

5.5.3 Effect of contact pressure (p)

Figure 5.12 displays the evolution of the dioxygen partial pressure profile along the median axes L_x and L_y (equivalently $L_{\parallel\delta}$ and $L_{\perp\delta}$) with respect to the contact pressure varying from 25 to 175 MPa. As the case of frequency, increasing the contact pressure induces an increase in the Archard power density factor triggering in turn a higher consumption of the dioxygen molecules. This restrains the oxygen gas availability towards the center of the interface shifting the contact from pure abrasive to mixed abrasive-adhesive wear.

EDX maps and line scans are compared with those predicted numerically by ADR approach at different contact pressures (Figure 5.13). The experimental and numerical results appear to be highly correlated as both of them clearly reflect the remarkable shift in the wear regime from pure abrasive wear at low pressure ($p=25$ MPa) to a mixed abrasive-adhesive wear when higher Archard power is dissipated in the interface.

Figure 5.14 displays the evolution of the experimental and numerical oxygen distance values d_O for contact pressures ranging from 25 to 175 MPa. The decreasing evolution of d_O is markedly detected by the ADR model where a simplified power law can be estimated such that:

$$d_O = 5.34 \times p^{-0.24} \quad (5.47)$$

A very good correlation is observed between the model and the experiments although no pressure calibration was done. This indirectly supports the stability of the model and the Archard power density factor as a pertinent variable to formalize the reaction rate of the di-oxygen molecules.

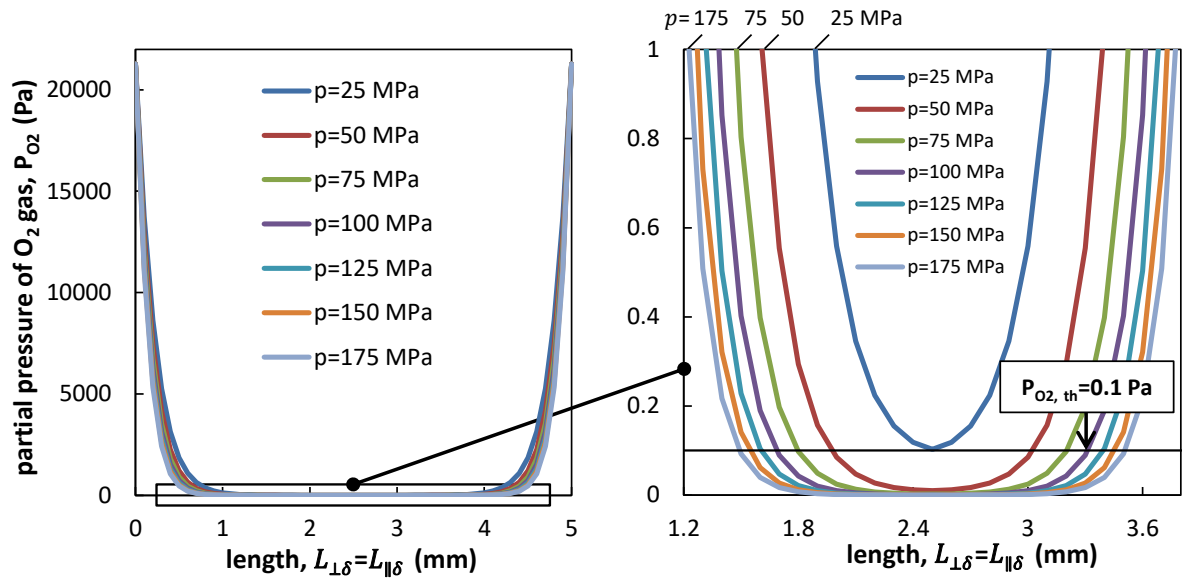


Figure 5.12: Evolution of the oxygen partial pressure with the increase in contact pressure from 25 to 175 MPa ($N=20000$ cycles, $f=1$ Hz, $\delta_g=\pm 100 \mu m$, and $A=5 \times 5=25 \text{ mm}^2$).

The ADR model slightly overestimates the oxygen distance observed experimentally. This comes from the fact that increasing the contact pressure compacts the surface roughness and the debris layer which reduces the porosity and hence the permeability of the latter. Therefore, the diffusion of dioxygen molecules towards the center of the interface will be very limited. However, in the current investigation and for the sake of simplicity, the porosity is assumed to be constant ($a=0.48$) whatever the loading condition. This fact can explain the slight discrepancy recognized between experimental and numerical ADR results. Undeniably, by introducing a dynamic porosity dependent on contact pressure (Equation 5.43), this difference can be easily reduced. Unfortunately due to the lack of experimental data the effect of contact pressure on porosity cannot be formalized.

5.5.4 Archard power density factor formulation

Figure 5.15 compiles the evolution of the experimental and numerical oxygen distance as a function of the Archard power density factor (i.e. “pv” factor) for various contact pressures and sliding frequencies. Interestingly, all data points appear to follow a single master curve which can be predicted by the ADR model as:

$$d_O = 0.87 \times \omega^{-0.22} \quad (5.48)$$

This very nice correlation embracing a wide range of experiments confirms the stability of the model and comes in agreement with the contact oxygenation concept (COC). This emphasizes that the higher the Archard power density dissipated in the contact, the faster the consumption of di-oxygen molecules and consequently the smaller the oxygen distance. Similar tendency

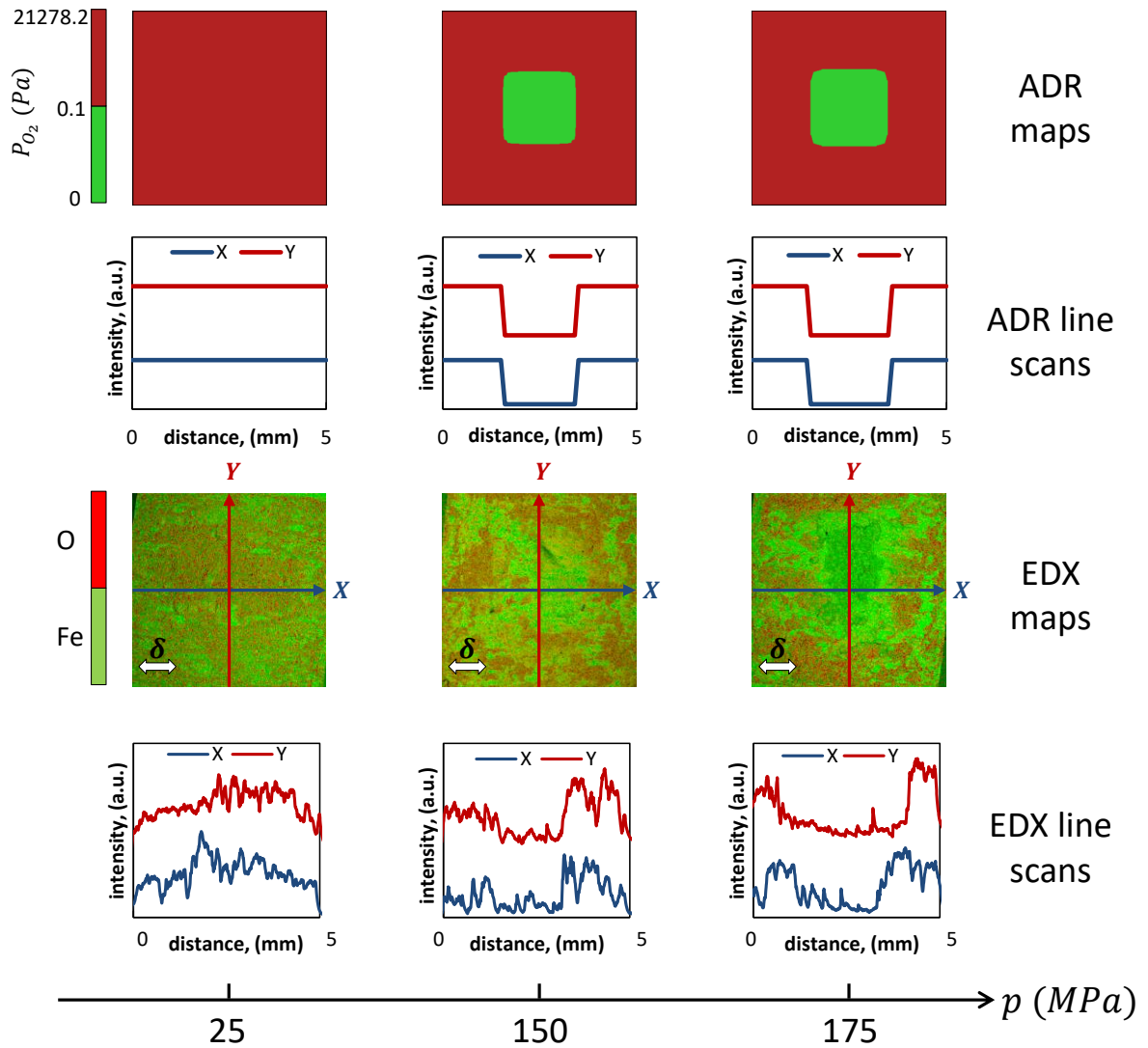


Figure 5.13: Correlation between EDX and numerical ADR maps and the corresponding line scans showing the growth of adhesion zone with the increase in the contact pressure from 25 to 175 MPa ($N=20000$ cycles, $f=1$ Hz, $\delta_g=\pm 100$ μm , and $A=5\times 5=25$ mm^2).

was observed in previous studies on titanium [55, 56] and steel alloys [51]. The given results are established for the studied steel interface. Other “non-noble” metallic materials, exhibiting different surface reactivity with oxygen like copper, aluminum or titanium alloys, may lead to different results. Hence, further works will be done to evaluate how the proposed formulation can be applied to predict the partition between abrasive and adhesive wear areas in fretting interfaces (i.e. the oxygen distance) for various metal alloys and various loading conditions.

5.5.5 Effect of contact area (A)

It was shown in Chapter 4 that the contact orientation with respect to the sliding direction has insignificant effect on the oxygen distance at least in the range investigated. Hence, in this

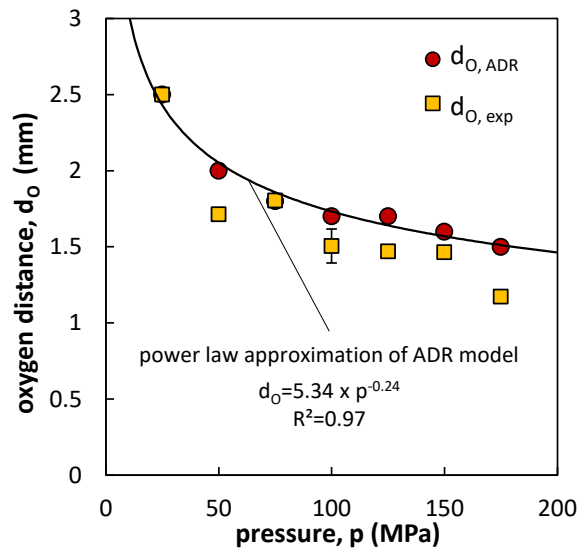


Figure 5.14: Correlation between the experimental ($d_{O,exp}$) and the predicted oxygen distance from ADR approach ($d_{O,ADR}$) as a function of the contact pressure from 25 to 175 MPa ($N=20000$ cycles, $f=1$ Hz, $\delta_g=\pm 100$ μm , and $A=5 \times 5=25$ mm^2).

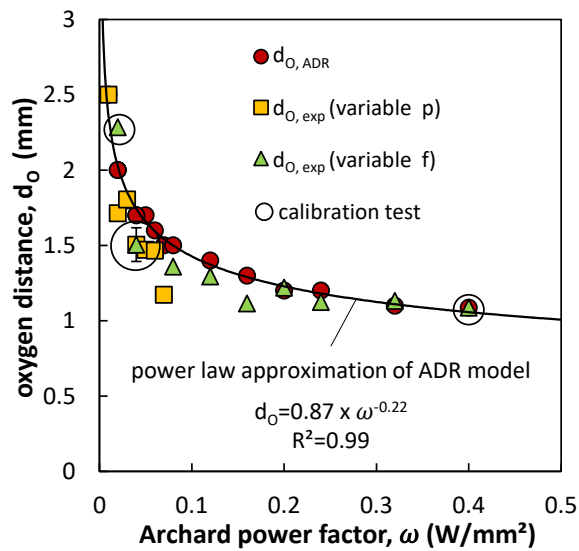


Figure 5.15: Correlation between the experimental ($d_{O,exp}$) and the predicted oxygen distance from ADR approach ($d_{O,ADR}$) as a function of Archard power density factor ω ($N=20000$ cycles, $\delta_g=\pm 100$ μm , and $A=5 \times 5=25$ mm^2).

chapter tests only test with variable $L_{\perp\delta}$ (i.e. L_y) will be compared with the ADR simulations at constant $L_{\parallel\delta}=5$ mm. The evolution of oxygen partial pressure with the apparent contact area is depicted in Figure 5.16. Indeed, assuming that contact size does not affect the dioxygen consumption rate, it is expected from COC to achieve homothetic oxygen partial pressure profiles. This tendency is effectively confirmed by the given ADR approach. For small contact area, P_{O_2} profile remains above $P_{O_2,th}$. On the other hand, P_{O_2} profile decreases below $P_{O_2,th}$ for larger

contact areas since the latter is large enough to consume the available dioxygen molecules before reaching the center of the contact.

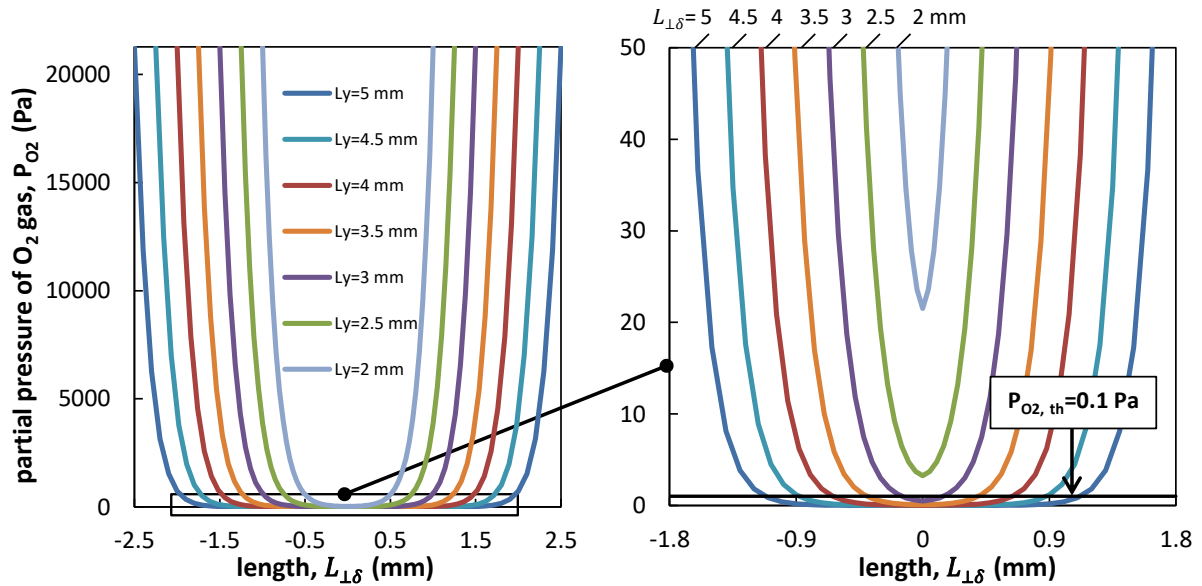


Figure 5.16: Evolution of the oxygen partial pressure with the increase in the apparent contact area from 10 to 25 mm^2 ($N=20000$ cycles, $p=100$ MPa, $\delta_g=\pm 100$ μm , and $f=1$ Hz).

Figure 5.17 compares the evolution of the EDX maps and line scans to those predicted numerically by ADR approach at different contact areas. Once again, good correlation is observed between numerical and experimental results. As reflected experimentally by EDX analysis, decreasing the contact area causes a remarkable recession in the adhesive wear until it completely vanishes when the contact area is less than 15 mm^2 . This tendency is predicted by the given ADR model where both numerical maps and line scans seem to highly mimic the experimental EDX observations.

Figure 5.18 illustrates the evolution of the experimental and numerical oxygen distance values d_O when variable contact area is investigated. Note that the data points are limited to the cases where the adhesion area is not zero (i.e. $A_{ad} > 0$). In fact, both experiments and simulation reveal the same tendency showing constant d_O around 1.60 mm whatever the contact size. However, ADR model seems to slightly overestimate the d_O oxygen distance which might be ascribed to a slight overestimation of the porosity and/or the threshold oxygen partial pressure. Nevertheless, the mean relative error is nearly 16% which indirectly supports the stability of the proposal.

5.5.6 Quantitative validation of ADR approach

The experimental oxygen distance “ $d_{O,exp}$ ” is compared with that expected by ADR approach “ $d_{O,ADR}$ ” such that the data points associated to pure abrasive wear (i.e. $A_{ad}=0$) are excluded from the analysis. By combining the results of variable contact area, contact pressure and sliding frequency, a good correlation emerges as shown in Figure 5.19a. This lends support to

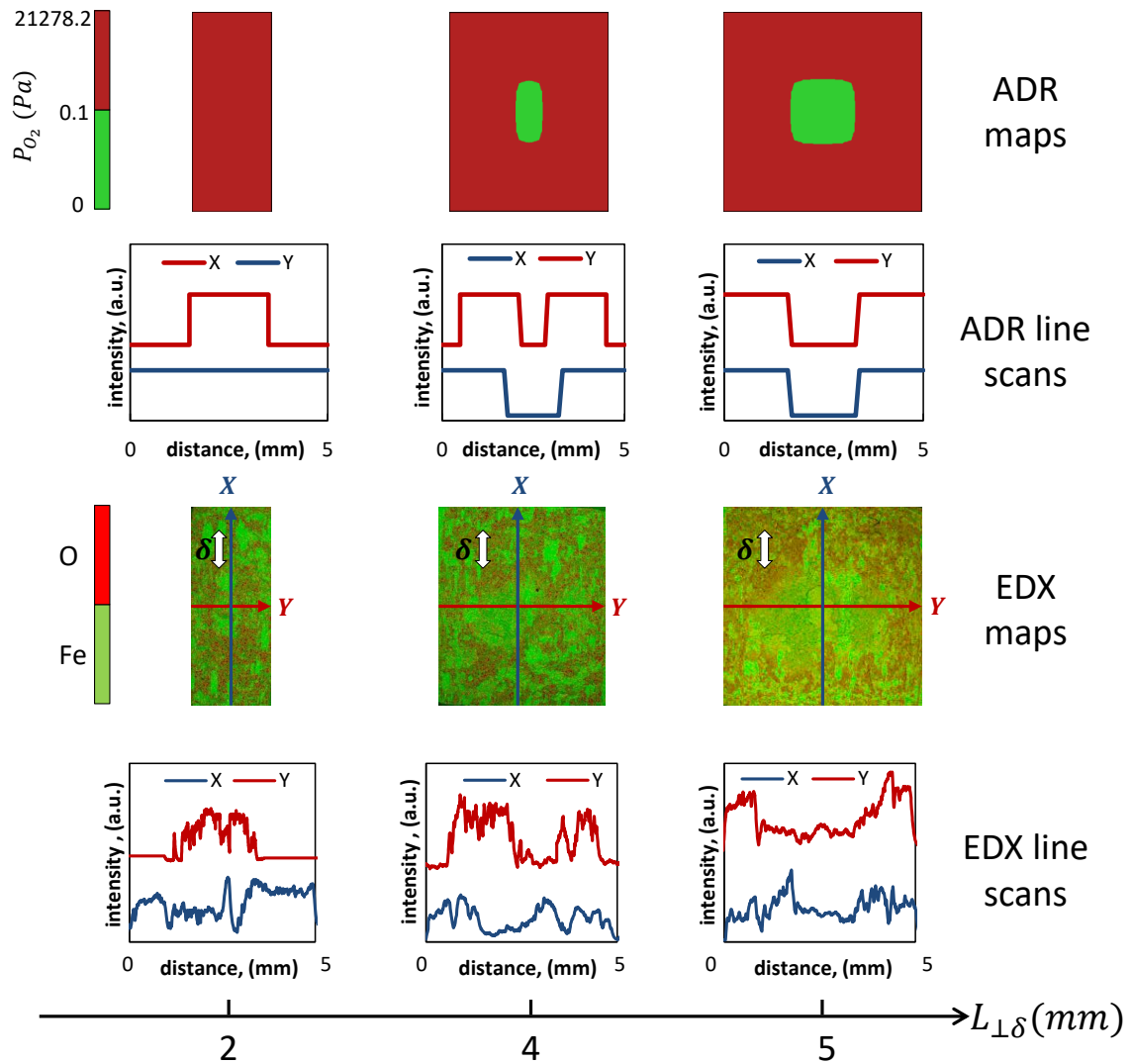


Figure 5.17: Correlation between EDX and numerical ADR maps and the corresponding line scans showing the growth of adhesion area with the increase of the apparent contact area from 10 to 25 mm^2 ($N=20000$ cycles, $p=100$ MPa, $\delta_g=\pm 100$ μm , and $f=1$ Hz).

the current ADR approach as an effective tool to predict the oxygen distance at different loading conditions.

Figure 5.19b compares the experimental abrasive wear area ($A_{ab,exp}$) to that foretold by ADR approach ($A_{ab,ADR}$) considering full abrasive and mixed abrasive-adhesive wear regimes. A very good correlation ($R^2=0.89$) unfolds between the experimental abrasion areas and those predicted by ADR model. The model was calibrated using only 3 frequency tests whereas Figure 5.19 compiles more than 24 experiments varying frequency, contact pressure and contact size. This indirectly supports the stability of the given ADR approach to predict the partition of abrasive and adhesive wear domains in fretting interfaces.

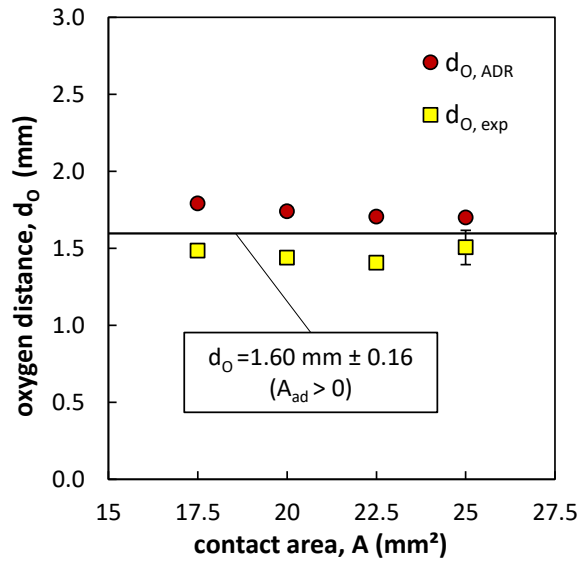


Figure 5.18: Correlation between the experimental ($d_{O,exp}$) and the predicted oxygen distance from ADR approach ($d_{O,ADR}$) as a function of the apparent contact area for $A_{ad} > 0$ (N=20000 cycles, p=100 MPa, $\delta_g = \pm 100 \mu m$, and f=1 Hz).

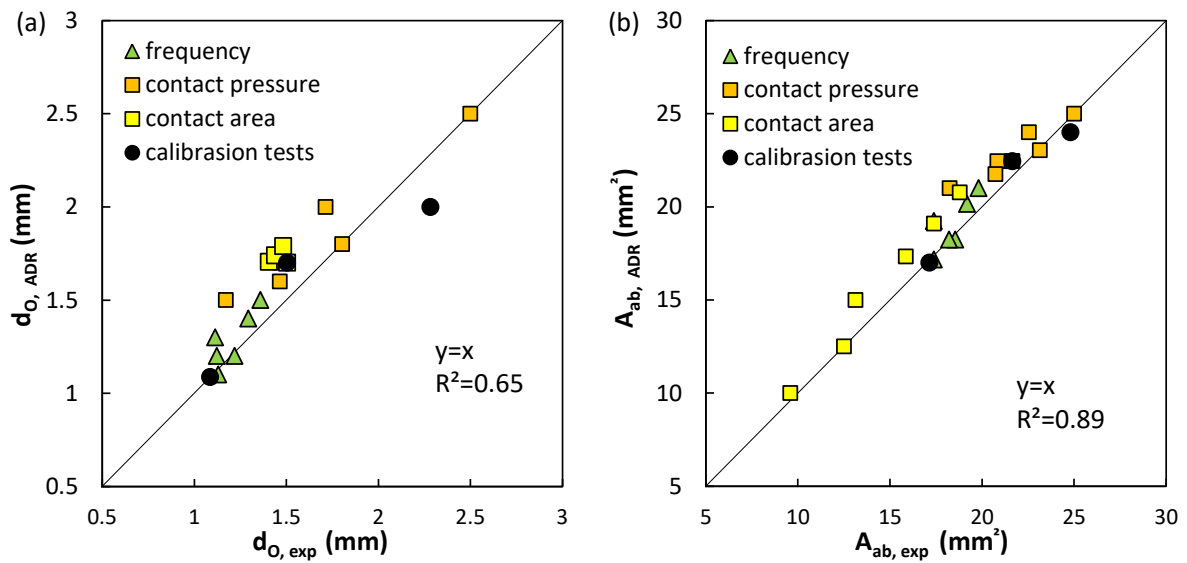


Figure 5.19: Comparing the experimental and the predicted results (ADR approach) for (a) the oxygen distance “ d_O ”; and (b) the abrasion area “ A_{ab} ”.

5.6 Discussion

The current chapter aims at explaining and modelling contact oxygenation process within a flat-on-flat fretting interface. An advection-dispersion-reaction approach (ADR) is suggested such that the debris bed is considered a compact powdery porous medium allowing the transport of atmospheric gases namely oxygen and nitrogen. The oxidation reaction of freshly exposed metal provides an important sink term for oxygen gas. This promotes a change of the gas

consumption inducing pressure and concentration gradients within the contact which trigger advection and dispersion processes. By assuming that nitrogen gas has a negligible interaction with the exposed metal during fretting, the given ADR model permits capturing the decay of oxygen partial pressure from the borders towards the center of the contact which explains the contact oxygenation concept. Defining a threshold oxygen partial pressure $P_{O_2, th}$, the partition between abrasion-oxidation and adhesion domains can be predicted whereby oxidation prevails whenever $P_{O_2} \geq P_{O_2, th}$, and adhesion is activated otherwise. Based on this assumption, oxygen distance can be defined numerically as the distance between the contact borders and the position where oxygen pressure starts to fall below $P_{O_2, th}$. This allows comparing experimental and numerical results by tracking oxygen distance value. Former studies showed that contact pressure and sliding frequency highly affect wear mechanisms [56]. Indeed, low loading conditions induce low Archard power density factor ω (i.e. equivalent “p.v” factor). This leads to pure abrasive wear over the whole interface. On the other hand, high Archard power density factor triggers composite adhesive-abrasive wear exhibiting metal transfers in the inner part of the contact enclosed by an abrasive wear corona on the lateral sides. This partition in wear mechanisms stems from the raise in surface shear strain rate, metal exposure rate and ultimately the rate of the reaction with the interfacial dioxygen molecules. As a result, higher oxygen consumption and consequently smaller oxygen distance will be obtained. Viewed in this light, increasing the Archard power density factor is translated in the ADR approach by increasing the reaction term of dioxygen molecules. Doing so, oxygen distance along with abrasion-adhesion EDX maps can be simulated.

The model is further validated for a wide range of sliding frequencies, contact pressures and contact sizes using plain crossed flat-on-flat samples. In fact, by decreasing the contact size, while keeping the same reaction rate, oxygen partial profiles will translate progressively from below to above $P_{O_2, th}$ which induces transition from mixed abrasive-adhesive to full abrasive domain.

Good predictions were achieved although many hypotheses have been considered to describe the interface. Thus, it appears interesting to evaluate how debris bed properties namely the porosity, particle size and permeability can influence these predictions. A sensitivity analysis was therefore carried out where these parameters are varied separately while fixing the tribological loadings on the reference condition (N=20000 cycles, p=100 MPa, $\delta_g = \pm 100 \mu m$, f=1 Hz and A=25 mm²) (Figure 5.20).

It appears that the particle size and the intrinsic permeability have a little effect on the oxygen distance which remained unchanged around $d_O \approx 1.7$ mm. A variation of the particle size from 1 to 10 μm and a fluctuation of the permeability from 2.27×10^{-15} to $2.27 \times 10^{-13} m^2$ lead to a small increase of the contact oxygenation (i.e. oxygen distance d_O) of less than 5%. This smooth rising can be attributed to the easier access of oxygen provided by the higher particle size and consequently higher permeability based on Equation 5.8. By contrast, the porosity of the debris bed plays a critical effect on the contact oxygenation. When this latter rose from 0.1 to 0.9,

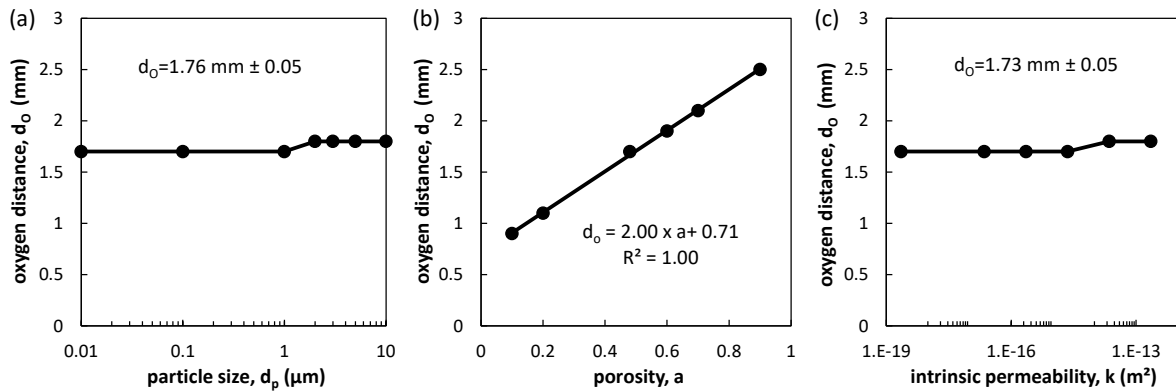


Figure 5.20: Evolution of the oxygen distance d_o as a function of (a) the particle size “ d_p ”, (b) the intrinsic permeability of the debris bed “ k ” and (c) the porosity “ a ” computed for the reference loading conditions (i.e. $N=20000$ cycles, $p=100$ MPa, $\delta_g=\pm 100 \mu\text{m}$, $f=1$ Hz and $A=25 \text{ mm}^2$).

the oxygen distance increased linearly from 0.9 to 2.5 mm shifting the interface from severely adhesive to pure abrasive wear. This is due to the fact that increasing the porosity, likewise the particle size and permeability, allows more access of oxygen to the inner part of the surface and consequently higher oxygen distance. However, the little sensitivity of the model to the particle size and permeability compared to the case of porosity stems from the fact that the former affect only advection process whereas the latter affects both advection and diffusion processes. This suggests also that the gas transport is much more governed by diffusion than by advection process which comes in agreement with previous studies reported in literature [162, 177]. Note that when increasing the particle size, the porosity and the permeability beyond $5 \mu\text{m}$, 0.8 and $5 \times 10^{-14} \text{ m}^2$ respectively, the time step has to be decreased by 10 to 100 times which implies higher computation cost. To conclude, it can be argued that among the debris bed properties, the driving factor is the porosity coefficient. This suggests that future development must be undertaken to establish direct and/or indirect identification procedures to properly formalize this value, taking into account for instance the effect of the contact pressure or the sliding conditions. However, applying a basic estimation of this latter variable, this investigation proposes that ADR model coupled with COC concept appears as a pertinent quantitative starting approach not only to explain the partition between abrasive-oxidative and adhesive wear but also the transition in wear mechanisms from mixed abrasion-adhesion to full abrasion when several loading conditions are considered.

As previously mentioned, this analysis only considers the dioxygen molecules as driving parameters of the wear processes. However, the ADR model is also able to establish the partition between dioxygen and dinitrogen concentrations within the interface. Figure 5.21a portrays the evolution of the partial pressures of oxygen and nitrogen gases along with the total pressure within the debris bed at the reference test in 2D and 3D. As expected by contact oxygenation concept, the partial pressure of O_2 gas is maximum at the borders of the contact. Then it decreases as the oxygen traverses the borders towards the center of the contact. On the other

hand, the partial pressure of N_2 is minimum at the borders (i.e. similar to ambient air condition) but increases inside the contact due to the advection process which tends to compensate the decay in the total pressure of the gas mixture. This conclusion is quite interesting as it suggests that in the inner part of the contact, an additional N_2 partial pressure is observed which can explain and potentially quantify the exotic nitriding process observed at room temperature in the inner part of titanium fretting interfaces (Figure 5.21b) [55, 56, 70].

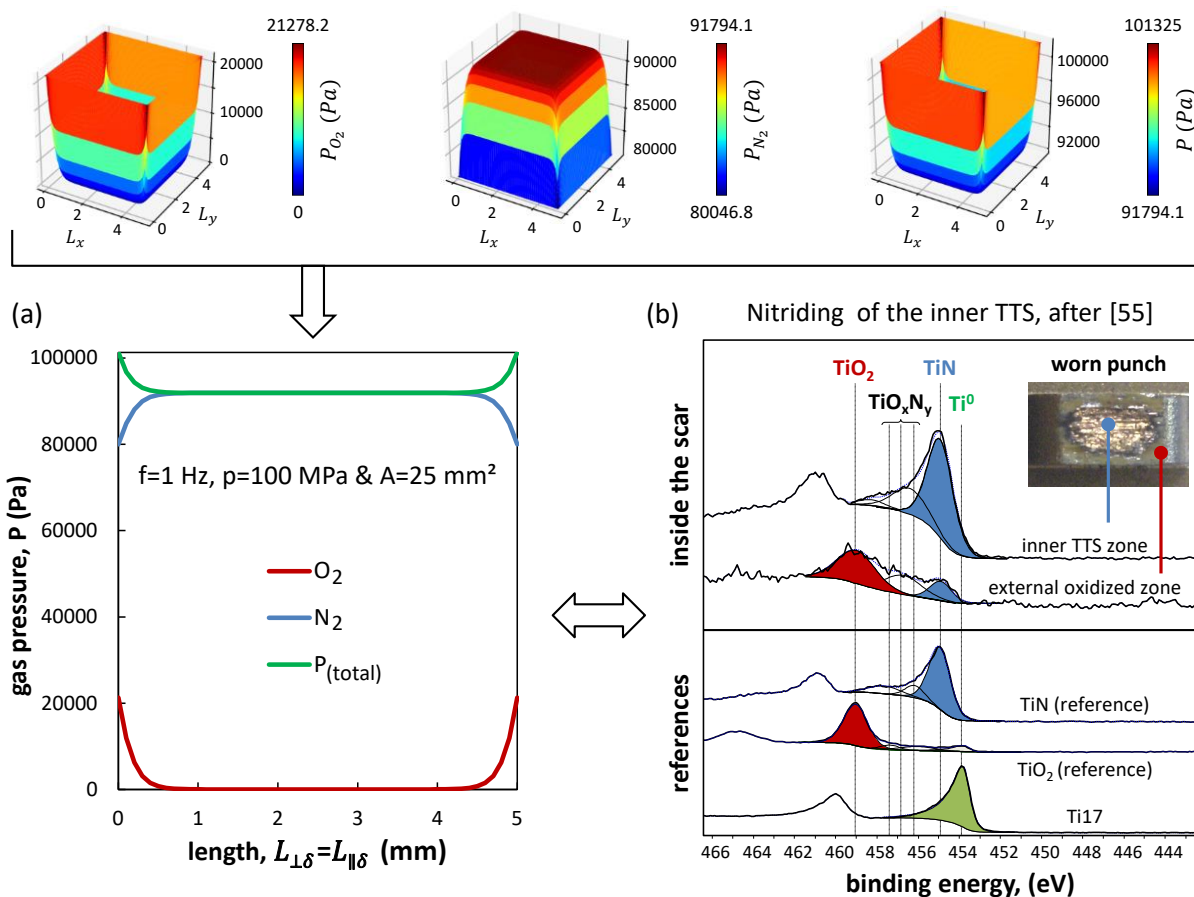


Figure 5.21: (a) 2D and 3D graphs showing the evolution of the partial pressures of oxygen and nitrogen gases along with the total pressure within the debris bed at the reference test; (b) XPS spectra of the inner adhesion zone and the surrounding oxidized abrasion corona giving evidence of Ti17 nitriding inside the TTS (after [55]).

On the other hand, by depriving oxygen and in turn increasing the concentration of nitrogen gas, such air distilling process presently modelled using ADR approach can explain the nitriding process observed in many closed fretting interfaces.

The given ADR approach appears as an interesting strategy to better predict the fretting wear phenomenon taking into account the tribo-oxidation processes operating within the interface. However, the present formulation is a first step which can be improved in many aspects to better formalize the effect of materials and contact loadings.

For instance, the given formulation does not consider the worn contact area extension classically observed for Hertzian contacts. Future developments are now required to combine both surface wear and ADR analyses in order to generalize this approach for usual sphere-on-flat and cylinder-on-flat fretting contacts.

The model considers a steady state description which was a posteriori confirmed by experiments where oxygen distance d_O stabilizes after a few hundreds of cycles (Chapter 4). However, there is a key interest to take into account the transient period particularly for a non-conformal Hertzian contacts showing variation in contact area and contact pressure.

This analysis must be also extended to other materials like titanium or bronze alloys to establish how their surface reactivity can influence adhesive wear extension and to check how the ADR model will capture such evolutions.

This material analysis should also be correlated with environmental investigations [46, 184]. Indeed, by performing fretting wear tests under variable oxygen partial pressure conditions, it will be possible to verify the stability of the ADR approach to predict the oxygen distance and consequently adhesive wear extension. This helps better quantify the $P_{O_2, th}$ threshold values as a function of the studied materials.

As said previously, the model can be further ameliorated by better formalizing the effect of the contact pressure which not only affects the oxygen consumption rate through friction power dissipation but also the porosity and the permeability of the debris bed.

Similar investigation must be undertaken regarding the effect of sliding amplitude whose role is not yet well understood in literature as it contributes not only in friction work dissipation but also on the ejection of the third body particles [194] which affect the intrinsic properties of the porous debris bed.

Hence, investigating and modelling all these aspects through a combined surface wear and ADR approach, appears as a challenging scientific project which will constitute our main objective in future investigations.

5.7 Conclusion

The purpose of this chapter is to explain and model contact oxygenation observed in fretting contacts. This is achieved by modelling oxygen transport using an advection-dispersion-reaction (ADR) approach by considering debris bed as compact powdery porous medium traversed by two gases: oxygen and nitrogen. From these investigations, the following points can be outlined:

- Using this ADR model, it was possible to predict the so-called oxygen distance (d_O) marking the transition between abrasive wear area in the outer part of the fretting scar and the adhesive wear area (i.e. metal transfer) observed in the inner part of the contact.

-ADR model, which was calibrated using only three fretting tests at different frequencies, was able to predict wide range of experimental conditions including sliding frequency, contact pressure and contact size. This, a posteriori, confirms the stability of this approach.

-Sensitivity analysis dedicated to study debris bed properties pointed out that the controlling factor of the interface properties is the porosity parameter. In the present investigation, a constant porosity value was assumed. Despite the simplicity of this hypothesis, good predictions were achieved. However, future investigations should be undertaken to better formalize this parameter taking into account, for instance, the effect of the contact pressure.

-The reaction rate coefficient of the model was formalized using a basic power-law formulation involving Archard power density factor. Although it is simple, the good prediction obtained using this approximation suggests that the Archard power density parameter (i.e. $p.v$ factor) seems to be a pertinent physical variable to formalize the reaction rate and finally predict the oxygen distance.

-ADR model was validated at different sliding frequencies, contact pressures and contact sizes. Nevertheless, it still needs to be extended in future development to capture the effect of the sliding amplitude and metal reactivity.

To conclude, despite its simplicity, the given ADR model provides, for the first time, a quantitative description of the contact oxygenation concept (COC) and appears as a challenging strategy to develop future multiphysics modelling of fretting wear processes.

General conclusion and perspectives

General conclusion

The purpose of this research work is to understand and model dry fretting wear of a flat-on-flat steel (34NiCrMo16) contact submitted to various loading conditions including number of fretting cycles, sliding amplitude, contact pressure, sliding frequency, contact size and contact orientation with respect to the sliding direction. This crossed flat contact configuration, being the pivot of this work, is particularly selected as it allows having a constant contact area and contact pressure during fretting wear extension. This is not the case for Hertzian configurations where the contact pressure changes with the test duration due to wear extension and the associated growth in the contact area. Hence, the main findings of this thesis are summarized as follows (Figure 5.22):

(a) Wear kinetics

- The multi-scale parametric experimental study of flat contact revealed that wear kinetics highly depends on the aforesaid loading conditions.
- A wear volume prediction model is established using a single energy wear rate where a weighted energy wear formulation is introduced by combining the impact of all loading parameters. The model was validated using experiments outside the calibration domain involving plain and macro-textured samples.
- It was noticed that under all the loading conditions, a mixed regime of abrasion and adhesion is prevalent in the interface. To interpret this composite wear regime and the related wear rate evolution, both the contact oxygenation concept (COC) and third body approach (TBA) were discussed.
- It was also possible to decouple the relative effect of COC and TBA regarding the contact size wear-rate fluctuations assuming that the lateral flow of debris particles against the sliding direction has a limited impact on wear kinetics. Although TBA appears the dominating factor at least for the studied conditions, it appears that COC plays a significant effect.

(b) Evolution of adhesive wear extension in fretting interface

- The evolution and transition of wear regimes (abrasion and adhesion) with respect to the load-

ing conditions is investigated by introducing the “oxygen distance, d_O ” defined as the distance between the contact extremities and the limits of adhesion domain.

- Increasing contact pressure and sliding frequency decreased oxygen distance and expanded adhesive wear area which can be attributed to the high friction power dissipation at the interface. This raises surface shear strain and the reaction rate with the interfacial dioxygen molecules causing an oxygen-starved environment towards the contact center. However, oxygen distance was shown to be stable with the number of cycles, sliding amplitude and contact area.

- An empirical oxygen-distance prediction model is proposed which depends on the contact pressure and the frequency. This model was validated by using plain and macro-textured samples.

(c) Modelling adhesive wear extension

- The evolution of contact oxygenation and oxygen distance with fretting loadings can be physically described by modelling oxygen transport using an advection-dispersion-reaction (ADR) approach by considering debris bed as compact powdery porous medium traversed by atmospheric gases.

- ADR model was calibrated using only three fretting tests at different frequencies assuming a basic power-law formulation of the reaction rate coefficient involving Archard power density factor.

- ADR was able to predict a wide range of experimental conditions including sliding frequency, contact pressure and contact size.

- Sensitivity analysis dedicated to study debris bed properties pointed out that the controlling factor of the interface properties is the porosity parameter.

Perspectives

- The proposed empirical wear-kinetics model assumed an averaged global wear-rate description neglecting the composite abrasive-adhesive nature of wear and consequently the inherited wear-rate local variations along the fretting scar. This suggests that future work needs to consider a composite wear model with wear rate dependent on the wear mechanisms (abrasion and adhesion) than the current global approach involving constant wear rate along the interface.

- More reliable decoupling approach of COC and TBA necessitates quantifying the effect of longitudinal and lateral third body flows in wear kinetics. So, upcoming work should investigate this aspect by applying for example DEM simulations or dedicated experimental campaigns to study the role of these TB flows.

- ADR approach, being a pertinent starting strategy for better analysis of fretting wear phenomenon, can be improved in many ways as combining both surface wear and ADR analyses in order to generalize this approach for usual Hertzian contacts.

- Very short (transient) and very long test durations should be further investigated in both wear

kinetics and ADR models especially for a non-conformal Hertzian contacts undergoing variation in contact area and contact pressure with the test duration.

- The wear kinetics and ADR analyses must be also extended to other materials like titanium, aluminum, chromium metals to check how their surface reactivity can influence adhesive wear extension.

- This material analysis should be also correlated with environmental investigations as performing fretting wear tests under variable oxygen partial pressure conditions which helps verify the stability of the ADR approach. This allows tracking wear kinetics at variable oxygen partial pressure conditions for different materials and loading conditions.

- Debris bed properties, namely porosity should be equally addressed since this parameter helps better formalize the effect of the contact pressure.

- Similar investigation must be undertaken regarding the effect of sliding amplitude as it contributes in both COC and TB flows making its physical interpretation and integration in ADR and wear kinetics models a real scientific challenge.

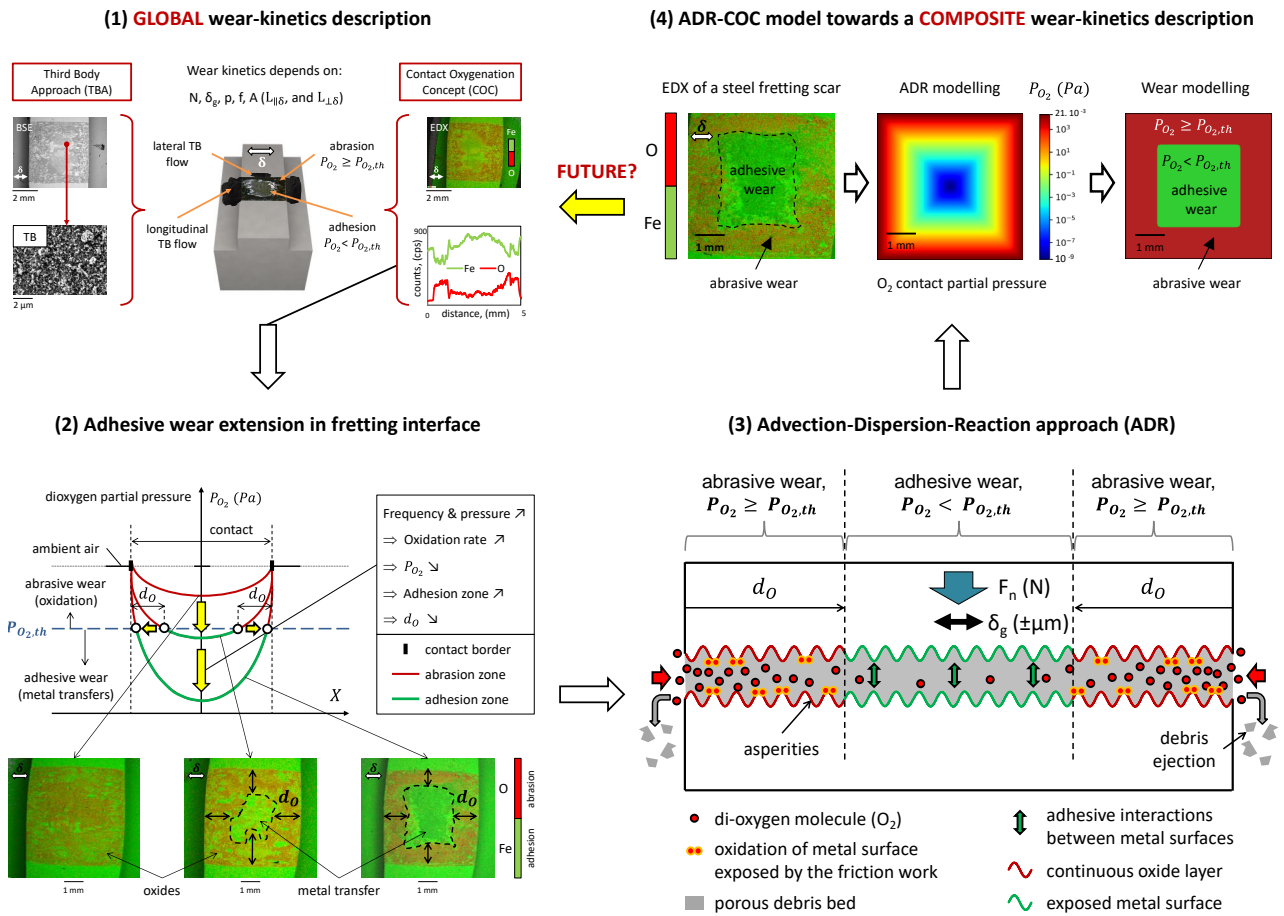


Figure 5.22: Summary of the research work conducted in this manuscript (2017-2020).

References

- [1] B. Bhushan, *Micro/nanotribology and its applications*, vol. 330. Springer Science & Business Media, 2012.
- [2] P. Jost, “Lubrication (tribology) - a report on the present position and industry’s needs,” 1966.
- [3] K. Holmberg and A. Erdemir, “Influence of tribology on global energy consumption, costs and emissions,” *Friction*, vol. 5, no. 3, pp. 263–284, 2017.
- [4] P. Ko, “Metallic wear—a review with special references to vibration-induced wear in power plant components,” *Tribology International*, vol. 20, no. 2, pp. 66–78, 1987.
- [5] E. Eden and W. Rose, “N. and cunningham, fl,” *Proc. Inst. Mech. Eng*, vol. 4, pp. 839–874, 1911.
- [6] G. Tomlinson, “The rusting of steel surfaces in contact,” *Proceedings of the Royal Society of London. Series A, Containing Papers of a Mathematical and Physical Character*, vol. 115, no. 771, pp. 472–483, 1927.
- [7] D. Godfrey, “Investigation of fretting by microscopic investigation,” *Nat. Advis. Comm. Aeronaut. Rep. 1009*, 1951.
- [8] D. Godfrey and J. M. Bailey, “Coefficient of friction and damage to contact area during the early stages of fretting i: Glass, copper, or steel against copper,” 1953.
- [9] J. Halliday and W. Hirst, “The fretting corrosion of mild steel,” *Proceedings of the Royal Society of London. Series A. Mathematical and Physical Sciences*, vol. 236, no. 1206, pp. 411–425, 1956.
- [10] A. Wayson, “A study of fretting on steel,” *Wear*, vol. 7, no. 5, pp. 435–450, 1964.
- [11] P. Hurricks, “The mechanism of fretting—a review,” *Wear*, vol. 15, no. 6, pp. 389–409, 1970.
- [12] D. Vingsbo and O. Soderberg, “On fretting maps,” *Wear*, vol. 126, no. 2, pp. 131–147, 1988.

- [13] Y. Berthier, L. Vincent, and M. Godet, “Velocity accommodation in fretting,” *Wear*, vol. 125, no. 1-2, pp. 25–38, 1988.
- [14] S. Fouvry, P. Kapsa, and L. Vincent, “Quantification of fretting damage,” *Wear*, vol. 200, no. 1-2, pp. 186–205, 1996.
- [15] J. Madge, S. Leen, I. McColl, and P. Shipway, “Contact-evolution based prediction of fretting fatigue life: effect of slip amplitude,” *Wear*, vol. 262, no. 9-10, pp. 1159–1170, 2007.
- [16] P. Hurricks, “The fretting wear of mild steel from room temperature to 200c,” *Wear*, vol. 19, no. 2, pp. 207–229, 1972.
- [17] L. Salles, L. Blanc, F. Thouverez, and A. Gousskov, “Dynamic analysis of fretting-wear in friction contact interfaces,” *International Journal of Solids and Structures*, vol. 48, no. 10, pp. 1513–1524, 2011.
- [18] J. Winkler, C. T. Georgakis, and G. Fischer, “Fretting fatigue behavior of high-strength steel monostrands under bending load,” *International Journal of Fatigue*, vol. 70, pp. 13–23, 2015.
- [19] Y. Xu, Z. Sun, and Y. Zhang, “Experimental and numerical investigations of fretting fatigue behavior for steel q235 single-lap bolted joints,” *Advances in Materials Science and Engineering*, vol. 2016, 2016.
- [20] QUAKETEK, “Seismic dampers – friction dampers, <https://www.quaketek.com/seismic-friction-dampers/>,” 2020.
- [21] B. Blanpain, H. Mohrbacher, E. Liu, J.-P. Celis, and J. Roos, “Hard coatings under vibrational contact conditions,” *Surface and Coatings Technology*, vol. 74, pp. 953–958, 1995.
- [22] H. Mohrbacher, J.-P. Celis, and J. Roos, “Laboratory testing of displacement and load induced fretting,” *Tribology international*, vol. 28, no. 5, pp. 269–278, 1995.
- [23] T. Lindley, “Fretting fatigue in engineering alloys,” *International journal of fatigue*, vol. 19, no. 93, pp. 39–49, 1997.
- [24] J. Hintikka, “Fretting induced friction, wear and fatigue in quenched and tempered steel,” 2016.
- [25] H. Heinrich, “Über die berührung fester elastischer körper,” *J. Die Reine Angew. Math*, vol. 92, pp. 156–171, 1881.
- [26] K. Johnson, “Contact mechanics cambridge univ,” *Press, Cambridge*, vol. 95, p. 365, 1985.
- [27] P. Arnaud, *Etude expérimentale et numérique de l’usure et de son influence sur les mécanismes de fissuration en fretting et fretting fatigue*. PhD thesis, Lyon, 2018.

- [28] N. Ohmae and T. Tsukizoe, “The effect of slip amplitude on fretting,” *Wear*, vol. 27, no. 3, pp. 281–294, 1974.
- [29] S. Gordelier and T. Chivers, “A literature review of palliatives for fretting fatigue,” *Wear*, vol. 56, no. 1, pp. 177–190, 1979.
- [30] S. Fouvry, P. Kapsa, and L. Vincent, “Analysis of sliding behaviour for fretting loadings: determination of transition criteria,” *Wear*, vol. 185, no. 1-2, pp. 35–46, 1995.
- [31] C. Mary, *Simulation expérimentale de l’usure du contact aube-disque de compresseur sous sollicitations de fretting*. PhD thesis, Ecole Centrale de Lyon, 2009.
- [32] R. D. Mindlin, “Compliance of elastic bodies in contact,” *J. Appl. Mech., ASME*, vol. 16, pp. 259–268, 1949.
- [33] L. Vincent, Y. Berthier, and M. Godet, “Testing methods in fretting fatigue: a critical appraisal,” in *Standardization of fretting fatigue test methods and equipment*, ASTM International, 1992.
- [34] P. Blanchard, C. Colombie, V. Pellerin, S. Fayeulle, and L. Vincent, “Material effects in fretting wear: application to iron, titanium, and aluminum alloys,” *Metallurgical Transactions A*, vol. 22, no. 7, pp. 1535–1544, 1991.
- [35] S. Fouvry, P. Kapsa, and L. Vincent, “An elastic–plastic shakedown analysis of fretting wear,” *Wear*, vol. 247, no. 1, pp. 41–54, 2001.
- [36] S. Fouvry, P. Kapsa, H. Zahouani, and L. Vincent, “Wear analysis in fretting of hard coatings through a dissipated energy concept,” *Wear*, vol. 203, pp. 393–403, 1997.
- [37] T. Quinn, “Review of oxidational wear: Part i: The origins of oxidational wear,” *Tribology International*, vol. 16, no. 5, pp. 257–271, 1983.
- [38] J. T. Burwell Jr, “Survey of possible wear mechanisms,” *Wear*, vol. 1, no. 2, pp. 119–141, 1957.
- [39] A. Misra and I. Finnie, “A classification of three-body abrasive wear and design of a new tester,” *Wear*, vol. 60, no. 1, pp. 111–121, 1980.
- [40] D. Tabor, “Wear—a critical synoptic view,” 1977.
- [41] P. Hurricks, “Some metallurgical factors controlling the adhesive and abrasive wear resistance of steels. a review,” *Wear*, vol. 26, no. 3, pp. 285–304, 1973.
- [42] F. Bowden, A. Moore, and D. Tabor, “The ploughing and adhesion of sliding metals,” *Journal of Applied Physics*, vol. 14, no. 2, pp. 80–91, 1943.
- [43] D. V. Keller Jr, “Adhesion between atomically clean surfaces,” tech. rep., SYRACUSE UNIV RESEARCH INST NY, 1964.

- [44] F. P. Bowden and G. Rowe, “The adhesion of clean metals,” *Proceedings of the Royal Society of London. Series A. Mathematical and Physical Sciences*, vol. 233, no. 1195, pp. 429–442, 1956.
- [45] A. Iwabuchi, “Fretting wear of inconel 625 at high temperature and in high vacuum,” *Wear*, vol. 106, no. 1-3, pp. 163–175, 1985.
- [46] A. Iwabuchi, T. Kayaba, and K. Kato, “Effect of atmospheric pressure on friction and wear of 0.45% c steel in fretting,” *Wear*, vol. 91, no. 3, pp. 289–305, 1983.
- [47] A. Merstallinger, E. Semerad, and B. Dunn, “Cold welding due to fretting under high vacuum, helium and in air,” in *7th European Space Mechanisms and Tribology Symposium*, vol. 410, p. 223, 1997.
- [48] T. Eyre and A. Baxter, “The formation of white layers at rubbing surfaces,” *Tribology*, vol. 5, no. 6, pp. 256–261, 1972.
- [49] E. Sauger, S. Fouvry, L. Ponsonnet, P. Kapsa, J. Martin, and L. Vincent, “Tribologically transformed structure in fretting,” *Wear*, vol. 245, no. 1-2, pp. 39–52, 2000.
- [50] S. Descartes and Y. Berthier, “Rheology and flows of solid third bodies: background and application to an mos1. 6 coating,” *Wear*, vol. 252, no. 7-8, pp. 546–556, 2002.
- [51] A. M. Kirk, P. H. Shipway, W. Sun, and C. J. Bennett, “The effect of frequency on both the debris and the development of the tribologically transformed structure during fretting wear of a high strength steel,” *Wear*, vol. 426, pp. 694–703, 2019.
- [52] V. Nurmi, J. Hintikka, J. Juoksukangas, M. Honkanen, M. Vippola, A. Lehtovaara, A. Mäntylä, J. Vaara, and T. Frondelius, “The formation and characterization of fretting-induced degradation layers using quenched and tempered steel,” *Tribology International*, vol. 131, pp. 258–267, 2019.
- [53] S. Descartes, C. Desrayaud, E. Niccolini, and Y. Berthier, “Presence and role of the third body in a wheel–rail contact,” *Wear*, vol. 258, no. 7-8, pp. 1081–1090, 2005.
- [54] E. Sauger, L. Ponsonnet, J. Martin, and L. Vincent, “Study of the tribologically transformed structure created during fretting tests,” *Tribology International*, vol. 33, no. 11, pp. 743–750, 2000.
- [55] C. Mary, S. Fouvry, J. Martin, and B. Bonnet, “Pressure and temperature effects on fretting wear damage of a cu–ni–in plasma coating versus ti17 titanium alloy contact,” *Wear*, vol. 272, no. 1, pp. 18–37, 2011.
- [56] S. Fouvry, P. Arnaud, A. Mignot, and P. Neubauer, “Contact size, frequency and cyclic normal force effects on ti–6al–4v fretting wear processes: an approach combining friction power and contact oxygenation,” *Tribology International*, vol. 113, pp. 460–473, 2017.

- [57] Z. Zhou, E. Sauger, J. Liu, and L. Vincent, “Nucleation and early growth of tribologically transformed structure (tts) induced by fretting,” *Wear*, vol. 212, no. 1, pp. 50–58, 1997.
- [58] J. Pezdernik, B. Podgornik, J. Vizintin, M. Kalin, and F. Vodopivec, “Three-body contact temperature fretting conditions,” *Tribology Series*, vol. 31, pp. 257–270, 1996.
- [59] J. Archard, “The temperature of rubbing surfaces,” *wear*, vol. 2, no. 6, pp. 438–455, 1959.
- [60] C. Colombie, Y. Berthier, A. Floquet, L. Vincent, and M. Godet, “Fretting: load carrying capacity of wear debris,” 1984.
- [61] E. Sproles Jr and D. Duquette, “Interface temperature measurements in the fretting of a medium carbon steel,” *Wear*, vol. 47, no. 2, pp. 387–396, 1978.
- [62] J. Greenwood and A. Alliston-Greiner, “Surface temperatures in a fretting contact,” *Wear*, vol. 155, no. 2, pp. 269–275, 1992.
- [63] D. Rigney, “Transfer, mixing and associated chemical and mechanical processes during the sliding of ductile materials,” *Wear*, vol. 245, no. 1-2, pp. 1–9, 2000.
- [64] P. Blanchard, *Usure induite en petits débattements: transformation tribologique superficielle d’alliages de titane*. PhD thesis, Ecully, Ecole centrale de Lyon, 1991.
- [65] E. Marc, *Analyse de la réponse tribologique d’un contact cylindre/plan soumis à des sollicitations de fretting sous chargement complexe: influence d’une solution Lithium-Bore*. PhD thesis, Lyon, 2018.
- [66] S. Descartes, M. Busquet, and Y. Berthier, “An attempt to produce ex situ tts to understand their mechanical formation conditions—the case of an ultra high purity iron,” *Wear*, vol. 271, no. 9-10, pp. 1833–1841, 2011.
- [67] S. Descartes, C. Desrayaud, and E. Rauch, “Inhomogeneous microstructural evolution of pure iron during high-pressure torsion,” *Materials Science and Engineering: A*, vol. 528, no. 10-11, pp. 3666–3675, 2011.
- [68] J. M. Shockley, C. Desrayaud, R. Chromik, and S. Descartes, “Significance of al₂o₃ particle morphology in the microstructure evolution of cold-sprayed al-al₂o₃ during unconstrained high-pressure torsion,” *Materials Science and Engineering: A*, vol. 684, pp. 510–516, 2017.
- [69] Y. Zhang, D. Choudhuri, T. W. Scharf, S. Descartes, and R. R. Chromik, “Tribologically induced nanolaminate in a cold-sprayed wc-reinforced cu matrix composite: a key to high wear resistance,” *Materials & Design*, vol. 182, p. 108009, 2019.
- [70] C. Mary, T. Le Mogne, B. Beaugiraud, B. Vacher, J.-M. Martin, and S. Fouvry, “Tribochemistry of a ti alloy under fretting in air: evidence of titanium nitride formation,” *Tribology letters*, vol. 34, no. 3, pp. 211–222, 2009.

- [71] H. Meng and K. Ludema, “Wear models and predictive equations: their form and content,” *Wear*, vol. 181, pp. 443–457, 1995.
- [72] J. Archard, “Contact and rubbing of flat surfaces,” *Journal of applied physics*, vol. 24, no. 8, pp. 981–988, 1953.
- [73] K. Johnson, “Contact mechanics and the wear of metals,” *Wear*, vol. 190, no. 2, pp. 162–170, 1995.
- [74] N. Fillot, I. Iordanoff, and Y. Berthier, “Simulation of wear through mass balance in a dry contact,” *J. Trib.*, vol. 127, no. 1, pp. 230–237, 2005.
- [75] H. Mohrbacher, B. Blanpain, J.-P. Celis, J. Roos, L. Stals, and M. Van Stappen, “Oxidational wear of tin coatings on tool steel and nitrided tool steel in unlubricated fretting,” *Wear*, vol. 188, no. 1-2, pp. 130–137, 1995.
- [76] S. Fouvry, T. Liskiewicz, P. Kapsa, S. Hannel, and E. Sauger, “An energy description of wear mechanisms and its applications to oscillating sliding contacts,” *Wear*, vol. 255, no. 1-6, pp. 287–298, 2003.
- [77] A. Dréano, S. Fouvry, and G. Guillonneau, “A tribo-oxidation abrasive wear model to quantify the wear rate of a cobalt-based alloy subjected to fretting in low-to-medium temperature conditions,” *Tribology International*, vol. 125, pp. 128–140, 2018.
- [78] C. Paulin, S. Fouvry, and S. Deyber, “Wear kinetics of ti-6al-4v under constant and variable fretting sliding conditions,” *Wear*, vol. 259, no. 1-6, pp. 292–299, 2005.
- [79] S. Fouvry, C. Paulin, and S. Deyber, “Impact of contact size and complex gross–partial slip conditions on ti-6al-4v/ti-6al-4v fretting wear,” *Tribology International*, vol. 42, no. 3, pp. 461–474, 2009.
- [80] A. Dreano, *Formalisation des mécanismes de tribo-oxydation d’un alliage de cobalt soumis à des sollicitations de fretting-usure: effet de la température*. PhD thesis, Lyon, 2019.
- [81] R. Merhej and S. Fouvry, “Contact size effect on fretting wear behaviour: application to an aisi 52100/aisi 52100 interface,” *Lubrication Science*, vol. 21, no. 3, pp. 83–102, 2009.
- [82] S. Fouvry and R. Merhej, “Introduction of a power law formulation to quantify the contact size effects on friction and wear responses of dry oscillating sliding contacts: application to a chromium steel interface,” *Wear*, vol. 301, no. 1-2, pp. 34–46, 2013.
- [83] A. Warmuth, S. Pearson, P. Shipway, and W. Sun, “The effect of contact geometry on fretting wear rates and mechanisms for a high strengthsteel,” *Wear*, vol. 301, no. 1-2, pp. 491–500, 2013.

- [84] A. Warmuth, P. Shipway, and W. Sun, “Fretting wear mapping: the influence of contact geometry and frequency on debris formation and ejection for a steel-on-steel pair,” *Proceedings of the Royal Society A: Mathematical, Physical and Engineering Sciences*, vol. 471, no. 2178, p. 20140291, 2015.
- [85] M. Godet, “The third-body approach: a mechanical view of wear,” *Wear*, vol. 100, no. 1-3, pp. 437–452, 1984.
- [86] D. Play and M. Godet, “Self-protection of high wear materials,” *ASLE TRANSACTIONS*, vol. 22, no. 1, pp. 56–64, 1979.
- [87] H. Heshmat and C. A. Heshmat, “The effect of slider geometry on the performance of a powder lubricated bearing,” *Tribology transactions*, vol. 42, no. 3, pp. 640–646, 1999.
- [88] H. Heshmat, “The effect of slider geometry on the performance of a powder lubricated bearing—theoretical considerations,” *Tribology transactions*, vol. 43, no. 2, pp. 213–220, 2000.
- [89] J. Bishop and C. M. Ettles, “The seizure of journal bearings by thermoelastic mechanisms,” *Wear*, vol. 79, no. 1, pp. 37–52, 1982.
- [90] T. Quinn, “Review of oxidational wear part ii: recent developments and future trends in oxidational wear research,” *Tribology international*, vol. 16, no. 6, pp. 305–315, 1983.
- [91] A. Dreano, S. Fouvry, and G. Guillonneau, “A combined friction energy and tribo-oxidation formulation to describe the high temperature fretting wear response of a cobalt-based alloy,” *Wear*, vol. 426, pp. 712–724, 2019.
- [92] Y. Sun, Y. Berthier, B. Fantino, and M. Godet, “A quantitative investigation of displacement accommodation in third-body contact,” *Wear*, vol. 165, no. 2, pp. 123–131, 1993.
- [93] N. Fillot, I. Iordanoff, and Y. Berthier, “Wear modeling and the third body concept,” *Wear*, vol. 262, no. 7-8, pp. 949–957, 2007.
- [94] M. Godet, “Third-bodies in tribology,” *Wear*, vol. 136, no. 1, pp. 29–45, 1990.
- [95] P. Arnaud, S. Fouvry, and S. Garcin, “A numerical simulation of fretting wear profile taking account of the evolution of third body layer,” *Wear*, vol. 376, pp. 1475–1488, 2017.
- [96] P. Arnaud and S. Fouvry, “A dynamical fea fretting wear modeling taking into account the evolution of debris layer,” *Wear*, vol. 412, pp. 92–108, 2018.
- [97] J. Ding, I. McColl, S. Leen, and P. Shipway, “A finite element based approach to simulating the effects of debris on fretting wear,” *Wear*, vol. 263, no. 1-6, pp. 481–491, 2007.
- [98] A. Ghosh, B. Leonard, and F. Sadeghi, “A stress based damage mechanics model to simulate fretting wear of hertzian line contact in partial slip,” *Wear*, vol. 307, no. 1-2, pp. 87–99, 2013.

- [99] S. Basseville, E. Héripré, and G. Cailletaud, “Numerical simulation of the third body in fretting problems,” *Wear*, vol. 270, no. 11-12, pp. 876–887, 2011.
- [100] H. Haddad, M. Guessasma, and J. Fortin, “A dem–fem coupling based approach simulating thermomechanical behaviour of frictional bodies with interface layer,” *International Journal of Solids and Structures*, vol. 81, pp. 203–218, 2016.
- [101] B. D. Leonard, A. Ghosh, F. Sadeghi, S. Shinde, and M. Mittelbach, “Third body modeling in fretting using the combined finite-discrete element method,” *International Journal of Solids and Structures*, vol. 51, no. 6, pp. 1375–1389, 2014.
- [102] I. Iordanoff, Y. Berthier, S. Descartes, and H. Heshmat, “A review of recent approaches for modeling solid third bodies,” *J. Trib.*, vol. 124, no. 4, pp. 725–735, 2002.
- [103] I. Iordanoff, B. Seve, and Y. Berthier, “Solid third body analysis using a discrete approach: influence of adhesion and particle size on macroscopic properties,” *J. Trib.*, vol. 124, no. 3, pp. 530–538, 2002.
- [104] S. Lim and M. Ashby, “Overview no. 55 wear-mechanism maps,” *Acta metallurgica*, vol. 35, no. 1, pp. 1–24, 1987.
- [105] S. Lim, M. Ashby, and J. Brunton, “Wear-rate transitions and their relationship to wear mechanisms,” *Acta metallurgica*, vol. 35, no. 6, pp. 1343–1348, 1987.
- [106] M. Esteves, A. Ramalho, and F. Ramos, “Fretting behavior of the aisi 304 stainless steel under different atmosphere environments,” *Tribology International*, vol. 88, pp. 56–65, 2015.
- [107] A. Ramalho, A. Merstallinger, and A. Cavaleiro, “Fretting behaviour of w–si coated steels in vacuum environments,” *Wear*, vol. 261, no. 1, pp. 79–85, 2006.
- [108] A. Iwabuchi, K. Kato, and T. Kayaba, “Fretting properties of sus304 stainless steel in a vacuum environment,” *Wear*, vol. 110, no. 3-4, pp. 205–216, 1986.
- [109] X. Jin, P. Shipway, and W. Sun, “The role of temperature and frequency on fretting wear of a like-on-like stainless steel contact,” *Tribology Letters*, vol. 65, no. 3, p. 77, 2017.
- [110] X. Jin, P. Shipway, and W. Sun, “The role of frictional power dissipation (as a function of frequency) and test temperature on contact temperature and the subsequent wear behaviour in a stainless steel contact in fretting,” *Wear*, vol. 330, pp. 103–111, 2015.
- [111] P.-J. Cunat, “Alloying elements in stainless steel and other chromium-containing alloys,” 2004.
- [112] A. R. Moustafa, *Mesure thermographique des effets dissipatifs accompagnant le fretting: d’une construction rapide des cartes d’amorçage vers une meilleure compréhension des mécanismes d’endommagement*. PhD thesis, Lyon, 2016.

- [113] R. Abbaschian and R. E. Reed-Hill, *Physical metallurgy principles*. Cengage Learning, 2008.
- [114] G. Speich and W. Leslie, “Tempering of steel,” *Metallurgical Transactions*, vol. 3, no. 5, pp. 1043–1054, 1972.
- [115] S. Fouvry, H. Gallien, and B. Berthel, “From uni-to multi-axial fretting-fatigue crack nucleation: Development of a stress-gradient-dependent critical distance approach,” *International Journal of Fatigue*, vol. 62, pp. 194–209, 2014.
- [116] S. Garcin, S. Fouvry, and S. Heredia, “A fem fretting map modeling: Effect of surface wear on crack nucleation,” *Wear*, vol. 330, pp. 145–159, 2015.
- [117] N. Corporation, “Raman spectroscopy, <https://www.nanophoton.net/raman-spectroscopy/lessons/lesson-1>,” 2020.
- [118] R. M. Cornell and U. Schwertmann, *The iron oxides: structure, properties, reactions, occurrences and uses*. John Wiley & Sons, 2003.
- [119] G. Guillonneau, *Nouvelles techniques de nano-indentation pour des conditions expérimentales difficiles: très faibles enfoncements, surfaces rugueuses, température*. PhD thesis, Ecole Centrale de Lyon, 2012.
- [120] W. C. Oliver and G. M. Pharr, “Measurement of hardness and elastic modulus by instrumented indentation: Advances in understanding and refinements to methodology,” *Journal of materials research*, vol. 19, no. 1, pp. 3–20, 2004.
- [121] A. M. Tobi, J. Ding, G. Bandak, S. Leen, and P. Shipway, “A study on the interaction between fretting wear and cyclic plasticity for ti-6al-4v,” *Wear*, vol. 267, no. 1-4, pp. 270–282, 2009.
- [122] S. Fouvry, P. Duo, and P. Perruchaut, “A quantitative approach of ti-6al-4v fretting damage: friction, wear and crack nucleation,” *Wear*, vol. 257, no. 9-10, pp. 916–929, 2004.
- [123] M. Cheikh, S. Quilici, and G. Cailletaud, “Presentation of ki-cof, a phenomenological model of variable friction in fretting contact,” *Wear*, vol. 262, no. 7-8, pp. 914–924, 2007.
- [124] Y. El Mendili, J.-F. Bardeau, N. Randrianantoandro, A. Gourbil, J.-M. Greneche, A.-M. Mercier, and F. Grasset, “New evidences of in situ laser irradiation effects on γ -fe₂o₃ nanoparticles: a raman spectroscopic study,” *Journal of Raman Spectroscopy*, vol. 42, no. 2, pp. 239–242, 2011.
- [125] O. N. Shebanova and P. Lazor, “Raman study of magnetite (fe₃o₄): laser-induced thermal effects and oxidation,” *Journal of Raman spectroscopy*, vol. 34, no. 11, pp. 845–852, 2003.
- [126] M. Nieuwoudt, J. Comins, and I. Cukrowski, “The growth of the passive film on iron in 0.05 m naoh studied in situ by raman micro-spectroscopy and electrochemical polarisation.

- part i: near-resonance enhancement of the raman spectra of iron oxide and oxyhydroxide compounds,” *Journal of Raman Spectroscopy*, vol. 42, no. 6, pp. 1335–1339, 2011.
- [127] S. J. Oh, D. Cook, and H. Townsend, “Characterization of iron oxides commonly formed as corrosion products on steel,” *Hyperfine interactions*, vol. 112, no. 1-4, pp. 59–66, 1998.
- [128] P. Colomban and A. Slodczyk, “Raman intensity: An important tool to study the structure and phase transitions of amorphous/crystalline materials,” *Optical materials*, vol. 31, no. 12, pp. 1759–1763, 2009.
- [129] A. Cruzado, M. Hartelt, R. Wäsche, M. Urchegui, and X. Gómez, “Fretting wear of thin steel wires. part 1: Influence of contact pressure,” *Wear*, vol. 268, no. 11-12, pp. 1409–1416, 2010.
- [130] R. Merhej, *Impact de la taille du contact sur le comportement tribologique du contact 100Cr6/100Cr soumis à des sollicitations de fretting*. PhD thesis, Ecully, Ecole centrale de Lyon, 2008.
- [131] J. Burwell and C. Strang, “On the empirical law of adhesive wear,” *Journal of Applied Physics*, vol. 23, no. 1, pp. 18–28, 1952.
- [132] N. Welsh, “Frictional heating and its influence on the wear of steel,” *Journal of Applied Physics*, vol. 28, no. 9, pp. 960–968, 1957.
- [133] N. Welsh, “The dry wear of steels i. the general pattern of behaviour,” *Philosophical Transactions of the Royal Society of London. Series A, Mathematical and Physical Sciences*, vol. 257, no. 1077, pp. 31–50, 1965.
- [134] N. Welsh, “The dry wear of steels ii. interpretation and special features,” *Philosophical Transactions of the Royal Society of London. Series A, Mathematical and Physical Sciences*, vol. 257, no. 1077, pp. 51–70, 1965.
- [135] R. Ward, “A comparison of reciprocating and continuous sliding wear,” *Wear*, vol. 15, no. 6, pp. 423–434, 1970.
- [136] E. Hayes and P. Shipway, “Effect of test conditions on the temperature at which a protective debris bed is formed in fretting of a high strength steel,” *Wear*, vol. 376, pp. 1460–1466, 2017.
- [137] B. Van Peteghem, S. Fouvry, and J. Petit, “Effect of variable normal force and frequency on fretting wear response of ti-6al-4v contact,” *Wear*, vol. 271, no. 9-10, pp. 1535–1542, 2011.
- [138] T. Zhu, P. Shipway, and W. Sun, “The dependence of wear rate on wear scar size in fretting; the role of debris (third body) expulsion from the contact,” *Wear*, vol. 440, p. 203081, 2019.

- [139] E. Marc, S. Fouvry, O. Graton, C. Phalippou, and H. Maitournam, “Fretting wear of a nitrided 316l/304l contact subject to in-phase normal force fluctuation in dry and lithium-boron solution: An rp-friction energy wear approach,” *Wear*, vol. 376, pp. 690–704, 2017.
- [140] G. Vaessen, C. Commissaris, and A. De Gee, “Fretting corrosion of cu-ni-al against plain carbon steel,” in *Proceedings of the Institution of Mechanical Engineers, Conference Proceedings*, vol. 183, pp. 125–128, SAGE Publications Sage UK: London, England, 1968.
- [141] M. Varenberg, G. Halperin, and I. Etsion, “Different aspects of the role of wear debris in fretting wear,” *Wear*, vol. 252, no. 11-12, pp. 902–910, 2002.
- [142] S. Jahanmir, N. Suh, and E. Abrahamson, “Microscopic observations of the wear sheet formation by delamination,” *Wear*, vol. 28, no. 2, pp. 235–249, 1974.
- [143] W. T. Becker and R. J. Shipley, “Fretting wear failures,” *ASM handbook*, vol. 11, 2002.
- [144] A. Saulot, I. Iordanoff, C. Safon, and Y. Berthier, “Numerical study of the wear flows in a plane contact,” in *Tribology Series*, vol. 43, pp. 85–93, Elsevier, 2003.
- [145] S. Baydoun, S. Fouvry, S. Descartes, and P. Arnaud, “Fretting wear rate evolution of a flat-on-flat low alloyed steel contact: A weighted friction energy formulation,” *Wear*, vol. 426, pp. 676–693, 2019.
- [146] P. Neumann, “Coarse slip model of fatigue,” *Acta metallurgica*, vol. 17, no. 9, pp. 1219–1225, 1969.
- [147] H. Proudhon, J. Li, F. Wang, A. Roos, V. Chiaruttini, and S. Forest, “3d simulation of short fatigue crack propagation by finite element crystal plasticity and remeshing,” *International Journal of Fatigue*, vol. 82, pp. 238–246, 2016.
- [148] D. Tumbajoy-Spinel, S. Descartes, J.-M. Bergheau, V. Lacaille, G. Guillonneau, J. Michler, and G. Kermouche, “Assessment of mechanical property gradients after impact-based surface treatment: application to pure α -iron,” *Materials Science and Engineering: A*, vol. 667, pp. 189–198, 2016.
- [149] D. Tumbajoy-Spinel, X. Maeder, G. Guillonneau, S. Sao-Joao, S. Descartes, J.-M. Bergheau, C. Langlade, J. Michler, and G. Kermouche, “Microstructural and micromechanical investigations of surface strengthening mechanisms induced by repeated impacts on pure iron,” *Materials & Design*, vol. 147, pp. 56–64, 2018.
- [150] J. Shockley, S. Descartes, P. Vo, E. Irissou, and R. Chromik, “The influence of al₂o₃ particle morphology on the coating formation and dry sliding wear behavior of cold sprayed al-al₂o₃ composites,” *Surface and Coatings Technology*, vol. 270, pp. 324–333, 2015.
- [151] R. W. Zimmerman, “The effect of microcracks on the elastic moduli of brittle materials,” *Journal of materials science letters*, vol. 4, no. 12, pp. 1457–1460, 1985.

- [152] X. Guo, P. Lai, L. Tang, J. Wang, and L. Zhang, “Effects of sliding amplitude and normal load on the fretting wear behavior of alloy 690 tube exposed to high temperature water,” *Tribology International*, vol. 116, pp. 155–163, 2017.
- [153] M. Lgried, T. Liskiewicz, and A. Neville, “Electrochemical investigation of corrosion and wear interactions under fretting conditions,” *Wear*, vol. 282, pp. 52–58, 2012.
- [154] J. Hintikka, A. Lehtovaara, and A. Mäntylä, “Fretting-induced friction and wear in large flat-on-flat contact with quenched and tempered steel,” *Tribology International*, vol. 92, pp. 191–202, 2015.
- [155] R. Neu, “Progress in standardization of fretting fatigue terminology and testing,” *Tribology International*, vol. 44, no. 11, pp. 1371–1377, 2011.
- [156] J. Juoksukangas, V. Nurmi, J. Hintikka, M. Vippola, A. Lehtovaara, A. Mäntylä, J. Vaara, and T. Frondelius, “Characterization of cracks formed in large flat-on-flat fretting contact,” *International Journal of Fatigue*, vol. 124, pp. 361–370, 2019.
- [157] S. Baydoun and S. Fouvry, “An experimental investigation of adhesive wear extension in fretting interface: Application of the contact oxygenation concept,” *Tribology International*, vol. 147, p. 106266, 2020.
- [158] S. Baydoun, P. Arnaud, and S. Fouvry, “Modelling adhesive wear extension in fretting interfaces: An advection-dispersion-reaction contact oxygenation approach,” *Tribology International*, p. 106490, 2020.
- [159] H. Abuluwefa, R. Guthrie, and F. Ajersch, “Oxidation of low carbon steel in multicomponent gases: Part i. reaction mechanisms during isothermal oxidation,” *Metallurgical and Materials Transactions A*, vol. 28, no. 8, pp. 1633–1641, 1997.
- [160] H. Abuluwefa, “Kinetics of high temperature oxidation of high carbon steels in multi-component gases approximating industrial steel reheat furnace atmospheres,” *Lecture notes in engineering and computer science*, 2012.
- [161] T. Benham, E. Leheup, and J. Moon, “The effect of debris chemistry on the debris formation and fretting behaviour of mild steel in co2 containing oxygen and water vapour,” *Wear*, vol. 177, no. 2, pp. 195–202, 1994.
- [162] V. Stein, J. Hettiaratchi, and G. Achari, “Numerical model for biological oxidation and migration of methane in soils,” *Practice Periodical of Hazardous, Toxic, and Radioactive Waste Management*, vol. 5, no. 4, pp. 225–234, 2001.
- [163] H. P. G. Darcy, *Les Fontaines publiques de la ville de Dijon. Exposition et application des principes à suivre et des formules à employer dans les questions de distribution d’eau, etc.* V. Dalamont, 1856.
- [164] C. K. Ho and S. W. Webb, *Gas transport in porous media*, vol. 20. Springer, 2006.

- [165] J. Dalton, “Xxvii. new theory of the constitution of mixed gases elucidated,” *The Philosophical Magazine*, vol. 14, no. 54, pp. 169–173, 1802.
- [166] C. Wilke, “A viscosity equation for gas mixtures,” *The journal of chemical physics*, vol. 18, no. 4, pp. 517–519, 1950.
- [167] J. Kozeny, “Über kapillare leitung der wasser in boden,” *Royal Academy of Science, Vienna, Proc. Class I*, vol. 136, pp. 271–306, 1927.
- [168] P. C. Carman, “Flow of gases through porous media,” *Butterworths Scientific Publications*, 1956.
- [169] M. S. Costanza-Robinson and M. L. Brusseau, “Gas-phase dispersion in porous media,” in *Gas Transport in Porous Media*, pp. 121–132, Springer, 2006.
- [170] A. Fick, “Über diffusion ann,” *Phys., Lpz*, vol. 170, p. 59–86, 1855.
- [171] D. Fairbanks and C. Wilke, “Diffusion coefficients in multicomponent gas mixtures,” *Industrial & Engineering Chemistry*, vol. 42, no. 3, pp. 471–475, 1950.
- [172] N. H. Chen and D. Othmer, “New generalized equation for gas diffusion coefficient.,” *Journal of Chemical and Engineering Data*, vol. 7, no. 1, pp. 37–41, 1962.
- [173] A. Kia, H. S. Wong, and C. R. Cheeseman, “Clogging in permeable concrete: A review,” *Journal of Environmental Management*, vol. 193, pp. 221–233, 2017.
- [174] P. Moldrup, C. Kruse, D. Rolston, and T. Yamaguchi, “Modeling diffusion and reaction in soils: Iii. predicting gas diffusivity from the campbell soil-water retention model,” *Soil science*, vol. 161, no. 6, pp. 366–375, 1996.
- [175] D. Werner, P. Grathwohl, and P. Höhener, “Review of field methods for the determination of the tortuosity and effective gas-phase diffusivity in the vadose zone,” *Vadose Zone Journal*, vol. 3, no. 4, pp. 1240–1248, 2004.
- [176] M. S. Costanza-Robinson and M. L. Brusseau, “Gas phase advection and dispersion in unsaturated porous media,” *Water Resources Research*, vol. 38, no. 4, pp. 7–1, 2002.
- [177] P. J. Binning, D. Postma, T. Russell, J. Wesselingh, and P. Boulin, “Advective and diffusive contributions to reactive gas transport during pyrite oxidation in the unsaturated zone,” *Water Resources Research*, vol. 43, no. 2, 2007.
- [178] J. F. Pickens and G. E. Grisak, “Scale-dependent dispersion in a stratified granular aquifer,” *Water Resources Research*, vol. 17, no. 4, pp. 1191–1211, 1981.
- [179] É. Clapeyron, “Mémoire sur la puissance motrice de la chaleur,” *Journal de l’École polytechnique*, vol. 14, pp. 153–190, 1834.

- [180] G. Straffelini and A. Molinari, “Dry sliding wear of ti-6al-4v alloy as influenced by the counterface and sliding conditions,” *Wear*, vol. 236, no. 1-2, pp. 328–338, 1999.
- [181] T. Jibiki, M. Shima, H. Akita, and M. Tamura, “A basic study of friction noise caused by fretting,” *Wear*, vol. 251, no. 1-12, pp. 1492–1503, 2001.
- [182] D. G. Poitout *et al.*, “Biomechanics and biomaterials in orthopedics,” 2004.
- [183] B. Bhushan, *Principles and applications of tribology*. John Wiley & Sons, 1999.
- [184] Y. Zhang, G. Mollon, and S. Descartes, “Significance of third body rheology in friction at a dry sliding interface observed by a multibody meshfree model: Influence of cohesion between particles,” *Tribology International*, p. 106188, 2020.
- [185] A. Kirk, P. Shipway, W. Sun, and C. Bennett, “Debris development in fretting contacts—debris particles and debris beds,” *Tribology International*, p. 105592, 2019.
- [186] L. Blades, D. Hills, D. Nowell, K. E. Evans, and C. Smith, “An exploration of debris types and their influence on wear rates in fretting,” *Wear*, p. 203252, 2020.
- [187] A. Yu and R. Zou, “Prediction of the porosity of particle mixtures,” *KONA Powder and Particle Journal*, vol. 16, no. 0, pp. 68–81, 1998.
- [188] N. Ouchiyama and T. Tanaka, “Porosity estimation from particle size distribution,” *Industrial & engineering chemistry fundamentals*, vol. 25, no. 1, pp. 125–129, 1986.
- [189] P. W. Glover, “Petrophysics,” *University of Aberdeen, UK*, 2000.
- [190] A. Schofield and C. Wroth, “On the yielding of soils,” *Géotechnique*, vol. 8, pp. 22–53, 1958.
- [191] D. Poquillon, J. Lemaitre, V. Baco-Carles, P. Tailhades, and J. Lacaze, “Cold compaction of iron powders—relations between powder morphology and mechanical properties: Part i: Powder preparation and compaction,” *Powder Technology*, vol. 126, no. 1, pp. 65–74, 2002.
- [192] A. S. Khanna, *Introduction to high temperature oxidation and corrosion*. ASM international, 2002.
- [193] F. P. Bowden, F. P. Bowden, and D. Tabor, *The friction and lubrication of solids*, vol. 1. Oxford university press, 2001.
- [194] A. Dreano, S. Fouvry, and G. Guillonneau, “Understanding and formalization of the fretting-wear behavior of a cobalt-based alloy at high temperature,” *Wear*, p. 203297, 2020.

AUTORISATION DE SOUTENANCE

Vu les dispositions de l'arrêté du 25 mai 2016,

Vu la demande du directeur de thèse

Monsieur S. FOUVRY

et les rapports de

M. P. SHIPWAY

Professeur - University of Nottingham - Room D2 Coates - University Park
Nottingham NG7 2RD - Royaume-Uni

et de

Mme C. LANGLADE

Professeur - Université de Technologie de Montbéliard - Bureau S207 - Pavillon S
Rue de Leupe - 90400 Sevenans

Madame BAYDOUN Soha

est autorisée à soutenir une thèse pour l'obtention du grade de **DOCTEUR**

Ecole doctorale Matériaux

Fait à Ecully, le 10 novembre 2020

P/Le directeur de l'E.C.L.
Le directeur des Etudes

Grégory VIAL
Directeur des études
École Centrale de Lyon

Grégory VIAL

